Computational modelling and analysis of coupled adhesion and friction in gecko spatula peeling

A Thesis Submitted
In Partial Fulfilment of the Requirements
for the Degree of
Doctor of Philosophy
by

Saipraneeth Gouravaraju
Roll No. 146103016

Department of Mechanical Engineering
Indian Institute of Technology Guwahati
Guwahati - 781039, India
October 2020

भारतीय प्रौद्योगिकी संस्थान गुवाहाटी
Indian Institute of Technology Guwahati

Declaration

I hereby declare that the information presented in the thesis titled **"Computational modelling and analysis of coupled adhesion and friction in gecko spatula peeling"** is entirely my own account of the research under the guidance of Dr. Sachin Singh Gautam. No part of this work has been submitted for the award of any degree, diploma, associate-ship, fellowship or its equivalent to any University or Institution. I have not violated any copyright and plagiarism law. In keeping with the general practice of reporting scientific observations, due acknowledgements have been made wherever the work described is based on the findings of other researchers.

October 2020 **Saipraneeth Gouravaraju**

भारतीय प्रौद्योगिकी संस्थान गुवाहाटी
Indian Institute of Technology Guwahati

Certificate

This is to certify that the thesis entitled **"Computational modelling and analysis of coupled adhesion and friction in gecko spatula peeling"** submitted by **Saipraneeth Gouravaraju**, Roll No. 146103016, to the Indian Institute of Technology Guwahati, for the award of the degree of Doctor of Philosophy in Mechanical Engineering, has been carried out by him under my supervision and guidance. The results contained in this thesis have not been submitted in part or full to any other University or Institute for award of any degree.

October 2020

Dr. Sachin Singh Gautam
Assistant Professor
Department of Mechanical Engineering
Indian Institute of Technology Guwahati
Guwahati - 781039, India.

भारतीय प्रौद्योगिकी संस्थान गुवाहाटी
Indian Institute of Technology Guwahati

Acknowledgements

This work has been possible only because of very many people who have helped me in various aspects of PhD work as well as life in general. Firstly, I am thankful to my supervisor Dr. Sachin Singh Gautam, whose ideas and encouragement helped me to stay focused, learn, adapt, and apply my efforts to always move forward in my research. I want to express my gratitude also to my Doctoral Committee members Prof. Dixit, Dr. Sharma, and Dr. Gooh Pattader. Their valuable inputs and encouragement have been beneficial in improving my research work.

I am also indebted to Prof. Ganguli (of IISc Bangalore), who first showed me the ropes in research during my time as a research assistant. Without that experience, I would not have acquired the research skills, which helped me in my PhD. I am very fortunate to have collaborated with Prof. Sauer (of RWTH Aachen, Germany). His immense knowledge and rigorous inputs have helped me in looking at my research work from a different perspective. I am also grateful to Dr. David Labonte (of Imperial College London) for his valuable feedback on my research work.

I would also like to thank my co-author Jyotindra for sharing his knowledge with me. I am grateful to Vishal and Kaushik for their friendship, support, so many enjoyable times, discussions on everything under the sun, and helping me in getting through stressful times. Without my lab mates Utpal, Shashi, Subhajit, Raktim, Purushottam, and Prateek, life in the lab would've been boring and monotonous. I am also thankful to my friend Sripal for countless discussions on our mutual interest.

Without the continued support and encouragement of my parents and my brother, I would not have been able to fulfil any of my goals.

भारतीय प्रौद्योगिकी संस्थान गुवाहाटी
Indian Institute of Technology Guwahati

Abstract

A systematic investigation of the coupled adhesion and friction in gecko spatula peeling from a flat, rigid substrate is carried out using a computational model. A framework capable of resolving atomic-scale interactions as well as the finite deformations of the interacting bodies is developed within the setting of nonlinear finite element (FE) analysis. A surface enrichment strategy is employed to accurately and efficiently capture the nonlinear van der Waals forces at the interface.

It is shown that partial sliding of the spatula in the peeling zone stretches the spatula, increasing its strain energy. This increase in strain energy is much higher for low peeling angles, which leads to an increase in the maximum pull-off forces. The spatula is shown to detach at a constant critical detachment angle, irrespective of the peeling angle and the shaft angle. It is also shown that the "frictional adhesion" behaviour, until now only observed from seta to toe levels, is also present at the spatula level. A detailed parametric study is carried out to investigate the influence of various parameters – such as the peeling angle, spatula shaft angle, spatula pad thickness, material stiffness, friction coefficient, and shaft length – on the pull-off forces and the critical detachment angle. It is shown that increasing the pad thickness beyond a certain level does not lead to a significant increase in the pull-off forces. Further, for pad thickness greater than 10 nm, for large peeling and shaft angles, the sliding of the spatula on the substrate is not observed. This behaviour is found to influence the invariance of the critical detachment angle. Even though decreasing the material stiffness, increases the pull-off forces due to the increase in compliance, it also increases the stresses inside the narrow peeling zone, which could potentially lead to material failure. For small friction coefficients, it is observed that the pull-off forces remain constant at low peeling angles. It has also been observed that the critical detachment angle remains invariant for a wide range of spatula shaft lengths. Comparison of the FE simulations using two-dimensional (2D) and three-dimensional (3D) spatula models strongly indicates that the 2D model can capture almost all the essential features of the peeling behaviour.

Bayesian regularization based backpropagation learning method is used to train an artificial neural network (ANN) models to predict certain aspects of the spatula peeling behaviour. It is shown that by augmenting the FE models with ANNs, a significant reduction in computational cost can be achieved without compromising on the accuracy.

Since the current computational framework is not limited by geometrical, kinematical, and material restrictions, it can be applied to analyse various features of the gecko adhesive system as well as similar biological adhesive systems.

भारतीय प्रौद्योगिकी संस्थान गुवाहाटी
Indian Institute of Technology Guwahati

Contents

भारतीय प्रौद्योगिकी संस्थान गुवाहाटी
Indian Institute of Technology Guwahati

List of Figures

भारतीय प्रौद्योगिकी संस्थान गुवाहाटी
Indian Institute of Technology Guwahati

List of Tables

भारतीय प्रौद्योगिकी संस्थान गुवाहाटी
Indian Institute of Technology Guwahati

Nomenclature

Latin symbols

A_{H}	Hamaker constant
A_k	Area in reference configuration
A_{pad}	Area of the spatula pad
$\mathbf{a}^l$	Output vector of layer l in a neural network
$\mathbf{a}_{\mathrm{o}}$	Predicted output vector of a neural network
$\boldsymbol{a}_\alpha$	Co-variant tangent vector
$\boldsymbol{a}^\alpha$	Contravariant tangent vector
a_k	Area in current configuration
$\boldsymbol{B}$	Left Green-Cauchy strain tensor
$\mathbf{b}$	Bias vector in neural network
b	Width of a strip
$\boldsymbol{C}$	Right Cauchy-Green deformation tensor
d_{sh}	Diameter of the spatula shaft
$\boldsymbol{E}$	Green-Lagrange strain tensor
E'	Storage modulus
E''	Loss modulus
E^*	Complex elastic modulus
E_0	Young's modulus
E_D	Sum of squared errors of a neural network
E_W	Sum of squared weights of a neural network
$\mathbf{e}$	Error vector of a neural network
$\boldsymbol{F}$	Deformation gradient
F_ϕ	Force between two particles corresponding to Lennard-Jones potential
$F_{\mathrm{N}}, F_\perp$	Normal or adhesive force

$\boldsymbol{F}_{\text{res}}$, F_{res}	Resultant pull-off force vector, its magnitude
F_{T}, $F_{\parallel}$	Tangential or frictional force
F_{vdw}	van der Waals force
$\mathbf{f}_{\text{c}}$	Contact force vector
$\mathbf{f}_{\text{ext}}$	External force vector
$\mathbf{f}_{\text{int}}$	Internal force vector
$\mathbf{f}^{l}$	Activation function at layer l in a neural network
f_{s}	Slip function
$\mathbf{H}$	Hessian matrix
h	Height (Thickness) of the strip or spatula pad
$\boldsymbol{I}$	Identity tensor
$\mathbf{I}_{d}$	Identity matrix of dimension d
$\boldsymbol{J}^{e}$	Transformation gradient from master element to the initial configuration
J	Jacobian
J_{c}	Surface stretch
$\boldsymbol{j}^{e}$	Transformation gradient from master element to current configuration
$\mathbf{k}$	System tangent matrix
$\mathbf{k}_{\text{int}}$	Internal tangent matrix
$\mathbf{k}_{\text{c}}$	Contact tangent matrix
L	Length of the strip
L_{pad}	Length of the spatula pad
L_{sh}	Length of the spatula shaft
M_{b}	Bending (peeling) moment
$\boldsymbol{N}_{k}$	Normal to the surface of body $\mathcal{B}_{k}$ in its reference configuration
$\mathbf{N}^{e}$	Shape function array of element e
N^{l}	Number of neurons in layer l in a neural network
$\boldsymbol{n}_{k}$	Normal to surface of body $\mathcal{B}_{k}$ in the current configuration
$\boldsymbol{n}_{\text{p}}$	Normal to the surface at the projection point $\boldsymbol{x}_{\text{p}}$
n_{el}	Number of finite elements
n_{sel}	Number of surface finite elements
n_{t}	Number of input and target vector pairs in a neural network
$\boldsymbol{P}$	First Piola-Kirchoff stress tensor
R, R_{sp}	Radius of the spatula
R_{0}	Global length scale
r	Distance between two interacting particles
r_{0}	Equilibrium distance of Lennard-Jones potential

r_{asp}	Curvature of the asperity
r_{JKR}	Contact radius obtained by JKR model
r_{eq}	Equilibrium distance between two interacting surfaces
r_{max}	Distance at which the absolute value of adhesive traction is maximum
r_s	Minimum distance between neighbouring bodies
$\boldsymbol{r}_{\text{T}}$	Total tangential slip
$\boldsymbol{r}_{\text{T}}^{\text{e}}$	Elastic sticking tangential slip
$\boldsymbol{r}_{\text{T}}^{\text{s}}$	Inelastic sliding tangential slip
$\boldsymbol{S}$	Second Piola-Kirchoff stress tensor
$\mathbf{s}$	Sensitivity of a neural network
$\boldsymbol{T}_{\text{a}}$	Adhesive traction
$\boldsymbol{T}_{\text{f}}$	Tangential traction
$\mathbf{t}_{\text{o}}$	Target output vector
T_{slide}	Sliding threshold
$\bar{\boldsymbol{u}}$	Applied displacement vector
$\mathbf{u}^e$	Nodal displacement vector of element e
$\mathbf{v}^e$	Nodal displacement variation vector of element e
$\mathbf{W}$	Weight matrix of an artificial neural network
W	Strain energy density function
$\bar{\mathbf{w}}$	Vector containing all the weights and biases of the neural network
w_{pad}	Width of the spatula pad
$\boldsymbol{X}$	Position Vector in the reference configuration
$\mathbf{X}^e$	Nodal position vector of element e in the initial configuration
$\mathbf{x}^e$	Nodal position vector of element e in the current configuration
$\boldsymbol{x}$	Position vector in the current configuration
$\boldsymbol{x}_{\text{p}}$	Position vector of project point

Greek Symbols

α	Resultant force angle
α^*	Critical detachment angle
α_{FT}	Adhesion parameter of Fuller and Tabor
β_{k0}	Particle density of body $\mathcal{B}_k (k = 1, 2)$ in the reference configuration
β_k	Particle density of body $\mathcal{B}_k (k = 1, 2)$ in the current configuration
γ	Plastic parameter
$\gamma_{\mathrm{L}}, \gamma_{\mathrm{W}}$	Material parameters
γ_{ep}	Number of effective parameters
δ_{ij}	Kronecker delta
ϵ	Energy scale of the Lennard-Jones potential
ε_{T}	Tangential penalty parameter
θ	Applied rotation angle
θ_{p}	Peeling angle
θ_{sh}	Spatula shaft angle
Λ	Lamé parameter
λ_{LM}	Levenberg-Marquardt damping factor
μ	Lamé parameter
μ_{r}	Regularization parameter
μ_{s}	Friction coefficient
μ_{Tabor}	Tabor parameter
ν	Poisson's ratio
ν_{r}	Regularization parameter
$\boldsymbol{\xi}$	Position vector of a point in two-dimensional parametric space
Π	Total potential energy
Π_{a}	Adhesion potential energy
Π_{int}	Internal potential energy
Π_{ext}	External potential energy
ρ_{k0}	Mass density of body $\mathcal{B}_k (k = 1, 2)$ in the reference configuration
τ_0	Critical shear stress
Φ_k	Adhesion potential field enveloping body $\mathcal{B}_k (k = 1, 2)$
ϕ	Lennard-Jones potential
φ	Deformation mapping
$\delta\varphi$	Variation of the deformation mapping
ϕ_m	Morse potential

Ω_{k0}	Domain of body $\mathcal{B}_k (k = 1, 2)$ in the reference configuration
Ω_k	Domain of body $\mathcal{B}_k (k = 1, 2)$ in the current configuration
$\partial\Omega_{k0}$	Surface of body $\mathcal{B}_k (k = 1, 2)$ in the reference configuration
$\partial\Omega_k$	Surface of body $\mathcal{B}_k (k = 1, 2)$ in the current configuration

Special symbols

$\mathcal{B}_k$	Interacting body
$\mathbb{C}$	Fourth-order material elasticity tensor
$\mathbb{C}_v$	Fourth-order material elasticity tensor in Voigt notation
$\mathbb{c}$	Fourth-order material elasticity tensor
$\mathbb{c}_v$	Fourth-order material elasticity tensor in Voigt notation
$\mathcal{D}_{\mathrm{s}}$	Dissipation due to inelastic slip
$\boldsymbol{\mathcal{I}}$	Fourth-order tensor
$\mathbb{I}$	Fourth-order identity tensor
$\mathcal{P}$	Two-dimensional parametric space

Mathematical symbols

$[\,.\,]$	Matrix representation of a tensor
$[\,.\,]^e$, $\{\,.\,\}^e$	Matrix, column vector containing nodal values of an element e
$[\,.\,]^T$, $\{\,.\,\}^T$	Transpose of a matrix, vector
$\lvert\,.\,\rvert$	Absolute value of a quantity
$\lVert\,.\,\rVert$	Norm of a matrix or vector
$\Delta(.)$	Incremental quantity
$(.)^t$	Quantity evaluated at time t
$(.)^{t+\Delta t}$	Quantity evaluated at time $t + \Delta t$
$\delta(.)$	Variation of a quantity
$\mathrm{d}(.)$	Differential of a quantity
$\partial(.)$	Partial derivative of a quantity
∇	Gradient operator
,	Partial Differentiation if the following subscript is a letter; for example $\mathbf{N}^e{}_{,x} = \frac{\partial \mathbf{N}^e}{\partial x}$

भारतीय प्रौद्योगिकी संस्थान गुवाहाटी
Indian Institute of Technology Guwahati

Chapter 1

Introduction

The extraordinary locomotion ability of geckos on all kinds of surfaces in nature and their ability to stick to surfaces even in an inverted position has long fascinated humankind. This fascination to understand and mimic gecko adhesion has generated a vast amount of scientific literature in the last two centuries. However, gecko adhesion research has greatly accelerated since the turn of the 21st century following the breakthrough work of Autumn et al. [1, 2], which revealed the clinging mechanism at the micro and nanoscales. This elucidation of adhesion mechanics led to a renewed interest in studying gecko adhesion and locomotion through the lenses of biology, material science, physics, micro and nanoscale engineering. Further, it has been revealed that gecko adhesive pads exhibit remarkable properties such as reversible and anisotropic adhesion, material independent adhesion, self-cleaning, anti-self matting [3]. This knowledge of gecko adhesion has inspired researchers to design and manufacture gecko-inspired synthetic adhesives that have found their way into a wide variety of applications (see Fig. 1.1) such as wall climbing robots [4–8], wearable medical devices [9], adhesive grippers for reduced gravity and space applications [10–12], and human climbing aides [13, 14].

1.1 Background on gecko adhesion

In the course of evolution, Gekkonid lizards (Geckos) started diverging from other lizards over two hundred million years ago [15]. Then, at least a hundred million years ago, geckos started evolving adhesive structures on their toe pads [16]. Although the adhesion capabilities of geckos were known to humans since the time of Aristotle [17], adhesive pad morphology has been discovered only in the 19th century [18–20]. These adhesive pads are found to have overlapping plate-like structures referred to as scansors, which are populated by microscopic keratinous hair-like outgrowths called setae [21].

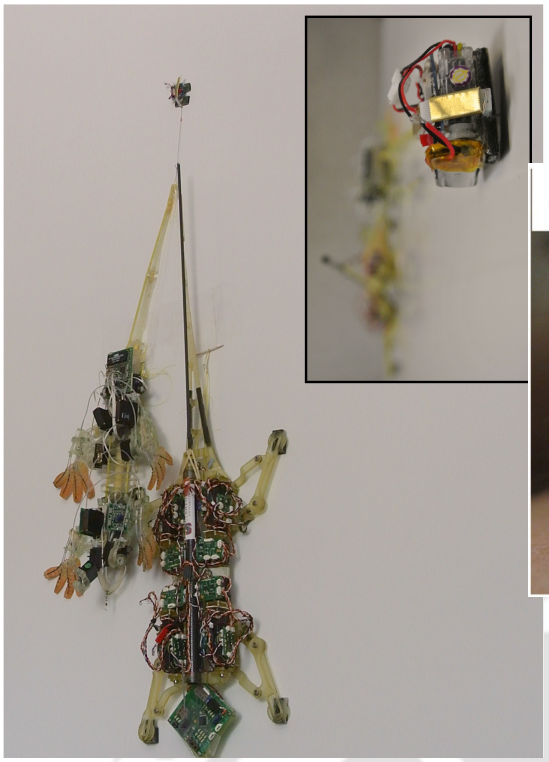

(a)

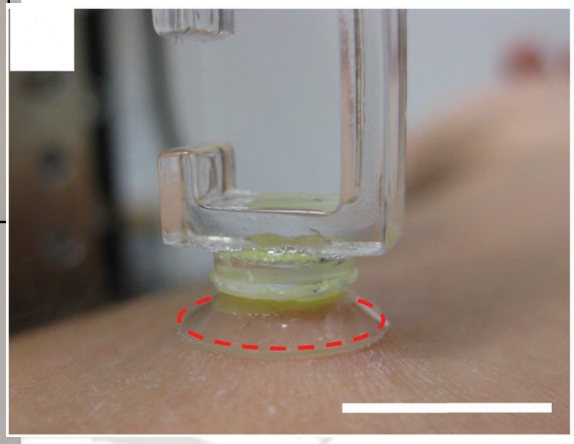

(b)

(c)

Figure 1.1: Applications of gecko synthetic adhesives (a) A miniature 9 g µtugbot climber hoisting two other gecko inspired robots Stickybot I and Stickybot III (Inset, View from the ceiling, looking down at the robots). *Source: Biomimetics and Dexterous Manipulation Lab, Stanford University*; (b) An attached skin-adhesive film to human forearm; dashed red line indicates the interfacing border between the adhesive film and the skin. Scale bar: 1 cm. Reproduced with permission from Drotlef et al. [9] ; (c) Catching objects in microgravity using a gecko inspired adhesive gripper. Reproduced with permission from Jiang et al. [10].

With advances in instrumentation, researchers were able to conduct functional studies of adhesive pad morphology, and various hypotheses were put forward to explain how geckos cling to different surfaces. Initially, two major theories of adhesion mechanism were advanced, viz. adhesive secretion and suction. However, Cartier [20] disproved the adhesive secretion theory citing the absence of secretory glands. The theory of scansors acting like suction cups and generating vacuum was widely suggested [18, 19, 21–23]. Whereas, Schmidt [24] believed that electrostatic attraction was the key to gecko adhesion. However, Dellit [25] disproved the vacuum hypothesis using carefully conducted experiments in a vacuum and showed that there was no difference in clinging forces as compared to normal conditions. Dellit [25] also refuted Schmidt's [24] electrostatic force theory by using X-rays to ionise the atmosphere and yet geckos still adhered to the surfaces. Dellit advanced the hypothesis that the geckos use setae as hooks to interlock with microscopic irregularities (surface roughness) in the surface. At the beginning of the 20^{th} century, Haase [26] hypothesized that intermolecular forces (*adhäsion*) are responsible for attachment. Haase [26] also observed that adhesion depended on the load and occurred only in the proximal direction (towards the animal), i.e. along the axis of the toe. Hora [27] observed that gecko attached to the surface only when the gecko is dragged backwards on a substrate and theorised that setae work simply as frictional devices with a very high coefficient of friction. Mahendra [28] performed various experiments on Indian house-gecko and reviewed various adhesion theories of that time. He criticized Haase's [26] hypothesis of intermolecular forces as it could not explain how a gecko can generate such high intermolecular forces and yet is able to detach quickly facilitating its rapid locomotion. Further, Mahendra [28] also objected to Hora's [27] theory of attachment via frictional forces following which it would be impossible for the gecko to stay attached on a vertical surface. With gravitational force acting vertically downwards, there is no normal force pressing down on the gecko pads to generate friction. Based on his experimental observations, Mahendra [28] agreed with Dellit's theory of setae interlocking.

Maderson [29] examined the setal structures on adhesive pads of a tokay gecko (*Gekko gecko*) more closely using a light microscope. He observed that the setae are very long and thin structures and have further terminal structures on them. Based on his observations, he cast doubts on the hypotheses of Mahendra [28] and Altevogt [30] that the adhesion is achieved by using the setae as hooks. Although light microscopy could not resolve the terminal structures on the setae, Maderson [29] observed that they are of the order 0.5 µm - 0.1 µm. Hence, Maderson [29] argued that it is not possible that the setae can be used as hooks to cling to the surface of the glass as there is no evidence that glass has irregularities of size comparable to that of terminal structures. Further, Maderson argued that electrostatic forces could not be ruled out as an adhesion mechanism.

Ruibal and Ernst [31], for the first time, used scanning electron microscopy to resolve the entire hierarchical pad morphology of geckos and anoline lizards. The authors have observed that in the case of anoline lizards, each seta terminates in a single spatula-like structure with width in the range of 0.6 - 0.8 μm. However, in case of tokay gecko, each seta on the adhesive pad branches into hundreds of flat nanoscale spatula-like structures (Figure 1.2) having a maximum width of 0.28 μm. This discovery of a large number of spatulae on setae, Ruibal and Ernst [31] argued, refutes the hypothesis of climbing by setae interlocking as pointed out previously by Maderson [29]. They proposed that adhesion appears to be due to friction. Previously, Dellit [25] observed that the setae of geckos are proximally curved, i.e. towards the animal and that, as pointed out by Haase [26] and Hora [27], attachment occurs only when the pads (and hence setae) are dragged proximally. As such, Dellit favoured the theory of setae interlocking. Ruibal and Ernst [31], however, observed that proximal dragging of the pads in anoline lizards exerts a tension on the seta and straightens it, which causes the spatula to flattens against the substrate. Thus increasing the area of contact and hence the frictional force. The authors believed that similar surface phenomenon happens in case of geckos and aids in their attachment to a wide variety of substrates.

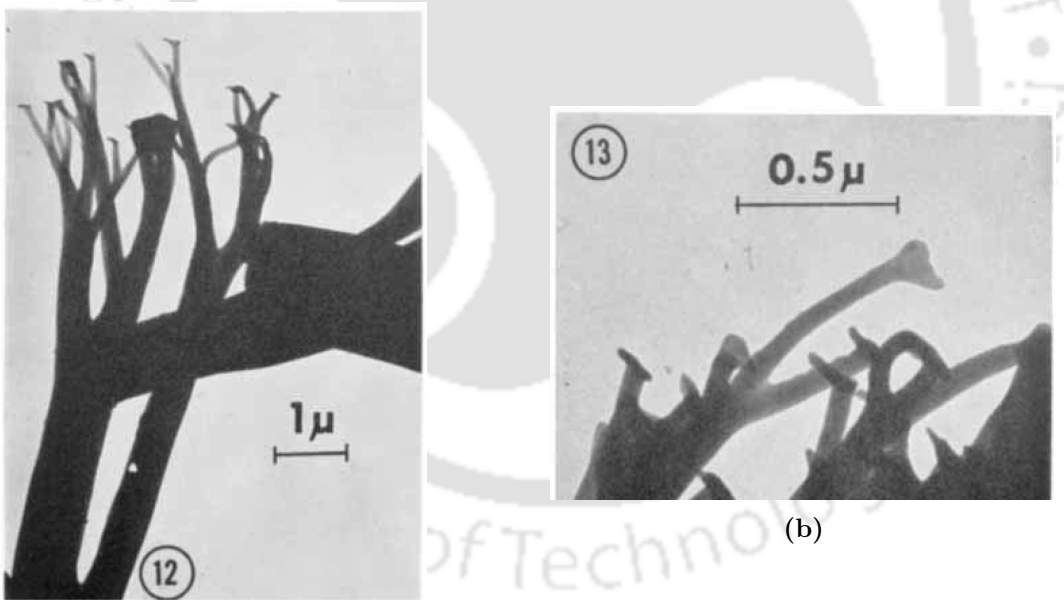

(a) (b)

Figure 1.2: Electron microscopy images of a single seta of a tokay gecko (*Gekko gecko*): (a) Terminal branching of the seta displaying spatular ends; (b) Enlarged view of the spatulae. Reproduced with permission from Ruibal and Ernst [31].

A turning point in gecko adhesion research came about with Hiller's [32–34] series of observational and experimental investigations into functional morphology of gecko adhesive system using scanning electron microscopy. He studied gecko adhesion on different substrates with varying surface tensions. It was observed that clinging

ability is directly proportional to the free surface energy of the surface. Hiller's experiments revealed that the setae adhered more strongly to hydrophilic surfaces when compared to hydrophobic surfaces. These observations strongly implied that as the surface energy increased, the adhesive strength increased. Based on these results, Hiller [32–34] argued that geckos employ intermolecular forces to adhere to surfaces as hypothesized first by Haase [26]. However, Hiller commented that which type of intermolecular forces are the dominant mechanism needs to be determined.

Stork [35] studied the adhesion of beetles *Chrysolina Polita*, which also contain fibrillar (hairy) structures on their legs, on different surfaces. Based on his observations, Stork suggested that beetles and in general many animals which employ fibrillar structures to adhere most likely make use of molecular adhesion with the substrate. Further, he argued that particularly van der Waals forces are more likely to be the mechanism of adhesion as they are present all the time. Stork observed that although van der Waals forces are weak, the sheer number of nanoscale spatulae making intimate contact with substrates could generate huge adhesive forces. Stork also observed that a thin fluid layer probably increases the adhesive forces due to capillary forces, but a thicker fluid layer reduces the adhesion due to intermolecular forces. Irschick et al. [36] conducted a comparative phylogenetic analysis of different lizard species having adhesive pads to understand the correlation between the attachment forces generated by the whole animal, total subdigital pad area, and body mass. It was observed that clinging ability is directly related to the pad area, even without considering the effect of body size. The clinging force increased more rapidly than the pad area as the body size is increased. However, it was observed that after removing the body size effects, 50% of the variation in clinging ability could not be explained. Out of the fourteen lizards tested by Irschick et al. [36], the tokay gecko (*Gekko gecko*) has the largest body mass of ≈ 43 g, pad area of ≈ 227 mm^2, and its two front feet can generate a total force of ≈ 20 N, which is almost 50 times its body weight. The tokay geckos are the heaviest animals known to employ hierarchical fibrillar structures to adhere [37]. Indeed, most of the insights into gecko adhesion have been obtained due to extensive studies carried out on the tokay gecko. More detailed reviews about the history and the development of the understanding of gecko adhesive structures and their function can be found in the papers by Russell [38], Autumn and Peattie [39], Autumn [40], Autumn et al. [15], Russell et al. [41], and the references therein.

1.2 Progress in gecko adhesion research

Although there was a general understanding of gecko adhesion mechanism (intermolecular forces), until Autumn et al.'s [1] work, there has been no significant

effort in reconciling the animal level adhesion, and the way setae are deployed at the microscopic level. Also, which type of the intermolecular forces (e.g. capillary forces, van der Waals forces) are actually responsible for gecko adhesion was also not clear. For the first time, Autumn et al. [1] performed experiments on an isolated seta of the tokay gecko and measured the clinging force it generates. Autumn et al. [1] used microelectromechanical (MEMS) force measurement methods the clinging force generated by a single seta of the tokay gecko as shown in Figure 1.3.

Initially, when the seta is brought into contact with the substrate and is removed by applying a perpendicular load, it did not adhere to the surface. Also, when the seta is dragged against its natural curvature, it resulted in forces as small as 0.3 μN. However, when the seta is pressed into the surface with some preload a shear force of ≈ 40 μN is measured, which is six times the clinging force predicted by Irschick et al.'s [36] whole-animal measurements. Further, with a maximum perpendicular preload of 15 μN and a maximum parallel drag of 5 μm, the shear force measured increased significantly to 194 ± 25 μN. This increase in the force generated is due to the fact that with a preload and subsequent parallel drag the pads of the terminal spatulae at the end of the seta come into contact with the substrate thus increasing the area over which the adhesive forces are acting.

Despite generating such large forces, Autumn et al. [1] found that, as the seta is pulled away from the surface of a wire as shown in Figure 1.3(G), the seta detached when the angle that the setal shaft makes with the wire surface is increased above $30.6 \pm 1.8°$. Further, Autumn et al. [1] found that this detachment angle varied only by 15% over a wide range of perpendicular forces. Moreover, as the detachment angle is increased above 30°, the seta detached instantaneously without any measurable force. This easy detachment behaviour is also observed by theoretical [42] and computational [43] models analysing the seta attachment and detachment. Sitti and Fearing [42] modelled the seta as a cantilever beam with a spherical spatula end. According to their model, just by changing the direction of the applied pull-off force, the contact between the spatula and the substrate can be broken easily. Inspired from the hierarchical structure of the gecko adhesive system, Sitti and Fearing [42] also proposed different methods to fabricate synthetic gecko setae and spatulae. They discussed different design parameters to achieve better adhesion such as the orientation of the setae, compliance to stick to a rough surface, material stiffness, and density for ensuring non-matting. Gao et al. [43] studied the design of gecko seta, which enables it strong attachment and easy detachment using a finite element (FE) model of the seta. The interaction between the seta and a rigid substrate is modelled by employing cohesive elements at the interacting interface. It is observed that when the seta is pulled at an angle less than 30°, the adhesive bonds between the seta and the substrate fail as the seta starts sliding on

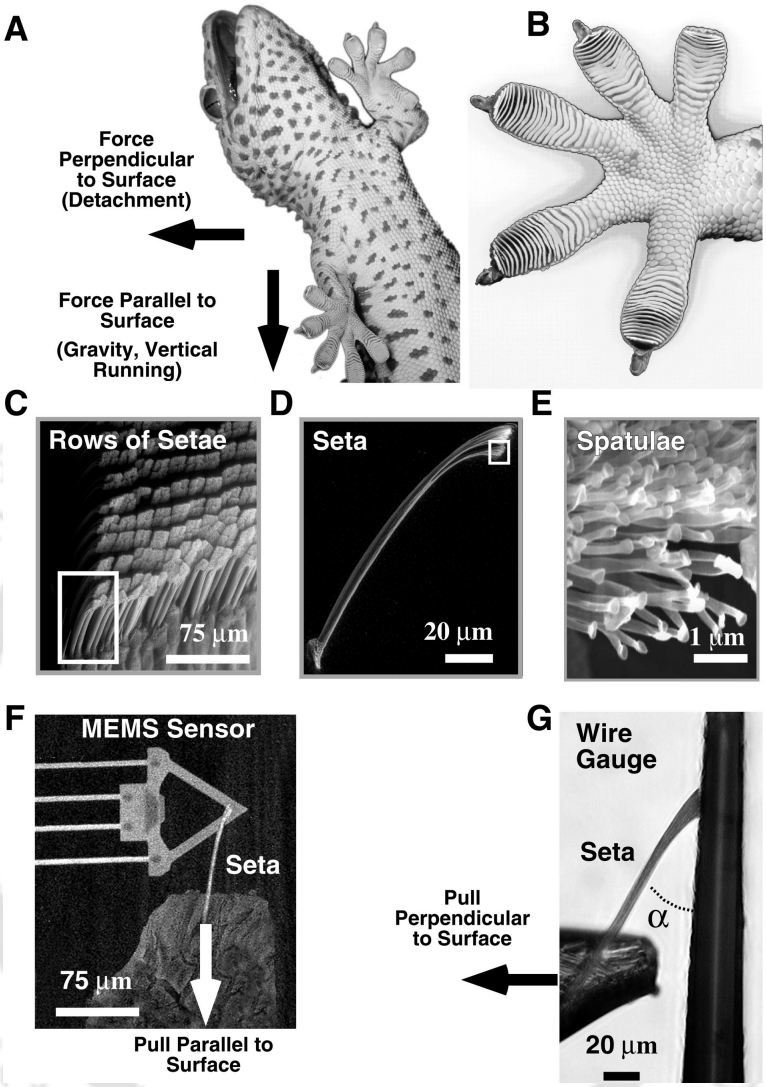

Figure 1.3: Hierarchical fibrillar structures of a Tokay gecko and the apparatus used for measuring the seta force measurement:
(A) to (E) show the hierarchy of the adhesive system from the gecko, toe, arrays of seta, seta, and spatulae, respectively;
(F) A single seta attached to a microelectromechanical (MEMS) sensor. The seta is dragged along the direction of the arrow shown and parallel forces generated are measured;
(G) Seta adhering to a aluminium bonding wire. The arrow indicates the direction (perpendicular to the surface) the seta is pulled. The forces perpendicular detachment forces are then measured. Here α denotes the angle between the shaft of the seta and the wire. Reproduced with permission from Autumn and Peattie [39].

the substrate and eventually the seta detaches from the substrate. However, when the seta is pulled at more than 30°, the seta simply detaches from the substrate without sliding. Chen et al. [44] studied the reversible adhesion of gecko toes using models of various elements in the hierarchy of the gecko toes viz. the spatula, the seta, and the toe. Their model showed that by changing the pull-off force angle from 30° to 90°, a 10 times reduction in the pull-off force could be achieved. At the seta level, it is observed that a uniform stress distribution can be achieved for values of seta diameter below a critical value. Also, due to the hierarchical nature of the adhesive system, the difference between the high attachment and low detachment forces is more pronounced as we move from the spatula to toe level.

The necessity of perpendicular preload and a parallel drag for the seta to engage can be reconciled with the directional and load-dependent behaviour observed at the whole-animal level by Hora [27] and Dellit [25]. Further, functional anatomical studies of the tokay gecko [45, 46] indicate that during attachment to and detachment from the substrate geckos display a peculiar roll-in and roll-off motion of its toes, called "digital hyperextension". The seta bearing scansors on the toe pads of the gecko are a series of overlapping plates, which the gecko can deploy independently. As such, during detachment, as the gecko hyperextends its toes, at any given moment, only a few setae are being detached, and thus significantly reducing the force required for detachment. According to Russell [38], geckos can apply the perpendicular preload by employing the branches of the blood sinuses and the parallel drag with the help of lateral digital tendons. However, it is yet to be experimentally shown how geckos are able to manipulate the hydrostatic pressure inside the blood sinuses. On the other hand, geckos apparently do not need to actively control these actions, as it is observed that they are able to stay attached even after death [47]. However, active control is extremely useful for a live gecko for hyperextending its toes to detach and then re-engage strongly and quickly to facilitate rapid locomotion.

Experiments of Autumn et al. [48] revealed that the frictional behaviour of gecko setae is unlike any of the other materials. The authors studied the attachment and detachment behaviour of isolated gecko setae, setal arrays, and toes. It was observed that when the setal arrays were loaded in the perpendicular direction and dragged in the distal direction (away from the animal) against their natural curvature, as shown in Figure 1.4a, the setal arrays compressed and did not adhere to the glass substrate. In this case, the frictional behaviour of setal arrays was consistent with the typical dry friction behaviour of solids, which is generally described by the Amontons-Coulomb friction law

$$F_{\parallel} = \mu_{\mathrm{s}} F_{\perp} \,, \tag{1.1}$$

where $F_{\parallel}$ and $F_{\perp}$ represent the tangential friction force and the normal adhesive force, respectively. Here, μ_s is the sliding friction coefficient, which for the distal drag is observed to be 0.31 ± 0.02.

However, Autumn et al. [48] observed that when the setal arrays were loaded and dragged in the proximal direction (towards the animal) along their natural curvature, the arrays briefly compressed and then adhered to the substrate. This resulted in tensile normal forces in the setal arrays. Even under these tensile normal loads, the setal arrays generated strong static and kinetic friction, which was significantly more than that observed in distal dragging as shown in Figure 1.4b. This behaviour appears to violate the Amontons' first law, according to which friction is proportional to the compressive normal load, and differs from the dry friction behaviour observed in other materials. Further, adhesive structures (toes, arrays of seta, and seta) in each level of gecko adhesive system were found to detach when the angle of the resultant force reached a particular value called the *critical detachment angle* α^*, irrespective of the applied load. It was also observed that for a given level of the hierarchy, this critical detachment angle was constant but differed among the hierarchical levels. These observations of invariance of critical detachment angle with the applied force cannot be explained by the traditional peeling models such as Kendall's model [49], which predicts that the detachment angle decreases as the forces are increased. To explain this coupled adhesion and friction, a phenomenological model called "frictional adhesion" was introduced by Autumn et al. [48], which defines a limiting normal adhesive force $F_{\perp}$ for a given critical detachment angle α^* and the frictional force $F_{\parallel}$

$$-\frac{F_{\perp}}{\tan \alpha^*} \leq F_{\parallel}\,, \tag{1.2}$$

According to the "frictional adhesion" model, geckos can stay attached to the substrate only if the angle between adhesive and frictional forces is less than the critical detachment angle. Although Autumn et al.'s experiments [1, 48] revealed that just by changing the resultant force angle various structures in the hierarchical adhesive system of geckos detach instantaneously, experiments of Gravish et al. [50] showed that not all paths of detachment are energy efficient. Investigation of detachment characteristics of setal arrays and single seta revealed that the angle of detachment influences the energy required for detachment. When the setae are detached by pulling at an angle of 30°, the setae required a net positive energy because of the frictional losses during sliding. However, when the setae are pulled at an angle of 130°, instantaneous detachment of the setae ensued as the energy stored due to tensile loading in the attachment phase is released. This type of shear sensitive reversible adhesion appears to be a common motif across adhesive pad bearing animals as observed by Labonte and Federle [51]. Their experiments on

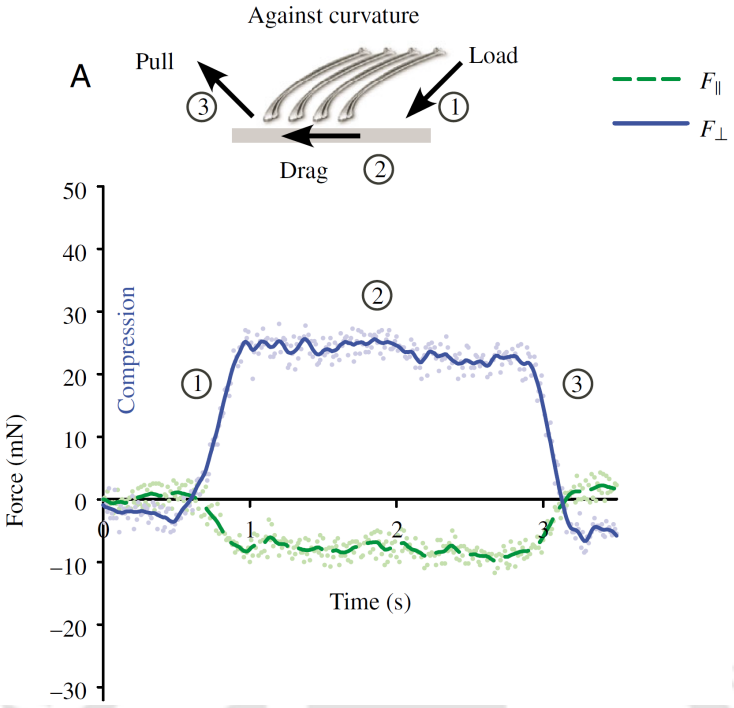

(a) When the setal arrays are dragged against their natural curvature, it resulted in compression of the setae. The frictional behaviour consistent with the Amontons-Coulomb friction is observed with a friction coefficient $\mu_s = 0.31 \pm 0.02$. Negative $F_\parallel$ represents the reaction forces during a drag to the left

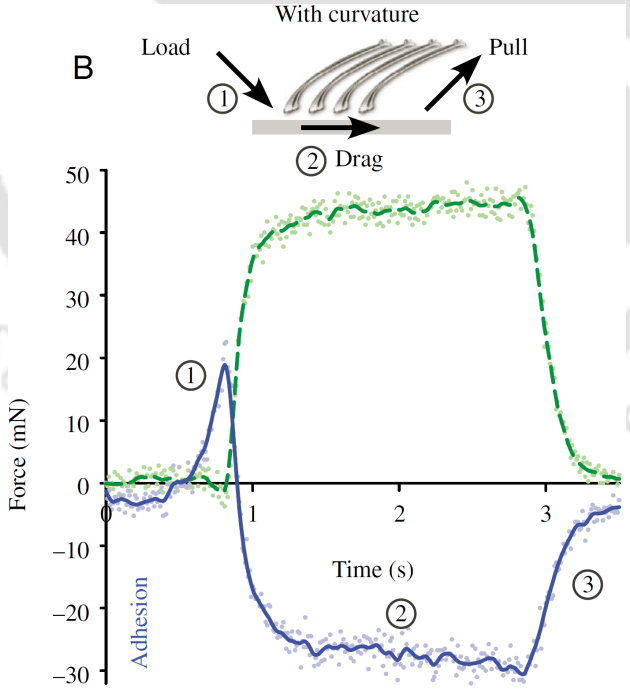

(b) When the setal arrays are dragged along their natural curvature, compression was observed initially, and then tension developed as the setae adhered. Positive $F_\parallel$ represents the reaction forces during a drag to the right.

Figure 1.4: Evolution of shear and normal forces during load (1), drag (2), and pull (3) experiments in isolated gecko setal arrays on a glass surface. Reprinted with permission from Autumn et al. [48].

Indian stick insect revealed that for large frictional forces, i.e. at small pull-off force angles, adhesion varied linearly with friction and for small frictional forces, i.e. at large pull-off force angles, the relationship between adhesion and friction fit very well with the inextensible tape peeling model. Further, it was observed that despite the significant difference in the morphology of insect pads and gecko pads, friction force was approximately twice that of adhesion force suggesting a similar critical detachment angle of 30°. Based on these observations, the authors hypothesised that the increase in the frictional forces is a result of partial sliding of the adhesive pad in the peel zone.

A tokay gecko has 14,400 seta per mm^2, and the total pad area of two front feet of a tokay gecko is approximately 227 mm^2 [39, 52]. If all the setae of the gecko (6.5 million) are engaged then, with each seta generating ≈ 200 μN, the two front feet of gecko can, in theory, generate a total force of approximately 650 N, which is 32 times the force generated by two front feet as measured by Irschick et al. [36]. Following these observations, it might appear that gecko adhesive pads are considerably overbuilt in the sense that by engaging all the setae it could generate more than 2600 times the force required to support its body mass of approximately 50 g. However, not all setae are of the same size and are not engaged simultaneously in the same orientation to generate optimal adhesive forces. Further, it has been observed that on rough surfaces, it is very difficult for all the spatulae to make intimate contact, which reduces the adhesive capability. It is suggested that this apparent high safety factor is useful in weathering difficult situations gecko experiences in its natural habitat such as escaping a predator, high-speed winds, and unexpected drops [40].

Based on the force values measured for a single seta, Autumn et al. [1] suggested that these values are consistent with the theory of van der Waals forces as the primary mechanism of adhesion. Assuming that the spatula end as a sphere with radius $R_{\text{sp}} = 200$ nm, interacting with a flat substrate, for van der Waals adhesion, the force F_{vdw} between them can be calculated as [53]

$$F_{\text{vdw}} = \frac{A_{\text{H}} R_{\text{sp}}}{6\, r_0^2}\,, \tag{1.3}$$

where A_{H} is the Hamaker constant which is taken as 10^{-19} J and $r_0 = 0.3$ nm is the equilibrium distance between any two particles interacting via van der Waals forces. Following Eq. (1.3), the force generated by each spatula is calculated as 400 nN, which when summed over for the entire seta (with 100 to 1000 spatulae) results in 40 μN to 400 μN per seta. The force of ≈ 200 μN per seta observed from the direct measurement by Autumn et al. [1] is within the range of values computed from Eq. (1.3).

Hiller's [32] experiments revealed that the adhesive force generated by the gecko is strongly affected by hydrophobicity/hydrophilicity of a surface indicated by the water contact angle. Hence, it was argued that it is reasonable to assume that the adhesion is due to thin-film capillary forces. However, the hydrophobic material employed by Hiller [32] is Polytetrafluoroethylene (PTFE), which is only weakly polarizable. As van der Waals forces are significantly influenced by the polarizability of the contacting bodies and not on the surface polarity, Autumn and Peattie [39] argued that the fact that geckos could not adhere to PTFE is consistent with the hypothesis of van der Waals forces as the adhesion mechanism. To resolve this issue, Autumn et al. [2] measured the adhesion forces on two semiconductor surfaces which are polarizable but with different hydrophobicity. Their results showed that irrespective of the hydrophobicity, gecko toes generated almost equal parallel forces on the surfaces of gallium arsenide (GaAs) (which is highly polarizable but highly hydrophobic with a water contact angle of 110°) and silicon dioxide (SiO_2) (which is strongly hydrophilic with a water contact angle of 0° and polarizable). Further, it was also observed that a single seta could generate an almost equal perpendicular force of 40 μN on both hydrophilic SiO_2 and hydrophobic Si surfaces. The authors also found that the setae are highly hydrophobic with a water contact angle of approximately 160.9°. This high contact angle is a result of the $\beta-$keratin protein which forms the seta material and the texture/roughness resulting from the spatula ends. Based on this measured normal adhesion force value and assuming that each spatula can be represented as a sphere of radius R, the authors computed the dimensions of the spatula. Following the Johnson–Kendall–Roberts (JKR) adhesive contact model [54], the radius of the spatula is estimated to be $0.13 - 0.16$ μm, which is close to empirically measured value [1]. The authors argued that, if the capillary forces are the dominant mechanism of adhesion, there should have been a difference in the adhesion forces generated on hydrophobic and hydrophilic surfaces. As there was no variation, it was concluded that van der Waals forces are the primary mechanism of adhesion. These results also suggest that the adhesive capability of geckos is, for the most part, independent of the adhering material.

Sun et al. [55] questioned Autumn et al.'s [2] conclusion of van der Waals forces as a major mechanism of gecko adhesion using atomic force microscopy measurements of the force generated by a single spatula in the air with varying relative humidity and water. The authors used a single toe from a house gecko (*Hemidactylus frenatus*). As the spatulae at the end of each seta are of uneven lengths, the authors argued that at any given moment, there is a low probability of more than one spatula adhering to the surface. They also utilized statistical methods to eliminate any discrepancy in the measurements. The authors measured a normal adhesive force of 11.8 nN for hydrophilic surface (water contact angle 30°) and 4.9 nN for hydrophobic surface (water contact angle 110°). It was also observed that

as the relative humidity is increased (or decreased), the adhesion force increased (or decreased). Presence of water (due to humidity or hydrophilic nature of the surface), the authors argued, decreases the contribution of van der Waals forces as it highly varies with the distance between the interacting bodies. So, the authors commented that high adhesion on hydrophilic surfaces must mean that in an ambient environment capillary force rather than van der Waals forces are the dominating mechanism. However, Huber et al. [56] refuted this conclusion experimentally, in which they measured the normal adhesion force generated by a single spatula on different surfaces of varying hydrophilicity and relative humidity. Although Huber et al. [56] observed similar adhesion behaviour as that of Sun et al. [55], the authors argued that capillary forces are not the primary mechanism of adhesion. This is because, in their experiments, Huber et al. [56] observed that even at very high relative humidity, capillary bridges which are responsible for capillary forces did not form on the surfaces. Even at 90% relative humidity, only adsorbed monolayers of water formed between the spatulae and the substrate. The size of a water molecule is approximately 0.3 nm, which is very much in the range of van der Waals forces. As such, Huber et al. [56] commented that the presence of adsorbed water monolayers must increase the number of van der Waals interactions and rejected the hypothesis of "real" capillary adhesion as the primary mechanism.

In their experiments at the whole-animal level, Niewiarowski et al. [57] observed that increasing the temperature from 12°C to 32°C, resulted in a twofold decrease in the measured clinging force. However, between these two temperatures, the relative humidity (RH) differed by 15%. Further, when RH is varied from 35% to 80% at a constant temperature of 12°C, it was observed that the clinging force more than doubled. However, at a constant temperature of 32°C, the effect of humidity was not significant. The authors note that according to capillary adhesion model, as the clinging force is directly proportional to temperature in Kelvin at a constant RH, there should only be a difference of 8% in the forces between 12°C and 35°C. However, their experimental observations show that the difference in the adhesion forces is significantly higher than 8%. These observations reveal that the effect of humidity on gecko adhesion is not so straightforward.

Research of Puthoff et al. [58] offered some explanation for the effect of humidity, in which the authors have shown that the reason behind the change in the clinging forces with humidity is the change in the mechanical properties of the seta material. The authors observed that, contrary to the predictions of capillary adhesion, humidity affected clinging forces similarly on both hydrophobic and hydrophilic surfaces. The authors have shown that as the humidity is increased, the setae softened and viscoelastic damping increased due to which the adhesion increased. The experimental results Prowse et al. [59] further corroborated these results, who measured

the influence of RH on tensile, fracture, and dynamic mechanical response of single seta and lamellae. By varying the RH from 30% to 80%, a threefold decrease in the magnitude of complex elastic modulus of both a single seta and the lamellae E^*[1] is observed. The authors also observed that when RH is increased from 30% to 80%, the dimensionless loss tangent[2], which describes the viscoelastic damping, increased three times. Further, the tension stress of single seta and the lamellae showed that the elastic modulus E_0 decreased from 3.7 GPa to 2.13 GPa as RH is increased from 30% to 80%. These results are in contradiction with the measurements of Huber et al. [60], who observed that the humidity did not influence the elastic modulus of the seta. However, Prowse et al. [59] argued that Huber et al. [60] conducted their experiments after their seta samples were initially kept in a high vacuum environment that could have permanently dehydrated the seta and altered its properties. This could also partially explain the high elastic modulus value 7.3 ± 1.0 GPa measured by Huber et al. [60] for a single gecko seta in tension. For the case of bending, both Huber et al. [60] and Peattie et al. [61], who conducted vibration analysis using Euler-Bernoulli model, measured similar values of material stiffness $E_0 = 1.7 \pm 0.6$ GPa and 1.6 ± 0.15 GPa, respectively.

1.3 Modelling adhesion and friction in gecko spatulae

This section presents a literature review on the modelling aspects of the gecko spatulae using experimental, analytical, and numerical methods. In each subsection, efforts of various researchers addressing different facets of adhesion and frictional behaviour of gecko spatulae are discussed.

1.3.1 Experimental studies

The complex hierarchical nature of the gecko adhesive system makes it a challenging research area. As such, researchers have studied each structure in the hierarchy separately as well as their coupled interactions. However, in most of the literature, the smallest element in the hierarchy of the gecko adhesive system that has been isolated and studied thoroughly is the seta. Although atomic/friction force microscopy techniques have been used to study adhesion and friction of solids and

[1] For a viscoelastic material, the dynamic material behaviour is described by the complex elastic modulus whose magnitude is defined in terms of the storage E' and loss E'' moduli as $|E^*| = \sqrt{(E')^2 + (E'')^2}$.

[2] Dimensionless loss tangent is defined as $\tan\delta = \dfrac{E''}{E'}$

to measure mechanical properties at the nanoscale [62–64], to the best of our knowledge the spatula level, at which the actual interaction with the substrate happens, has not been investigated in isolation. This could be due to the difficulty in isolating this nanoscale structure and controlling its orientation in three-dimensional space. The orientation of these structures is key to achieving high friction and adhesion, as demonstrated by Hill et al. [65]. However, some researchers employed different techniques to study the spatula adhesion experimentally. One of the first experimental studies on gecko spatula adhesion is due to Huber et al. [66], who employed atomic force microscopy to measure the adhesive force generated by individual spatulae on a glass surface (having surface roughness less than 10 nm). For this purpose, two individual setae of a tokay gecko with all but four spatulae cut off has been employed. First, a perpendicular preload of 90 nN is applied, followed by a 7 μm parallel drag (maintaining the perpendicular preload) is applied to the seta. After this, the seta is retracted vertically upwards, and the pull-off forces are measured. They measured that the pull-off force for each spatula is about 10 nN. Further, it was observed that in multiple trials, in 54% of cases only two out of four spatulae adhered to the surface and in 44% of the cases only one out of four spatulae adhered. Three spatulae adhered in less than 3% of the trials and all the four spatulae never adhered to the surface. This could explain the very high safety factor of the gecko adhesive pads. However, it is known that geckos generate a substantial amount of shear forces [1]. Whereas, Huber et al.'s [66] experiments are limited to measuring the clinging force in the normal direction.

The influence of surface roughness on the adhesive forces generated by the gecko at both nano and micro scales has been investigated by Huber et al. [67]. Similar to their previous studies [56, 66], two different specimens of isolated seta with only four spatulae at their end are used for nanoscale experiments. Atomic force microscopy is employed to measure the adhesion force generated by the setae at ambient conditions on different surfaces with root mean square (RMS) roughness ranging from 20 nm to 1100 nm. The pull-off force corresponding to a single spatula is found to be minimum for 100 nm to 300 nm RMS roughness and increased on either side of these values. At the macroscale, live geckos were unable to stay attached to substrates with small roughness (RMS value of 90 nm). However, for very rough substrates (RMS value of 3 μm) as well as very smooth substrates geckos developed strong adhesion. This pull-off force behaviour corresponding to roughness is quite different from typical bulk materials, for which the pull-off forces monotonically decrease with an increase in surface roughness. The authors argued that this is due to the fact that unlike bulk solids, the hierarchical nature of these fibrillar structures aids the geckos in attaching to different rough surfaces. Further, as noted by Persson et al. [68], even though the spatula is made of β-keratin, which is a stiff material, it is a very thin structure and can easily adapt to surfaces with

very small roughness as well as very large roughness. However, when the roughness value is close to the dimension of the spatula (around 200 nm) it fails to adapt to the surface. Thus, at these intermediate roughness values, only some part of the spatula pad can effectively adhere using van der Waals forces, which greatly varies with the separation distance. Recently, Pillai et al. [69] conducted macroscale experiments of gecko adhesion on artificial rough substrates that are more close to the surfaces geckos encounter in their natural habitat. Their results also show that clinging performance of the geckos was impaired on intermediate roughness.

As RMS value alone cannot describe all the aspects of surface topography, Pugno and Lepore [70] considered gecko adhesion on surfaces differing in a number of topographical parameters including RMS roughness, waviness, and roughness amplitude. Their results showed that for intermediate roughness values (RMS = 618 nm, waviness = $7 - 8\mu$m, and roughness amplitude = 1 μm) pull-off force generated increases. In addition, they noted that the increase in adhesion force is consistent with the theory of Briggs and Briscoe [71], who observed that the pull-off force depends on the adhesion parameter α_{FT} defined by Fuller and Tabor [72]. This adhesion parameter is a function of standard deviation (SD) of the surface asperity distribution, mean radius of curvature of the asperity (r_{asp}), surface energy per unit area (or work of adhesion w_{adh}) , and Young's modulus (E_0) and is given as

$$\alpha_{\mathrm{FT}} = \frac{4\,\mathrm{SD}}{3}\left(\frac{4E_0}{3\pi\, w_{\mathrm{adh}}\sqrt{r_{\mathrm{asp}}}}\right)^{2/3}. \tag{1.4}$$

1.3.2 Analytical models

Adhesive contact of solids can be modelled using the well known Johnson-Kendall-Roberts (JKR) contact model [54]. Johnson et al. [54] extended the Hertz contact theory [73] to account for the elastic deformation due to adhesive force acting in the contact zone. The force of adhesion is then computed using energy balance between elastic, potential, and surface energies. The authors assumed that the attractive forces are finite in the contact zone and zero everywhere else. For a spherical solid with radius R in adhesive contact with a flat surface, the relationship between the contact radius r_{JKR} and the applied load F is given as

$$r_{\mathrm{JKR}}^3 = \frac{3R}{4E_0^*}\left(F + 3\pi R w_{\mathrm{adh}} + \sqrt{6\pi R F w_{\mathrm{adh}} + (3\pi R w_{\mathrm{adh}})^2}\right), \tag{1.5}$$

where w_{adh} is the work of adhesion (or adhesion energy), which is defined as the energy per unit area required to separate two bodies in adhesion and E_0^* is the average plane strain modulus. The expression for contact radius in Eq. (1.5) reduces to the Hertz contact radius when the adhesion energy is zero, i.e. $w_{\mathrm{adh}} = 0$. Then,

the magnitude of pull-off force required to separate the interacting bodies is obtained as

$$F_{\mathrm{JKR}} = \frac{3}{2}\pi R w_{\mathrm{adh}}\,, \tag{1.6}$$

which is independent of the elastic modulus.

Autumn et al. [2] showed that the JKR model can be applied to gecko adhesion to estimate the size of the spatula for the adhesion forces measured in their experiments on a single seta. Taking the 40 μN adhesion force measured for a single seta and the adhesion energy of 50 to 60 mJ/m^2 for van der Waals interaction, the radius of the spatula (modelled as a sphere) can be estimated using Eq. (1.6) as $R = R_{\mathrm{JKR}} = 82$ to 98 nm or 164 to 196 nm diameter. This value is very close to the value 200 nm observed by Rizzo et al. [74] in their electron microscopy analyses. This suggests that for a given adhesion energy, more adhesion per unit area is generated for a smaller size of the spatulae.

Following Eq. (1.6), which shows that the pull-off force is proportional to the size of the fibril, Arzt et al. [75] argued that by splitting the seta contact into n sub contacts (spatulae) having $(R/\sqrt{n})$ radius each, due to self-similar scaling, the total adhesion force increases as the square root of the number of contacts n and the adhesive stress scales as the inverse of the radius R. This suggests that contact splitting enhances adhesion. These conclusions, Arzt et al.'s [75] argued, are in-line with their comparative analysis of various animals with fibrillar adhesive structures in which the setal density scaled as $(\mathrm{mass})^{2/3}$. However, this conclusion of the adhesive force scaling with the linear dimension rather than the area has been questioned by Federle [76]. He argued that Arzt et al.'s [75] "force scaling" assumes that all the setae (or terminal spatulae) detach simultaneously and that the stress distribution is uniform over all the setae (or spatulae). However, as the animal detaches by peeling such that the stress concentration is only at the edge of the adhesive pad will result in a non-uniform load sharing in the setae (or spatulae). In this case, the pull-off force would be much smaller than that predicted by "force scaling". Further, by surveying the morphology of a variety of species with fibrillar adhesive structures that employ either 'wet' or 'dry' adhesion or both, Peattie and Full [61] rejected the hypothesis of spatula density scaling with the body mass. Using the phylogenetic analysis, Peattie and Full [61] predicted that within a group, animals with lower body mass might possess larger safety factor or needless adhesive pad area per body mass than animals with higher body mass.

As observed by Tang et al. [77], the applicability of JKR theory [54] to analyse the advantage of contact splitting is limited by the intrinsic features of the theory. Mainly, JKR theory is applicable only for spherical contacts, while the terminal features in various biological adhesives are plate-like structures. It also ignores the contact forces outside the contact region, which once again limits the accuracy of

its predictions. On the other hand, Derjaguin–Muller–Toporov (DMT) theory [78], although accounts for the contact forces outside, as pointed out by Tang et al. [77], just like JKR theory it also predicts that as the radius of the sphere R decreases the pull-off stress increases boundlessly, i.e. as $R \to 0$, $\sigma_{\text{pull-off}} \to \infty$. However, by considering the limits on the size of the contact region and the Tabor parameter, Tang et al. [77] defined the regions of validity of JKR and DMT theories.

Gao and Yao [79] investigated the importance of the spatula end shape and size in achieving optimal adhesion. It was suggested that only if the size of spatulae is in the order of 100 nm shape-insensitive optimal adhesion is possible. This research has been further extended by Gao et al. [43], who studied the advantages of nanoscale spatulae evolved on gecko toe pads and their importance in robust adhesion. The authors modelled the spatula as an elastic cylinder with a flat tip interacting with a rigid substrate. It was found that as the radius of the cylinder is decreased to a critical value, the stress in the contact area reaches the theoretical strength. Also, the nanometer size of the spatulae has been found to be essential in achieving optimum and flaw tolerant adhesion, i.e. the spatula structures fail, only when they reach the theoretical strength and rupture rather than due to build-up of stress concentration and eventual failure due to crack propagation [80, 81]. Further, it was observed that compared to the JKR model based hemispherical spatula model, the flat-ended spatula reaches the maximum adhesion strength more quickly, i.e. the radius of hemispherical spatula needs to be decreased to few atomic spacings whereas the flat-ended spatulae need to be around 225 nm.

The gecko spatula is rather a very thin structure, only $5 - 10$ nm thick and is 200 nm at its widest edge. As such, many researchers modelled the spatula as a thin film/strip and employed peeling models to study different aspects of gecko adhesion [82–84]. One of the first peeling models is due to Kendall [49], in which the fracture theory has been applied to peeling of an elastic film from a rigid substrate. A linearly elastic thin film of thickness h, width b, and Young's modulus E_0, when peeled steadily by a constant force F at an angle of α, is related to the work of adhesion w_{adh} as

$$\frac{1}{2E_0h}\left(\frac{F}{b}\right)^2 + \frac{F}{b}(1-\cos\alpha) = w_{\text{adh}}\,, \tag{1.7}$$

which is quadratic in F/b. The first term on the left-hand side in Eq. (1.7) is due to the recoverable strain energy stored in the film and the second term is due to the external work done by the pull-off force F considering the film to be inextensible. The positive root of Eq. (1.7) then gives the steady-state pull-off force as

$$\frac{F}{b} = E_0h\left[\sqrt{(1-\cos\alpha)^2 + 2\frac{w_{\text{adh}}}{E_0h}} - (1-\cos\alpha)\right]\,. \tag{1.8}$$

Huber et al. [66] employed Kendall's model [49] to verify their experimental results of pulling the spatula in perpendicular direction. Considering the pull-off force value of $F = 10$ nN measured by Huber et al. [66] for vertical pulling ($\alpha = 90°$) and assuming that the stored strain energy is negligible, for a strip of width $b = 200$ nm, Kendall's model predicts the work of adhesion to be $w_{\text{adh}} \approx F/b \approx 50$ mJ/m^2. This value is within the range of $10 - 100$ mJ/m^2 typical for intermolecular interactions [85]. Chen et al. [44] studied the peeling of a spatula from a rigid substrate employing Kendall's peeling model [49] to illustrate the reversible adhesion of geckos. It was shown that by changing the orientation of the pull-off force, the gecko is able to achieve high attachment and low detachment forces. Peng and Chen [86] investigated the effect of relative humidity and the presence of water layers on the adhesion forces of a nanofilm. It is shown that due to the presence of adsorbed water monolayers, the disjoining pressure between the nanofilm and the water molecules compensates for the reduction in the van der Waals forces between the nanofilm and the substrate. However, for relative humidities greater than 90%, the water droplets are formed on the substrate and the adhesion forces decrease.

Peng [87] studied the adhesive interaction between a finite length elastic nanofilm with a rough surface having sinusoidal roughness. The author also investigated the effect of nanofilm thickness using a model based on Lennard-Jones potential to describe the van der Waals adhesion. It was found that for the case of film length larger than the wavelength of the surface roughness, adhesion decreased with increasing roughness. Whereas, for the case of film length smaller than the wavelength of the surface roughness, adhesion decreased initially and then increased. These results are similar to the experimental observations of Huber et al. [67]. It was also observed that the small thickness of the spatula makes it compliant enough to make intimate contact with the rough surface and also aids in resisting the fracture of the spatula pad.

Although the above discussed analytical models provided insights into some of the aspects of gecko adhesion, they do not address the interplay between friction and adhesion. Molecular mechanisms of dry friction are varied in nature, which include asperity interlocking, their deformation, interfacial plastic yielding, wear, fracture in case of brittle materials, viscous dissipation in case of rubber-like materials, and adhesion in case of nanoscale interactions and when other dominant forces are absent [88]. Friction can emerge from these individual mechanisms or a combination of them. The Amontons-Coulomb friction law in Eq. (1.1) in general can model the friction between two surfaces where adhesive interactions are absent. However, as discussed by Jagota and Hui [37], Amontons-Coulomb law is unable to explain different aspects of friction such as time dependence of static friction [89–91], a sudden drop from static friction to sliding friction without any slip [92], and the

effect of tangential loading [93]. Moreover, as noted by Persson et al. [94], for smooth surfaces or soft elastic solids such as polymers, where the real contact area approaches apparent contact area due to very strong adhesion, Eq.(1.1) cannot describe the relationship between the normal load and the friction force.

Derjaguin [95] proposed a generalization of Eq. (1.1) for the interfacial friction and adhesion in crystal layers by introducing additional parameter to account for adhesion

$$F_{\parallel} = \mu_{\mathrm{s}}(F_0 + F_{\perp}) = \mu_{\mathrm{s}} A_{\mathrm{real}}(p_0 + p_{\perp}) \tag{1.9}$$

where $F_{\parallel}$ is the friction force, $p_{\perp}$ is the average pressure corresponding to the normal force $F_{\perp}$, $p_0 = F_0/A_{\mathrm{real}}$ is a constant corresponding to adhesion force F_0 that depends only on the materials of the contacting surfaces, and A_{real} is the real/true contact area. Homola et al. [96] later criticized this model, as their experimental results on molecularly smooth mica showed that at small and negative normal loads, friction no longer linearly scaled with the load. Hence, for the case of smooth, undamaged surfaces where adhesive interactions are present, Homola et al. [96] proposed that the interfacial friction can be described by

$$F_{\parallel} = \tau_0 A_{\mathrm{real}} + \mu_{\mathrm{s}} F_{\perp}\,, \tag{1.10}$$

where τ_0 is the critical shear stress at the contact interface and is constant for a given material. For small normal loads, Eq. (1.10) reduces to

$$F_{\parallel} \approx \tau_0 A_{\mathrm{real}}\,, \tag{1.11}$$

and is independent of the normal load $F_{\perp}$. For this case, Homola et al. [96] observed that the real contact area can be predicted by the JKR theory [54]. This is in contradiction to the Amontons-Coulomb law in Eq. (1.1), as the sliding friction now varies nonlinearly with the normal load. However, it was observed that for damaged mica surfaces, Amontons-Coulomb law still holds. The relation in Eq. (1.11) is similar to Bowden and Tabor's [97] equation for the sliding friction in adhesive contact of nominally flat surfaces. But as observed by Jagota and Hui [37], in Bowden and Tabor's theory, it is assumed that the asperities undergo plastic deformation and thus true contact area is proportional to the normal load. As such, the critical shear stress τ_0 originates from different mechanisms in the theories of Homola et al. [96] and Bowden and Tabor [97]. Majidi et al. [98] employed a model similar to that of Homola et al. [96] to show that even for gecko-inspired microfibre arrays manufactured from stiff materials like thermoplastics can generate high friction forces. It was found that the higher interfacial strength of these stiff materials increases the effective friction coefficient. However, it was observed that their fibre arrays did not display any normal adhesion.

Tian et al. [99] used a thin strip model of the spatula to estimate the adhesion and friction forces. The spatula pad is assumed to interact with a rigid substrate via van der Waals forces. The frictional forces are assumed to originate from a sinusoidal potential and act only in the region where the spatula pad is at an equilibrium distance r_0. The authors assumed that the van der Waals forces act only in a narrow transition region (where $r > r_0$) from the pad to the shaft called the "peel zone", which is curved and has a radius R_p. The total attractive force F_vdw acting in this peel zone at a given pull-off force angle α is then obtained as

$$F_\mathrm{vdw}(\alpha) = \frac{A_\mathrm{H}\, b\, \sqrt{R_\mathrm{p}}}{16\sqrt{2}\,[r_0 + R_\mathrm{p}(1-\cos\alpha)]^{5/2}}\,, \tag{1.12}$$

where the radius $R_\mathrm{p} = 4215 \times \alpha^{-1.35}$ is obtained from an empirical relation. The maximum friction force acting only in the contacting region (where $r = r_0$) is then obtained using the attractive force $F_\mathrm{c,vdw}$ in the contact region of length L_c as [100]

$$F_\mathrm{f}^\mathrm{max} = \mu_\mathrm{s} F_\mathrm{c,vdw} = \mu_\mathrm{s} L_\mathrm{c} b P_\mathrm{vdw}\,, \tag{1.13}$$

where P_vdw is the van der Waals force per unit area and is obtained by considering the spatula and the rigid substrate as half-spaces within the contact region [53]

$$P_\mathrm{vdw} = \frac{A_\mathrm{H}}{6\pi r_0^3}\,. \tag{1.14}$$

A simple force balance then gives the normal (F_N) and tangential (F_T) component of the total force acting on the spatula at a given pull-off force angle α

$$F_\mathrm{N} = F\sin\alpha = F_\mathrm{vdw}\,, \quad F_\mathrm{T} = F\cos\alpha = F_\mathrm{vdw}\cot\alpha\,, \tag{1.15}$$

which shows that the entire normal force acting on the spatula is given only by the van der Waals forces acting in the peel zone.

Combining Eqs. (1.13) and (1.15) and observing that the entire pad will slip if $F_\mathrm{T} \geq F_\mathrm{f}^\mathrm{max}$, Tian et al.'s [99] model essentially reduces to the "frictional adhesion" model of Autumn et al. [48]

$$\tan\alpha \geq \frac{F_\mathrm{vdw}}{F_\mathrm{f}^\mathrm{max}}\,. \tag{1.16}$$

Tian et al.'s [99] model predicts that by varying the pull-off force angle, the pull-off force can vary by two orders of magnitude. However, their model did not consider the bending stiffness of the spatula. Moreover, as observed by Jagota and Hui [37], their model does not consider the deformation behaviour of the spatula as such variation of the friction force with distance from the substrate is not addressed.

Pesika et al. [101] applied a newly developed tape peeling model called peel-

zone model (PZ model), which is based on the experimental observations of the tape peeling, to study the gecko spatula peeling. Similar to Tian et al.'s [99] model, the curvature of the peel zone is assumed to be approximately circular. In this peel-zone model, there is an angle α_0 below which the geometry of peel zone varies with the pulling angle α but remains constant above α_0. This angle α_0 is determined from experimental observations, which depends on the tackiness of the tape and is an intrinsic property of the interacting system. Then, the tangential and normal forces are derived from the force balance. The PZ model differs from Kendall's peeling model [49] by an angle-dependent multiplier. As such, the PZ model predicts lower values of pull-off force than Kendall's model. This model has been later extended by Zhou et al. [102] to include the effect of peeling velocity on the pull-off forces.

The proximal drag of gecko toes during attachment is known to decrease the angle at which the setae are inclined to the substrate, which in turn decreases the spatula shaft angle. This dragging at a low angle also results in stretching of the spatula and pretension builds up. By employing a generalized Kendall's peeling model that accounts for the pre-tension, Chen et al. [103] showed that the pre-tension significantly increases the pull-off forces when pulled at smaller angles and decreases it when pulled at a larger angle. As such for a given pre-tension F_0, the generalized Kendall's model is given as

$$\frac{F^2 - F_0^2}{2Eh} - \frac{FF_0}{Eh} + F(1 - \cos\alpha) = w_{\text{adh}}\,, \tag{1.17}$$

which can be solved to obtain the pull-off force for a given α and pre-tension F_0. It is observed that stable adhesion occurs only if the applied force F lies between the two roots of Eq. (1.17), i.e. $F_2 \leq F \leq F_1$, where $F_2 < F_1$. It is shown that compared to Kendall's peeling model, the pretension increases the pull-off force at small α and decreases at large α. Moreover, for large enough pre-tension the pull-off force drops to zero at a critical pull-off force angle α_{cr}. This model was later extended by Peng and Chen [104] to study the effect of uniform and non-uniform pre-tension on the peeling behaviour of a two-level hierarchical system. Their results show that pre-tension at the spatula level contributes significantly to strong reversible adhesion at the seta as well as the animal level.

Zeng et al. [105] employed JKR contact theory [54] and sliding frictional theory of Homola et al. [96] to analyse the "frictional adhesion" behaviour of elastic fibrils with different geometries. Further, the authors suggested that by optimally placing the flexible and tilted fibrillar structures on an area of 230 cm^2 even human beings can effectively support their weight on rough vertical surfaces. Yamaguchi et al. [106] employed a curved beam model to analyse the "frictional adhesion" behaviour of gecko setal arrays. In their study, the authors modelled both the spatula and the seta as curved beams. It is shown that this model at the spatula level is able

to describe the attachment, stretching due to parallel drag, and snapping off the substrate. Whereas, at the seta level, the geometry of the curved beam is able to demonstrate the coupling of friction and adhesion and dependence on the pull-off force angle, which aids in strong attachment and easy detachment. The authors also investigated the effect of drag velocities on the normal and tangential forces. It is observed that as drag velocity is increased, the normal force and the tangential force increase, which the authors suggested is due to the fact that the spatula stretches more when stretched faster.

Jagota and Hui [37] conducted a systematic review of studies on bio-mimetic and bio-inspired adhesive structures to understand the principles behind the adhesion, friction, and compliance of the employed fibrillar structures. They analysed various aspects such as their structure, surface and mechanical properties, and mechanisms of adhesion. The authors further discussed various experimental techniques, analytical models presented in the literature to understand the principles of adhesion and friction and how they can aid in designing better synthetic adhesives. Furthermore, the authors also presented a new tape peeling model, which can be considered as an extension of Kendall's model [49]. In this model, the spatula pad is modelled as a thin plate-like structure in tension. Then, the energy balance between the van der Waals adhesion energy per unit area w_{adh}, friction energy required to slide a unit area of the spatula pad, and potential energy acquired due to work done by the pull-off force F results in

$$\frac{F^2}{2E_0b^2h}(1-\cos^2\alpha)+\frac{F}{b}(1-\cos\alpha)=w_{\text{adh}}\,, \tag{1.18}$$

which includes the stretching of the spatula pad explicitly and upon solving gives the expression for pull-off force as

$$\frac{F}{b}=\frac{E_0h}{1+\cos\alpha}\left[-1+\sqrt{1+4\frac{w_{\text{adh}}\left(\dfrac{1+\cos\alpha}{1-\cos\alpha}\right)}{2E_0h}}\right]. \tag{1.19}$$

By explicitly accounting for the frictional sliding at the interface, the analytical model of Begley et al. [107] can analyse large deformation peeling of elastic tape. The authors analysed double-sided peeling and single-sided peeling. Analytical expressions have been derived for energy release rate and the steady-state pull-off force for a given angle of detachment accounting for the frictional sliding at the contact interface. Their model is very similar to the model of Jagota and Hui [37]. Contrary to models that consider pure sticking, like Kendall's model [49], in Begley et al.'s [107] model, the tangential component of the pull-off force does

not contribute to the energy released during peeling. Further, it was shown that the frictional sliding increases the critical pull-off force compared to pure sticking. Experimental and analytical investigations of double peeling of an elastic tape by Afferrante et al. [108] showed that there exists a limiting value of pull-off force angle at which the pull-off force reaches a maximum. Any further increase in the pull-off force above the maximum value resulted in the complete detachment of the tape. Gialamas et al. [109] presented an analytical approach to model the peeling of a nonlinear Neo-Hookean tape with its entire length in contact with the substrate. The authors modelled the tape as a thin membrane and as such, ignored the effect of bending stiffness. A Dugdale type cohesive zone model [110] describing the traction-separation relationship in the contact interface is employed.

Using the principle of minimum potential energy, Peng and Chen [111] derived an analytical model to investigate the bending stiffness influence on the pull-off forces. The van der Waals forces are assumed to be responsible for the interfacial adhesion. The authors derived a closed-form solution to the quadratic equation similar to Eq. (1.7) with additional terms to account for the thin film bending stiffness. Their results showed that bending stiffness significantly influences the pull-off forces. However, after reaching steady-state peeling, the pull-off force was unaffected by the bending energy. The peeling behaviour of finite length thin-films was investigated by Peng et al. [112] using both theoretical and finite element models. It was shown that initial adhesion length influences the steady-state peeling process of finite film length tapes unlike infinitely long thin-films used in classical peeling models. It was also observed that initial adhesion length of the film and the length which is not in adhesion, and its stiffness significantly affect the maximum pull-off force. He et al. [113] presented a theoretical model for the peeling of a hyperelastic beam that accounts for its bending stiffness and large stains in the beam using a finite strain Euler beam model [114]. The boundary value problem derived from the variational method is then solved using numerical procedures. It is shown that when the beam is pulled at low angles the bending effect significantly increases the pull-off forces as compared to those predicted by the Kendall peeling model [49].

For a more comprehensive understanding of the vast amount of literature available on adhesion and friction models of geckos and the advancements in the design and manufacturing of bio-inspired synthetic adhesives one can refer to various review papers and the references therein [37, 41, 115–119].

1.3.3 Numerical models

This section presents a literature review on various numerical models used to analyse the gecko spatula adhesion. Local interface models, which describe the local traction at the interface in terms of the separation between the interacting surfaces, can be employed to model van der Waals adhesion and friction in gecko spatula peeling. Interfacial adhesion due to van der Waals forces is generally described by the Lennard-Jones potential $\phi(r)$ [53, 85]. For a pair of molecules separated by a distance r this Lennard-Jones potential is a function of the depth of potential well ϵ and the equilibrium distance r_0 and is given as [85]

$$\phi(r) = \epsilon \left[\left(\frac{r_0}{r} \right)^{12} - 2 \left(\frac{r_0}{r} \right)^{6} \right], \tag{1.20}$$

and can be visualized as shown in Figure 1.5.

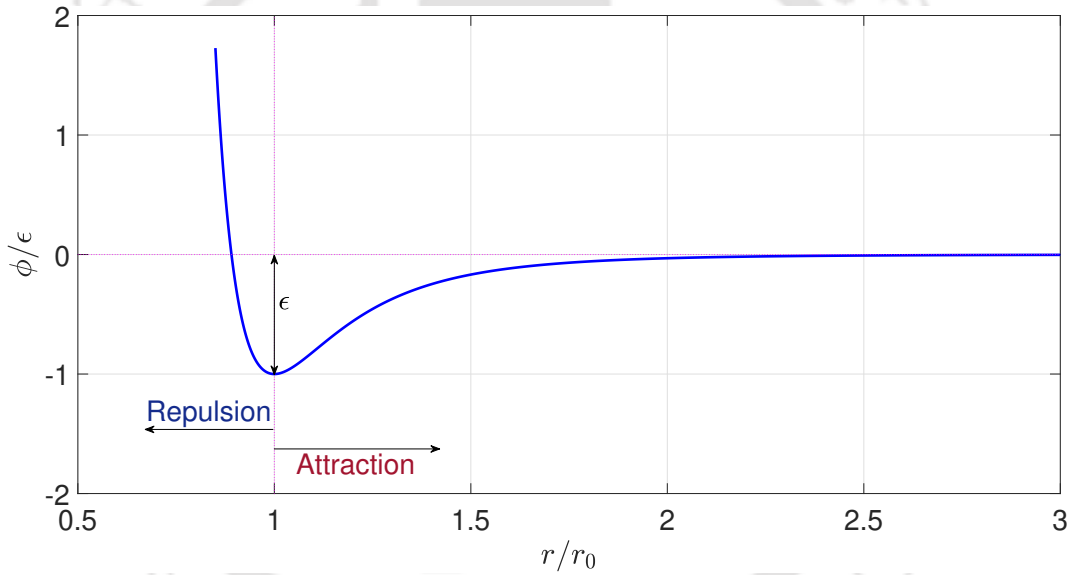

Figure 1.5: Variation of Lennard-Jones potential with the separation distance.

The global adhesion potential Π_a between two interacting bodies can then be obtained by integrating Eq. (1.20) for all the interactions between all the molecules in the interacting bodies as [120]

$$\Pi_a = \int_{\Omega_1} \int_{\Omega_2} \beta_1 \, \beta_2 \, \phi(r) \, \mathrm{d}v_2 \, \mathrm{d}v_1 \,, \tag{1.21}$$

where β_k $(k = 1, 2)$ is the molecular density of body $\mathcal{B}_k$ in the deformed configuration Ω_k.

Before discussing computational works that model gecko spatulae peeling, a few methods employed by researchers in continuum formulations to derive the governing

equation of motion based on the total adhesion potential in Eq. (1.21) are briefly presented. A general continuum formulation involving the double volume integral in Eq. (1.21) tends to be expensive. As such, some researchers employed approximation techniques, which can be computationally less intense, while retaining the accuracy. A general approximation technique is to transform the volume integrals to surface integrals [120]. A typical surface based traction-separation law for Lennard-Jones potential based van der Waals adhesion can be obtained by taking the gradient of the total adhesion potential in Eq. (1.21). This gives the adhesive traction $\boldsymbol{t}_{\mathrm{a}}$ as

$$\boldsymbol{t}_{\mathrm{a}} = \frac{A_{\mathrm{H}}}{2\pi r_0^3}\left[\frac{1}{45}\left(\frac{r_0}{r_s}\right)^9 - \frac{1}{3}\left(\frac{r_0}{r_s}\right)^3\right]\boldsymbol{n}_{\mathrm{p}} \tag{1.22}$$

where $\boldsymbol{n}_{\mathrm{p}}$ is the surface normal and $r_{\mathrm{s}} = \|\boldsymbol{r}_s\|$ is the normal distance between the interacting surfaces.

Many researchers employed different methods to approximate the double volume integrals with double surface integrals. One such approximation is given by Derjaguin approximated [85, 121], in which the total force between two curved bodies, approximated as half-spaces, is related to the interaction energy per unit area multiplied by a geometric factor that is a function of their radii which are much greater than the interaction range. This type of approximation has been extensively used in solving a variety of adhesive contact problems including coalescence of crystals during film growth [122], elastic and elasto-plastic adhesive contact [123–126], asperity based contact [127, 128], particle adhesion [129], asymmetric adhesion [130]. In order to address the geometrical limitations of the Derjaguin approximation [85, 121], Argento et al. [131] presented a new continuum formulation, in which the body forces are partitioned to obtain effective surface tractions. The surface tractions are obtained from the Young-Laplace relation, which describes the surface tractions as a function of surface energy and curvature. Ardito et al. [132] employed the proximity force approximation, in which the nodes on the interacting surfaces are paired and only interact with each other to bypass the calculation of surface integrals. Furthermore, to more accurately capture the deformation behaviour of interacting bodies, some authors employed body force formulations instead of surface force formulations [120, 133–136]. However, even in these formulations, some approximations are made, such as considering the master body as a flat half-space in the vicinity of the projection point from the surface of the slave body. In addition to a body force formulation, Sauer and Wriggers [120] also introduced a more efficient surface force formulation, by projecting the body forces onto the surface of the neighbouring body and obtaining an effective surface traction. A general continuum formulation for adhesive contact, which is due to interatomic interactions, applicable for large deformation analysis, capable of capturing interactions at various length scales along

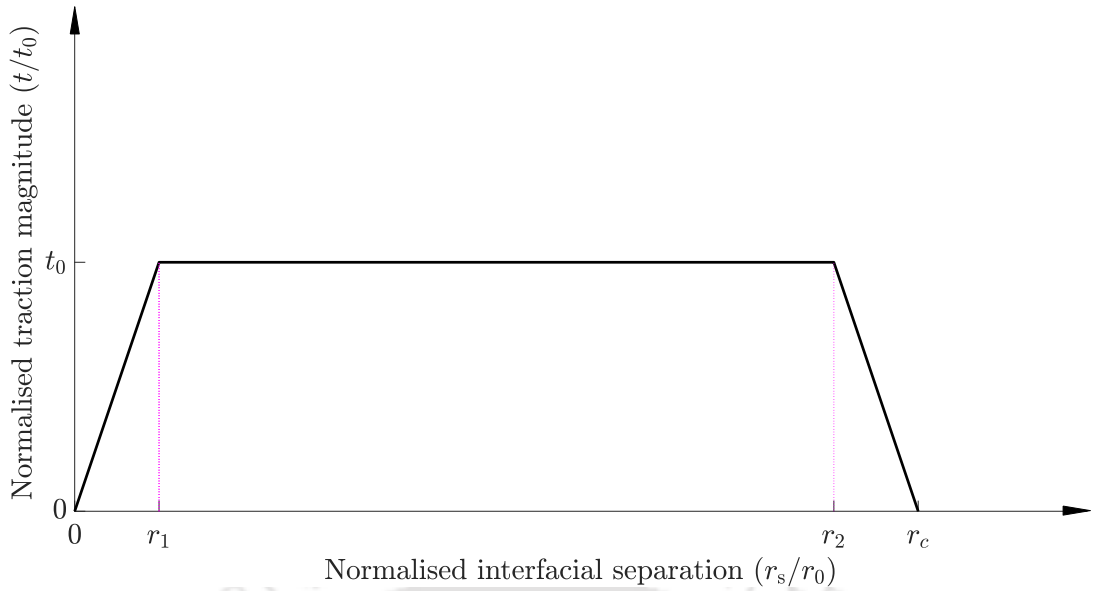

Figure 1.6: Illustration of tri-linear traction-separation law.

with its finite element implementation has been presented by Sauer and Li [137, 138]. This model, called the coarse-grained contact model (CGCM) is derived from the homogenization of the molecular dynamics description of interactions between the atoms of the interacting bodies. In the current thesis, this CGCM is employed to formulate the normal adhesion between gecko spatula and the rigid substrate.

Next, various spatula peeling models are described. Gao et al. [43] employed finite element analysis to illustrate the flaw tolerant adhesion in nanoscale structures like gecko spatula, which is represented by a flat-ended cylinder. Instead of the traction-separation laws as in Eq. (1.22) based on the total adhesion potential (1.21), Gao et al. [43] employed a cohesive zone model of Tvergaard and Hutchinson [139, 140] to fit traction-separation laws. In this model, a layer of cohesive elements is used to represent the van der Waals interactions between the two contacting surfaces. A generalized tri-linear traction-separation law for the Tvergaard-Hutchinson model is used. It can be defined as [141]

$$\boldsymbol{t}(\boldsymbol{r}) = -\bar{\boldsymbol{r}} \times \begin{cases} t_0 \dfrac{r}{r_1} & \text{if } 0 \le r \le r_1\,, \\ t_0 & \text{if } r_1 \le r \le r_2\,, \\ t_0 \dfrac{r - r_c}{r_2 - r_c} & \text{if } r_2 \le r \le r_c\,, \\ 0 & \text{if } r_c \le r\,, \end{cases} \tag{1.23}$$

where $r := \|\boldsymbol{r}\|$ denotes the magnitude of the interfacial separation and $\bar{\boldsymbol{r}} = \boldsymbol{r}/\|\boldsymbol{r}\|$ represents its direction (see Figure 1.6). Here t_0, r_1, r_2, and r_c are model parameters, which depend on the interacting materials.

One of the earliest computational studies of peeling of adhesive tape was carried out by Crocombe and Adams [142]. The authors employed the cohesive fracture theory of Anderson et al. [143] within the setting of finite element analysis. Finite element analysis of Gao et al. [43] showed that as the spatula size decreases the stress distribution in the contact area becomes more uniform and stress concentration vanishes as the size decreases below a critical value. In addition to a generalized Kendall's peeling model, as discussed in section 1.3.2, Chen et al. [103] also employed finite element modelling in Abaqus/Standard to analyse peeling behaviour of a spatula modelled as a two-dimensional thin strip. The authors, using cohesive elements deforming according to a traction-separation law to model the adhesive interactions, demonstrated the way in which a spatula can generate pretension as it is dragged on a rigid substrate. Peng et al. [144] investigated the influence of various parameters viz. adhesion length, material stiffness, roughness, thickness, and pull-off angle on the gecko spatula pull-off force by employing the finite element method. The gecko spatula is represented by a thin nanofilm. The interfacial contact is once again represented by the Tvergaard and Hutchinson model [140]. It is observed that at a particular pull-off force angle, the pull-off force remains invariant only if the length of the film is larger than the effective adhesion length. The effective adhesion length is defined as the length at which the interfacial tractions reach the theoretical interfacial strength. It is also observed that at smaller angles, the tangential component of the pull-off force dominates, while at larger angles, normal component dominates. Furthermore, the authors have shown that the viscoelastic property of the spatulae aids in its reversible adhesion. Using computational modelling and analysis, Cheng et al. [145] demonstrated the process in which the geckos achieve strong attachment and easy detachment. The van der Waals interactions are modelled using a triangular traction-separation law. The finite element simulations are carried out in the commercial software ABAQUS. The authors' simulations showed as the gecko begins attachment, its toes are rolled in, and setae are pulled proximally, which causes the spatula pads to slide on the surface and make contact developing a linear distribution of tensile forces. Then, as the gecko disengages, it changes the pulling angle of the setae, thus creating an instability at the interface, which then leads to a complete detachment of the spatula pads from the substrate.

Sauer [146] presented a three-dimensional multiscale model for studying seta and spatula adhesion based on the CGCM of Sauer and Li [137]. This is illustrated in Figure 1.7. Geometrically exact finite beam elements [147, 148] are employed in the finite element analysis of both seta and the spatula peeling. After obtaining the load-displacement relation for each spatula, this effective load is then transferred to the nodes of FE mesh of setal tips. Sauer [149] further extended this multiscale model to simulate dynamic peeling of seta and spatula. The author investigated the rate effects by varying the pull-off velocity by two orders of magnitude. It

was observed that the maximum pull-off force reached during the peeling process increased significantly with the increase in pull-off velocity.

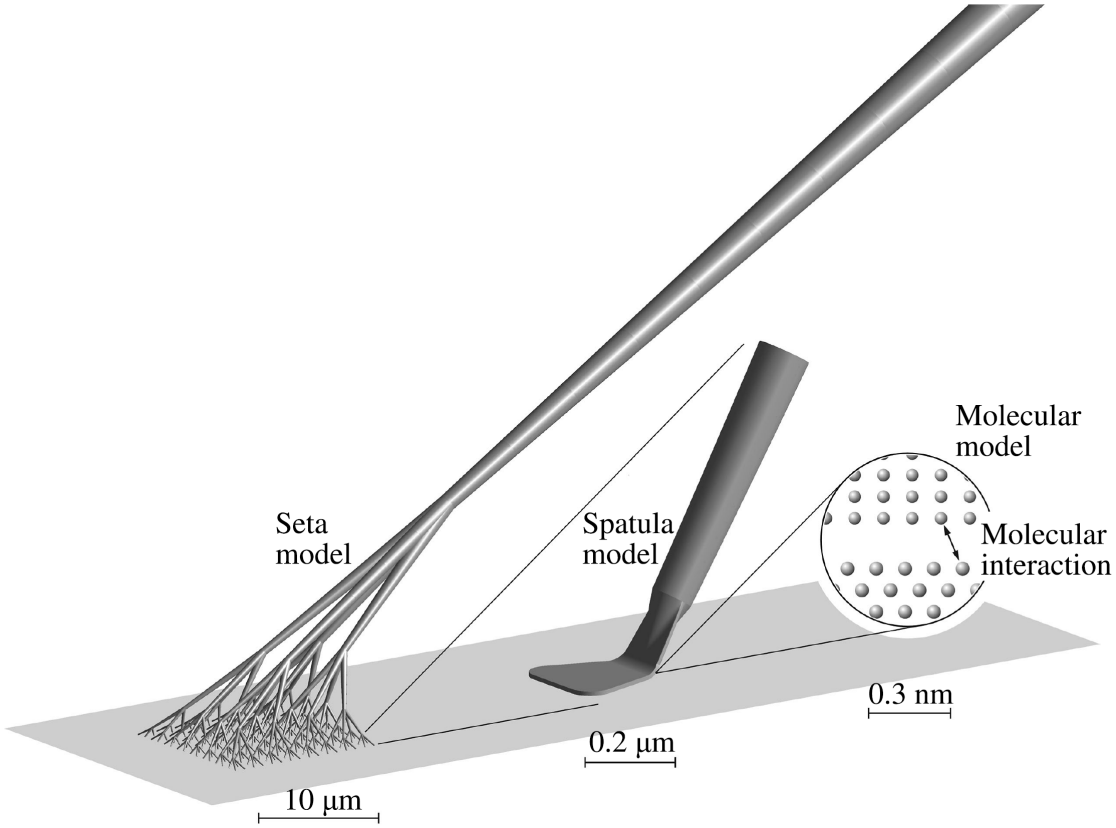

Figure 1.7: Multiscale model of a gecko seta. Reprinted with permission from Sauer [149].

Earlier, Bhushan et al. [150] also presented a hierarchical model with two-levels to represent the structure of gecko setae, using linear elastic springs in each level. The authors used this model to investigate the adhesion of seta and spatulae with rough surfaces with varying roughness amplitude and correlation length. Each branch of the seta is assumed to be beam with a bending stiffness. By assuming that the spatulae ends and the rough surface asperities can be represented as spheres, the adhesive forces are obtained following DMT theory [78]. By employing a numerical algorithm, the authors simulated the contact between the rough surface and the hierarchical seta model. It was found that the hierarchical structure enhanced adhesion on rough surfaces in general. But the relative increase in adhesion with surface roughness was observed to be not so straightforward and depended on the particular roughness amplitude and correlation length. It can be observed that these conclusions are similar to the experimental observations [67, 70, 151, 152]. This model was extended by Kim and Bhushan [153, 154] to simulate three-levels of hierarchy to study the effect of the applied load and stiffness on the adhesion characteristics. It was observed that the adhesion enhancement obtained by the

multiscale nature of the adhesive system increased with increasing applied load and decreasing spring stiffness. Furthermore, the influence of the capillary forces on the gecko adhesion was also examined by the authors in [155]. The authors employed a numerical method to evaluate the elliptical integrals formulated for capillary forces. Both the Laplace force due to the pressure difference across the water interface and the surface tension force due to the formation of the meniscus are considered. For the evaluation of solid-solid adhesion between the spatulae and the substrate the authors employed the DMT adhesion theory [78] as the spatula material β-keratin is a very stiff glassy polymer (Young's modulus $E_0 \approx 2$ GPa). All the three forces, viz. Laplace force, surface tension force, adhesion force, displayed distinct behaviours depending on the hydrophobicity of the surface and the relative humidity.

Schargott [156] has presented a three-dimensional hierarchical model for adhesive pads with three, four, and five levels of hierarchy. Each structure in the hierarchy is modelled as a beam with a square cross-section. Numerical simulations are carried out to evaluate the adhesion performance of three, four, and five layered structures on stochastic rough surfaces. It is observed that hierarchical structures with vertical beams although were able to reduce the effective modulus of the overall structure, it is the tilting of the beams, the high aspect ratio, combined with the hierarchical construction that made the overall structure compliant enough to adhere to the substrates. This reveals the principle through which gecko adhesive pads achieve the effective elastic modulus for tack as dictated by the Dalhquist criterion [157, 158] as also noted by various other researchers [68, 159–161]. It was further observed that enhancement in adhesion performance on stochastic rough surfaces is obtained by increasing the number of layers.

Sauer and co-workers studied the gecko spatula peeling extensively using various computational models. Sauer and Holl [162] presented a detailed three-dimensional (3D) geometry of the gecko spatula based on the electron microscopy images [74]. The surface force formulation developed by Sauer and Wriggers [120] is employed for the 3D nonlinear finite element analysis of the peeling of the spatula. In order to accurately capture the contact tractions due to highly nonlinear van der Waals adhesion a surface enrichment strategy proposed by Sauer [163] is used. In this strategy, the contact surface is described by higher-order interpolation functions, whereas the bulk is described by the standard linear Lagrange interpolation functions. The detailed parametric study showed that the spatula can generate strong adhesion over a wide range of material and geometrical parameters. This 3D FE model was utilized by Gautam and Sauer [164] to investigate the dynamic peeling behaviour of gecko spatula. The effect of finite bending stiffness on the spatula peeling behaviour was studied by Sauer [165]. The spatula is modelled as a thin strip and the finite element analysis based on a geometrically exact finite beam model

utilized to demonstrate that as the bending stiffness increases, the pull-off force increases significantly. The continuum theory and the corresponding nonlinear finite element formulation of this geometrically exact beam theory are presented in [166]. This two-dimensional beam formulation is based on the work of Reissner [167]. Also, the developed formulation is then used to study the peeling behaviour of the gecko spatula, whose interactions are described using both van der Waals adhesion and cohesive zone models. It is shown that this new beam formulation is both accurate and highly efficient compared to the 3D formulations in [149, 162]. Recently, Grill et al. [168] also presented a computational model for molecular interactions of three-dimensional slender beams based on the geometrically exact beam formulation of Reisnner [167]. They also proposed a new strategy to reduce the computationally expensive double 3D integrals to more efficient double one-dimensional integrals. Their model employs various interaction potentials such as Lennard-Jones, electrostatic, steric exclusion, and van der Waals adhesion. The authors then applied this developed model to study the pull-off behaviour of adhesive elastic fibers [169].

By employing Lennard-Jones potential to represent the surface interactions, Zhang et al. [170] developed a finite element model to investigate the effect of tip geometry of the nanoscale adhesive structures on their adhesion performance with a nanoscale hemisphere. It was observed that at the nanoscale, the adhesion performance not only depended on the equivalent radius of the structure but also on the adhesion area and the sticking area. Their numerical simulations showed that among flat, cup, mushroom, and spherical tips, cup tips provided best adhesive performance and mushroom the worst. However, many other researchers showed that the mushroom-shaped fibrillar adhesives display superlative adhesive performance when compared to flat and spherical tips while outperforming even spatula tips in terms of the normal pull-off forces and the enhancement of adhesion through size reduction [171–177]. This superior performance of mushroom-shaped terminal features is attributed to various mechanisms owing to its geometry such as no stress singularity at the edge, the suction effect due to the formation of pressure void inside the area of contact, distribution of contact stress, increase in the contact area [177]. Unlike spatula structures which exhibit shear induced adhesion, mushroom-shaped structures do not require any preload to engage [178]. Further, it has been observed that mushroom-shaped adhesives are more suited for passive applications, unlike spatula structures which serve more dynamic applications such as rapid locomotion of geckos. In nature, mushroom-shaped adhesive structures are observed in terrestrial as well as aquatic organisms such as male Chrysomelid beetles, spiders, Echinoderms, corals, jellyfish, algae, plants, and bacteria [172].

Numerical simulations of Pantano et al. [179] investigates the advantage of a particular geometrical feature of the spatulae structures, i.e. their gradual tapering

of the pads in terms of both thickness and width. By modelling the van der Waals adhesion by Lennard-Jones potential, the authors carried out finite element analysis in the commercial software ABAQUS. From the results obtained it is observed that the negative gradient of the thickness aids in enhancing the resistance to detachment. Whereas, the positive gradient of the width contributes to the stability of the detachment. Mergel et al. [180] applied the geometrically exact beam formulation of Sauer and Mergel [166], to perform shape optimization of adhesive structures. A two-dimensional beam with continuously varying cross-section is considered. A genetic algorithm is used for optimization to maximize the contact surface of the beam, external work done in peeling, and minimize the strain energy. Their results showed that, for given model parameters, the optimal shape of the beam closely resembles the gecko spatula. Furthermore, it was shown that the increase of the width towards the tip increased the maximum pull-off force, which is similar to the observations of Pantano et al. [179]. The authors further extended the model to study the effect of peeling direction on the optimum shape by using a cohesive zone model of Xu and Needleman [181] to account for normal as well as tangential debonding [182]. The nanoscale spatula-shaped terminal feature of fibers has been shown to aid gecko adhesion on microscale rough surfaces by Gillies and Fearing [183]. The authors modelled the fibers as a combination of linear spring along the length and a rotational spring at the base. Numerical simulations of arrays of these hairs have shown that the spatula-shaped hairs provide ten times larger adhesive forces than hemispherical-shaped tips.

Interatomic interactions can also be modelled by Morse potential $\phi_m(r)$, which for a two atoms separated by distance r is defined as [184]

$$\phi_m(r) = D(e^{-2a(r-r_0)} - 2e^{-a(r-r_0)}), \tag{1.24}$$

where D represents is the bond-dissociation energy, r_0 is the equilibrium distance, and a is a material parameter that characterizes the width of the potential well. Chiu et al. [185] used Eq. (1.24) to model the interaction between the atoms in a nanoscale thin film. Finite element analysis is performed in LS-DYNA software package to investigate the effect of size and atomic vacancies to understand material sliding, stress development. Filippov et al. [186] numerically investigated the contact formation dynamics of spatulae on rough surfaces by describing the van der Waals interactions by Morse potential (1.24). Their numerical simulations show that under shear loading, the spatulae spread on both the smooth and the rough surface, thus increasing the contact area even in case of prior misalignment. It was also shown that there exists optimum shear force at which the contact is maximum; hence the adhesion is maximum, but there is no slip. Further, similar to the observations of Pantano et al. [179], the negative thickness gradient was found

to enhance adhesion. Mishra et al. [187] investigated the adhesion and debonding characteristics of an elastic film cast on various patterned rigid surfaces by employing finite element analysis. It was found that the surface features of the films cast on the patterned surfaces depended only on the RMS value of the roughness irrespective of the pattern. Further, it was found that during debonding, the rate of peeling increased the work of adhesion. Kovalev et al. [188] also investigated the spatula adhesion behaviour on surfaces composed of individual round particles and numerically generated rough surfaces derived from surface topography of real surfaces. Numerical experiments of adhesion of a two-dimensional elastic spatula on different rough surfaces showed that for surfaces with the characteristic size of the roughness in the range of the spatula size, adhesion dropped as only some part of the spatula makes contact with the substrate. These results are in agreement with the experimental observations [67].

Most of the numerical models discussed above, especially the van der Waals adhesion models, do not consider the contribution of friction at the interface. Also, in some of the numerical simulations [150, 153–155], the underlying adhesive contact description is derived from analytical models such as the DMT theory [78]. Further, the numerical approaches employing the cohesive zone models [43, 103, 144, 145] although consider the tangential tractions they do not account for the frictional sliding at the interface. However, it has been established that the geckos attach to surfaces by generating much larger frictional forces than the normal adhesion [1]. Hence, in order to realistically model the coupled adhesion-friction behaviour of the spatula computational models incorporating the friction contribution are needed.

Various researchers have incorporated sliding friction according to the Amontons-Coulomb law (see Eq. (1.1)) in cohesive zone models. In the computational formulation of Tvergaard [189] and the subsequent generalization of Lissenden and Herakovich [190], the sliding friction is brought into the model when the interfacial debonding is complete, and the interface can only sustain compressive loads and tangential tractions. In modelling decohesion behaviour in composites, Chaboche et al. [191] extended the frictional formulation of Tvergaard [189] to allow for continuity between the tensile and compressive loading conditions. A thermodynamic coupled adhesion-friction contact model has been developed by Raous et al. [192, 193] that accounts for sliding friction even for partial debonding conditions. This model was extended by Cocou et al. [194] to account for recoverable adhesion for the case dynamic adhesive contact between rubber and glass. Snozzi et al. [195] presented a mixed-mode debonding model for fracture of brittle materials that can capture the interfacial behaviour starting from the nucleation of crack to the pure frictional sliding state where the friction is represented by Eq. (1.1). Similar cohesive zone models that model sliding friction according to Amontons-Coulomb law

using micromechanical approaches for masonry structures have also been developed by other authors [196–198].

Deng et al. [199] performed friction force microscopy experiments of an AFM tip sliding on a nanoscale graphite structure. It was observed that when the adhesion between the tip and the graphite increases, a partial delamination of atomic layers of graphite occur and the friction increases as the load decreases as the tip is retracted. To understand this, the authors performed FE analysis (see supplementary information S1 of [199]) of adhesion between the tip and the graphite, in which the van der Waals adhesion is modelled using the Lennard-Jones potential in Eq. (1.20) and the adhesive friction is introduced using the reduced model of Homola et al. [96] in Eq. (1.11) with a constant shear strength corresponding to local compression in the interface. Jiang and Park [200] proposed a Gaussian-type potential in addition to the Lennard-Jones potential to describe the interfacial friction and adhesion for layered structures like graphene. This model, however, is applicable only for static friction.

Most of the friction models discussed above, model the sliding friction only when the local normal stress is compressive. However, as discussed in sections 1.2 and 1.3.2, in case of gecko adhesion, it has been experimentally observed that the adhesive structures generate high friction when the local stresses are tensile [48]. Further, experimental observations of Eason et al. [201] have shown that in gecko adhesive pads, during attachment and detachment, there is a non-uniform stress distribution and the local contact stresses vary from tensile to compressive with the same contact area. To address these issues, Mergel et al. [202] developed two continuum-based phenomenological contact models for adhesive friction that account for sliding friction for both local compression and tension. In both the models authors define a threshold value for the static friction beyond which the interacting surfaces are sliding with respect to each other. Further, for both the models, a cut-off distance is defined beyond which it is assumed that the interacting surfaces do not experience friction. In the first model, called "Model DI", the sliding threshold is equal to a constant shear strength which is independent of the separation distance between the surfaces. In the second model, called "Model EA", which can be considered as a generalized local form of Eq. (1.10), the sliding threshold is a function of normal adhesive traction (derived from Lennard-Jones potential) which in turn is a function of the separation distance. The authors showed that these models could accurately predict the frictional sliding behaviour of elastomers on glass. A detailed finite element framework incorporating these coupled adhesion and friction models can be found in [203]. As such, in the current thesis, "Model EA" is employed to capture the coupled adhesion and friction in gecko spatula peeling.

1.4 Artificial neural networks

Machine learning (ML) techniques have found applications in a wide range of data-driven research areas including computational mechanics [204–210]. The probabilistic and flexible nature of machine learning enhances the capabilities of conventional computational models. Artificial neural network (ANN), a subset of ML, is one of such successful statistical methods that has been used in various engineering problems to analyse discrete data and find complex interrelations therein [211–214]. ANNs are modelled to loosely mimic the neural network in a brain such that each artificial neuron communicates with other connected artificial neurons similar to synapses in the brain [215]. The inputs to each of these artificial neurons and their connections to other neurons are associated with a weight value. These neurons are generally grouped into layers to form a network. Typically, a neural network has an input layer and an output layer, with one or more hidden layers. At each layer, the collection of neurons receive a weighted input, which is passed to a nonlinear function called activation function in that layer, which produces an output. The neural network formed by these layers is trained by comparing the network output corresponding to a given input with the target output. The difference between the network output and the target output, called the error, is then used to adjust the weighted associations at each layer. Thus, the network *learns* to produce an output close to the target output by successive iterations. This iterative process is stopped when a certain criterion is met.

ANNs have been employed to study various problems in the computational mechanics, such as inverse problems [216, 217], constitutive modelling [218–220], fracture [221], and damage detection [222, 223]. Using ANNs, Manevitz et al. [224] predicted the optimal placement of nodes on a two-dimensional geometry to generate a finite element mesh. Rapetto et al. [225] employed ANNs to predict the relationship between the surface roughness parameters and the real contact area in elastic contact between a rough surface and a flat rigid substrate. Gyurova et al. [226] predicted sliding friction and wear characteristics of polymer composites using ANNs. Liang et al. [214] proposed a fast and accurate method based on deep learning to estimate the stress distribution in aortic walls of the human heart. Hamdia et al. [227] used a deep neural network algorithm to understand the material response of a flexoelectric cantilever nanobeam. They obtained the data for training by solving the governing differential equations using NURBS based isogeometric analysis. Gu et al. [228] used neural networks to propose a new design methodology for bio-inspired hierarchical composite materials. The designs are optimized based on strength and the toughness of the materials. The finite element (FE) analysis is used to obtain the training and testing data. They have shown

that employing neural networks can significantly reduce the high computational costs involved in FE simulations. It was observed that their neural network could evaluate billions of material designs in a matter of hours, for which the finite element method would take years to solve. Oisihi and Yoshimura [229] proposed a new local node-to-segment contact search method using deep neural networks to reduce the high computational times involved. Recently, this work has been extended by Oishi and Yagawa [230] to surface-to-surface local contact search between arbitrarily curved surfaces, which are described by non-uniform rational B-spline (NURBS) basis functions. Nowell and Nowell [231] used ANNs to predict the total fretting fatigue life of an aluminium alloy. Using deep learning techniques, Kim et al. [232] performed shape optimization to design adhesive pillars with uniform stress distribution and high adhesive strength. The deep neural networks combined with genetic optimization could predict the stress distribution in the interface and the detachment mechanism with great accuracy and computational efficiency. Khoei et al. [233] used backpropgation learning method based neural network with Nelder-Mead method [234], to develop a novel efficient stress recovery technique in adaptive finite element method. It was observed that their neural network model particular performed much better than the conventional superconvergent patch recovery (SPR) technique and weighted superconvergent patch recovery (WSPR) technique, especially in the regions of high stress-concentrations.

Backpropagation algorithm is a learning method, in which the neural network is trained to form associations between the input and output pairs. In this algorithm, first, the inputs are propagated forward through the input, hidden, and output layers. Then, the error gradients, called the sensitivities, are propagated back to the input layer. At the end of each iteration, the weight values are updated accordingly to reduce the error. Backpropagation learning method is extensively used to train neural networks [235] in machine learning. However, backpropagation algorithm tends to be slow and are prone to overfitting during training. To address these issues associated with backpropagation algorithms, several generalization methods such as Bayesian regularization (BR) [236, 237] and Levenberg–Marquardt (LM) [238] are used. Generalization methods minimize the likelihood of overfitting the training data. The LM optimization method, especially, decreases the computational time of the backpropagation algorithm by increasing the convergence rate [239]. Both the BR and LM methods are often employed owing to their advantage in obtaining a lower mean squared error [240]. However, it has been observed that Bayesian regularization performs better than LM [240] with BR achieving the highest correlation coefficient and the lowest sum of square errors. As such, Bayesian regularization has been employed to successfully study various problems such as constitutive modelling, data mining, predicting stock price movement, magnetic shielding, and chemical adsorption [241–245].

1.5 Objective of the thesis

From the literature discussed in this chapter, which is by no means an exhaustive list, the following observations can be made:

- Experimental investigations, though have contributed to a vast amount of knowledge about gecko adhesive system. Yet, there have been no direct studies that explored the coupled adhesion and friction behaviour at the spatula level.

- Most of the analytical models that study the peeling of gecko spatula, though provide insights into the various aspects of the peeling behaviour, they are applicable only in the regime of steady-state peeling. However, it has been observed that steady state peeling generally occurs, only if the structures are quite long [112]. As such, most of the analytical models are unable to predict the whole peel-off process, including the snap-off behaviours.

- Numerical models although can describe the peeling process, most of these studies which model the van der Waals adhesion using Lennard-Jones potential do not include the contribution of friction. Some of the cohesive zone models that include friction are only applicable for compressive normal loads. However, it has been established that geckos can generate sliding friction even when for tensile loads [48].

- There have been very few studies, which employed a three-dimensional spatula model to analyse its peeling behaviour. Although Sauer and Holl [162] performed a three-dimensional FE analysis, in their work the contribution of interfacial friction was not considered.

- Numerical analyses using methods such as FEM, require large computational time. As mentioned in the previous section, the use of machine learning techniques such as artificial neural networks has the potential to reduce these computational costs, while retaining the accuracy of the numerical methods.

Based on the above observations, the objective of the present work is to conduct a systematic investigation of the coupled adhesion and friction behaviour in gecko spatula peeling using a continuum-based computational model that captures the contribution of sliding friction even under tensile loading. To achieve this objective, several sub-objectives are set. They are as follows.

- To develop a computational framework in the setting of nonlinear finite element analysis to study the peeling behaviour of a gecko spatula.

- To understand the strong attachment and easy detachment behaviour of the spatulae as well as to perform a detailed investigation of the influence of various material and geometrical parameters on the pull-off forces.

- To explore the possibility of presence of the critical detachment angle and the "frictional adhesion" phenomenon, until now only observed from seta to toe levels of gecko in the literature, at the spatula level.

- To carry out a detailed study in order to understand the influence of different parameters on the critical detachment angle.

- To extend the computational framework to study the peeling behaviour of the gecko spatula using a three-dimensional finite element model.

- To develop an artificial neural network model to predict a few important aspects of the spatula peeling behaviour such as the maximum normal pull-off force, the maximum tangential pull-off force, and the resultant force angle at the detachment.

1.6 Structure of the thesis

The thesis is organized into six chapters which are followed by three appendices and references. The thesis is structured as follows.

Chapter 1: This chapter introduces the current state of gecko adhesion research. First, the beginnings of gecko adhesion research starting from the discovery of adhesive pads and the microscopic structures populating them is presented. Next, the efforts by various researchers understanding various aspects of gecko adhesion are presented. Then, advances in modelling the gecko spatula adhesion and friction employing different experimental, analytical, and numerical methods is detailed. Finally, the application of artificial neural networks in solving different computational mechanics problems are presented.

Chapter 2: In this chapter, the continuum formulation of the computational model employed in the current thesis to study gecko spatula peeling is presented. First, the formulation of coarse-grained contact model used to model the adhesive contact between the spatula and the substrate is described. Then, the adhesive friction model used to study the frictional behaviour at the contact interface of the spatula and the substrate is presented along with its algorithmic treatment.

Chapter 3: In this chapter, the finite element formulation of the weak form derived in Chapter 2 is presented. Using isoparametric mapping the force equilibrium equations are derived for adhesive friction contact between two bodies. Also, the internal and contact tangent matrices are derived. Further, the surface enrichment strategy used for accurate and efficient evaluation of the contact tractions is also discussed.

Chapter 4: This chapter presents and discusses the numerical results obtained using the framework of nonlinear finite element analysis developed in previous chapters. The finite element formulation is first validated using an example problem from the literature. Next, by modelling the gecko spatula as a two-dimensional thin strip in plane-strain, the coupled adhesion and friction behaviour of the gecko spatula is investigated. This investigation is carried out by examining the normal and tangential pull-off forces generated and by studying the presence of critical detachment angle observed at the spatula level. Further, a detailed parametric study is carried out to understand the influence of various parameters on the pull-off forces and the critical detachment angle. Finally, the finite element formulation is extended to study the peeling of gecko spatulae using a three-dimensional model. Using this 3D model, frictionless and frictional peeling behaviour of the gecko spatula is investigated.

Chapter 5: This chapter discusses the application of artificial neural networks to predict some aspects of the peeling behaviour. A Bayesian regularization based backpropagation learning method is employed to train the neural networks. The input data set is taken from the finite element simulations in Chapter 4. Using the optimized parameters obtained from training the neural networks predictions are made, which are then compared to the FE results to evaluate the performance of the neural networks.

Chapter 6: This chapter concludes the thesis by summarizing the work done and provides an outlook on expanding the current work.

भारतीय प्रौद्योगिकी संस्थान गुवाहाटी
Indian Institute of Technology Guwahati

Chapter 2

Mathematical Formulation

In this chapter, the quasi-continua model employed to study the nanoscale adhesion and friction due to intermolecular interactions between two deformable solids is presented. In order to study to the frictionless adhesive contact at the nanoscale, the coarse-grained contact model (CGCM) proposed by Sauer and Li [137] is used. Mergel et al.'s [202] "Model EA" is employed to model the coupling of adhesion and friction. First, a brief overview of the concept of CGCM is presented in section 2.1. The governing weak form for the normal adhesive contact is derived in section 2.2. In section 2.3 the adhesive friction model and its algorithmic treatment are described.

2.1 Coarse-grained contact model

Interaction of nanoscale solids where the effects of atomic-scale interactions become significant is generally studied using the molecular dynamics (MD) simulations [246]. However, MD simulations become computationally quite expensive as the size of the system being analysed increases. In addition, for many practical applications, such detailed atomic description is not required. On the other hand, macroscale continuum contact mechanics models are only governed by the impenetrability constraints. As such, to model the interaction of solids governed by molecular interactions, Sauer and Li [137] proposed a multiscale, quasi-continuum model which considers the intermolecular interactions of the deforming bodies and utilizes the continuum framework to capture their finite deformations.

In the quasi-continuum model [247–249], named coarse-grained contact model (CGCM), the continuum description used to model the interactions of two bodies at the macro-scale is combined with the atomic scale interaction potentials employed to describe the interactions at the atomic scale. The CGCM takes the form of constitutive relations to model the material response under external or internal loads from the continuum hypothesis. For the hyperelastic material considered in

this thesis, stored energy function W is employed to derive the material response. From the atomic-scale interactions, the CGCM employs the inter-solid potential ϕ describing the interaction between the atoms/molecules of participating bodies and the intrasolid potential ψ describing the interaction between the atoms/molecules of the same body. The intrasolid potential ψ and intersolid potential ϕ are then used to derive the constitutive relation such as an internal potential $W = W(\psi)$ and an external potential field $\Phi = \Phi(\phi)$, respectively.

The continuum formulation of the CGCM can be derived either by coarse-graining the molecular dynamics description or by using the setting of large deformation continuum mechanics. In this thesis, the latter approach, originally presented by Sauer and Li [138], is employed and is detailed in the following sections. For the derivation of the continuum formulation from molecular dynamics, readers are referred to [137]. More detailed descriptions of continuum contact mechanics can be found in [250], [251], and [252].

2.2 Weak form of normal adhesion

In this section, the weak form governing the normal adhesive interaction of two solid bodies undergoing large deformations in the framework of continuum mechanics is derived. The problems considered in this thesis are of quasi-static nature, and as such, the inertial effects are not considered in the formulation.

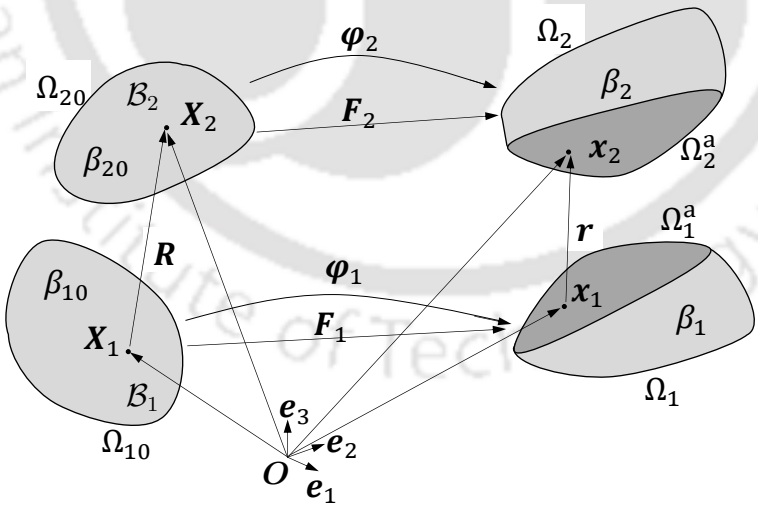

Figure 2.1: Illustration of adhesive contact between two deformable solids. Adapted with permission from Sauer and Li [137].

Consider two deformable bodies $\mathcal{B}_1$ and $\mathcal{B}_2$ occupying initial (and reference) configurations Ω_{10} and Ω_{20} with initial atomic (or particle) densities β_{10} and β_{20}, respectively as shown in the Figure 2.1. These two bodies $\mathcal{B}_1$ and $\mathcal{B}_2$ undergo

deformation due to the interaction between their atoms and occupy current (or deformed) configurations Ω_1 and Ω_2. Then, an initial (and reference) point with position vector $\boldsymbol{X}_k \in \Omega_{k0}$ in body $\mathcal{B}_k$ will now occupy a position $\boldsymbol{x}_k \in \Omega_k$ in the current (deformed) configuration, where $k = 1, 2$. The positions $\boldsymbol{X}_k$ and $\boldsymbol{x}_k$ are related by the expression

$$\boldsymbol{x}_k = \boldsymbol{\varphi}_k(\boldsymbol{X}_k), \tag{2.1}$$

where the one-to-one and orientation-preserving mapping $\boldsymbol{\varphi}_k$ is known as the deformation mapping. The deformation gradient $\boldsymbol{F}_k$ corresponding to $\boldsymbol{\varphi}_k$ is then defined as

$$\boldsymbol{F}_k := \frac{\partial \boldsymbol{\varphi}_k}{\partial \boldsymbol{X}_k}. \tag{2.2}$$

Corresponding to this deformation gradient $\boldsymbol{F}_k$, a Lagrangian strain measure known as the Green-Lagrange tensor is defined as [253]

$$\boldsymbol{E}_k = \frac{1}{2}\left(\boldsymbol{C}_k - \boldsymbol{I}\right), \tag{2.3}$$

where $\boldsymbol{C}_k = \boldsymbol{F}_k^{\mathrm{T}}\boldsymbol{F}_k$ is the right Cauchy-Green deformation tensor and $\boldsymbol{I}$ is the identity tensor.

The determinant of the deformation gradient tensor, $J_k = \det \boldsymbol{F}_k$, called the *Jacobian*, relates the infinitesimal volume elements $\mathrm{d}v_k \in \Omega_k$ and $\mathrm{d}V_k \in \Omega_{k0}$ as well as the particle densities $\beta_{k0} \in \Omega_{k0}$ and $\beta_k \in \Omega_k$ as

$$\mathrm{d}v_k = J_k \, \mathrm{d}V_k, \quad \beta_{k0} = J_k \beta_k. \tag{2.4}$$

In this thesis, it is assumed that there is no influx or efflux of particles. Hence, from the principle of conservation of mass it follows that

$$\beta_{k0} \, \mathrm{d}V_k = \beta_k \, \mathrm{d}v_k \quad \text{and} \quad \rho_{k0} \, \mathrm{d}V_k = \rho_k \, \mathrm{d}v_k, \tag{2.5}$$

where ρ_{k0} and ρ_k are mass densities of body $\mathcal{B}_k$ in undeformed and deformed configurations, respectively.

Assuming that the current system is conservative, the total potential energy Π of the system is the sum of the internal $\Pi_{\mathrm{int}k}$, external $\Pi_{\mathrm{ext}k}$ potential energies of each body, and the adhesion potential Π_{a} between them, i.e.

$$\Pi = \sum_{k=1}^{2} \left[\Pi_{\mathrm{int}k} - \Pi_{\mathrm{ext}k}\right] + \Pi_{\mathrm{a}}. \tag{2.6}$$

A constitutive relation that governs the internal response of the material is used

to calculate the internal potential energy $\Pi_{\text{int}k}$ in Eq. (2.6) as

$$\Pi_{\text{int}k} = \int_{\Omega_{k0}} W_k(\boldsymbol{F}_k)\, \mathrm{d}V_k. \tag{2.7}$$

where $W_k(\boldsymbol{F}_k)$ is the strain energy density function. In this thesis, the interacting bodies are considered to be compressible Neo-Hookean materials with nonlinear stress-strain response for which the strain energy density function $W(\boldsymbol{F}_k)$ is defined as [254]

$$W(\boldsymbol{F}_k) = \frac{\Lambda}{2}\left(\ln J_k\right)^2 + \frac{\mu}{2}\left(I_1 - 3\right) - \mu \ln J_k, \tag{2.8}$$

where $I_1 = \mathrm{tr}(\boldsymbol{B}_k) = \mathrm{tr}(\boldsymbol{C}_k)$. Here, the tensor $\boldsymbol{B}_k = \boldsymbol{F}_k \boldsymbol{F}_k^{\mathrm{T}}$ represents the left Cauchy-Green tensor. Further, Λ and μ are material Lamé constants defined as

$$\Lambda = \frac{2\,\mu\,\nu}{(1-2\nu)} \quad \text{and} \quad \mu = \frac{E_0}{2\,(1+\nu)}, \tag{2.9}$$

where E_0 and ν are the Young's modulus and Poisson's ratio of the material, respectively.

The second Piola-Kirchoff stress tensor $\boldsymbol{S}_k$ is then derived from the strain energy density function $W(\boldsymbol{F}_k)$ as

$$\boldsymbol{S}_k := \frac{\partial W(\boldsymbol{F}_k)}{\partial \boldsymbol{E}_k} = 2\,\frac{\partial W(\boldsymbol{F}_k)}{\partial \boldsymbol{C}_k} = \Lambda\, \ln J_k\, \boldsymbol{C}_k^{-1} + \mu\,(\boldsymbol{I} - \boldsymbol{C}_k^{-1}), \tag{2.10}$$

and the corresponding Cauchy stress tensor $\boldsymbol{\sigma}_k$ is related to the second Piola-Kirchoff stress tensor $\boldsymbol{S}_k$ as

$$\begin{aligned} \boldsymbol{\sigma}_k &= J_k^{-1} \boldsymbol{F}_k\, \boldsymbol{S}_k\, \boldsymbol{F}_k^{\mathrm{T}} \\ &= \frac{(\Lambda\, \ln J_k)}{J_k}\, \boldsymbol{I} + \frac{\mu}{J_k}\left(\boldsymbol{F}_k \boldsymbol{F}_k^{\mathrm{T}} - \boldsymbol{I}\right). \end{aligned} \tag{2.11}$$

The tangent of the second Piola-Kirchoff stress tensor $\boldsymbol{S}_k$ known as the material or Lagrangian elasticity tensor $\mathbb{C}_k$ can be obtained by differentiating Eq. (2.10) with respect to the right Cauchy-Green deformation tensor $\boldsymbol{C}_k$ as [254]

$$\mathbb{C}_k = 2\,\frac{\partial \boldsymbol{S}_k}{\partial \boldsymbol{C}_k} = \Lambda\, \boldsymbol{C}_k^{-1} \otimes \boldsymbol{C}_k^{-1} + 2(\mu - \Lambda \ln J_k)\, \boldsymbol{\mathcal{I}}, \tag{2.12}$$

where the fourth-order tensor $\boldsymbol{\mathcal{I}}$ is defined as

$$\boldsymbol{\mathcal{I}} = -\frac{\partial \boldsymbol{C}_k^{-1}}{\partial \boldsymbol{C}_k}; \quad \mathcal{I}_{pqrs} = \frac{\partial (\boldsymbol{C}_k^{-1})_{pq}}{\partial (\boldsymbol{C}_k)_{rs}}. \tag{2.13}$$

Then, the Eulerian or spatial elasticity tensor $\mathbb{c}_k$ corresponding to the Cauchy stress tensor $\boldsymbol{\sigma}_k$ can be obtained by pushing forward the material elasticity tensor $\mathbb{C}_k$ in

Eq. (2.12) as [254]

$$\mathfrak{c}_k = \frac{\Lambda}{J_k}\, \boldsymbol{I} \otimes \boldsymbol{I} + \frac{2\mu^*}{J_k}\, \mathbb{I}, \tag{2.14}$$

where $\mu^* := \mu - \Lambda \ln J_k$ is the modified shear modulus and $\mathbb{I}$ represents the fourth-order identity tensor. This fourth-order identity tensor is obtained by pushing forward the fourth-order tensor $\boldsymbol{\mathcal{I}}$. Its components are expressed in terms of the Kronecker delta: $\mathbb{I}_{pqrs} = (\delta_{pr}\delta_{qs} + \delta_{ps}\delta_{qr})/2$ [254]. The spatial elasticity tensor $\mathfrak{c}$ can be written in Voigt notation by dropping the subscript k as

$$\mathfrak{c}_v = \frac{1}{J}\begin{bmatrix} 2\mu^*+\Lambda & \Lambda & \Lambda & 0 & 0 & 0 \\ \Lambda & 2\mu^*+\Lambda & \Lambda & 0 & 0 & 0 \\ \Lambda & \Lambda & 2\mu^*+\Lambda & 0 & 0 & 0 \\ 0 & 0 & 0 & \mu^* & 0 & 0 \\ 0 & 0 & 0 & 0 & \mu^* & 0 \\ 0 & 0 & 0 & 0 & 0 & \mu^* \end{bmatrix}. \tag{2.15}$$

2.2.1 Adhesion potential

In CGCM, the intersolid potential $\phi(r)$, i.e. the interaction potential between the particles of the two bodies with position vectors $\boldsymbol{x}_1 \in \Omega_1$ and $\boldsymbol{x}_2 \in \Omega_2$, and separated by a distance $r = |\boldsymbol{r}| = |\boldsymbol{x}_2 - \boldsymbol{x}_1|$ is assumed to be due to the van der Waals forces. These van der Waals interactions between any two particles separated by a distance r are in general described by the Lennard-Jones potential [85] as

$$\phi(r) = \epsilon\left[\left(\frac{r_0}{r}\right)^{12} - 2\left(\frac{r_0}{r}\right)^{6}\right], \tag{2.16}$$

where ϵ and r_0 represent energy and length scales and are material specific constants. Here, the first term gives the steric repulsion for distances smaller than r_0 and the second term describes the attraction as the distance between the particles increases beyond r_0 as shown in Fig 2.2. The force, $F_\phi(r)$, between the particles corresponding to the potential $\phi(r)$ is given as

$$F_\phi(r) = -\frac{\partial\phi(r)}{\partial r} = \frac{12\epsilon}{r_0}\left[\left(\frac{r_0}{r}\right)^{13} - \left(\frac{r_0}{r}\right)^{7}\right]. \tag{2.17}$$

Eq 2.17 shows that $r = r_0$ is the equilibrium distance at which there is no force acting on the particles as shown in Figure 2.2. Further, ϵ is the energy at $r = r_0$.

2.2.2 Weak form derivation

From Figure 2.2, it can be observed that as the distance r between the particles increases the interaction potential weakens very quickly. For example, when $r = 2r_0$,

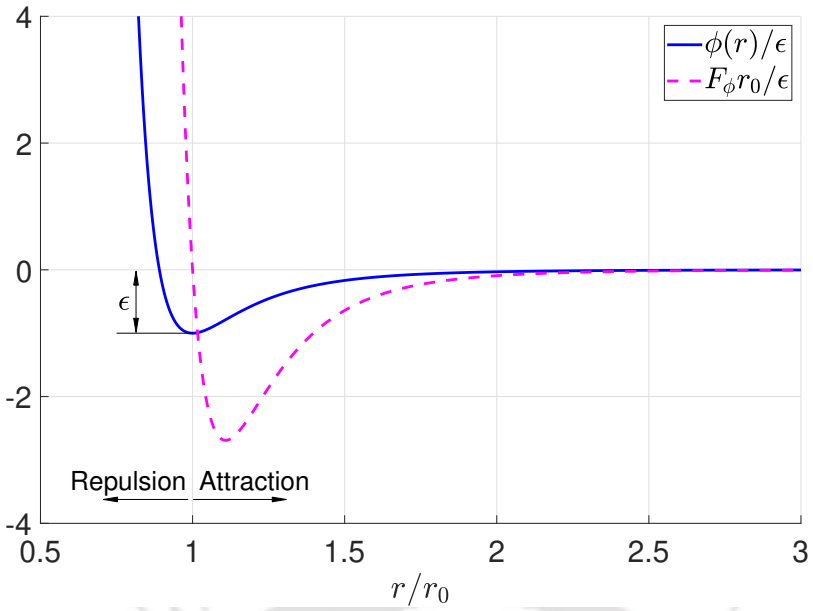

Figure 2.2: Lennard-Jones potential $\phi(r)$ acting between two particles separated by a distance r and the corresponding force $F_\phi(r)$. Here r_0 is the equilibrium distance at which no force acts between the particles.

the absolute value of the adhesion potential is only 3% of the value at $r = r_0$. As such, for the case of interaction between the particles in two different bodies there is cut-off distance r_c beyond which the interactions are negligible. Hence, in computing the total adhesive interaction potential only a subset $\Omega_k^{\mathrm{a}} \subseteq \Omega_k$ of the total domain is considered. The total adhesive interaction potential can then be obtained by summing the interactions of all the particles in body $\mathcal{B}_1$ with each particle of body $\mathcal{B}_2$ and vice-versa as

$$\Pi_{\mathrm{a}} = \int_{\Omega_1^{\mathrm{a}}} \int_{\Omega_2^{\mathrm{a}}} \beta_1\, \beta_2\, \phi(r)\, \mathrm{d}v_2\, \mathrm{d}v_1 = \int_{\Omega_{10}^{\mathrm{a}}} \int_{\Omega_{20}^{\mathrm{a}}} \beta_{10}\, \beta_{20}\, \phi(r)\, \mathrm{d}V_2\, \mathrm{d}V_1\,. \tag{2.18}$$

For quasi-static motion, principle of stationary potential energy states that at equilibrium, among all the admissible variations $\delta\boldsymbol{\varphi}$ for the actual motion $\boldsymbol{\varphi}$ the total potential energy has a stationary value. Therefore, at equilibrium

$$\delta\Pi = \sum_{k=1}^{2} [\delta\Pi_{\mathrm{int}k} - \delta\Pi_{\mathrm{ext}k}] + \delta\Pi_{\mathrm{a}} = 0\,, \quad \forall \delta\boldsymbol{\varphi}_k. \tag{2.19}$$

The variation of the internal potential energy $\delta\Pi_{\mathrm{int},k}$ can be written as

$$\delta\Pi_{\mathrm{int}k} = \int_{\Omega_{k0}} \mathrm{Grad}(\delta\boldsymbol{\varphi}_k) : \boldsymbol{P}_k\, \mathrm{d}V_k = \int_{\Omega_k} \mathrm{grad}(\delta\boldsymbol{\varphi}_k) : \boldsymbol{\sigma}_k\, \mathrm{d}v_k, \tag{2.20}$$

where $\mathrm{Grad}(\cdot)$ and $\mathrm{grad}(\cdot)$ are the gradient operators with respect to the initial and current configurations, respectively. Here, $\boldsymbol{P}_k$ is the first Piola-Kirchoff stress

tensor and is related to the second Piola-Kirchoff stress tensor as

$$\boldsymbol{P}_k = \boldsymbol{F}_k \, \boldsymbol{S}_k. \tag{2.21}$$

Using Eq. (2.18), Eq. (2.5), and the chain rule the variation of the adhesion potential can be calculated as

$$\delta\Pi_{\mathrm{a}} = \int_{\Omega_1^{\mathrm{a}}} \int_{\Omega_2^{\mathrm{a}}} \beta_1 \beta_2 \left(\frac{\partial \phi(r)}{\partial \boldsymbol{x}_1} \cdot \delta\boldsymbol{\varphi}_1 \, + \, \frac{\partial \phi(r)}{\partial \boldsymbol{x}_2} \cdot \delta\boldsymbol{\varphi}_2 \right) \mathrm{d}v_2 \, \mathrm{d}v_1. \tag{2.22}$$

Rearranging and grouping the terms gives

$$\delta\Pi_{\mathrm{a}} = - \int_{\Omega_1^{\mathrm{a}}} \delta\boldsymbol{\varphi}_1 \cdot \beta_1 \, \boldsymbol{b}_{\mathrm{a}1} \mathrm{d}v_1 \, - \int_{\Omega_2^{\mathrm{a}}} \delta\boldsymbol{\varphi}_2 \cdot \beta_2 \, \boldsymbol{b}_{\mathrm{a}2} \mathrm{d}v_2, \tag{2.23}$$

where $\boldsymbol{b}_{\mathrm{a}1}$ and $\boldsymbol{b}_{\mathrm{a}2}$ are considered to be the body forces defined as

$$\begin{aligned} \boldsymbol{b}_{\mathrm{a}1}(\boldsymbol{x}_1) &:= -\frac{\partial \Phi_2}{\partial \boldsymbol{x}_1}, & \Phi_2(\boldsymbol{x}_1) &:= \int_{\Omega_2^{\mathrm{a}}} \beta_2 \, \phi(r) \, \mathrm{d}v_2, \\ \boldsymbol{b}_{\mathrm{a}2}(\boldsymbol{x}_2) &:= -\frac{\partial \Phi_1}{\partial \boldsymbol{x}_2}, & \Phi_1(\boldsymbol{x}_2) &:= \int_{\Omega_1^{\mathrm{a}}} \beta_1 \, \phi(r) \, \mathrm{d}v_1. \end{aligned} \tag{2.24}$$

The body force $\boldsymbol{b}_{\mathrm{a}k}$ acting at the point $\boldsymbol{x}_k \in \Omega_k$ of body $\mathcal{B}_k$ emerges from the interactions with the field Φ_l enveloping the body $\mathcal{B}_l$, where $l \neq k$. Pulling the gradient into the integration and from the definition of force of the Lennard-Jones potential $F(r)$ in Eq. (2.17), the expressions for the body forces in Eq. (2.24) can be further simplified as

$$\begin{aligned} \boldsymbol{b}_{\mathrm{a}1}(\boldsymbol{x}_1) &= \int_{\Omega_1^{\mathrm{a}}} \beta_2 \, F_\phi(r) \, \bar{\boldsymbol{r}} \, \mathrm{d}v_2, \\ \boldsymbol{b}_{\mathrm{a}2}(\boldsymbol{x}_2) &= - \int_{\Omega_2^{\mathrm{a}}} \beta_1 \, F_\phi(r) \, \bar{\boldsymbol{r}} \, \mathrm{d}v_1, \end{aligned} \tag{2.25}$$

where $\bar{\boldsymbol{r}} = \dfrac{\boldsymbol{r}}{r}$ is the unit vector between the points $\boldsymbol{x}_1$ and $\boldsymbol{x}_2$. Using Eqs. (2.20) and (2.23), the variation of the total potential energy in Eq. (2.19) can be written as

$$\delta\Pi = \sum_{k=1}^{2} \left[\int_{\Omega_k} \mathrm{grad}(\delta\boldsymbol{\varphi}_k) : \boldsymbol{\sigma}_k \, \mathrm{d}v_k \, - \int_{\Omega_k^{\mathrm{a}}} \delta\boldsymbol{\varphi}_k \cdot \beta_k \, \boldsymbol{b}_{\mathrm{a}k} \, \mathrm{d}v_k \, - \, \delta\Pi_{\mathrm{ext}k} \right] = 0 \,, \quad \forall \delta\boldsymbol{\varphi}_k, \tag{2.26}$$

which forms the governing weak form of the system of interacting bodies shown in Figure 2.1.

To evaluate the body forces $\boldsymbol{b}_{\mathrm{a}k}$ due to the adhesive interaction between the two bodies, Sauer and Wriggers [120] proposed two methods namely the "body force (BF)" formulation and the "surface force (SF)" formulation. In both of these

formulations, a point $\boldsymbol{x}_k \in \Omega_k$ of body $\mathcal{B}_k$, is projected normally on to the surface $\partial\Omega_l$ of the neighbouring $\mathcal{B}_l$ ($l \neq k$). The corresponding projection point on the surface is denoted as $\boldsymbol{x}_\mathrm{p} \in \partial\Omega_l$. Further, at the point of projection body $\mathcal{B}_l$ is approximated as a half-space. Accuracy of this assumption is examined by Sauer and Wriggers [120] and it was found that for bodies with radius greater than 9 nm, the half-space assumption is very accurate. Following this, body force at point $\boldsymbol{x}_k$ which is at a distance r_k from the projection point $\boldsymbol{x}_\mathrm{p}$ (i.e. r_k is the normal distance between the point $\boldsymbol{x}_k$ and the projection point $\boldsymbol{x}_\mathrm{p}$ on the surface $\partial\Omega_l$) is obtained as [120]

$$\boldsymbol{b}_{ak}(r_k) = \pi\,\beta_l\,\epsilon\,r_0^2\left[\frac{1}{5}\left(\frac{r_0}{r_\mathrm{k}}\right)^{10} - \left(\frac{r_0}{r_\mathrm{k}}\right)^{4}\right]\boldsymbol{n}_\mathrm{p}. \tag{2.27}$$

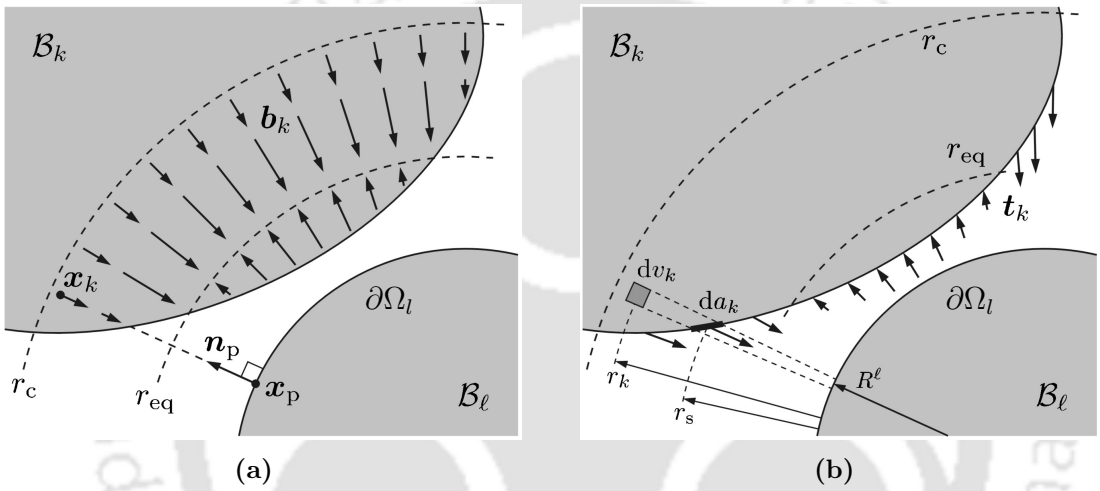

Figure 2.3: Illustration of body force and surface force formulations (a) Computation of the minimum distance r_s from $\boldsymbol{x}_k$ to the surface $\partial\Omega_l$ at the projection point $\boldsymbol{x}_\mathrm{p}$ (b) Projection of body forces in $\mathcal{B}_k$ on to the surface $\partial\Omega_k$ to obtain an effective surface traction $\boldsymbol{t}_k$. Here, r_eq denotes the equilibrium distance and r_c is the cut-off distance after which the effect of intermolecular forces is assumed to be zero. Reprinted from Sauer and Wriggers [120] with permission from Elsevier.

In this thesis, only the "surface force (SF)" formulation is used owing to its efficiency and accuracy [120]. In this approach, an effective surface traction corresponding to the body force $\boldsymbol{b}_{ak}$ is obtained by projecting it parallelly onto the surface of the body $\mathcal{B}_k$ as is illustrated in Figure 2.3. A volume element $\mathrm{d}v_k \in \Omega_k$ of body $\mathcal{B}_k$ is projected onto its surface giving an area element $\mathrm{d}a_k$ opposite to the direction of normal $\boldsymbol{n}_\mathrm{p}$ to the surface $\partial\Omega_l$ ($l \neq k$) and can be written as

$$\mathrm{d}v_k = c_l(r_k)\,\mathrm{d}r_k\,\cos(\alpha_k)\,\mathrm{d}a_k\,, \quad \text{with } c_l(r_k) = \left(\frac{R_1^l + r_k}{R_1^l + r_s}\right)\left(\frac{R_2^l + r_k}{R_2^l + r_s}\right), \tag{2.28}$$

where R_1^l and R_2^l are the principal surface radii of curvature of $\partial\Omega_l$ of body $\mathcal{B}_l$ and r_s is the normal distance between the interacting surfaces. Here, α_k denotes the angle

that the area element $\mathrm{d}a_k$ makes with the projection $-\boldsymbol{n}_\mathrm{p}$, i.e. $\cos(\alpha_k) = -\boldsymbol{n}_\mathrm{p} \cdot \boldsymbol{n}_k$. Then, the weak form (2.26) can be rewritten as

$$\sum_{k=1}^{2} \left[\int_{\Omega_k} \mathrm{grad}(\delta\boldsymbol{\varphi}_k) : \boldsymbol{\sigma}_k \, \mathrm{d}v_k \; - \; \int_{\partial\Omega_k^\mathrm{a}} \delta\boldsymbol{\varphi}_k \cdot \boldsymbol{t}_{\mathrm{a}k} \, \mathrm{d}a_k \; - \; \delta\Pi_{\mathrm{ext}k} \right] = 0 \,, \quad \forall \delta\boldsymbol{\varphi}_k, \tag{2.29}$$

where $\boldsymbol{t}_{\mathrm{a}k}$ is the effective surface traction which is defined as

$$\boldsymbol{t}_{\mathrm{a}k} \; := \; \cos(\alpha_k) \int_{r_s}^{r_\mathrm{c}} c_l(r_k) \, \beta_k \, \boldsymbol{b}_{\mathrm{a}k}(r_k) \, \mathrm{d}r_k, \tag{2.30}$$

where $\boldsymbol{b}_{\mathrm{a}k}$ is the body force given by Eq. (2.27) and c_l is defined in Eq. (2.28). In order to integrate analytically it is further assumed that the particle density β_k is constant between the integration limits r_c and r_k. As shown in Figure 2.3, r_c denotes the cut-off distance after which the effect of intermolecular forces is assumed to be negligible. Whereas r_k is the normal distance between the interior point $\boldsymbol{x}_k$ of body $\mathcal{B}_k$ and the projection point $\boldsymbol{x}_\mathrm{p}$. This leads to

$$\boldsymbol{t}_{\mathrm{a}k} \; \approx \; \cos(\alpha_k) \, \beta_k \int_{r_s}^{r_\mathrm{c}} c_l(r_k) \, \boldsymbol{b}_{\mathrm{a}k}(r_k) \, \mathrm{d}r_k. \tag{2.31}$$

Setting $r_c = \infty$, using Eq. (2.27), and performing the integration results in

$$\boldsymbol{t}_{\mathrm{a}k}(r_s) = \pi \, \cos(\alpha_k) \, \beta_k \, \beta_l \, \epsilon \, r_0^3 \left[\frac{f_1(R_1^l, R_2^l)}{45} \left(\frac{r_0}{r_\mathrm{s}} \right)^9 - \frac{f_2(R_1^l, R_2^l)}{3} \left(\frac{r_0}{r_\mathrm{s}} \right)^3 \right] \boldsymbol{n}_\mathrm{p}, \tag{2.32}$$

where f_1 and f_2 are functions of surface radii of curvature of body $\mathcal{B}_l$ and are approximated as unity for all the problems in this thesis. Introducing Hamaker's constant $A_\mathrm{H} = 2\pi^2 \beta_{10} \beta_{20} \epsilon r_0^6$ [85], the effective surface traction can be written as

$$\boldsymbol{t}_{\mathrm{a}k}(r_s) \; = \frac{t_{\mathrm{a}k} \, \boldsymbol{n}_\mathrm{p}}{J_k J_l} \,, \quad t_{\mathrm{a}k} = \cos(\alpha_k) \, \frac{A_\mathrm{H}}{2\pi r_0^3} \left[\frac{1}{45} \left(\frac{r_0}{r_\mathrm{s}} \right)^9 - \frac{1}{3} \left(\frac{r_0}{r_\mathrm{s}} \right)^3 \right], \tag{2.33}$$

Nanson's formula [255] relates the area differentials in initial and current configurations as

$$\boldsymbol{n}_k \mathrm{d}a_k \; = \; J_k \boldsymbol{F}_k^{-\mathrm{T}} \boldsymbol{N}_k \mathrm{d}A_k, \tag{2.34}$$

where $\boldsymbol{N}_k$ is the outward normal to the surface $\partial\Omega_{k0}$. Then, the weak form in Eq. (2.29) can be rewritten in the reference configuration as

$$\sum_{k=1}^{2} \left[\int_{\Omega_{k0}} \mathrm{Grad}(\delta\boldsymbol{\varphi}_k) : \boldsymbol{P}_k \, \mathrm{d}V_k \; - \; \int_{\partial\Omega_{k0}^\mathrm{a}} \delta\boldsymbol{\varphi}_k \cdot \boldsymbol{T}_{\mathrm{a}k} \, \mathrm{d}A_k \; - \; \delta\Pi_{\mathrm{ext}k} \right] = 0 \,, \quad \forall \delta\boldsymbol{\varphi}_k, \tag{2.35}$$

where $\boldsymbol{T}_{\mathrm{a}k}$ is the effective surface traction in the reference configuration and is

defined as

$$\boldsymbol{T}_{ak} := \frac{\theta_k\, T_{ak}\boldsymbol{n}_{\mathrm{p}}}{J_l} \quad \text{with} \quad T_{ak}(r_{\mathrm{s}}) = \frac{A_{\mathrm{H}}}{2\pi r_0^3}\left[\frac{1}{45}\left(\frac{r_0}{r_{\mathrm{s}}}\right)^9 - \frac{1}{3}\left(\frac{r_0}{r_{\mathrm{s}}}\right)^3\right]. \tag{2.36}$$

Here, $J_l = \det \boldsymbol{F}_l$ is the determinant of the deformation gradient $\boldsymbol{F}_l$ of body $\mathcal{B}_l$ and represents its volume change due to deformation and $\theta_k := -\boldsymbol{n}_{\mathrm{p}} \cdot \boldsymbol{F}_k^{-T}\boldsymbol{N}_k$, which characterizes the influence of the angle between the surfaces and the influence of the dilation of body $\mathcal{B}_k$ at the surface. Investigations of Sauer and Wriggers [120] showed that even for problems with moderate to strong adhesion, such as gecko spatula adhesion, sufficiently accurate results can be obtained by setting $\theta_k = 1$. Therefore, in the current thesis it is assumed that the value of θ_k is unity [162].

In order to satisfy the impenetrability condition for contact between two bodies and to account for the resulting ill-conditioning, regularization of the the effective surface traction $T_{ak} = \|\boldsymbol{T}_{ak}\|$, referred to as adhesive traction from here on, for very small normal gaps $r_{\mathrm{s}} \longrightarrow 0$ is done by modifying the adhesive traction as (see Figure 2.4)

$$T_{ak}^{\mathrm{reg}}(r_{\mathrm{s}}) = \begin{cases} T_{ak}(r_{\mathrm{s}}), & r_{\mathrm{s}} \geq r_{\mathrm{reg}}, \\ T_{ak}(r_{\mathrm{reg}}) + T'_{ak}(r_{\mathrm{reg}})(r_{\mathrm{s}} - r_{\mathrm{reg}}) & r_{\mathrm{s}} < r_{\mathrm{reg}}, \end{cases} \tag{2.37}$$

where r_{reg} is a regularisation distance and is chosen to be equal to the equilibrium distance r_{eq} [202]. Here, T'_{ak} indicates the derivative of the adhesive traction T_{ak} with respect to r_{s} and is given as

$$T'_{ak}(r_{\mathrm{s}}) = \frac{\partial T_{ak}(r_{\mathrm{s}})}{\partial r_{\mathrm{s}}} = -\frac{A_{\mathrm{H}}}{2\pi r_0^4}\left[\frac{1}{5}\left(\frac{r_0}{r_{\mathrm{s}}}\right)^{10} - \left(\frac{r_0}{r_{\mathrm{s}}}\right)^4\right]. \tag{2.38}$$

Sauer and Li [138] defined two material parameters γ_{L} and γ_{W} that characterize the weak form given by Eqs.(2.29) and (2.35). The first parameter γ_{L} characterizes the size of the chosen geometry with respect to the length scale of the interaction potential $\phi(r)$ and is defined as

$$\gamma_{\mathrm{L}} := \frac{R_0}{r_0}, \tag{2.39}$$

where R_0 is the global length scale of the problem under consideration and r_0 is the length scale of Lennard-Jones potential $\phi(r)$ defined in Eq. (2.16).

The second parameter γ_{W} characterizes the internal elastic energy density due to the deformation with respect to the energy density due to the adhesive interactions

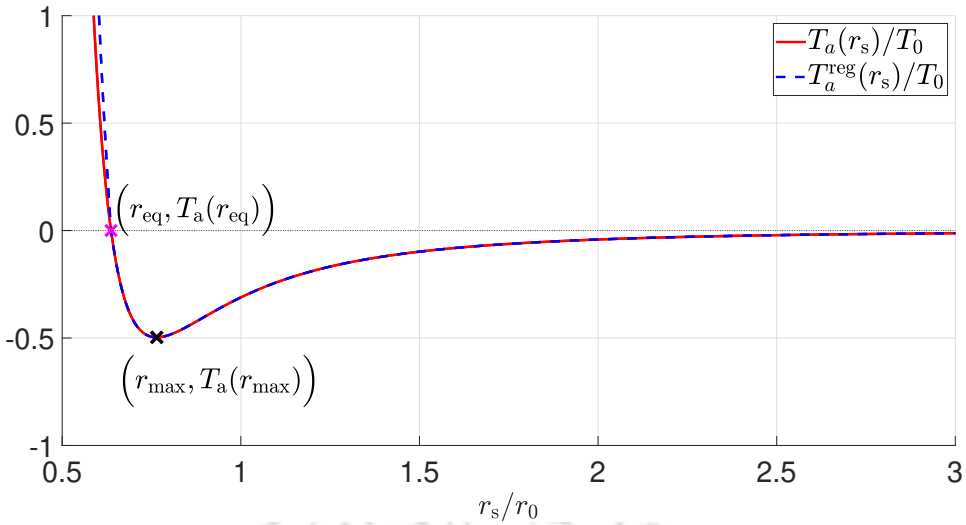

Figure 2.4: Evolution of adhesion traction with the separation distance. Here $T_0 = A_H/(2\pi r_0^3)$.

and is defined as

$$\gamma_W := \frac{E_0}{\left(\frac{A_H}{2\pi r_0^3}\right)}. \tag{2.40}$$

Considering the Tabor parameter [256] for adhesion between a cylinder of radius R and a flat rigid substrate

$$\mu_{Tabor} = \left(\frac{R\, w_{adh}}{E_0^* r_0^3}\right)^{1/3}, \tag{2.41}$$

where $E_0^* = E_0/(1-\nu^2)$ and w_{adh} is the work of adhesion. In CGCM, the work of adhesion can be computed from the adhesive traction $\boldsymbol{T}_a$ as [162]

$$w_{adh} = -\int_{r_{eq}}^{\infty} \|\boldsymbol{T}_a(r_s)\|\, dr_s = \sqrt[3]{15}\,\frac{A_H}{16\pi r_0^2}. \tag{2.42}$$

Then, the two material parameters γ_L and γ_W can be related to the Tabor parameter as

$$\mu_{Tabor} = \left(\frac{\sqrt[3]{15}\,\pi}{8}\right)^{2/3}\left(\frac{\gamma_L}{(\gamma_W)^2}\right)^{1/3}. \tag{2.43}$$

2.3 Adhesive friction formulation

The weak form derived in the previous section considers only the normal forces developed due to the intermolecular interactions. In order to evaluate the frictional forces developed due to adhesive interactions between the bodies in Figure 2.1, Mergel et al. [202] proposed two models based on the coarse-grained contact model discussed in section 2.2. In this thesis, "Model EA" of Mergel et al. [202] which is

based on the extended Amontons' Law of Derjaguin [95] is employed. In this model, a tangential (or frictional) traction $\boldsymbol{T}_{\mathrm{f}k}$ corresponding to a normal traction due to adhesion $\boldsymbol{T}_{\mathrm{a}k}$ is obtained. Following the sign convention of Laursen [252] the total contact traction is computed as

$$\boldsymbol{T}_{ck} = \boldsymbol{T}_{\mathrm{a}k} - \boldsymbol{T}_{\mathrm{f}k}, \quad \text{in the reference configuration,} \tag{2.44}$$

$$\boldsymbol{t}_{ck} = \boldsymbol{t}_{\mathrm{a}k} - \boldsymbol{t}_{\mathrm{f}k}, \quad \text{in the current configuration.} \tag{2.45}$$

The weak form (2.35) can then be modified as

$$\sum_{k=1}^{2}\left[\int_{\Omega_{k0}} \mathrm{Grad}(\delta\boldsymbol{\varphi}_k) : \boldsymbol{P}_k \,\mathrm{d}V_k \;-\; \int_{\partial\Omega^{\mathrm{a}}_{k0}} \delta\boldsymbol{\varphi}_k \cdot \boldsymbol{T}_{ck}\,\mathrm{d}A_k \;-\; \delta\Pi_{\mathrm{ext}k}\right] = 0\,, \quad \forall\delta\boldsymbol{\varphi}_k, \tag{2.46}$$

and in the current configuration,

$$\sum_{k=1}^{2}\left[\int_{\Omega_k} \mathrm{grad}(\delta\boldsymbol{\varphi}_k) : \boldsymbol{\sigma}_k \,\mathrm{d}v_k \;-\; \int_{\partial\Omega^{\mathrm{a}}_{k}} \delta\boldsymbol{\varphi}_k \cdot \boldsymbol{t}_{ck}\,\mathrm{d}a_k \;-\; \delta\Pi_{\mathrm{ext}k}\right] = 0\,, \quad \forall\delta\boldsymbol{\varphi}_k. \tag{2.47}$$

The tangential traction varies within the contact area and is defined for both compressive and tangential normal loads. The interacting bodies are either in sticking or sliding with respect to each other based on a criterion for the magnitude of tangential traction, which is given as (the subscript k is dropped for brevity)

$$\|\boldsymbol{T}_{\mathrm{f}}(\boldsymbol{r}_{\mathrm{s}}, \boldsymbol{r}_{\mathrm{T}})\| \begin{cases} = T_{\mathrm{slide}} & \text{for sliding,} \\ < T_{\mathrm{slide}} & \text{for sticking.} \end{cases} \tag{2.48}$$

where $\boldsymbol{r}_{\mathrm{T}}$ is the tangential slip and T_{slide} denotes the sliding threshold. The sliding threshold is obtained first by shifting the adhesive traction $T_{\mathrm{a}}(r_{\mathrm{s}})$ by a value equal to the adhesive traction $T_{\mathrm{a}}(r_{\mathrm{cut}})$ at a cut-off distance r_{cut} beyond which frictional forces are zero. The expression for r_{cut} is given by

$$r_{\mathrm{cut}} = s_{\mathrm{cut}}\, r_{\mathrm{max}} + (1 - s_{\mathrm{cut}})\, r_{\mathrm{eq}}, \qquad s_{\mathrm{cut}} \in [0, 1], \tag{2.49}$$

where r_{max} is the distance at which the adhesive traction T_{n} given by Eq. (2.36) has the global minimum and s_{cut} is a parameter taking values between 0 and 1.

Then, the sliding threshold is proportional to $T_{\mathrm{a}}(r_{\mathrm{s}}) + |T_{\mathrm{a}}(r_{\mathrm{cut}})|$ and is defined as (also see Figure 2.5),

$$T_{\mathrm{slide}}(r_{\mathrm{s}}) = \begin{cases} \dfrac{\mu_{\mathrm{s}}}{J_{cl}}\left[T_{\mathrm{a}}(r_{\mathrm{s}}) - T_{\mathrm{a}}(r_{\mathrm{cut}})\right], & r_{\mathrm{s}} < r_{\mathrm{cut}}, \\ 0, & r_{\mathrm{s}} \geq r_{\mathrm{cut}}, \end{cases} \tag{2.50}$$

where J_{cl} is the local surface stretch of the neighbouring body and is related to the volume change J_l as $J_l = J_{cl} \cdot \lambda_l$ where λ_l is the stretch along the thickness. For van der Waals potential $\phi(r)$ which is effective only for short-range $\lambda_l \approx 1$ [257]. For biological adhesives, the static friction coefficient takes similar values as the kinetic friction coefficient [202]. As such, in this work, it is assumed that the value of the friction coefficient μ_s is the same for sticking and sliding. In the current thesis, the cut-off distance r_{cut} is taken to be equal to r_{max}, i.e. $s_{cut} = 0$, in order to capture sliding friction even for tensile loading. If $s_{cut} = 0$, the sliding traction is given only for compressive forces, which is equivalent to the Amontons-Coulomb friction law.

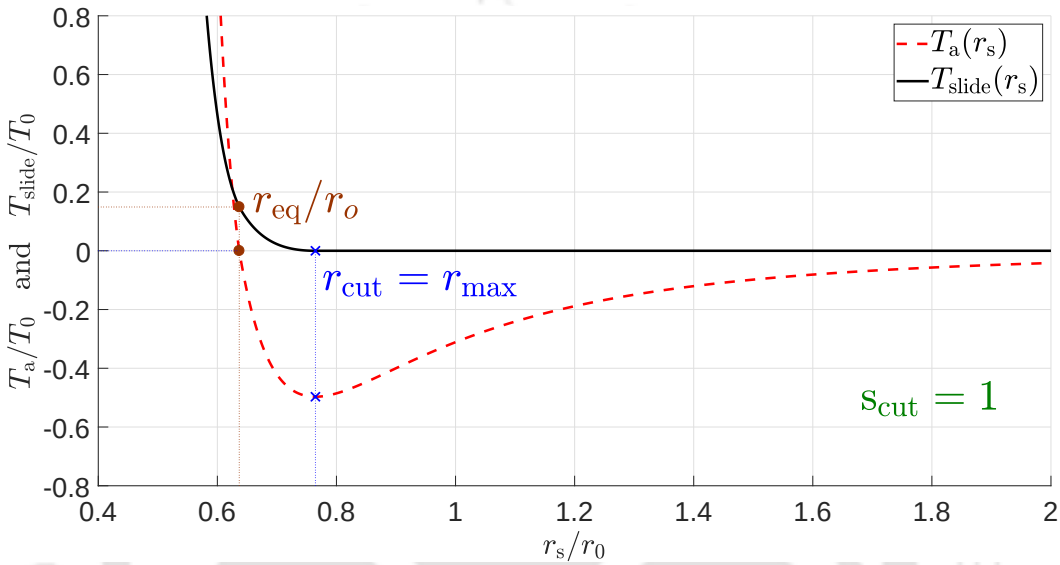

Figure 2.5: Variation of adhesive traction T_a and sliding threshold T_{slide} with the normal distance r_s according to adhesive friction model ("Model EA") of Mergel et al. [202]. Here, $T_0 = A_H/(2\pi r_0^3)$, $\mu_s = 0.3$, and $s_{cut} = 1$.

The elasto-plasticity framework is used to formulate the constitutive equations for the friction [250]. Following penalty regularization, the tangential slip is divided into two parts: an elastic sticking part $\boldsymbol{r}_T^e$, and an inelastic (or plastic) sliding part $\boldsymbol{r}_T^s$, i.e.

$$\boldsymbol{r}_T = \boldsymbol{r}_T^e + \boldsymbol{r}_T^s. \tag{2.51}$$

For sticking, the tangential traction is given by a linear force-gap dependence

$$\boldsymbol{T}_f = \varepsilon_T \, \boldsymbol{r}_T^e \; = \varepsilon_T \left(\boldsymbol{r}_T - \boldsymbol{r}_T^s \right), \tag{2.52}$$

where ε_T is the penalty parameter and is equivalent to the elasticity modulus. The inelastic tangential slip $\boldsymbol{r}_T^s$ is determined using a constitutive evolution equation. The dissipation due to inelastic slip $\boldsymbol{r}_T^s$ and the relative plastic tangential velocity $\dot{\boldsymbol{r}}_T^s$ can be introduced as

$$\mathcal{D}_s = \boldsymbol{T}_f \cdot \dot{\boldsymbol{r}}_T^s \; \geq \; 0. \tag{2.53}$$

Considering an elastic domain of feasible contact tractions

$$\mathbb{E}_t := \{\boldsymbol{T}_\mathrm{f} \in \mathbb{R}^2 \mid f_s(\boldsymbol{T}_\mathrm{f}) \leq 0\}, \tag{2.54}$$

where f_s is the slip function containing all possible tangential tractions and defined as

$$f_\mathrm{s}(\boldsymbol{T}_\mathrm{f}) = \|\boldsymbol{T}_\mathrm{f}\| - T_\mathrm{slide} \leq 0. \tag{2.55}$$

The evolution equation can then be derived from the principle of maximum dissipation. It states that for the given inelastic (plastic) slip velocity $\dot{\boldsymbol{r}}^\mathrm{s}_\mathrm{T}$, the true tangential traction $\boldsymbol{T}_\mathrm{f}$ resisting the sliding motion is such that it maximizes the dissipation $\mathcal{D}_\mathrm{s}$ [250] i.e.,

$$(\boldsymbol{T}_\mathrm{f} - \boldsymbol{T}^*_\mathrm{f}) \cdot \dot{\boldsymbol{r}}^\mathrm{s}_\mathrm{T} \geq 0 \quad \forall\, \boldsymbol{T}^*_\mathrm{f} \in \mathbb{E}_t. \tag{2.56}$$

where $\boldsymbol{T}^*_\mathrm{f}$ is any tangential traction in the domain of feasible contact tractions $\mathbb{E}_t$. Then, the constitutive evolution equation for the plastic slip is obtained by differentiating the slip function f_s with respect to the tangential traction $\boldsymbol{T}_\mathrm{f}$, i.e.

$$\dot{\boldsymbol{r}}^\mathrm{s}_\mathrm{T} = \gamma \frac{\partial f_\mathrm{s}}{\partial \boldsymbol{T}_\mathrm{f}} = \gamma\, \boldsymbol{n}_\mathrm{T} \qquad \text{with} \quad \boldsymbol{n}_\mathrm{T} = \frac{\boldsymbol{T}_\mathrm{f}}{\|\boldsymbol{T}_\mathrm{f}\|}, \tag{2.57}$$

where the plastic parameter $\gamma \geq 0$ is determined from the Karush-Kuhn-Tucker conditions similar to those in plasticity. These are given by [250]

$$\gamma \;\geq\; 0, \qquad f_s(\boldsymbol{T}_\mathrm{f}) \;\leq\; 0, \qquad \gamma \cdot f_\mathrm{s}(\boldsymbol{T}_\mathrm{f}) = 0. \tag{2.58}$$

Furthermore, during sliding as $f_\mathrm{s} = 0$, the tangential traction satisfies

$$\boldsymbol{T}_\mathrm{f} = T_\mathrm{slide}\, \boldsymbol{n}_\mathrm{T}. \tag{2.59}$$

2.3.1 Algorithmic treatment of adhesive friction

For solving Eq. (2.55) and Eq. (2.57), the unbiased frictional formulation of Sauer and De Lorenzis [258], which is based on the classical predictor-corrector algorithm is used.

Before proceeding with the algorithmic treatment of the frictional formulation for a general three-dimensional problem, description of the interacting surfaces in terms of two-dimensional parametric space is presented. In order to map the three-dimensional surface $\partial\Omega$ to a two-dimensional parametric space $\mathcal{P}$, a mapping between the surface point $\boldsymbol{x} \in \partial\Omega$ and a point in parametric space $\boldsymbol{\xi} \in \mathcal{P}$ is sought as

$$\boldsymbol{x} = \boldsymbol{x}(\boldsymbol{\xi}), \quad \boldsymbol{\xi} = \{\xi^1, \xi^2\}. \tag{2.60}$$

To determine the normal distance between the surfaces of two interacting bodies, first the closest point of projection $\boldsymbol{x}_\mathrm{p} \in \partial\Omega_l$ for an arbitrary surface point $\boldsymbol{x}_k \in \partial\Omega_k (l \neq k)$ needs to be determined. Then, the normal gap vector is defined as $\boldsymbol{r}_s := \boldsymbol{x}_\mathrm{p} - \boldsymbol{x}_k$. The projection point is defined in terms of its parametric coordinate $\boldsymbol{\xi}_\mathrm{p}$ as $\boldsymbol{x}_\mathrm{p} = \boldsymbol{x}_l(\boldsymbol{\xi}_\mathrm{p})$. Further, at this projection point the surface $\partial\Omega_l$ can be described by the surface normal $\boldsymbol{n}_\mathrm{p}$ and the co-variant and contravariant tangent vectors $\boldsymbol{a}^\mathrm{p}_\alpha$ and $\boldsymbol{a}^\alpha_\mathrm{p}$ $(\alpha = 1, 2)$ which are defined as

$$\boldsymbol{a}^\mathrm{p}_\alpha := \left.\frac{\partial \boldsymbol{x}_l(\boldsymbol{\xi})}{\partial \xi^\alpha}\right|_{\boldsymbol{\xi}_\mathrm{p}}, \tag{2.61}$$

$$\boldsymbol{a}^\alpha_\mathrm{p} := a^{\alpha\beta}_\mathrm{p}\boldsymbol{a}^\mathrm{p}_\beta, \qquad \left[a^{\alpha\beta}_\mathrm{p}\right] = \left[a^\mathrm{p}_{\alpha\beta}\right]^{-1}, \qquad a^\mathrm{p}_{\alpha\beta} = \boldsymbol{a}^\mathrm{p}_\alpha \cdot \boldsymbol{a}^\mathrm{p}_\beta, \tag{2.62}$$

$$\boldsymbol{n}_\mathrm{p} := \frac{\boldsymbol{a}^\mathrm{p}_1 \times \boldsymbol{a}^\mathrm{p}_2}{\|\boldsymbol{a}^\mathrm{p}_1 \times \boldsymbol{a}^\mathrm{p}_2\|}. \tag{2.63}$$

where $a^\mathrm{p}_{\alpha\beta}$ and $a^{\alpha\beta}_\mathrm{p}$ represent the co-variant and contra-variant components of the metric tensor characterizing the basis at $\boldsymbol{x}_\mathrm{p}$.

The parametric coordinates $\boldsymbol{\xi}_\mathrm{p}$ can then be determined by solving the nonlinear equation [257]

$$(\boldsymbol{x}_\mathrm{p} - \boldsymbol{x}_k) \cdot \boldsymbol{a}^\mathrm{p}_\alpha = 0\,, \quad \alpha = 1, 2. \tag{2.64}$$

As the bodies deform, the projection point $\boldsymbol{x}_\mathrm{p}$ moves on the surface $\partial\Omega_l$. Considering a pseudo-time step from t to $t + \Delta t$, the parametric coordinates of the projection point are updated as

$$\boldsymbol{\xi}^{t+\Delta t}_\mathrm{p} = \boldsymbol{\xi}^t_\mathrm{p} + \Delta\boldsymbol{\xi}^{t+\Delta t}_\mathrm{p}. \tag{2.65}$$

Similar to the decomposition in Eq. (2.51), $\boldsymbol{\xi}^t_\mathrm{p}$ can be divided into sticking part $\boldsymbol{\xi}^t_\mathrm{e}$ and sliding part $\boldsymbol{\xi}^t_\mathrm{s}$, i.e.

$$\boldsymbol{\xi}^t_\mathrm{p} = \boldsymbol{\xi}^t_\mathrm{e} + \boldsymbol{\xi}^t_\mathrm{s}. \tag{2.66}$$

Following Sauer and De Lorenzis [258], displacement of the projection point $\boldsymbol{\xi}_\mathrm{p}$ is given as

$$\Delta\boldsymbol{\xi}^{t+\Delta t}_\mathrm{p} = \left[\left(\boldsymbol{x}^{t+\Delta t}_l\left(\boldsymbol{\xi}^{t+\Delta t}_\mathrm{p}\right) - \boldsymbol{x}^t_l\left(\boldsymbol{\xi}^t_\mathrm{p}\right)\right) \cdot \left(\boldsymbol{a}^\alpha_\mathrm{p}\right)^t\right] \boldsymbol{a}^\mathrm{p}_\alpha. \tag{2.67}$$

The tangential traction $(\boldsymbol{T}_\mathrm{f})^t$ is given in analogy to Eq. (2.52),

$$(\boldsymbol{T}_\mathrm{f})^t = \varepsilon_\mathrm{T}\left[\boldsymbol{x}^t_l\left(\boldsymbol{\xi}^t_\mathrm{p}\right) - \boldsymbol{x}^t_l\left(\boldsymbol{\xi}^t_\mathrm{s}\right)\right]. \tag{2.68}$$

Then, the trial traction corresponding to the sticking state at time $t + \Delta t$ is given as

$$(\boldsymbol{T}_\mathrm{f})^{t+\Delta t}_\mathrm{tr} = \varepsilon_\mathrm{T}\left[\boldsymbol{x}^{t+\Delta t}_l\left(\boldsymbol{\xi}^{t+\Delta t}_\mathrm{p}\right) - \boldsymbol{x}^{t+\Delta t}_l\left(\boldsymbol{\xi}^t_\mathrm{s}\right)\right]. \tag{2.69}$$

The trial function can then be used to determine the stick/slip state:

1. If $f_s = \left\| \left(\boldsymbol{T}_{\mathrm{f}}\right)_{\mathrm{tr}}^{t+\Delta t} \right\| - T_{\mathrm{slide}}^{t+\Delta t} < 0$, then the projection point $\boldsymbol{x}_{\mathrm{p}}$ is in sticking state. The tangential traction is then obtained as

$$\left(\boldsymbol{T}_{\mathrm{f}}\right)^{t+\Delta t} = \left(\boldsymbol{T}_{\mathrm{f}}\right)_{\mathrm{tr}}^{t+\Delta t} \quad \text{and} \quad \boldsymbol{\xi}_{\mathrm{s}}^{t+\Delta t} = \boldsymbol{\xi}_{\mathrm{s}}^{t}. \tag{2.70}$$

2. If $f_s = \left\| \left(\boldsymbol{T}_{\mathrm{f}}\right)_{\mathrm{tr}}^{t+\Delta t} \right\| - T_{\mathrm{slide}}^{t+\Delta t} \geq 0$, then the projection point $\boldsymbol{x}_{\mathrm{p}}$ is sliding state. Then, an additional corrector step is preformed to determine the actual tangential traction $\left(\boldsymbol{T}_{\mathrm{f}}\right)^{t+\Delta t}$.

In the sliding state, the inelastic slip velocity can be written in terms of parametric coordinates as

$$\dot{\boldsymbol{r}}_{\mathrm{T}}^{s} = \dot{\boldsymbol{\xi}}_{\mathrm{s}}^{\alpha} = \dot{\xi}_{\mathrm{s}}^{\alpha}\, \boldsymbol{a}_{\alpha}^{\mathrm{s}}, \tag{2.71}$$

where $\boldsymbol{a}_{\alpha}^{\mathrm{s}}$ is the co-variant tangent vector at $\boldsymbol{\xi}_s$ and is given as

$$\boldsymbol{a}_{\alpha}^{\mathrm{s}} = \left.\frac{\partial \boldsymbol{x}_l}{\partial \xi^{\alpha}}\right|_{\boldsymbol{\xi}_{\mathrm{s}}}. \tag{2.72}$$

Then, the evolution equation in Eq. (2.57) in parametric coordinates can be written as

$$\dot{\xi}_s^{\alpha} = \gamma(\boldsymbol{n}_{\mathrm{T}} \cdot \boldsymbol{a}_{\mathrm{s}}^{\alpha}), \tag{2.73}$$

which is then discretized in time using implicit Euler method to yield,

$$\left(\xi_{\mathrm{s}}^{\alpha}\right)^{t+\Delta t} \approx \left(\xi_{\mathrm{s}}^{\alpha}\right)^{t} + \Delta\gamma^{t+\Delta t}\, \boldsymbol{n}_{\mathrm{T}}^{t+\Delta t} \cdot \left(\boldsymbol{a}_{\mathrm{s}}^{\alpha}\right)^{t+\Delta t}. \tag{2.74}$$

Using Eq. 2.74, the updated coordinates of the point $\boldsymbol{x}_l(\boldsymbol{\xi}_{\mathrm{s}})$ can be obtained as

$$\boldsymbol{x}_l^{t+\Delta t}\left(\boldsymbol{\xi}_{\mathrm{s}}^{t+\Delta t}\right) = \boldsymbol{x}_l^{t+\Delta t}\left(\boldsymbol{\xi}_{\mathrm{s}}^{t}\right) + \Delta\gamma^{t+\Delta t}\, \boldsymbol{n}_{\mathrm{T}}^{t+\Delta t}. \tag{2.75}$$

Then, the tangential traction during sliding at time $t + \Delta t$, defined in Eq. (2.68) for any time t, can be obtained by using Eq. (2.75) as

$$\boldsymbol{T}_{\mathrm{f}}^{t+\Delta t} = \varepsilon_{\mathrm{T}} \left[\boldsymbol{x}_l^{t+\Delta t}\left(\boldsymbol{\xi}_{\mathrm{p}}^{t+\Delta t}\right) - \boldsymbol{x}_l^{t+\Delta t}\left(\boldsymbol{\xi}_{\mathrm{s}}^{t}\right) - \Delta\gamma^{t+\Delta t}\, \boldsymbol{n}_{\mathrm{T}}^{t+\Delta t} \right]. \tag{2.76}$$

Using Eq. (2.69), it can be written as

$$\boldsymbol{T}_{\mathrm{f}}^{t+\Delta t} = \left(\boldsymbol{T}_{\mathrm{f}}\right)_{\mathrm{tr}}^{t+\Delta t} - \varepsilon_{\mathrm{T}}\, \Delta\gamma^{t+\Delta t}\, \boldsymbol{n}_{\mathrm{T}}^{t+\Delta t}, \tag{2.77}$$

By rearranging the terms, Eq. (2.77) can be rewritten as

$$\left(\|\boldsymbol{T}_{\mathrm{f}}^{t+\Delta t}\| + \varepsilon_{\mathrm{T}}\, \Delta\gamma^{t+\Delta t}\right) \boldsymbol{n}_{\mathrm{T}}^{t+\Delta t} = \| \left(\boldsymbol{T}_{\mathrm{f}}\right)_{\mathrm{tr}}^{t+\Delta t} \| \left(\boldsymbol{n}_{\mathrm{T}}\right)_{\mathrm{tr}}^{t+\Delta t}, \tag{2.78}$$

which then implies that

$$\boldsymbol{n}_{\mathrm{T}}^{t+\Delta t} = (\boldsymbol{n}_{\mathrm{T}})_{\mathrm{tr}}^{t+\Delta t}\,. \tag{2.79}$$

The scalar $\Delta\gamma^{t+\Delta t}$ can be determined by setting the slip function $f_{\mathrm{s}}^{t+\Delta t} = 0$ as

$$\Delta\gamma^{t+\Delta t} = \frac{\| (\boldsymbol{T}_{\mathrm{f}})_{\mathrm{tr}}^{t+\Delta t} \| - T_{\mathrm{slide}}^{t+\Delta t}}{\varepsilon_{\mathrm{T}}}. \tag{2.80}$$

It should be noted that, since $\Delta\boldsymbol{\xi}_{\mathrm{e}}^{t+\Delta t}$ is assumed to be very small, $(\boldsymbol{a}_{\mathrm{s}}^{\alpha})^{t+\Delta t}$ is equal to $\left(\boldsymbol{a}_{\mathrm{p}}^{\alpha}\right)^{t+\Delta t}$. Finally, the algorithm that can be used to determine the frictional tractions for adhesive friction is summarized in Algorithm 1.

Algorithm 1: Predictor-Corrector algorithm for adhesive friction.

Step 1. Known values at pseudo-time t, $t + \Delta t$

$\boldsymbol{\xi}_{\mathrm{p}}^{t}$, $\boldsymbol{\xi}_{\mathrm{s}}^{t}$	Parametric coordinates of the projection and sliding points at t
$\boldsymbol{x}_{k}^{t+\Delta t}$, $\boldsymbol{x}_{l}^{t+\Delta t}$	Position of the surface points corresponding to body $\mathcal{B}_k$ and $\mathcal{B}_l$ at $t + \Delta t$
$\boldsymbol{\xi}_{\mathrm{p}}^{t+\Delta t}$	Parametric coordinate of the projection point at $t + \Delta t$

Step 2. Compute trial step (Elastic Predictor):

$$\text{Trial traction at } t+\Delta t: \quad (\boldsymbol{T}_{\mathrm{f}})_{\mathrm{tr}}^{t+\Delta t} = \varepsilon_{\mathrm{T}} \left[\boldsymbol{x}_{l}^{t+\Delta t}\left(\boldsymbol{\xi}_{\mathrm{p}}^{t+\Delta t}\right) - \boldsymbol{x}_{l}^{t+\Delta t}\left(\boldsymbol{\xi}_{\mathrm{s}}^{t}\right) \right]$$

$$\text{Trial function at } t+\Delta t: \quad (f_s)_{\mathrm{tr}}^{t+\Delta t} = \left\| (\boldsymbol{T}_{\mathrm{f}})_{\mathrm{tr}}^{t+\Delta t} \right\| - T_{\mathrm{slide}}^{t+\Delta t}$$

Step 3. Check slip criterion:

if $(f_s)_{\mathrm{tr}}^{t+\Delta t} \leq 0$ **then**

sticking; set $\Delta\gamma^{t+\Delta t} = 0$;

elseif $(f_s)_{\mathrm{tr}}^{t+\Delta t} > 0$ **then**

sliding; set $\Delta\gamma^{t+\Delta t} = \dfrac{f_{\mathrm{s}}^{t+\Delta t}}{\varepsilon_{\mathrm{T}}}$

Step 4. Radial return mapping (Inelastic Corrector):

Compute the parametric coordinates of the slip point at $t + \Delta t$ as:

$$(\xi_{\mathrm{s}}^{\alpha})^{t+\Delta t} \approx (\xi_{\mathrm{s}}^{\alpha})^{t} + \Delta\gamma^{t+\Delta t}\, \boldsymbol{n}_{\mathrm{T}}^{t+\Delta t} \cdot (\boldsymbol{a}_{\mathrm{s}}^{\alpha})^{t+\Delta t} \; ; \quad \boldsymbol{n}_{\mathrm{T}}^{t+\Delta t} = \frac{(\boldsymbol{T}_{\mathrm{f}})_{\mathrm{tr}}^{t+\Delta t}}{\left\| (\boldsymbol{T}_{\mathrm{f}})_{\mathrm{tr}}^{t+\Delta t} \right\|}$$

Obtain the tangential traction by projecting the trial traction onto the slip surface as:

$$(\boldsymbol{T}_{\mathrm{f}})^{t+\Delta t} = (\boldsymbol{T}_{\mathrm{f}})_{\mathrm{tr}}^{t+\Delta t} - \Delta\gamma^{t+\Delta t}\, \varepsilon_{\mathrm{T}}\, \boldsymbol{n}_{\mathrm{T}}^{t+\Delta t}$$

Go to step 1.

Chapter 3

Finite Element Formulation

In this chapter, the weak form derived in chapter 2 is discretized using the finite element method. The force equilibrium equation is derived by approximating the displacement field using the interpolation functions. Then, the internal and contact force vectors and tangent matrices are given in sections 3.2 and 3.3. Next, the surface enrichment strategy used for accurate and efficient computation of the contact solution is discussed in section 3.4. The finite element formulation followed here is based on Wriggers [259].

3.1 Finite element discretization

In finite element method, the domain (Ω_{k0} or Ω_k) of the each interacting body $\mathcal{B}_k (k = 1, 2)$ is decomposed into a finite number $n_{el,k}$ of smaller subdomains called (bulk) elements,

$$\Omega_{k0} \approx \Omega_{k0}^h = \bigcup_{e=1}^{n_{el,k}} \Omega_{k0}^e \quad \text{and} \quad \Omega_k \approx \Omega_k^h = \bigcup_{e=1}^{n_{el,k}} \Omega_k^e, \tag{3.1}$$

where Ω_{k0}^h and Ω_k^h represent the finite element approximated initial and current geometry of the body, respectively. The boundaries ($\partial\Omega_{k0}$ or $\partial\Omega_k$) of these interacting bodies are also divided into $n_{sel,k}$ number of surface elements,

$$\partial\Omega_{k0} \approx \partial\Omega_{k0}^h = \bigcup_{e=1}^{n_{sel,k}} \partial\Omega_{k0}^e \quad \text{and} \quad \partial\Omega_k \approx \partial\Omega_k^h = \bigcup_{e=1}^{n_{sel,k}} \partial\Omega_k^e, \tag{3.2}$$

Each of these finite elements is connected to the other element through nodes and each element is assumed to contain n_e number of nodes (for a volume element $n_e = n_{ve}$ and for a surface element $n_e = n_{se}$). The field variable such as displacement $\boldsymbol{u}_k$ of each finite element belonging to body $\mathcal{B}_k$ and its variation $\delta\boldsymbol{\varphi}_k$ are then

approximated as

$$\boldsymbol{u}_k \approx \boldsymbol{u}_k^h = \sum_{I=1}^{n_e} N_{Ik}\mathbf{u}_{Ik} = \mathbf{N}_k^e\mathbf{u}_k^e, \qquad \delta\boldsymbol{\varphi}_k \approx \delta\boldsymbol{\varphi}_k^h = \sum_{I=1}^{n_e} N_{Ik}\mathbf{v}_{Ik} = \mathbf{N}_k^e\mathbf{v}_k^e, \tag{3.3}$$

where $\mathbf{N}_k^e$, $\mathbf{u}_k^e$, and $\mathbf{v}_k^e$ represent arrays containing shape functions, displacements, and variations of all the nodes of element e. They are given as

$$\mathbf{N}_k^e = \begin{bmatrix} N_1\mathbf{I}_d \\ N_2\mathbf{I}_d \\ \vdots \\ N_{n_e}\mathbf{I}_d \end{bmatrix}_k^{\mathrm{T}}, \qquad \mathbf{u}_k^e = \begin{Bmatrix} \mathbf{u}_1 \\ \mathbf{u}_2 \\ \vdots \\ \mathbf{u}_{n_e} \end{Bmatrix}_k, \qquad \text{and} \quad \mathbf{v}_k^e = \begin{Bmatrix} \mathbf{v}_1 \\ \mathbf{v}_2 \\ \vdots \\ \mathbf{v}_{n_e} \end{Bmatrix}_k, \tag{3.4}$$

where $\mathbf{I}_d$ is the identity matrix of dimension d and $\mathbf{u}_{Ik} = [u_1, u_2, u_3, ..., u_d]_{Ik}^{\mathrm{T}}$ and $\mathbf{v}_{Ik} = [v_1, v_2, v_3, ..., v_d]_{Ik}^{\mathrm{T}}$ are the nodal displacement and variation of the node I of body $\mathcal{B}_k$ for a $d-$dimensional problem and N_{Ik} is the chosen shape function. It should be noted that $\mathbf{N}_k^e$ is different from the outward normal $\boldsymbol{N}_k$ to the surface $\partial\Omega_{k0}$ in the reference configuration.

In the current thesis, isoparametric concept [250] is followed which means the geometry and the field variables are both approximated using the same shape functions. As such, the position of any particle $\boldsymbol{X}_k \in \Omega_{k0}$ (or $\boldsymbol{x}_k \in \Omega_k$) is approximated using the same shape functions N_{Ik} as

$$\boldsymbol{X}_k \approx \boldsymbol{X}_k^h = \sum_{I=1}^{n_e} N_{Ik}\mathbf{X}_{Ik} = \mathbf{N}_k^e\mathbf{X}_k^e, \qquad \boldsymbol{x}_k \approx \boldsymbol{x}_k^h = \sum_{I=1}^{n_e} N_{Ik}\mathbf{x}_{Ik} = \mathbf{N}_k^e\mathbf{x}_k^e, \tag{3.5}$$

where $\mathbf{X}_k^e$ and $\mathbf{x}_k^e$ represent positions of all the nodes of element e in initial and current configurations. They are given as

$$\mathbf{X}_k^e = \begin{Bmatrix} \mathbf{X}_1 \\ \mathbf{X}_2 \\ \vdots \\ \mathbf{X}_{n_e} \end{Bmatrix}_k \quad \text{and} \quad \mathbf{x}_k^e = \begin{Bmatrix} \mathbf{x}_1 \\ \mathbf{x}_2 \\ \vdots \\ \mathbf{x}_{n_e} \end{Bmatrix}_k, \quad \text{with} \quad \mathbf{u}_k^e = \mathbf{x}_k^e - \mathbf{X}_k^e, \tag{3.6}$$

where $\mathbf{X}_{Ik}$ and $\mathbf{x}_{Ik}$ are the vectors containing positions of the node I in $d-$dimensions. These are given as

$$\mathbf{X}_{Ik} = \begin{Bmatrix} X_1 \\ X_2 \\ \vdots \\ X_d \end{Bmatrix}_{Ik}, \qquad \mathbf{x}_{Ik} = \begin{Bmatrix} x_1 \\ x_2 \\ \vdots \\ x_d \end{Bmatrix}_{Ik}. \tag{3.7}$$

The shape functions N_{Ik} are evaluated numerically in terms of a local orthogonal coordinate system $\boldsymbol{\xi}^* \in [-1,\,1]^d$ within a master element $\Omega_\square$, i.e. $N_{Ik} = N_{Ik}(\boldsymbol{\xi}^*)$. This master element can be mapped to each element either in the initial Ω^e_{k0} or current Ω^e_k configurations as shown in Fig. 3.1. Thus, each point in any given element $\boldsymbol{X}^h_k = \boldsymbol{X}^h_k(\boldsymbol{\xi}^*) \in \Omega^e_{k0}$ or $\boldsymbol{x}^h_k = \boldsymbol{x}^h_k(\boldsymbol{\xi}^*) \in \Omega^e_k$ is mapped in a one-to-one fashion to the coordinates $\boldsymbol{\xi}^*$. The deformation gradient $\boldsymbol{F}^e_k$ and its determinant can then be written as

$$\boldsymbol{F}^e_k = \boldsymbol{j}^e_k(\boldsymbol{J}^e_k)^{-1} \quad \text{and} \quad J^e_k = \det(\boldsymbol{F}^e_k) = \frac{\det(\boldsymbol{j}^e_k)}{\det(\boldsymbol{J}^e_k)}, \tag{3.8}$$

where the gradients $\boldsymbol{j}^e_k$ and $\boldsymbol{J}^e_k$ are transformations from master element to current and initial configurations, respectively. These transformations are known as elemental Jacobians and are defined as [259]

$$\boldsymbol{j}^e_k \;:=\; \mathrm{Grad}_{\boldsymbol{\xi}^*}(\boldsymbol{x}^h_k) = \frac{\partial \boldsymbol{x}^h_k}{\partial \boldsymbol{\xi}^*} = \sum_{I=1}^{n_e} \mathbf{x}^e_{Ik} \otimes \frac{\partial N_{Ik}}{\partial \boldsymbol{\xi}^*}, \tag{3.9}$$

$$\boldsymbol{J}^e_k \;:=\; \mathrm{Grad}_{\boldsymbol{\xi}^*}(\boldsymbol{X}^h_k) = \frac{\partial \boldsymbol{X}^h_k}{\partial \boldsymbol{\xi}^*} = \sum_{I=1}^{n_e} \mathbf{X}^e_{Ik} \otimes \frac{\partial N_{Ik}}{\partial \boldsymbol{\xi}^*}, \tag{3.10}$$

which can be used to relate the partial derivatives of the shape functions with respect to the global coordinates $\boldsymbol{x}^h_k$ and $\boldsymbol{X}^h_k$ and the partial derivates of the shape functions with respect to the local coordinate system $\boldsymbol{\xi}^*$ as

$$\frac{\partial N_{Ik}}{\partial \boldsymbol{\xi}^*} = (\boldsymbol{j}^e_k)^T \, \frac{\partial N_{Ik}}{\partial \boldsymbol{x}^h_k}, \tag{3.11}$$

$$\frac{\partial N_{Ik}}{\partial \boldsymbol{\xi}^*} = (\boldsymbol{J}^e_k)^T \, \frac{\partial N_{Ik}}{\partial \boldsymbol{X}^h_k}. \tag{3.12}$$

A master surface element $\partial\Omega_\square$ can be introduced similar to the bulk element $\Omega_\square$ for which the surface stretch is given as

$$J^e_{ck} = \frac{j^e_{\mathrm{a}k}}{J^e_{\mathrm{A}k}}, \quad \text{with } j^e_{\mathrm{a}k} = \sqrt{\det(a^k_{\alpha\beta})}, \quad \text{and} \quad J^e_{\mathrm{a}k} = \sqrt{\det(A^k_{\alpha\beta})},, \tag{3.13}$$

where $a^k_{\alpha\beta}$ and $A^k_{\alpha\beta}$ are the co-variant components of the metric tensor in current and reference configurations. The volume and surface elements can then be written in terms of master elements as

$$\mathrm{d}v_k = \det(j^e_{ak})\,\mathrm{d}\boldsymbol{\xi}^*, \quad \mathrm{d}V_k = \det(J^e_{ak})\,\mathrm{d}\boldsymbol{\xi}^*, \tag{3.14}$$

$$\mathrm{d}a_k = j^e_{ak}\,\mathrm{d}\boldsymbol{\xi}^\dagger, \qquad \mathrm{d}A_k = J^e_{ak}\,\mathrm{d}\boldsymbol{\xi}^\dagger, \qquad \boldsymbol{\xi}^\dagger \in [-1,\,1]^{d-1}. \tag{3.15}$$

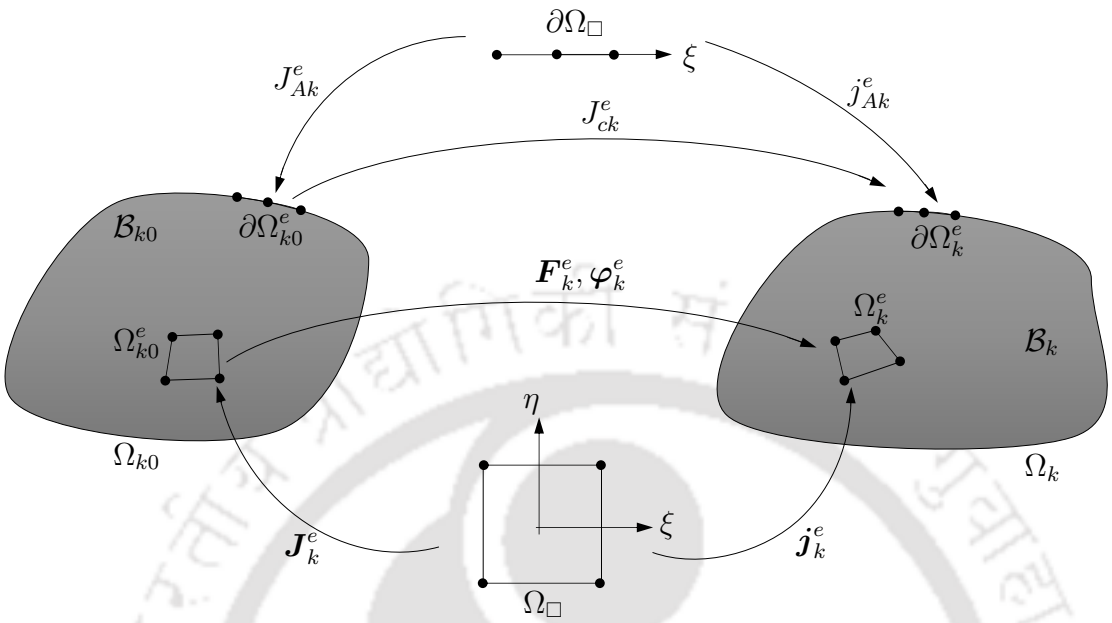

Figure 3.1: Two-dimensional isoparametric mapping of the bulk $\Omega_\square$ and surface $\partial\Omega_\square$ master elements to their respective finite elements in the deforming body in reference and current configurations.

Using the relations in Eq. (3.3) and performing an assembly over all the volume and surface elements, the weak form in Eq. (2.46) can then be rewritten as

$$\sum_{k=1}^{2} \mathbf{v}_k^{\mathrm{T}} \left[\mathbf{f}_{\mathrm{int}k} + \mathbf{f}_{ck} - \mathbf{f}_{\mathrm{ext}k}\right] = \mathbf{0}, \quad \forall\, \mathbf{v}_k \in \mathcal{V}_k, \tag{3.16}$$

where $\mathbf{f}_{\mathrm{int}k}$, $\mathbf{f}_{ck}$, and $\mathbf{f}_{\mathrm{ext}k}$ denote the global internal, contact, and external nodal force vectors for body $\mathcal{B}_k$, respectively. In the current work, as there are no external forces acting, $\mathbf{f}_{\mathrm{ext}k} = \mathbf{0}$. Since, the variations $\mathbf{v}_k$ are arbitrary, Eq. (3.16) leads to

$$\mathbf{f}(\mathbf{u}) := \sum_{k=1}^{2} \left[\mathbf{f}_{\mathrm{int}k} + \mathbf{f}_{ck} - \mathbf{f}_{\mathrm{ext}k}\right] = \mathbf{0}, \tag{3.17}$$

where

$$\mathbf{f}_{\mathrm{int}k} = \bigcup_{e=1}^{n_{el}} \mathbf{f}^e_{\mathrm{int}k} \quad \text{and} \quad \mathbf{f}_{ck} = \bigcup_{e=1}^{n_{el}} \mathbf{f}^e_{ck}. \tag{3.18}$$

Here, $\mathbf{f}^e_{\mathrm{int}k}$ and $\mathbf{f}^e_{ck}$ represent the elemental internal and contact force vectors of body $\mathcal{B}_k$ $(k = 1, 2)$, respectively.

3.2 Internal force vector and tangent matrix

The first term in weak form (2.46) represents the virtual work done by the internal forces which in the discretized form can be written as

$$\delta W_{\text{int}k} = \bigcup_{e=1}^{n_{el}} \int_{\Omega^e_{k0}} \text{Grad}(\delta\boldsymbol{\varphi}_k) : \boldsymbol{P}^e_k \, \text{d}V_k. \tag{3.19}$$

Using the relation given by Eq. (2.21) and rules of tensor inner product, Eq. (3.19) can be written as

$$\delta W_{\text{int}k} = \bigcup_{e=1}^{n_{el}} \int_{\Omega^e_{k0}} (\boldsymbol{F}^e_k)^{\text{T}} \text{Grad}(\delta\boldsymbol{\varphi}_k) : \boldsymbol{S}^e_k \, dV_{\text{k}} \tag{3.20}$$

$$= \bigcup_{e=1}^{n_{el}} \int_{\Omega^e_{k0}} \frac{1}{2}\Big[(\boldsymbol{F}^e_k)^{\text{T}} \, \text{Grad}(\delta\boldsymbol{\varphi}_k) + \text{Grad}^{\text{T}}(\delta\boldsymbol{\varphi}_k) \, \boldsymbol{F}^e_k\Big] : \boldsymbol{S}^e_k \, dV_{\text{k}}, \tag{3.21}$$

which follows from the fact that $\boldsymbol{S}$ is symmetric. From the definition of Green-Lagrange strain $\boldsymbol{E}$ (see Eq. (2.3)) it follows that

$$\delta\boldsymbol{E}^e_k = \frac{1}{2}\Big[(\boldsymbol{F}^e_k)^{\text{T}} \, \text{Grad}(\delta\boldsymbol{\varphi}_k) + \text{Grad}^{\text{T}}(\delta\boldsymbol{\varphi}_k) \, \boldsymbol{F}^e_k\Big]. \tag{3.22}$$

Using Eq. (3.3), Eq. (3.22) can be written in index notation as

$$(\delta E^e_k)_{IJ} = \frac{1}{2}\Big[(F_k)_{Im}\mathbf{N}^e_{k,J} + \mathbf{N}^e_{k,I}\,(F^e_k)_{mB}\Big]\text{v}^e_{km}, \tag{3.23}$$

where $\mathbf{N}^e_{k,I} = \partial\mathbf{N}^e_k/\partial X_{kI}$. In order to incorporate into matrix formulation, quantities are generally expressed in Voigt notation. For the variation of Green-Lagrange strain tensor $\delta\boldsymbol{E}^e$ in case of a three-dimensional problem it reduces to a vector with six independent components

$$\delta\boldsymbol{E}^e = \begin{Bmatrix} \delta E_{11} \\ \delta E_{22} \\ \delta E_{33} \\ 2\,\delta E_{12} \\ 2\,\delta E_{23} \\ 2\,\delta E_{13} \end{Bmatrix} = \mathbf{B}_{\text{TL}}\,\mathbf{v}^e, \tag{3.24}$$

where $\mathbf{B}_{\text{TL}}$ is known as the elemental strain-displacement operator matrix corresponding to material description. It is assembled from individual nodal contributions $\mathbf{B}_{\text{TL}} = [\mathbf{B}^1_{\text{TL}}, \mathbf{B}^2_{\text{TL}}, \cdots, \mathbf{B}^{n_e}_{\text{TL}}]$. Here, the subscript "TL" represents total Lagrangian formulation. For a three dimensional problem the nodal strain-

displacement matrix is given by

$$\mathbf{B}_{\mathrm{TL}}^{I} = \begin{bmatrix} F_{11}N_{I,X_1} & F_{21}N_{I,X_1} & F_{31}N_{I,X_1} \\ F_{12}N_{I,X_2} & F_{22}N_{I,X_2} & F_{32}N_{I,X_2} \\ F_{13}N_{I,X_3} & F_{23}N_{I,X_3} & F_{33}N_{I,X_3} \\ F_{11}N_{I,X_2} + F_{12}N_{I,X_1} & F_{21}N_{I,X_2} + F_{22}N_{I,X_1} & F_{31}N_{I,X_2} + F_{32}N_{I,X_1} \\ F_{11}N_{I,X_3} + F_{13}N_{I,X_1} & F_{21}N_{I,X_3} + F_{23}N_{I,X_1} & F_{31}N_{I,X_3} + F_{33}N_{I,X_1} \\ F_{12}N_{I,X_3} + F_{13}N_{I,X_2} & F_{22}N_{I,X_3} + F_{23}N_{I,X_2} & F_{32}N_{I,X_3} + F_{33}N_{I,X_2} \end{bmatrix}, \tag{3.25}$$

where $N_{I,X_i} = \partial N_I / \partial X_i$ represent the partial derivatives of the shape functions with respect to the reference coordinates. Substituting Eq. (3.24) into Eq. (3.21) and writing in matrix notation

$$\delta W_{\mathrm{int}k} = \bigcup_{e=1}^{n_{el}} (\mathbf{v}_k^e)^{\mathrm{T}} \int_{\Omega_{k0}^e} \mathbf{B}_{\mathrm{TL}}^{\mathrm{T}} \, \boldsymbol{S}_{vk}^e \, \mathrm{d}V_k, \tag{3.26}$$

where $\boldsymbol{S}_{vk}^e$ denotes the Voigt notation representation of the second Piola-Kirchoff stress tensor, which for the case of three-dimension is given as

$$\boldsymbol{S}_k^e = \boldsymbol{S}_{vk}^e = [S_{11}^e \, , \, S_{12}^e \, , \, S_{13}^e \, , \, S_{22}^e \, , \, S_{23}^e \, , \, S_{33}^e]^{\mathrm{T}}. \tag{3.27}$$

Then, the elemental internal force vector in the reference configuration can be computed as

$$\mathbf{f}_{\mathrm{int}k}^e = \int_{\Omega_{k0}^e} \mathbf{B}_{\mathrm{TL}}^{\mathrm{T}} \, \boldsymbol{S}_{vk}^e \, dV_{\mathrm{k}}, \tag{3.28}$$

and in the current configuration as

$$\mathbf{f}_{\mathrm{int}k}^e = \int_{\Omega_k^e} \mathbf{B}_{\mathrm{UL}}^{\mathrm{T}} \, \boldsymbol{\sigma}_{vk}^e \, dv_{\mathrm{k}}, \tag{3.29}$$

with the Cauchy stress tensor $\boldsymbol{\sigma}_k^e$ can be written using the Voigt notation as

$$\boldsymbol{\sigma}_k^e = \boldsymbol{\sigma}_{vk}^e = [\sigma_{11}^e \, , \, \sigma_{12}^e \, , \, \sigma_{13}^e \, , \, \sigma_{22}^e \, , \, \sigma_{23}^e \, , \, \sigma_{33}^e]^{\mathrm{T}}. \tag{3.30}$$

Here, $\mathbf{B}_{\mathrm{UL}}$ is the elemental strain-displacement operator matrix corresponding to the spatial description. The subscript "UL" denotes the updated Lagrangian formulation. It is also assembled from individual nodal contributions $\mathbf{B}_{\mathrm{UL}} = [\mathbf{B}_{\mathrm{UL}}^1 \, , \mathbf{B}_{\mathrm{UL}}^2 \, , \cdots , \mathbf{B}_{\mathrm{UL}}^{n_e}]$ similar to its material description equivalent matrix given by Eq. (3.25) as

$$\mathbf{B}_{\mathrm{UL}}^{I} = \begin{bmatrix} N_{I,x_1} & 0 & 0 \\ 0 & N_{I,x_2} & 0 \\ 0 & 0 & N_{I,x_3} \\ N_{I,x_2} & N_{I,x_1} & 0 \\ N_{I,x_3} & 0 & N_{I,x_1} \\ 0 & N_{I,x_3} & N_{I,x_2} \end{bmatrix}, \tag{3.31}$$

where $N_{I,x_i} = \partial N_I / \partial x_i$ represent the partial derivatives of the shape functions with respect to the current coordinates.

The internal tangent matrix is obtained by linearizing the internal virtual work $\delta\Pi_{\mathrm{int}k}$ (see Appendix A for details). It contains two parts: one corresponding to the material nonlinearities $\mathbf{k}_{\mathrm{mat}}$ and the second corresponding to the geometrical nonlinearities $\mathbf{k}_{\mathrm{geo}}$. For a given element e they are given as

$$\mathbf{k}_{\mathrm{geo}k}^{e} = \int_{\Omega_{k0}^{e}} (\mathbf{N}_{k,X_i}^{e})^{\mathrm{T}}\, S_{ij}\, \mathbf{N}_{k,X_i}^{e}\, \mathbf{I}\, \mathrm{d}V_k = \int_{\Omega_{k}^{e}} (\mathbf{N}_{k,x_i}^{e})^{\mathrm{T}}\, \sigma_{ij}\, \mathbf{N}_{k,x_j}^{e}\, \mathbf{I}\, \mathrm{d}v_k, \tag{3.32}$$

$$\mathbf{k}_{\mathrm{mat}k}^{e} = \int_{\Omega_{k0}^{e}} \mathbf{B}_{\mathrm{TL}}^{\mathrm{T}}\, \mathbb{C}_{vk}\, \mathbf{B}_{\mathrm{TL}}\, \mathrm{d}V_k = \int_{\Omega_{k}^{e}} \mathbf{B}_{\mathrm{UL}}^{\mathrm{T}}\, \mathbb{c}_{vk}\, \mathbf{B}_{\mathrm{UL}}\, \mathrm{d}v_k, \tag{3.33}$$

where $\mathbb{C}_v$ is the fourth-order elasticity tensor associated with the second Piola-Kirchoff stress tensor $\boldsymbol{S}$ written in Voigt notation whose components can be obtained from

$$\mathbb{C} = 2\,\frac{\partial \boldsymbol{S}}{\partial \boldsymbol{C}} \tag{3.34}$$

$$= \Lambda\, \boldsymbol{C}^{-1} \otimes \boldsymbol{C}^{-1} + 2\,(\mu - \Lambda \ln J)\, \boldsymbol{\mathcal{I}}, \tag{3.35}$$

where $\boldsymbol{\mathcal{I}}$ is the fourth-order tensor defined as

$$\boldsymbol{\mathcal{I}} = -\frac{\partial \boldsymbol{C}^{-1}}{\partial \boldsymbol{C}}; \quad \mathcal{I}_{pqrs} = \frac{\partial (\boldsymbol{C}^{-1})_{pq}}{\partial \boldsymbol{C}_{rs}}. \tag{3.36}$$

3.3 Contact force vector and tangent matrix

For a given finite element e, the contact force vector $\mathbf{f}_{ck}^{e}$ can be derived from the virtual work done by the contact tractions which from the weak form (2.46) is given as

$$\mathbf{f}_{ck}^{e} = -\int_{\partial\Omega_{k0}^{\mathrm{ae}}} \delta\boldsymbol{\varphi}_k \cdot \boldsymbol{T}_{ck}\, \mathrm{d}A_k = -\int_{\partial\Omega_{k}^{\mathrm{ae}}} \delta\boldsymbol{\varphi}_k \cdot \boldsymbol{t}_{ck}\, \mathrm{d}a_k. \tag{3.37}$$

This can then be rewritten using the relations in Eq. (3.3) as

$$\mathbf{f}_{ck}^{e} = -\int_{\partial\Omega_{k0}^{\mathrm{ae}}} (\mathbf{N}_{k}^{e})^{\mathrm{T}} \boldsymbol{T}_{ck}\, \mathrm{d}A_k = -\int_{\partial\Omega_{k}^{\mathrm{ae}}} (\mathbf{N}_{k}^{e})^{\mathrm{T}} \boldsymbol{t}_{ck}\, \mathrm{d}a_k. \tag{3.38}$$

From Eq. (2.44)

$$\mathbf{f}^e_{ck} = -\int_{\partial\Omega^{ae}_{k0}} (\mathbf{N}^e_k)^{\mathrm{T}} \left(\boldsymbol{T}_{ak} - \boldsymbol{T}_{fk}\right) \mathrm{d}A_k \;=\; -\int_{\partial\Omega^{ae}_{k0}} (\mathbf{N}^e_k)^{\mathrm{T}} \left(\boldsymbol{t}_{ak} - \boldsymbol{t}_{fk}\right) \mathrm{d}a_k, \tag{3.39}$$

The contact tangent matrices can be obtained by linearizing the contact forces (see Appendix B for details) as

$$\mathbf{k}^e_{ckk} = \frac{\partial \mathbf{f}^e_{ck}}{\partial \mathbf{u}^e_k} = -\int_{\partial\Omega^{ae}_{k0}} (\mathbf{N}^e_k)^{\mathrm{T}} \left[\frac{\partial \boldsymbol{T}_{ak}}{\partial \mathbf{u}^e_k} - \frac{\partial \boldsymbol{T}_{fk}}{\partial \mathbf{u}^e_k}\right] \mathrm{d}A_k, \tag{3.40}$$

$$\mathbf{k}^e_{ckl} = \frac{\partial \mathbf{f}_{ck}}{\partial \mathbf{u}^e_l} = -\int_{\partial\Omega^{ae}_{k0}} (\mathbf{N}^e_k)^{\mathrm{T}} \left[\frac{\partial \boldsymbol{T}_{ak}}{\partial \mathbf{u}^e_l} - \frac{\partial \boldsymbol{T}_{fk}}{\partial \mathbf{u}^e_l}\right] \mathrm{d}A_k. \tag{3.41}$$

3.4 Enrichment strategy

The nonlinear finite element equation (3.17) is solved using the Newton-Raphson method. For this, as both the contact force vector and the internal force vector are nonlinear owing to the contact, material, and geometric nonlinearities present in the system, Eq. (3.17) needs to be linearized as

$$\mathbf{f}(\mathbf{u}) + \frac{\partial \mathbf{f}}{\partial \mathbf{u}} \Delta\mathbf{u} = 0\,, \tag{3.42}$$

where the partial derivative of the force vector with respect to the displacement field represents the system tangent matrix $\mathbf{k}$, which is obtained from the internal and contact tangent matrices as

$$\begin{aligned} \mathbf{k} &= \mathbf{k}_{\mathrm{int}} + \mathbf{k}_{\mathrm{c}} \\ &= \frac{\partial \mathbf{f}_{\mathrm{int}}(\mathbf{u})}{\partial \mathbf{u}} + \frac{\partial \mathbf{f}_{\mathrm{c}}(\mathbf{u})}{\partial \mathbf{u}}, \end{aligned} \tag{3.43}$$

which are obtained from the assembly of elemental internal and contact force vectors and tangent matrices. At each iteration, Eq. (3.42) is then solved using Newton-Raphson method until the convergence criterion such as $R = \mathbf{f}(\mathbf{u}) \cdot \Delta\mathbf{u} < \epsilon_{\mathrm{tol}}$ is met. Here, ϵ_{tol} is the convergence tolerance.

However, in numerically solving the contact integrals some difficulties arise. As demonstrated by Sauer [163], highly nonlinear nature of the interfacial interactions due to van der Waals adhesion necessitates accurate evaluation of the surface force vectors and tangent matrices (see Eqs. (3.39), (B.2), and (B.2)). Further, it was observed that in numerical methods such as FEM, employing coarse finite element meshes along with standard Lagrangian four-noded quadrilateral elements, although efficient, results in poor convergence in the Newton-Raphson iterations. This is due

to the inaccurate representation of the contact surface. One way to address these convergence issues is to represent the interacting bodies with very fine meshes. However, refining the mesh uniformly in the surface as well as in the bulk leads to very high computational cost, which is not desirable from the point of efficiency. Further, accuracy of the solution is governed for the most part by the description of the contact interface. As such, Sauer [163] addressed these issues by introducing a surface enrichment strategy for finite element simulations based on p-refinement. In this strategy, the contact surface is locally enriched using higher-order Lagrange polynomials for their description, while bulk of the body is approximated using only linear interpolation.

In the present work, two types of enriched contact finite elements are considered for the surface description: quadratic (second-order) and quartic (fourth-order). They are denoted as Q1C2 and Q1C4, respectively. The formulation of these elements can then be derived from the standard linear elements denoted as Q1 in which the displacement field in a given element Ω^e for a two-dimensional problem is approximated as

$$\boldsymbol{u}_e^h = \sum_{i=1}^{4} N_i^0 \mathbf{u}_i, \tag{3.44}$$

where the shape functions N_i^0 are given as

$$N_1^0(\xi,\eta) = \frac{1}{4}(1-\xi)(1-\eta), \tag{3.45}$$

$$N_2^0(\xi,\eta) = \frac{1}{4}(1+\xi)(1-\eta), \tag{3.46}$$

$$N_3^0(\xi,\eta) = \frac{1}{4}(1+\xi)(1+\eta), \tag{3.47}$$

$$N_4^0(\xi,\eta) = \frac{1}{4}(1-\xi)(1+\eta). \tag{3.48}$$

The description of Q1C2 elements can then be obtained by inserting an additional node at $(\xi,\eta) = (0,-1)$ between node 1 and 2 as shown in Fig. 3.2a which gives the modified shape functions as

$$N_5(\xi,\eta) = \frac{1}{2}(1-\xi^2)(1-\eta), \tag{3.49}$$

$$N_1(\xi,\eta) = N_1^0 - \frac{1}{2}N_5, \tag{3.50}$$

$$N_2(\xi,\eta) = N_2^0 - \frac{1}{2}N_5, \tag{3.51}$$

with the modified shape functions corresponding to the nodes 3 and 4 remaining the same, i.e. $N_3 = N_3^0$ and $N_4 = N_4^0$.

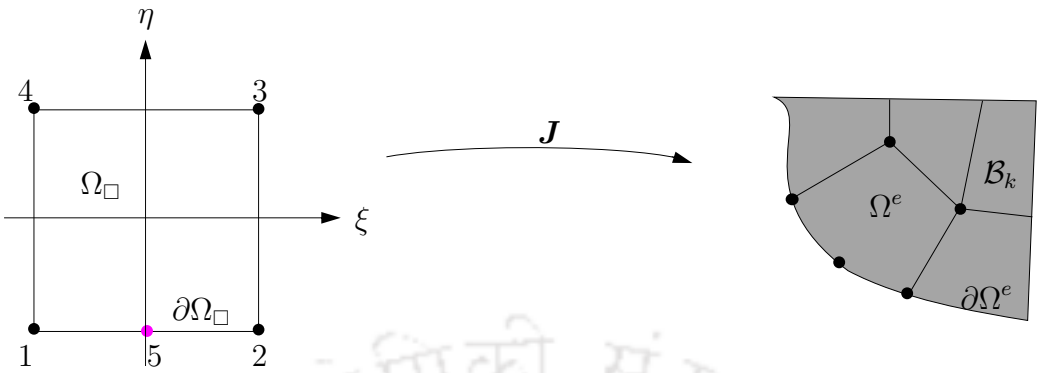

(a) Mapping of enriched contact element Q1C2 from master element to corresponding domain.

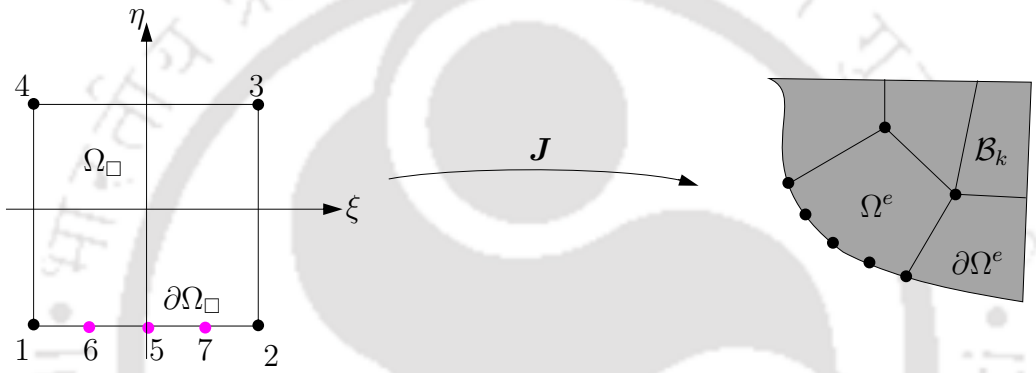

(b) Mapping of enriched contact element Q1C4 from master element to corresponding domain.

Figure 3.2: Representation of enriched contact elements. Adapted with permission from Sauer [163].

Then, the displacement field of the element Ω^e is approximated as

$$\boldsymbol{u}_e^h = \sum_{i=1}^{5} N_i \mathbf{u}_i. \tag{3.52}$$

The description of the Q1C4 contact elements can be obtained similarly by inserting three additional nodes at $(\xi, \eta) = (0, -1), (-0.5, -1)$, and $(0.5, -1)$ as shown in Figure 3.2b and the corresponding shape functions are defined as

$$N_5(\xi, \eta) = 2\left(\xi^4 - \frac{5}{4}\xi^2 + \frac{1}{4}\right)(1 - \eta), \tag{3.53}$$

$$N_6(\xi, \eta) = -\frac{4}{3}\left(\xi^4 - \frac{1}{2}\xi^3 - \xi^2 + \frac{1}{2}\xi\right)(1 - \eta), \tag{3.54}$$

$$N_7(\xi, \eta) = -\frac{4}{3}\left(\xi^4 + \frac{1}{2}\xi^3 - \xi^2 - \frac{1}{2}\xi\right)(1 - \eta). \tag{3.55}$$

Then, with N_3^0 and N_4^0 remaining the same, the modified shape functions for the enriched contact surface element follow

$$N_1 = N_1^0 - \frac{1}{2}N_5 - \frac{3}{4}N_6 - \frac{1}{4}N_7, \tag{3.56}$$

$$N_2 = N_2^0 - \frac{1}{2}N_5 - \frac{1}{4}N_6 - \frac{3}{4}N_7. \tag{3.57}$$

With this, the displacement field in the interior of the contact element is interpolated as

$$\boldsymbol{u}_e^h = \sum_{i=1}^{7} N_i \mathbf{u}_i. \tag{3.58}$$

The modified shape functions obtained for both Q1C2 and Q1C4 elements satisfy the property

$$N_a(\xi_b, \eta_b) = \delta_{ab}, \tag{3.59}$$

at nodes a and b. Here, δ_{ab} is the Kronecker delta such that

$$\delta_{ab} = \begin{cases} 1 & \text{if } a = b, \\ 0 & \text{otherwise.} \end{cases} \tag{3.60}$$

Further, the modified shape functions also satisfy the property of the partition of unity

$$\sum_{i=1}^{n_e^{\text{enrich}}} N_i = 1, \quad \forall\, \xi, \eta, \tag{3.61}$$

where n_e^{enrich} is the number of nodes in the enriched element. For a Q1C2 element $n_e^{\text{enrich}} = 5$ and for a Q1C4 element $n_e^{\text{enrich}} = 7$.

Similar descriptions can be obtained for three-dimensional (3D) elements. However, in case of a three-dimensional element a transitional element is required between the enriched contact elements and the trilinear element in the bulk. In 3D, for an eight-noded trilinear brick element, the standard Lagrangian shape functions can be obtained by

$$N_i^0 = \frac{1}{8}(1 + \xi_i\xi)(1 + \eta_i\eta)(1 + \zeta_i\zeta), \tag{3.62}$$

where $(\xi, \eta, \zeta) = (\pm 1, \pm 1, \pm 1)$ denote the corner coordinates of the master element shown in Figures 3.3 and 3.4.

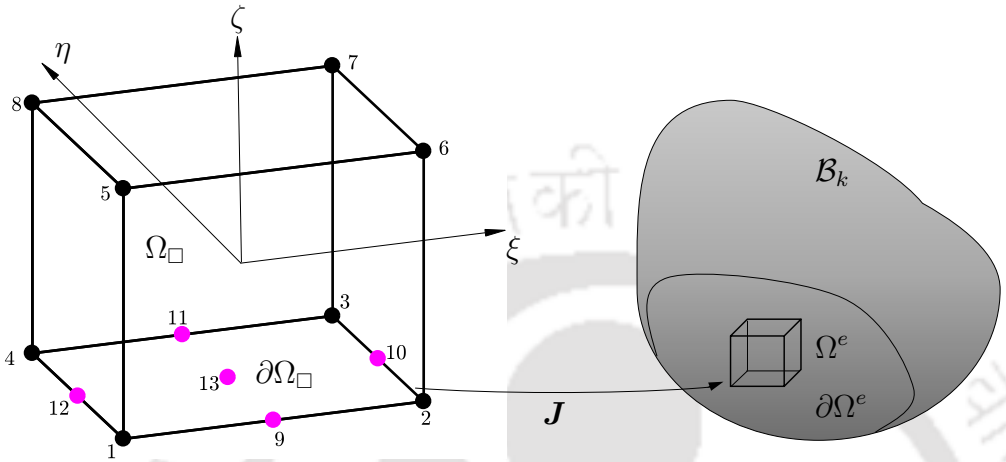

(a)

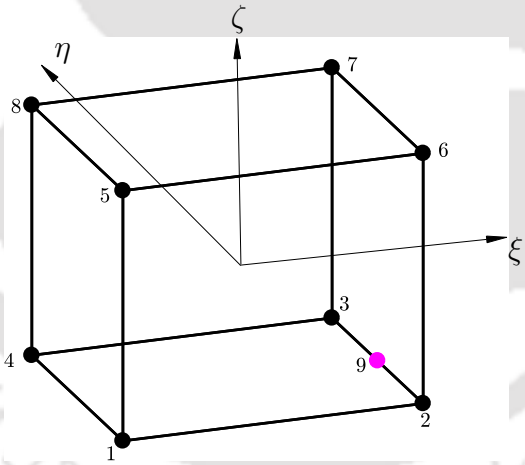

(b)

Figure 3.3: Representation of a three-dimensional enriched contact element Q1C2 (a) Mapping of Q1C2 master element to corresponding finite element in the current domain. (b) Depiction of a transition element Q1T2 connecting a Q1C2 element to a Q1 element.

Then, a 3D equivalent of the Q1C2 element can be obtained by inserting five extra nodes, out of which four are in between the corner nodes and one is at the center of the contact surface as shown in Figure 3.3. Similar to the 2D case, shape functions corresponding to the interior nodes $5, 6, 7$, and 8 remain the same as those in Eq. (3.62), i.e. $N_5 = N_5^0$, $N_6 = N_6^0$, $N_7 = N_7^0$, and $N_8 = N_8^0$. Then, the modified shape functions for a Q1C2 element in 3D, which satisfy both the properties given by Eqs. (3.59) and (3.61), can be obtained by multiplying the biquadratic Lagrangian shape functions with $(1-\zeta)/2$ for the ζ direction as [163]

$$\begin{aligned}
N_1 &= \tfrac{1}{8}(\xi^2-\xi)(\eta^2-\eta)(1-\zeta)\\
N_2 &= \tfrac{1}{8}(\xi^2+\xi)(\eta^2-\eta)(1-\zeta)\\
N_3 &= \tfrac{1}{8}(\xi^2+\xi)(\eta^2+\eta)(1-\zeta)\\
N_4 &= \tfrac{1}{8}(\xi^2-\xi)(\eta^2+\eta)(1-\zeta)\\
N_9 &= \tfrac{1}{4}(1-\xi^2)(\eta^2-\eta)(1-\zeta)\\
N_{10} &= \tfrac{1}{4}(\xi^2+\xi)(1-\eta^2)(1-\zeta)\\
N_{11} &= \tfrac{1}{4}(1-\xi^2)(\eta^2+\eta)(1-\zeta)\\
N_{12} &= \tfrac{1}{4}(\xi^2-\xi)(1-\eta^2)(1-\zeta)\\
N_{13} &= \tfrac{1}{2}(1-\xi^2)(1-\eta^2)(1-\zeta),
\end{aligned} \tag{3.63}$$

which can then be employed to approximate the elemental displacement field as

$$\boldsymbol{u}_e^h = \sum_{i-1}^{13} N_i \mathbf{u}_i. \tag{3.64}$$

Each 3D Q1C2 contact element, thus, has 13 nodes and 39 degrees of freedom. In addition, a transition element is also defined which is needed to connect a Q1C2 element to a Q1 element. This transitional element, denoted as Q1T2, has one extra node along an edge in an eight-noded brick element. Then, the new shape functions corresponding Q1T2 element shown in Figure 3.3b can be obtained as [163]

$$\begin{aligned}
N_2 &= \tfrac{1}{8}(1+\xi)(\eta^2-\eta)(1-\zeta)\\
N_3 &= \tfrac{1}{8}(1+\xi)(\eta^2+\eta)(1-\zeta)\\
N_9 &= \tfrac{1}{4}(1+\xi)(1-\eta^2)(1-\zeta).
\end{aligned} \tag{3.65}$$

A Q1C4 contact element in 3D can similarly be obtained by placing 21 extra nodes on the contact surface, out of which 12 are in between the corner nodes on the edges and 9 are in the center of the surface as shown in Figure 3.4a. Similar to a 3D Q1C2 element, the interior shape functions N_5, N_6, N_7, and N_8 remain the same and the new shape functions for corresponding to other nodes can be obtained

by multiplying the biquartic shape functions with $(1-\zeta)/2$ for the ζ direction as

$$
\begin{aligned}
N_1 &= \tfrac{2}{3}\xi(\xi-1)(\xi^2-\tfrac{1}{4})\ \tfrac{2}{3}\eta(\eta-1)(\eta^2-\tfrac{1}{4})\ \tfrac{1}{2}(1-\zeta)\\
N_2 &= \tfrac{2}{3}\xi(\xi+1)(\xi^2-\tfrac{1}{4})\ \tfrac{2}{3}\eta(\eta-1)(\eta^2-\tfrac{1}{4})\ \tfrac{1}{2}(1-\zeta)\\
N_3 &= \tfrac{2}{3}\xi(\xi+1)(\xi^2-\tfrac{1}{4})\ \tfrac{2}{3}\eta(\eta+1)(\eta^2-\tfrac{1}{4})\ \tfrac{1}{2}(1-\zeta)\\
N_4 &= \tfrac{2}{3}\xi(\xi-1)(\xi^2-\tfrac{1}{4})\ \tfrac{2}{3}\eta(\eta+1)(\eta^2-\tfrac{1}{4})\ \tfrac{1}{2}(1-\zeta)\\
N_9 &= \tfrac{8}{3}\xi(\xi-\tfrac{1}{2})(1-\xi^2)\ \tfrac{2}{3}\eta(\eta-1)(\eta^2-\tfrac{1}{4})\ \tfrac{1}{2}(1-\zeta)\\
N_{10} &= 4\,(\xi^2-1)(\xi^2-\tfrac{1}{4})\ \tfrac{2}{3}\eta(\eta-1)(\eta^2-\tfrac{1}{4})\ \tfrac{1}{2}(1-\zeta)\\
N_{11} &= \tfrac{8}{3}\xi(\xi+\tfrac{1}{2})(1-\xi^2)\ \tfrac{2}{3}\eta(\eta-1)(\eta^2-\tfrac{1}{4})\ \tfrac{1}{2}(1-\zeta)\\
N_{12} &= \tfrac{2}{3}\xi(\xi-1)(\xi^2-\tfrac{1}{4})\ \tfrac{8}{3}\eta(\eta-\tfrac{1}{2})(1-\eta^2)\ \tfrac{1}{2}(1-\zeta)\\
N_{13} &= \tfrac{8}{3}\xi(\xi-\tfrac{1}{2})(1-\xi^2)\ \tfrac{8}{3}\eta(\eta-\tfrac{1}{2})(1-\eta^2)\ \tfrac{1}{2}(1-\zeta)\\
N_{14} &= 4\,(\xi^2-1)(\xi^2-\tfrac{1}{4})\ \tfrac{8}{3}\eta(\eta-\tfrac{1}{2})(1-\eta^2)\ \tfrac{1}{2}(1-\zeta)\\
N_{15} &= \tfrac{8}{3}\xi(\xi+\tfrac{1}{2})(1-\xi^2)\ \tfrac{8}{3}\eta(\eta-\tfrac{1}{2})(1-\eta^2)\ \tfrac{1}{2}(1-\zeta)\\
N_{16} &= \tfrac{2}{3}\xi(\xi+1)(\xi^2-\tfrac{1}{4})\ \tfrac{8}{3}\eta(\eta-\tfrac{1}{2})(1-\eta^2)\ \tfrac{1}{2}(1-\zeta)\\
N_{17} &= \tfrac{2}{3}\xi(\xi-1)(\xi^2-\tfrac{1}{4})\ 4\,(\eta^2-1)(\eta^2-\tfrac{1}{4})\ \tfrac{1}{2}(1-\zeta)\\
N_{18} &= \tfrac{8}{3}\xi(\xi-\tfrac{1}{2})(1-\xi^2)\ 4\,(\eta^2-1)(\eta^2-\tfrac{1}{4})\ \tfrac{1}{2}(1-\zeta)\\
N_{19} &= 4\,(\xi^2-1)(\xi^2-\tfrac{1}{4})\ 4\,(\eta^2-1)(\eta^2-\tfrac{1}{4})\ \tfrac{1}{2}(1-\zeta)\\
N_{20} &= \tfrac{8}{3}\xi(\xi+\tfrac{1}{2})(1-\xi^2)\ 4\,(\eta^2-1)(\eta^2-\tfrac{1}{4})\ \tfrac{1}{2}(1-\zeta)\\
N_{21} &= \tfrac{2}{3}\xi(\xi+1)(\xi^2-\tfrac{1}{4})\ 4\,(\eta^2-1)(\eta^2-\tfrac{1}{4})\ \tfrac{1}{2}(1-\zeta)\\
N_{22} &= \tfrac{2}{3}\xi(\xi-1)(\xi^2-\tfrac{1}{4})\ \tfrac{8}{3}\eta(\eta+\tfrac{1}{2})(1-\eta^2)\ \tfrac{1}{2}(1-\zeta)\\
N_{23} &= \tfrac{8}{3}\xi(\xi-\tfrac{1}{2})(1-\xi^2)\ \tfrac{8}{3}\eta(\eta+\tfrac{1}{2})(1-\eta^2)\ \tfrac{1}{2}(1-\zeta)\\
N_{24} &= 4\,(\xi^2-1)(\xi^2-\tfrac{1}{4})\ \tfrac{8}{3}\eta(\eta+\tfrac{1}{2})(1-\eta^2)\ \tfrac{1}{2}(1-\zeta)\\
N_{25} &= \tfrac{8}{3}\xi(\xi+\tfrac{1}{2})(1-\xi^2)\ \tfrac{8}{3}\eta(\eta+\tfrac{1}{2})(1-\eta^2)\ \tfrac{1}{2}(1-\zeta)\\
N_{26} &= \tfrac{2}{3}\xi(\xi+1)(\xi^2-\tfrac{1}{4})\ \tfrac{8}{3}\eta(\eta+\tfrac{1}{2})(1-\eta^2)\ \tfrac{1}{2}(1-\zeta)\\
N_{27} &= \tfrac{8}{3}\xi(\xi-\tfrac{1}{2})(1-\xi^2)\ \tfrac{2}{3}\eta(\eta+1)(\eta^2-\tfrac{1}{4})\ \tfrac{1}{2}(1-\zeta)\\
N_{28} &= 4\,(\xi^2-1)(\xi^2-\tfrac{1}{4})\ \tfrac{2}{3}\eta(\eta+1)(\eta^2-\tfrac{1}{4})\ \tfrac{1}{2}(1-\zeta)\\
N_{29} &= \tfrac{8}{3}\xi(\xi+\tfrac{1}{2})(1-\xi^2)\ \tfrac{2}{3}\eta(\eta+1)(\eta^2-\tfrac{1}{4})\ \tfrac{1}{2}(1-\zeta).
\end{aligned}
\tag{3.66}
$$

A 3D Q1C4 contact element, thus, has a total of 29 nodes and 87 degrees of freedom. The displacement field of the contact element can then be approximated using these shape functions as

$$\boldsymbol{u}_e^h = \sum_{i-1}^{29} N_i \mathbf{u}_i. \tag{3.67}$$

A transition element denoted as Q1T4 connecting a Q1C4 element to a Q1 element can be obtained by placing three extra nodes on an edge as shown in Figure 3.4b

and the modified shape functions follow as

$$
\begin{aligned}
N_2 &= \tfrac{1}{2}(1+\xi)\,\tfrac{2}{3}\,\eta(\eta-1)(\eta^2-\tfrac{1}{4})\,\tfrac{1}{2}(1-\zeta)\\
N_3 &= \tfrac{1}{2}(1+\xi)\,\tfrac{2}{3}\,\eta(\eta+1)(\eta^2-\tfrac{1}{4})\,\tfrac{1}{2}(1-\zeta)\\
N_9 &= \tfrac{1}{2}(1+\xi)\,\tfrac{8}{3}\,\eta(\eta-\tfrac{1}{2})(1-\eta^2)\,\tfrac{1}{2}(1-\zeta)\\
N_{10} &= \tfrac{1}{2}(1+\xi)\,4\,(\eta^2-\tfrac{1}{4})(\eta^2-1)\,\tfrac{1}{2}(1-\zeta)\\
N_{11} &= \tfrac{1}{2}(1+\xi)\,\tfrac{8}{3}\,\eta(\eta+\tfrac{1}{2})(1-\eta^2)\,\tfrac{1}{2}(1-\zeta).
\end{aligned}
\tag{3.68}
$$

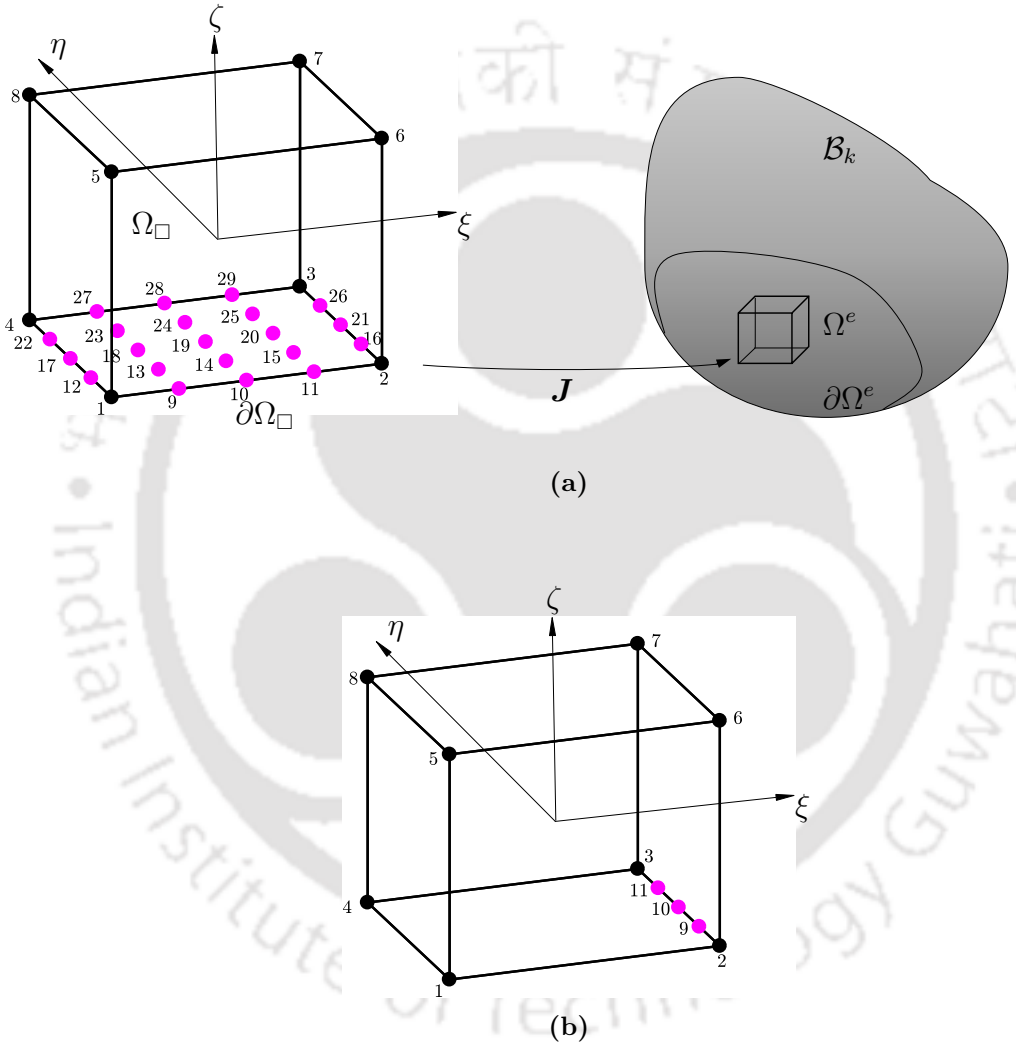

Figure 3.4: Representation of a three-dimensional enriched contact element Q1C4 (a) Mapping of Q1C4 master element to corresponding finite element in the current domain. (b) A transition element Q1T4 that can connect to Q1C4 element to a Q1 element.

भारतीय प्रौद्योगिकी संस्थान गुवाहाटी
Indian Institute of Technology Guwahati

Chapter 4

Spatula Peeling - Numerical Results and Discussion

In this chapter, numerical results for the gecko spatula peeling problem obtained using an in-house MATLAB code developed for implementing the finite element formulation presented in Chapter 3 are discussed. Section 4.1 presents the validation of the FE formulation. Section 4.2 discusses the two-dimensional spatula model employed in this study and the different types of peeling simulations carried out in this work. Section 4.3 discusses the coupled adhesion and friction behaviour of the gecko spatula based on the finite element peeling analysis[1]. Finally, Section 4.4 presents the three dimensional spatula model and the corresponding finite element results.

4.1 Validation of the formulation

Based on the continuum formulation and the corresponding nonlinear finite element (FE) discretization presented in Chapters 2 and 3, an in-house nonlinear FE code is developed. The implementation is validated by solving an example problem from the literature. As the goal of the current thesis is to analyse the peeling of a gecko spatula, which is often modelled as a thin strip [99, 144], it is only appropriate to verify the validity of the formulation with a relevant example problem such as peeling of a thin two-dimensional strip. Further, improvement in the contact solution obtained using the different surface enrichment strategies employed is also investigated. The results are then compared with the peeling results of Sauer [165].

[1]All the results in this section, except for section 4.3.1f, are published in The Journal of Adhesion at https://doi.org/10.1080/00218464.2020.1719838 and https://doi.org/10.1080/00218464.2020.1746652. As such, all the figures are taken from these papers and the permission for the same has been obtained from the journals.

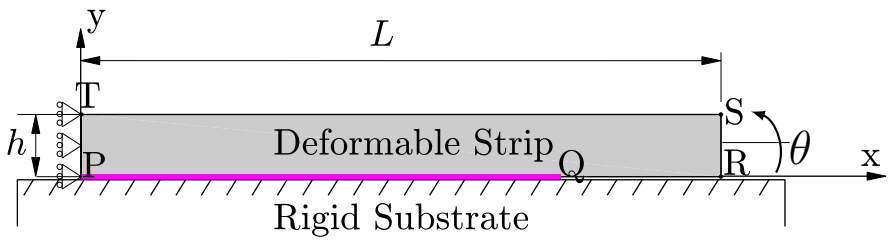

Figure 4.1: The set-up of peeling of a deformable strip from a rigid substrate. The strip is peeled off by applying a rotation angle θ to its right end RS. Adhesion is considered only for bottom (PQ) 75% of the strip.

The set-up of the adhesive contact between a deformable strip and a rigid substrate, as shown in Figure 4.1, is taken from Sauer [165]. The deformable strip has the dimensions $L \times h = 200R_0 \times 10R_0$, where $R_0 = 1\,\text{nm}$. The elastic response of the strip is described using an isotropic, Neo-Hookean material model with Young's modulus $E_0 = 2$ GPa and Poisson's ratio $\nu = 0.2$. It is assumed that the adhesive interactions, due to van der Waals forces, act only on the bottom 75% of the strip. The adhesive traction $\boldsymbol{T}_\text{a}$ in Eq. (2.36) is computed using $r_0 = 0.4\,\text{nm}$ and Hamaker's constant $A_\text{H} = 10^{-19}$ J. These values correspond to gecko adhesion [99].

The strip, initially at equilibrium with the rigid substrate, is peeled off by applying a rotation θ to its right end (RS), yielding a constant peeling moment. Three different finite element meshes are considered: mesh m_1 has 160×8 elements, mesh m_2 has 240×12 elements, mesh m_3 has 320×16 elements along the length (x-) and height (y-) directions, respectively. The bending moment M_b required to peel off the strip is shown in Figure 4.2 for the m_2 mesh. It can be observed that the bending moment initially increases linearly and after a certain rotation angle it remains constant. However, on enlarging the bending moment curve, it can be seen that the bending moment is not actually constant but oscillates around a mean line. These oscillations are due to the inability of the FE mesh to capture the nonlinear interfacial tractions. Moreover, convergence of the Newton-Raphson iterative method employed in solving this nonlinear peeling problem, is significantly influenced as these oscillations lead to uneven convergence rates. For coarse mesh m_1 in conjunction with Q1C1 elements, the peeling computations do not even converge and fail. Further, as shown in Figure 4.3, as the strip is peeled off, very high stresses are generated in a very narrow peeling zone. In order to alleviate the convergence issues as well as accurately resolve the stresses in the peeling zone, one can employ finer finite element meshes. However, this is computationally expensive. To overcome this issue, surface enrichment strategies can be used, in which only the contact surface is discretized using higher-order Lagrange polynomials, while the bulk is described using standard linear Lagrange polynomials.

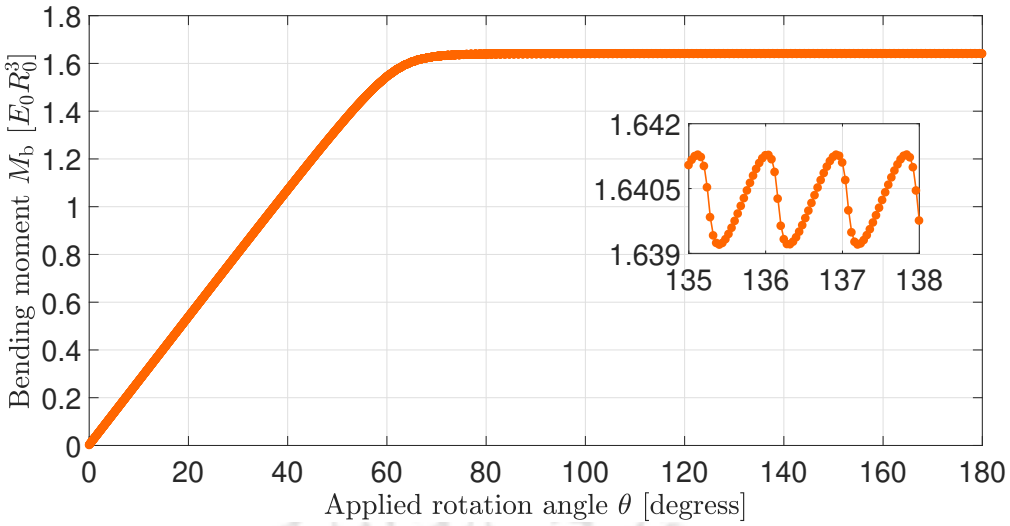

Figure 4.2: Variation of the bending moment with applied rotation angle θ with Q1C1 elements used for contact surface description. Inset shows the enlarged view of the bending moment. Here $E_0R_0^3 = 2$nN-nm.

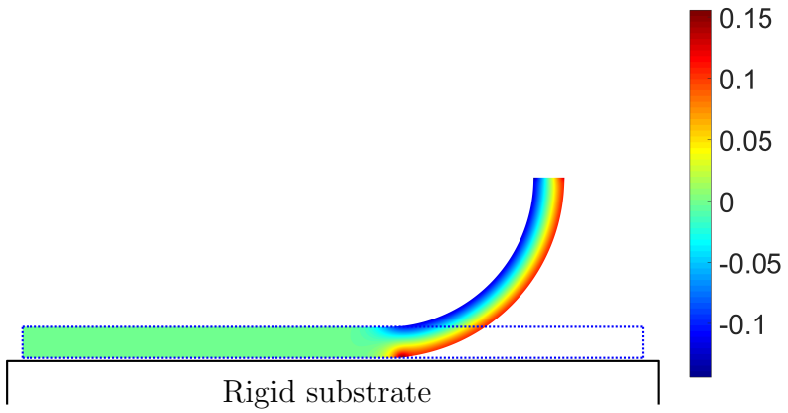

Figure 4.3: Deformed configuration of the strip at rotation angle $\theta = 90°$. The colourbar represents the normalised stress $I_1/E_0 = \mathrm{tr}(\boldsymbol{\sigma})/E_0$.

For the purpose of accurate and efficient contact description, the two surface enrichment strategies described in Chapter 3, viz. Q1C2 and Q1C4 are employed. As such, in this peeling problem, only the finite elements in the bottom 75% of the contact surface, which experience the interfacial interactions are approximated using Q1C2 and Q1C4 elements. Whereas, finite elements in the bulk are approximated using the standard linear Lagrangian elements. Performance of these contact elements are compared with the Q1C1 formulation for the three finite element meshes, m_1, m_2, and m_3. Table 4.1 shows the total number of degrees of freedom corresponding to the three different contact formulations and mesh sizes. The peeling performance is mainly characterized by the oscillation error ΔM_b, the wavelength of the oscillations $\Delta\theta$, the minimum and maximum average slopes of the bending moment curve $M_{\mathrm{b},\theta} = \partial M_\mathrm{b}/\partial\theta$.

Table 4.1: Total number of degrees of freedom for different contact elements and meshes.

Element	Mesh m_1 (160×8)	Mesh m_2 (240×12)	Mesh m_3 (320×16)
Q1C1	2898	6266	10914
Q1C2	3138	6626	11394
Q1C4	3618	7346	12354

Figures 4.4 and 4.5 depict the enlarged views of the part of the bending moment curves between $\theta = 135°$ and $138°$ obtained with the Q1C1, Q1C2, and Q1C4 formulations for meshes m_2 and m_3, respectively. For a given mesh, the oscillation error reduces as the contact surface is descritized using higher-order elements. For mesh m_2, the Q1C2 formulation produces 3.7 times less oscillation error (ΔM_b) and the Q1C4 formulation produces almost 10 times less oscillation error, when compared to the Q1C1 formulation. The minimum average slope $\min(M_{b,\theta})$ reduces by a factor of 11 for the Q1C2 formulation and by a factor of 34 for the Q1C4 formulation when compared to the Q1C1 formulation. The wavelength $\Delta\theta$, however, remains the same for all the three formulations but varies for different mesh sizes. The presence of more number of degrees of freedom (DOFs) along the contact surface enables the Q1C2 and Q1C4 elements to capture the nonlinear adhesive tractions much more accurately than the Q1C1 formulation as shown in Table 4.1. Comparison of the peeling performance of the Q1C1, the Q1C2, and the Q1C4 element formulations for three different finite element meshes is shown in Table 4.2. The results obtained by Sauer [163] for the same meshes and the contact elements are shown in Table 4.3. From this, it is clear that the current results match very well with those of Sauer [165].

The results discussed show that the Q1C4 formulation performs better than both the Q1C2 and Q1C1 formulations for all three meshes due to the advantage of large number of DOFs along the contact surface, which aids in accurate contact solution computation. In Table 4.4 performance of the Q1C4 elements is compared for three different mesh sizes. As the mesh size increases, the oscillation error reduces. But the computational time also increases as the mesh size increases. However, the most gain in performance is achieved just by changing the mesh size from m_1 to m_2. Comparing meshes m_1 and m_2, for a decrease of 87% in ΔM_b and 86% in $\min(M_{b,\theta})$ the computational time increases by 50%. Whereas, from mesh m_2 to m_3 although there is an additional 11% and 12% reduction in ΔM_b and $\min(M_{b,\theta})$, it comes at cost of 120% increase in the computational time compared to mesh m_1. Therefore, it can be concluded that the Q1C4 formulation along with mesh m_2 provides sufficiently accurate results with good computational efficiency.

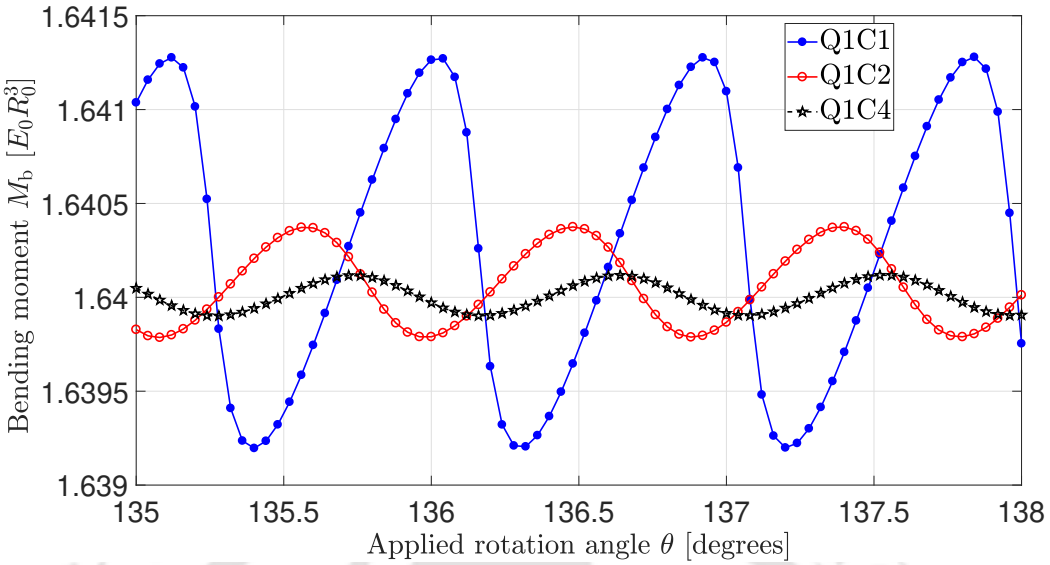

Figure 4.4: Comparison of the variation of the bending moment M_b with the applied rotation angle θ for three different contact surface descriptions with mesh m_2.

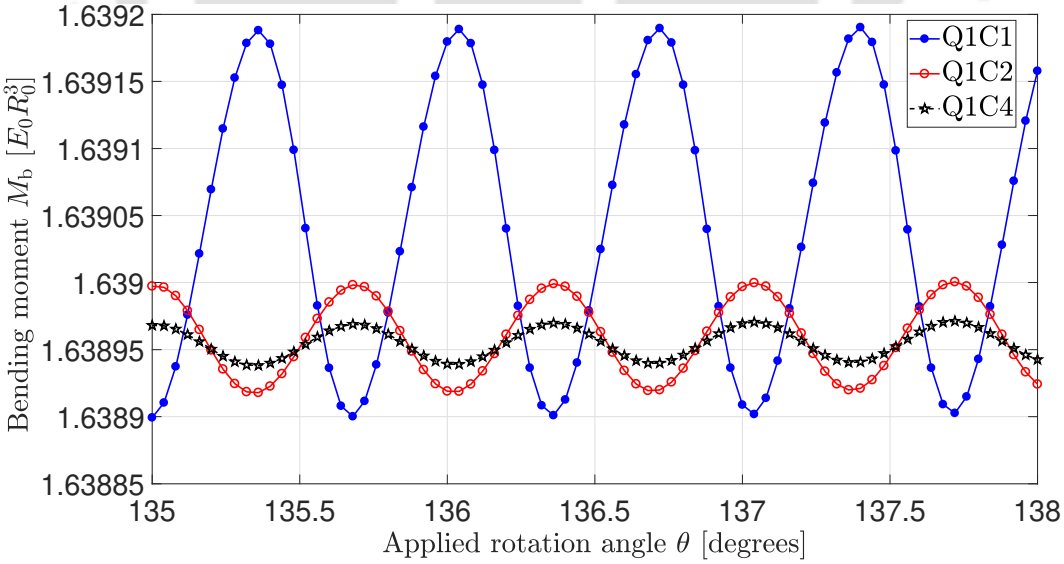

Figure 4.5: Comparison of the variation of the bending moment M_b with the applied rotation angle θ for three different contact surface descriptions with mesh m_3.

Table 4.2: Comparison of the performance of different elements used for contact surface description with different mesh sizes. The code failed to converge for Q1C1 element with mesh m_1.

Element	Mesh	Oscillation error $\Delta M_b \times 10^{-3}$	Wavelength $\Delta\theta$	$\min(M_{b,\theta})$ $\times 10^{-3}$	$\max(M_{b,\theta})$ $\times 10^{-3}$
Q1C1	m_1 (160×8)	–	–	–	–
Q1C2	m_1 (160×8)	4.0984	1.3600	−75.6570	5.3850
Q1C4	m_1 (160×8)	1.6364	1.3599	−5.5430	2.8892
Q1C1	m_2 (240×12)	2.1013	0.9199	−27.0876	4.5176
Q1C2	m_2 (240×12)	0.5609	0.9200	−2.3148	1.6809
Q1C4	m_2 (240×12)	0.2169	0.9199	−0.7975	0.7072
Q1C1	m_3 (320×16)	0.2705	0.6800	−1.3952	1.1313
Q1C2	m_3 (320×16)	0.0826	0.6799	−0.3828	0.3616
Q1C4	m_3 (320×16)	0.0329	0.6799	−0.1414	0.1399

Table 4.3: Comparison of the performance of different elements used for contact surface description with different mesh sizes as obtained by Sauer [163]. The code failed to converge for Q1C1 element with mesh m_1.

Element	Mesh	Oscillation error $\Delta M_b \times 10^{-3}$	Wavelength $\Delta\theta$	$\min(M_{b,\theta})$ $\times 10^{-3}$	$\max(M_{b,\theta})$ $\times 10^{-3}$
Q1C1	m_1 (160×8)	–	–	–	–
Q1C2	m_1 (160×8)	4.612	1.363	−100.003	5.539
Q1C4	m_1 (160×8)	1.798	1.363	−6.619	2.998
Q1C1	m_2 (240×12)	2.267	0.9081	−23.55	4.699
Q1C2	m_2 (240×12)	0.6082	0.9090	−2.461	1.806
Q1C4	m_2 (240×12)	0.2283	0.9090	−0.7978	0.7553
Q1C1	m_3 (320×16)	0.2684	0.6812	−1.385	1.131
Q1C2	m_3 (320×16)	0.0914	0.6815	−0.4388	0.3958
Q1C4	m_3 (320×16)	0.0405	0.6815	−0.1902	0.1764

Table 4.4: Comparison of the performance of Q1C4 elements at different mesh sizes. The results of mesh m_1 with Q1C4 formulation is used for reference.

Mesh	Oscillation error ΔM_b (%)	Downward slope error $\min(M_{b,\theta})$ (%)	Computational time (%)
m_1 (160×8)	100	100	100
m_2 (240×12)	13.20	14.38	150
m_3 (320×16)	2.08	2.55	220

4.2 Spatula model

As mentioned in the previous section, owing to its thin structure, gecko spatula is often modelled in the literature as a two-dimensional strip [99, 103, 144, 165]. Hence, in the current thesis, a similar approach is followed, and the spatula is represented by a thin strip having $L \times h$ as previously shown in Figure 4.1. As such, the words "strip" and "spatula" are used interchangeably in the following text. It is considered that the bottom 75% of the strip surface ("PQ") is in adhesion, while the rest 25% ("QR") is not. Hence, "PQ" represents the bottom surface of the spatula pad, while "QR" represents the bottom surface of the spatula shaft.

The finite element mesh m_2 is employed due to its computational efficiency and accuracy, as discussed in the previous section. This mesh contains 240×12 elements along x and y directions. Plane strain[2] finite element simulations are carried out using the same parameters as those mentioned in section 4.1. These are once again listed in Table 4.5 [99, 158, 163]. As the current thesis also studies the influence of some of the parameters listed here, it should be noted that unless mentioned otherwise the parameters given in Table 4.5 should be considered as default parameters. This results in $\gamma_W = 25.266$ and $\gamma_L = 2.50$ according to Eqs. (2.40) and (2.39). The friction coefficient $\mu_s = 0.3$ corresponds to the experimental data on gecko seta friction on glass surfaces [1, 2, 48]. The initial area of the spatula pad is taken as $A_{pad} = 49,524 R_0^2$ [162]. Then from the parameters in Table 4.5, the average width of the pad for the strip configuration becomes $w_{pad} = 330.16 R_0$.

4.2.1 Application of peeling

The spatula is peeled off the rigid substrate in four different ways:

1. In "Type I" simulations, the spatula is peeled off the rigid substrate from its initial configuration by applying a displacement $\bar{\boldsymbol{u}}$ to the right end (RS) at an

[2] As the spatula is very wide (up to a few hundred nm), plane strain is a reasonable simplification of the full 3D case.

Table 4.5: Geometrical, material, and adhesion parameters used in the current study. Here, $R_0 = 1$ nm is introduced for normalization.

Length (L)	$200R_0$
Height (h)	$10R_0$
Young's Modulus (E_0)	2 GPa
Poisson's ratio (ν)	0.2
Friction coefficient (μ_s)	0.3
Equilibrium distance (r_0)	0.4 nm
Hamaker's constant (A_H)	10^{-19} J

angle called peeling angle θ_p as shown in Figure 4.6a.

2. In "Type II" simulations, first an external rotation is applied to the right end (RS) of the strip. After achieving a desired rotation angle θ_{sh}, called the shaft angle, on the right end, a displacement $\bar{\boldsymbol{u}}$ is applied at a constant peeling angle $\theta_p = 90°$. As shown in Figure 4.6b, the shaft angle θ_{sh} represents the direction of the cross-section normal $\hat{\mathbf{n}}$ with respect to the horizontal.

3. In "Type III" simulations, similar to "Type II" peeling, the spatula is first rotated up to a desired shaft angle θ_{sh} and then the displacement is applied at an angle equal to that of the shaft angle $\theta_p = \theta_{sh}$. Hence, as visualized in Figure 4.6c, the displacement direction is along the direction of the cross-section normal $\hat{\mathbf{n}}$ at "RS".

   In all the three types of simulations, the displacement $\bar{\boldsymbol{u}}$ is applied through its horizontal and vertical components $u_x = \bar{u}\cos\theta_p$ and $u_y = \bar{u}\sin\theta_p$ on each node of "RS", where $\bar{u} = \|\bar{\boldsymbol{u}}\|$ is the magnitude of the applied displacement. This results in a tangentially constrained motion of the spatula shaft. As such, these three types of peeling simulations can broadly be classified as *tangentially-constrained* peeling. In addition, unlike Kendall type peeling models [49], in the current analysis, the bending stiffness of the strip is considered to be finite. As a consequence, the resultant pull-off force $\boldsymbol{F}_{res}$ is not parallel to the applied displacement $\bar{\boldsymbol{u}}$. Instead $\boldsymbol{F}_{res}$ acts in the direction (see Figures 4.6b and 4.6c)

$$\alpha = \arctan(F_N/F_T)\,, \tag{4.1}$$

   where F_N and F_T are its normal and tangential components. Particularly, it should be noted that, peeling with $\theta_p = 90°$ is not equivalent to peeling with a force perpendicular to the substrate, i.e. with $\alpha = 90°$, in these three *tangentially-constrained* peeling simulations.

Therefore, "Type I" peeling is used to study the influence of the peeling angle at a constant shaft angle of $\theta_{\text{sh}} = 0°$, whereas "Type II" and "Type III" peeling simulations both are used to study the influence of the shaft angle as well as peeling angle.

4. In addition to the three peeling simulations described above, another peeling simulation which is called the "vertical pulling" (discussed in section 4.3.1g) is also carried out. In this, for any given shaft angle $\theta_{\text{sh}} = 0°$ to $90°$ (with $\theta_{\text{sh}} = 0°$ indicating the initial configuration), a vertical displacement $\bar{\boldsymbol{u}}_y$, i.e. perpendicular to the substrate, is applied on the shaft end RS. As such, the shaft end RS is free to move in the tangential direction. Hence, the resultant force $\boldsymbol{F}_{\text{res}}$ is parallel to the applied displacement $\bar{\boldsymbol{u}}_y$. As such, this peeling can be contrasted with the first three *tangentially-constrained* peeling simulations as it describes the *tangentially-free* peeling.

In order to completely peel off the spatula adhering to the substrate in its initial configuration (shown in Figure 4.1), a certain amount of energy must be expended, the absolute value of which can be computed from the work of adhesion w_{adh} as [162]

$$\Pi_{\text{a},0} = \text{A}_{\text{pad}}\, w_{\text{adh}} \quad \text{where} \quad w_{\text{adh}} = -\int_{r_{\text{eq}}}^{\infty} \|\boldsymbol{T}_{\text{a}}(r_{\text{s}})\|\, \text{d}r_{\text{s}} = \sqrt[3]{15}\, \frac{A_{\text{H}}}{16\pi r_0^2}\,, \tag{4.2}$$

and A_{pad} is the initial area of the spatula pad in contact with the susbtrate. As the spatula is gradually peeled off the substrate, the adhesion energy Π_{a} increases from $-\Pi_{\text{a},0}$, and eventually becomes zero when the spatula is completely peeled off.

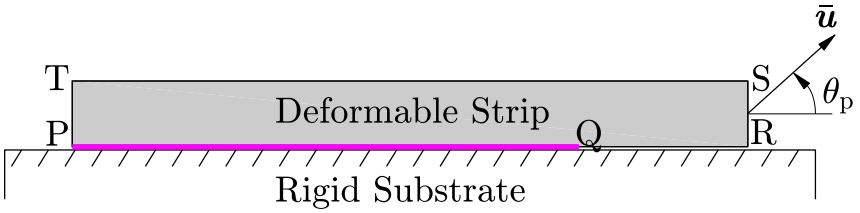

(a) Type I peeling: peeling from the initial configuration by applying a displacement $\bar{\boldsymbol{u}}$ in the direction θ_{p}, called the peeling angle.

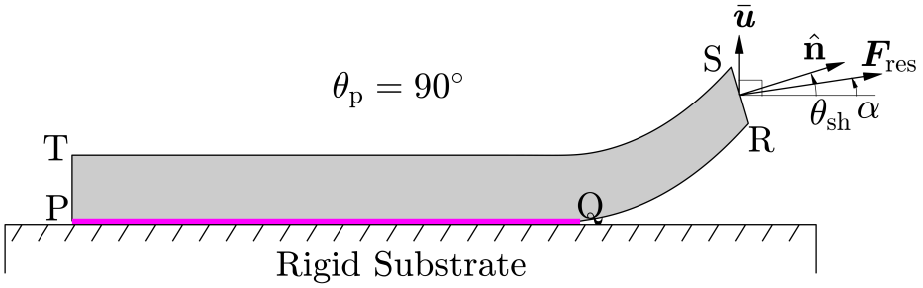

(b) Type II peeling: peeling from different rotated configurations at a constant peeling angle of $\theta_{\mathrm{p}} = 90°$. Here, $\hat{\mathbf{n}}$ denotes the normal to the cross-section at "RS" and θ_{sh} is the angle $\hat{\mathbf{n}}$ makes with the horizontal, while α is the angle resultant force $\boldsymbol{F}_{\mathrm{res}}$ makes with the horizontal.

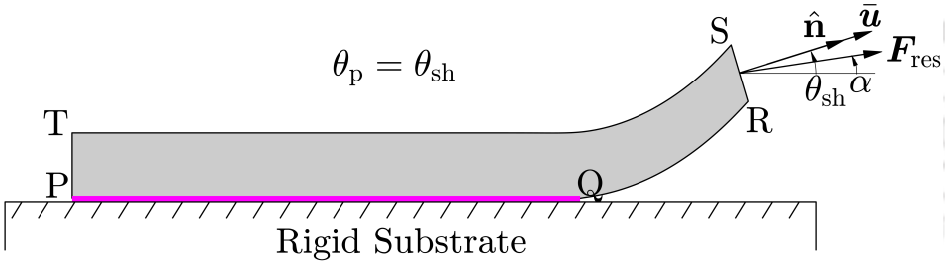

(c) Type III peeling: peeling from different rotated configurations by applying displacement $\bar{\boldsymbol{u}}$ in the direction of the normal to the cross-section $\hat{\mathbf{n}}$ at "RS". Therefore, the peeling angle is equal to the shaft angle, $\theta_{\mathrm{p}} = \theta_{\mathrm{sh}}$.

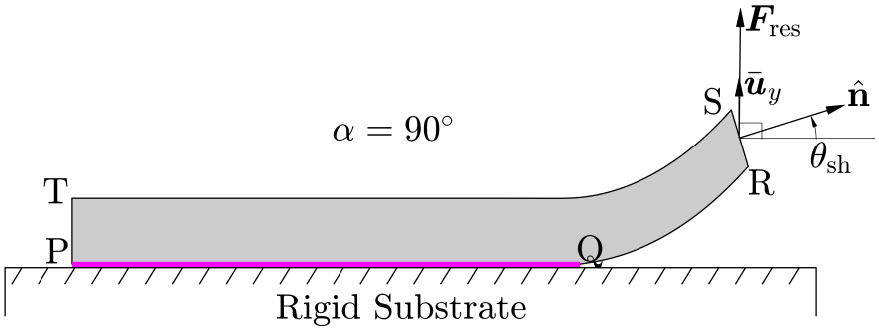

(d) Vertical pulling: peeling from different rotated configurations by applying displacement $\bar{\boldsymbol{u}}_y$ only in the vertical direction. Therefore, the resultant force angle is in the direction of the vertical displacement $\bar{\boldsymbol{u}}_y$, i.e. $\alpha = 90°$.

Figure 4.6: Visualization of different types of peeling simulations.

4.3 Coupled adhesion and friction behaviour

In this section, a detailed investigation into the normal (adhesive) and tangential (frictional) behaviour exhibited by the gecko spatula as it is peeled off a rigid substrate is presented for the four peeling simulations discussed in the last section. The peeling behaviour is studied first by examining the pull-off forces and the influence of various parameters such as the peeling angle, shaft angle, pad thickness, material stiffness, and spatula size on them. Next, presence of the critical detachment angle at the spatula level and its variation with different parameters is analysed. It should be noted that unless stated otherwise the results correspond to "Type I" peeling.

To begin with, typical peel off behaviour of the spatula for a given peeling angle θ_p is described. This forms the basis for the discussion in the next sections.

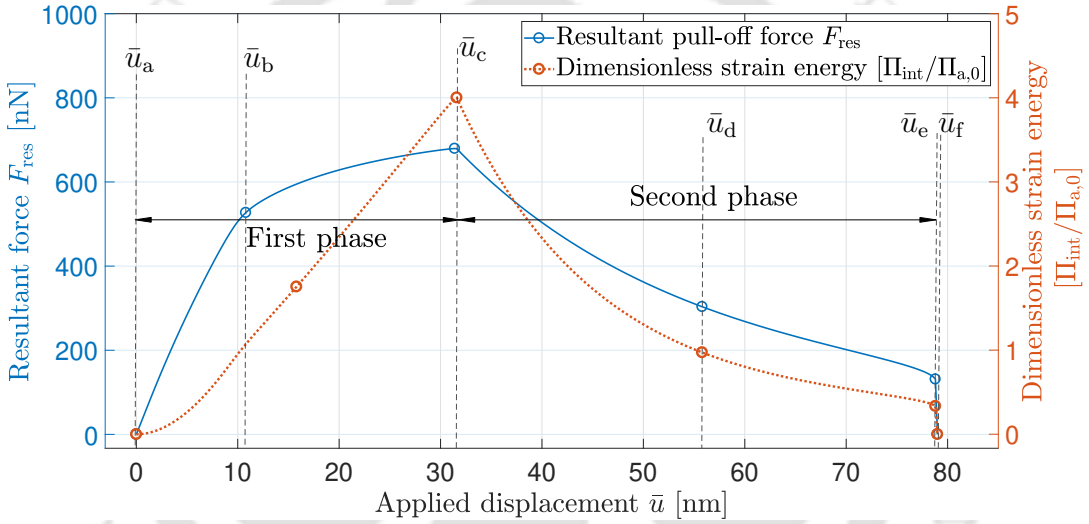

Figure 4.7: Evolution of the magnitude of the resultant pull-off force $F_{res} = \|\boldsymbol{F}_{res}\|$ and the dimensionless strain energy (see Eq. (2.7)) with the magnitude of applied displacement $\bar{u} = \|\bar{\boldsymbol{u}}\|$ for peeling angle $\theta_p = 60°$ in "Type I" peeling. Here, $\Pi_{a,0} = 1.523 \times 10^{-15}$ J.

Peeling of the spatula from the substrate for any given peeling angle can be divided into two phases. This can be illustrated with the help of Figure 4.7, where the evolution of the magnitude of the resultant pull-off force $F_{res} = \|\boldsymbol{F}_{res}\|$ and the dimensionless strain energy (see Eq. 2.7) with the magnitude of the applied displacement $\bar{u} = \|\bar{\boldsymbol{u}}\|$ for $\theta_p = 60°$ are shown[3]. The first phase begins from the point of zero pull-off force (denoted by "$\bar{u}_a$") and ends at the maximum value of the pull-off force (denoted by "$\bar{u}_c$"). The second phase is from "$\bar{u}_c$" to "$\bar{u}_e$", the point at which the spatula pad snaps-off from the substrate. Figure 4.8 shows the strip deformation at the displacements marked in Figure 4.7.

[3]In the following text, for simplicity, the quantities F_{res} and $\bar{u}$ are referred to as resultant pull-off force and applied displacement, respectively.

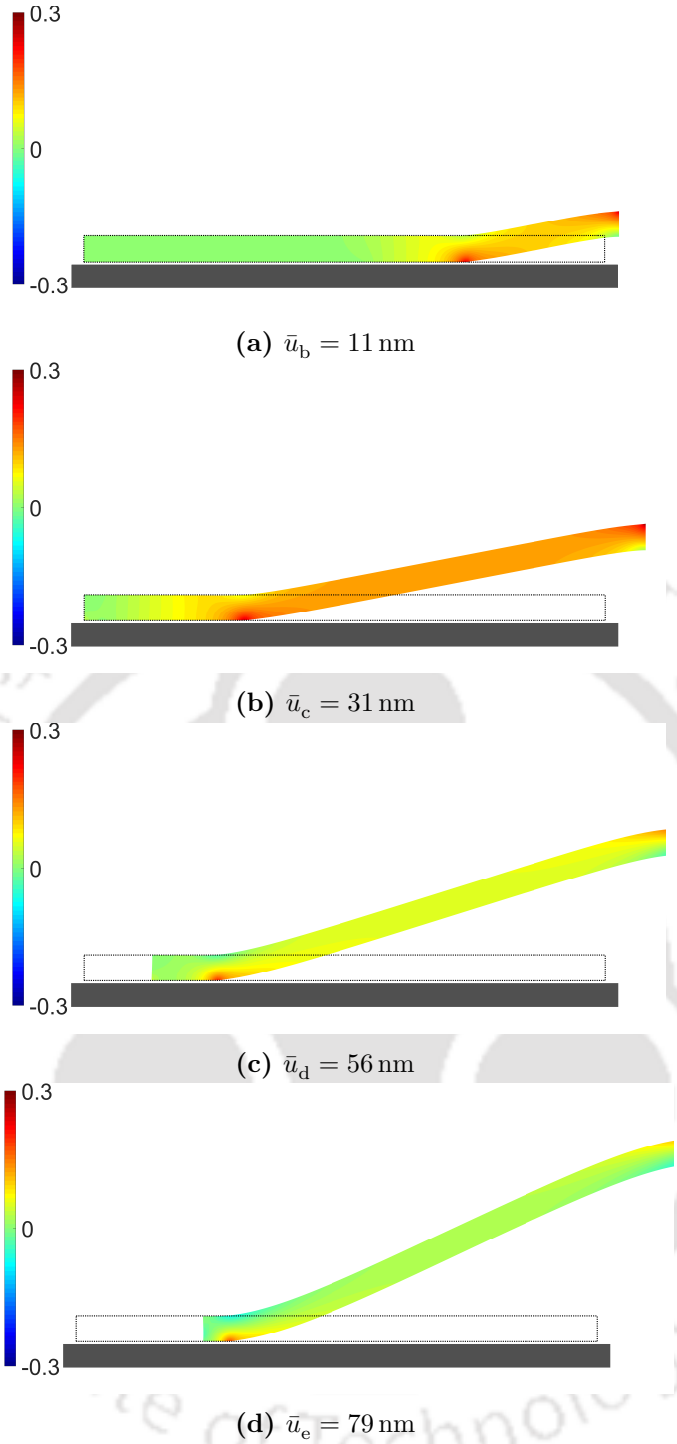

Figure 4.8: Deformed configurations of the spatula for peeling angle $\theta_p = 60°$ at the applied displacements $\bar{u}$ marked in Figure 4.7 ($\bar{u}_b$ to $\bar{u}_e$). The spatula remains in partial sticking contact until $\bar{u}_c$, beyond which full sliding ensues. The colourbar shows the normalised stresses $I_1/E_0 = \text{tr}(\boldsymbol{\sigma})/E_0$.

In the first phase, the spatula remains in partial sticking contact and is being continuously stretched while peeling (Figures 4.8a and 4.8b). Moreover, in this phase, a part of the spatula pad behind the peeling front, that is still in contact, starts sliding as the spatula is pulled by the applied displacement. However, the

rest of the spatula pad remains in sticking contact. This leads to stretching of the spatula, resulting in an increase in the stored strain energy of the spatula as shown in Figure 4.7. As a result, the force required to peel-off the spatula from the substrate increases. After reaching the force maximum at $\bar{u}_c$, the spatula pad begins to fully slide on the substrate as it is peeled off (Figures 4.8c and 4.8d). In this second phase, the strain energy that has been stored during the first phase is gradually released (see Figure 4.7). As the displacement is applied beyond "$\bar{u}_e$" the remaining part of the spatula pad immediately snaps-off from the surface releasing all the stored strain energy. At point "$\bar{u}_f$" the spatula is completely peeled off the surface.

4.3.1 Pull-off forces

This section[4] presents a detailed discussion on the influence of various parameters on the spatula pull-off forces. Further, easy detachment of the spatula via vertical pulling is also discussed.

4.3.1a Influence of the peeling angle

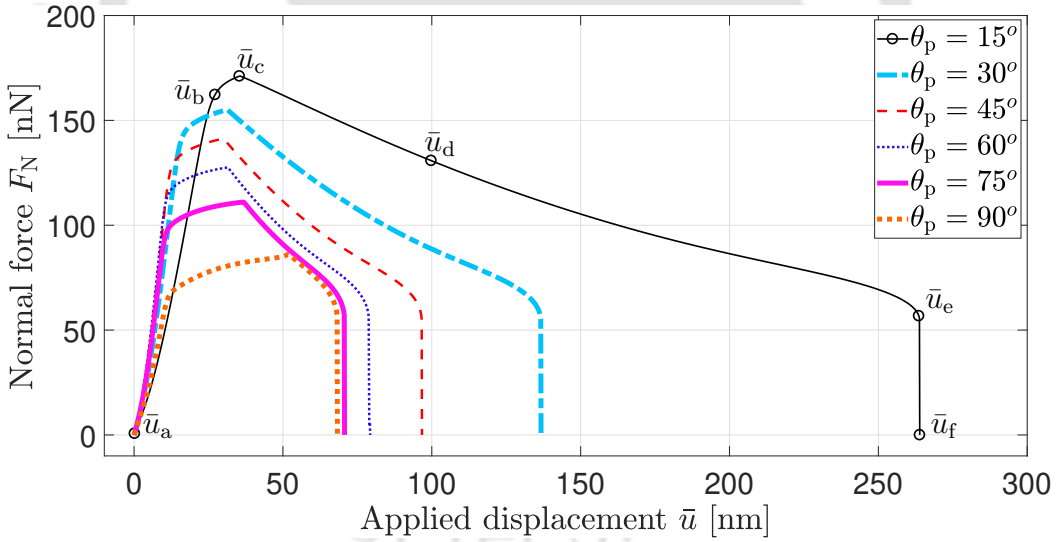

Figure 4.9: Evolution of the normal pull-off force F_N with the applied displacement $\bar{u}$ for different peeling angles θ_p. "Type I" peeling. Here, the marked points $\bar{u}_a$ to $\bar{u}_f$ on the $\theta_p = 15°$ curve are analogous to those in Figure 4.7.

Evolution of the normal (F_N) and tangential (F_T) (which is equal to the interfacial friction force F_f) components of the pull-off force with the applied displacement $\bar{u}$ from initial configuration is shown in Figures 4.9 and 4.10. For all cases, both the normal and the tangential pull-off force increase up to a maximum value and

[4] A version of the results in this section, except for section 4.3.1f, are published in The Journal of Adhesion and can be found at https://doi.org/10.1080/00218464.2020.1719838

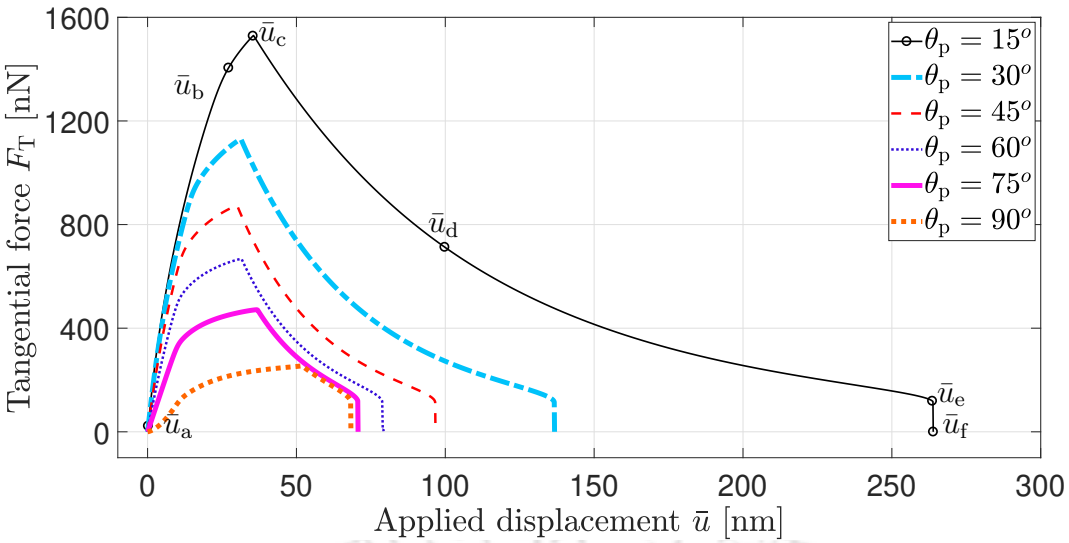

Figure 4.10: Evolution of the tangential pull-off force F_T with the applied displacement $\bar{u}$ for different peeling angles θ_p. "Type I" peeling. Here, the marked points $\bar{u}_a$ to $\bar{u}_f$ on the $\theta_p = 15°$ curve are analogous to those in Figure 4.7.

then decrease after that. Further, this maximum value decreases with increasing peeling angle. This can also be seen from Figure 4.11, where the maximum values of the normal component F_N, tangential component F_T, and the resultant pull-off force F_{res} (occurring at "$\bar{u}_c$" in Figure 4.7) for different peeling angles are plotted. These results show that the friction force is the major contributor to the total force generated by the spatula. Further, the friction force increases more rapidly than the adhesion force as the peeling angle decreases. By decreasing the peeling angle from 90° to 10°, the adhesion force increases by a factor of two, whereas the friction force increases almost by a factor of seven. The maximum normal (F_N^{max}) and frictional force (F_T^{max}) values of approximately 174 nN and 1723 nN, respectively, are observed for $\theta_p = 10°$.

As discussed at the beginning of the section 4.3, in the first phase, the spatula is stretched as it is peeled off the substrate due to partial sticking/sliding in the peeling zone, which increases the strain energy. This increase in strain energy is much higher for low peeling angles as compared to high peeling angles as observed from Figure 4.12, where the evolution of dimensionless strain energy with the applied displacement $\bar{u}$ is plotted for different peeling angles. From these results combined with those in Figures 4.9, 4.10, and 4.11, it can be stated that the stretching of the spatula due to partial sliding close to the peel front leads to the increase in pull-off forces at small peeling angles. These results confirm the hypothesis of Labonte and Federle [51] that the partial sliding of the attached spatula pad could be one of the reasons for increased pull-off forces at small peeling angles. It should be noted that the curves for $\theta_p = 90°$ in all these figures, as discussed in section 4.2.1, corresponds to *tangentially-constrained* peeling. This results in the generation of considerable

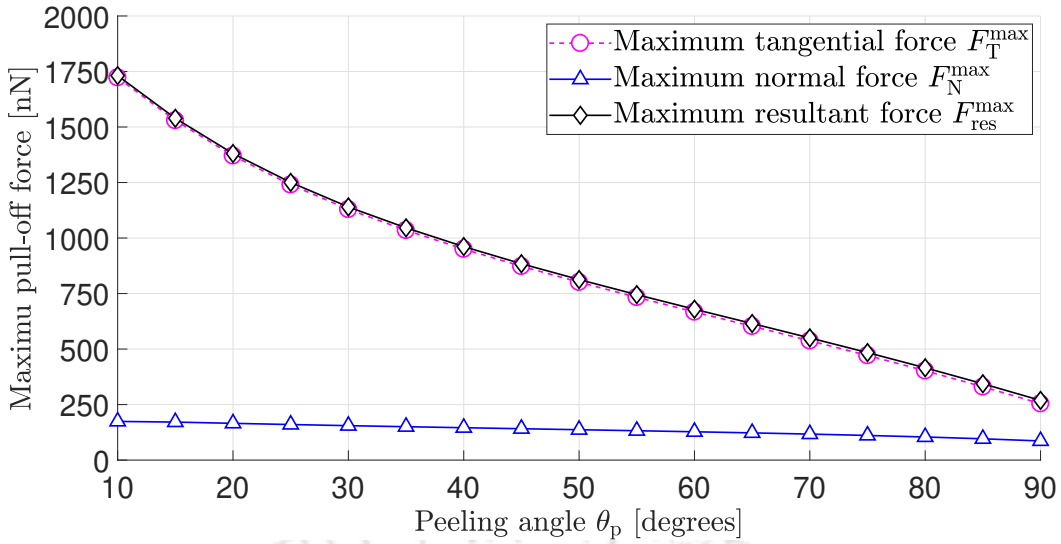

Figure 4.11: Evolution of the maximum pull-off force with peeling angle θ_{p} for "Type I" peeling.

friction forces. Hence, this is not equivalent to pulling the strip with a force acting perpendicular to the substrate, i.e. $\alpha = 90°$, which implies zero friction forces.

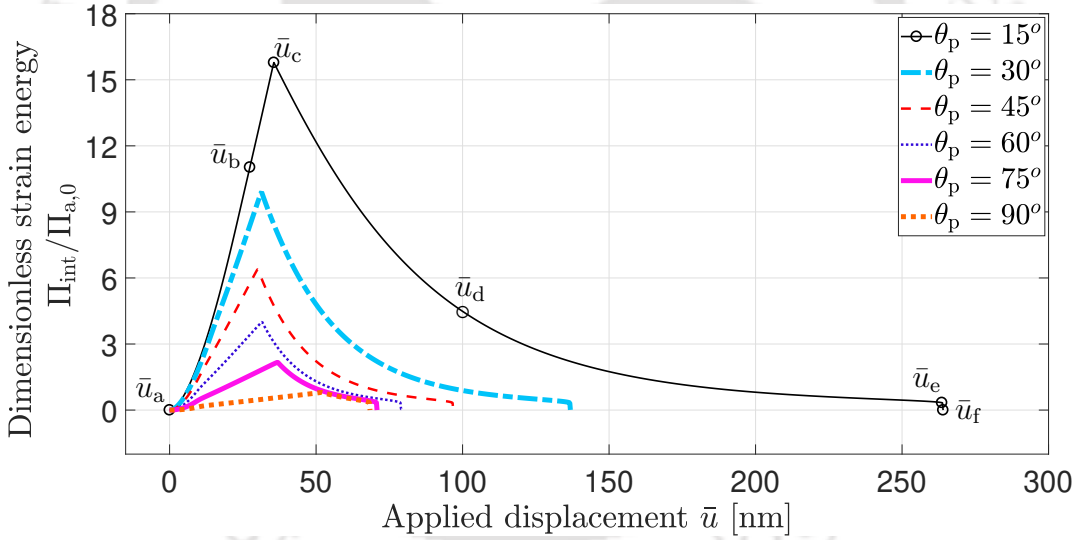

Figure 4.12: Evolution of the dimensionless strain energy with the applied displacement $\bar{u}$ for different peeling angles θ_{p} ("Type I" peeling). The points $\bar{u}_{\mathrm{a}}$ to $\bar{u}_{\mathrm{f}}$ for the $\theta_{\mathrm{p}} = 15°$ are analogous to those discussed in Figure 4.7. Here, $\Pi_{\mathrm{a},0} = 1.523 \times 10^{-15}$ J.

Figure 4.13 shows the evolution of normal (F_{N}) and tangential (F_{T}) forces up to the point of detachment $\bar{u}_{\mathrm{e}}$ for different peeling angles θ_{p}. As the spatula is peeled at higher angles, the so-called "adhesion region" [260], i.e. the range of the normal (F_{N}) and the tangential (F_{T}) pull-off forces throughout the peeling process up to $\bar{u}_{\mathrm{e}}$, decreases. In addition, for all the peeling angles, from the onset of sliding to detachment, i.e. from $\bar{u}_{\mathrm{c}}$ to $\bar{u}_{\mathrm{e}}$, the spatula follows a similar peeling path. But the maximum force values reached ($\bar{u}_{\mathrm{c}}$) decrease with increasing θ_{p}, while they remain

the same at the point of detachment ($\bar{u}_e$). Further, the spatulae store more strain energy when peeled at small angles and high pull-off forces are reached. Then, it can be understood that the spatula can remain attached at higher values of normal and tangential forces. However, at high peeling angles, the adhesion region is very small and thus detachment of the spatula can be easily accomplished. These observations are similar to the conclusions drawn by Hu and Greaney [260] and Sekiguchi et al. [261] in their respective experimental and analytical studies on setae inclined at different angles.

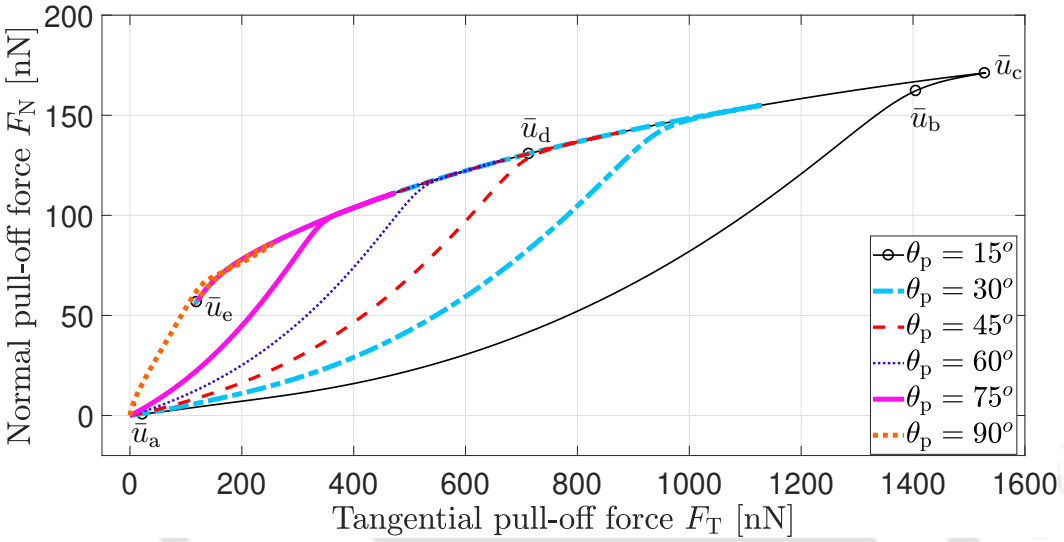

Figure 4.13: Evolution of the normal F_N and the tangential F_T pull-off forces for different peeling angles θ_p ("Type I" peeling).

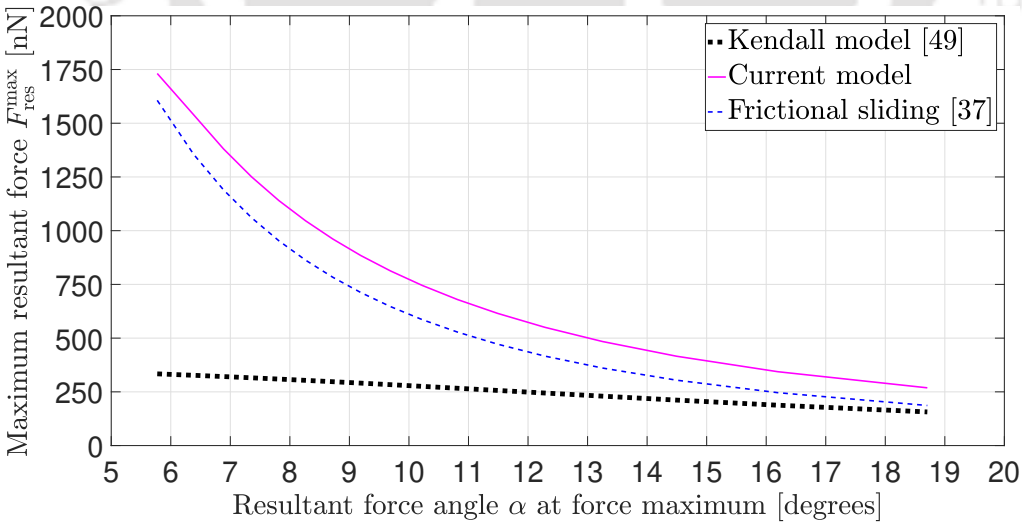

Figure 4.14: Comparison of different peeling models.

Dependency of the maximum pull-off force on the corresponding force angle α (at "$\bar{u}_c$" in Figure 4.7) as obtained by the current model is compared with that of Kendall's peeling model [49] and the frictional sliding model of [37] in Figure 4.14.

The latter model is identical to the frictional sliding model of Begley et al. [107]. The current model predicts a similar trend as that of the other two models: the pull-off force is high for very low force angles and rapidly decreases as the force angle is increased. This behaviour is also consistent with experimental observations and other analytical models [51, 99, 103, 201]. However, the current coupled adhesion-friction model predicts larger pull-off forces than those of Kendall's [49] and the frictional sliding model of Jagota and Hui [37]. Both the current model and Jagota and Hui's [37] model incorporate the influence of the frictional sliding of the spatula. As such, both models predict larger pull-off forces than the Kendall peeling model [49]. Further, the current adhesive-friction model also includes the influence of the non-zero bending stiffness of the spatula[5], which is absent in the peeling model of Jagota and Hui [37]. Also, as α increases, all the three curves approach each other. However, even for vertical pulling i.e. $\alpha = 90°$, the effect of non-zero bending stiffness still contributes to slightly larger pull-off forces and is discussed in section 4.3.1g.

4.3.1b Influence of the shaft angle

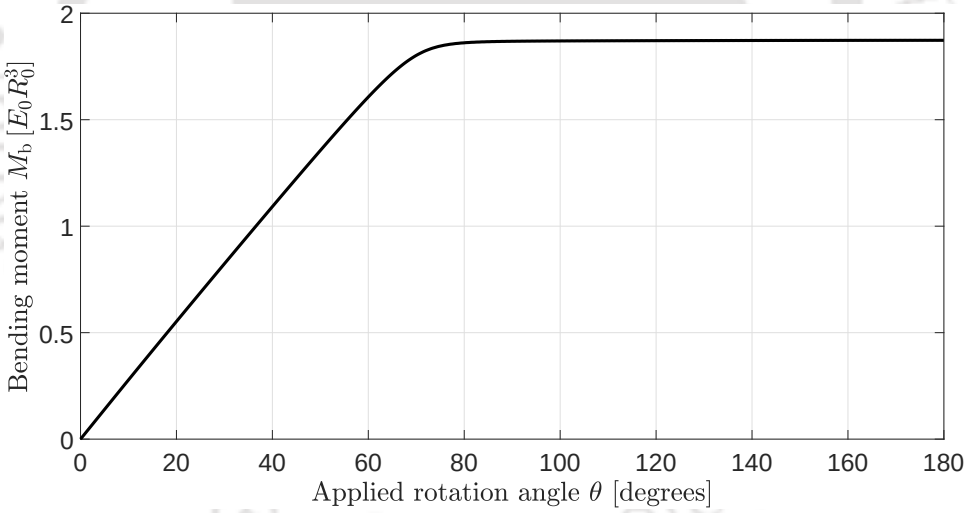

Figure 4.15: Evolution of the bending moment M_b with the applied rotation $\theta = \theta_{sh}$. Here, $E_0R_0^3 = 2\,\text{nN·nm}$.

In order to understand the influence of the shaft angle θ_{sh} on the pull-off forces, it is varied for a given peeling angle θ_p. This is achieved by first applying the rotation angle θ_{sh} at the right end of the strip (CD), and then applying the displacement $\bar{u}$ to that end at an angle θ_p, see Figure 4.6b.

Figure 4.15 shows the evolution of bending moment M_b that is required to achieve the desired shaft angle $\theta = \theta_{sh}$. These results show that this bending

[5]The non-zero bending stiffness implies a bending moment at end CD.

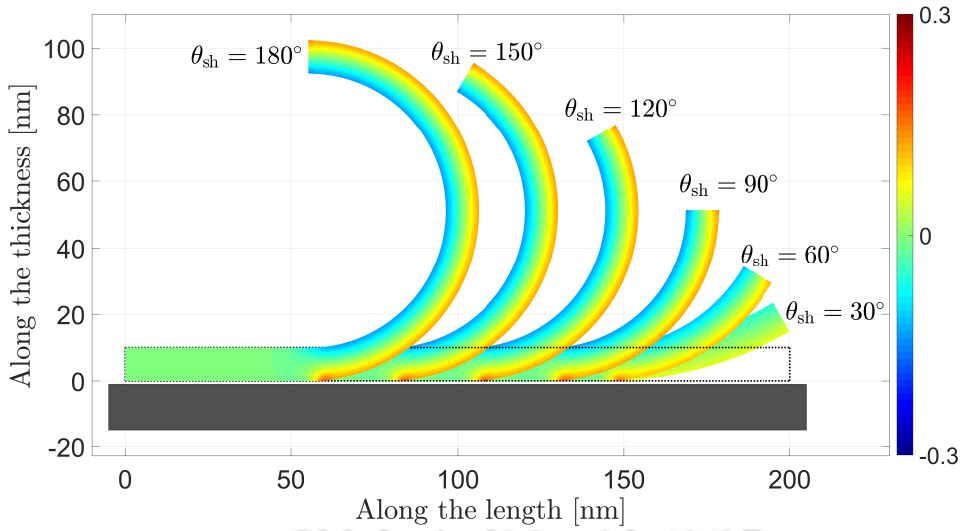

Figure 4.16: Deformed configurations of the strip for various rotation angles. The colourbar shows the normalised stresses $I_1/E_0 = \mathrm{tr}(\boldsymbol{\sigma})/E_0$.

moment reaches a constant value after a certain angle. The deformed configuration of the strip at different shaft angles is shown in Figure 4.16.

Once the desired spatula shaft angle is obtained, the spatula is peeled-off by applying a displacement at a peeling angle of $\theta_p = 90°$. This corresponds to the "Type II" peeling described in section 4.2.1. Figure 4.17 depicts variation of the resultant pull-off forces for various spatula shaft angles. For a given peeling angle θ_p, the pull-off forces are observed to decrease as the spatula shaft angle increases. This is due to the fact that as the shaft angle increases, the spatula pad area that is still in contact with the substrate decreases as shown in Figure 4.16. As a result, the force that is required to detach the spatula from the substrate reduces. Also, the influence of the shaft angle is more pronounced for $\theta_{sh} > 60°$, as the maximum force reached decreases more rapidly. This can also be understood by examining the deformed configurations in Figure 4.16. Here, it is clear that there is not much change in the spatula pad area for small shaft angles. It is only after $\theta_{sh} > 60°$ that the spatula pad area still-in-contact reduces more rapidly.

Similar results are observed for "Type III" peeling as illustrated in Figure 4.18. Comparison of these results with the maximum values for "Type I" peeling shown in Figure 4.11 indicates that for the same peeling angle $\theta_p = 15°$, just be changing the shaft angle from $\theta_{sh} = 0°$ to 15°, the maximum resultant pull-off force decreased by 20%. This reduction is even higher ($\approx 30\%$) when the shaft angle is changed from $\theta_{sh} = 0°$ to 30° for the same peeling angle of $\theta_p = 30°$. This demonstrates the importance of inclination of the spatulae shafts for increasing and decreasing the clinging forces generated by a gecko for its rapid locomotion.

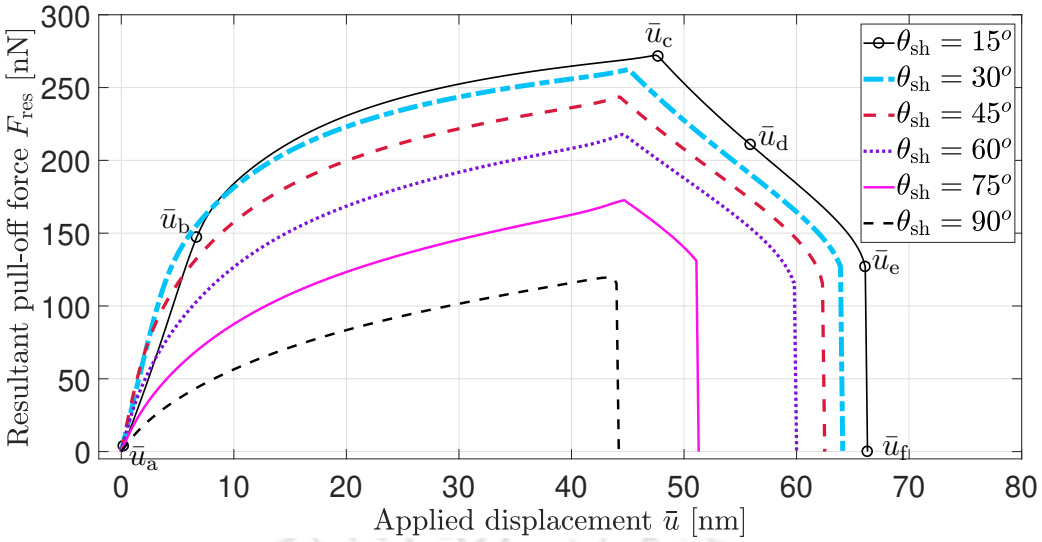

Figure 4.17: Evolution of the resultant pull-off force F_{res} with the applied displacement $\bar{u}$ for different shaft angles θ_{sh} and peeling angle $\theta_p = 90°$ ("Type II" peeling). The points $\bar{u}_a$ to $\bar{u}_f$ for the $\theta_{sh} = 15°$ are analogous to those discussed in Figure 4.7.

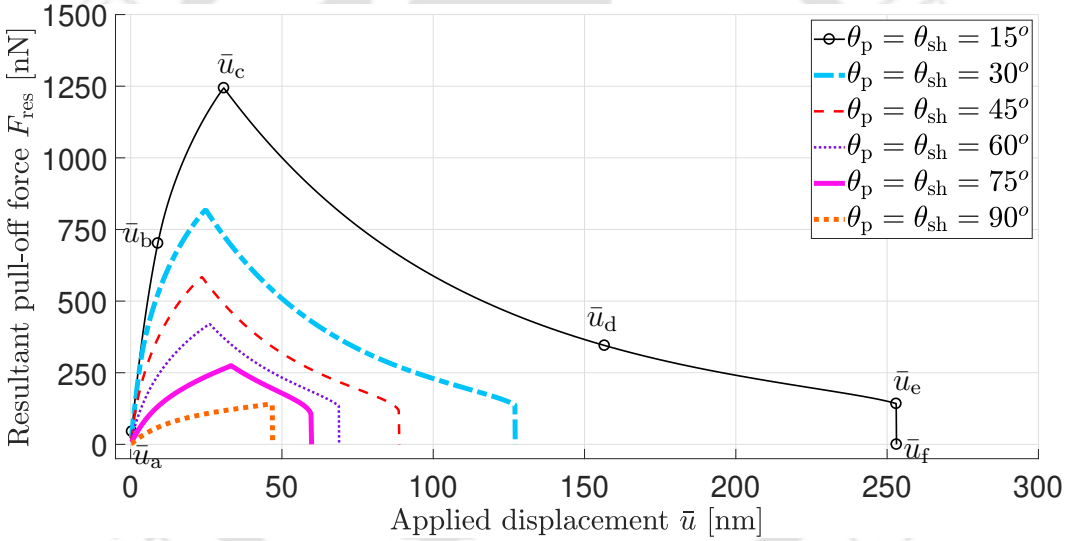

Figure 4.18: Evolution of the resultant pull-off force F_{res} with the applied displacement $\bar{u}$ for different peeling and shaft angles $\theta_p = \theta_{sh}$ ("Type III" peeling). The points $\bar{u}_a$ to $\bar{u}_f$ for the $\theta_p = \theta_{sh} = 15°$ are analogous to those discussed in Figure 4.7

4.3.1c Estimation of the pull-off force at seta level

Although there have been no direct measurements of friction as well as normal forces at the spatula level for different peeling angles in the literature, Autumn et al. [1, 39] observed a maximum friction force of approximately 200 µN and a maximum normal force of $20 - 40$ nN for a single seta. Taking the number of spatulae per seta to be $100 - 1000$ [99], the maximum friction and normal forces for a single spatula are estimated to be $200 - 2000$ nN and $20 - 400$ nN, respectively. The values, 1723 and 174 nN obtained here (see Figure 4.11), fit well within these ranges.

At first, these maximum friction and adhesion forces obtained here might appear to be an overestimation when summed over the maximum limit of 1000 spatulae per seta. However, Figure 4.14 shows that these values correspond to a very low force angle $\alpha = 5.77°$. Tian et al. [99] calculated a maximum friction force of 900 nN at a resultant force angle close to $\alpha = 8°$. The corresponding friction force obtained in the current work is 1139 nN. The difference between these observations can be attributed to the fact that in case of Tian et al. [99], the strip thickness is $h = 5$ nm and the friction coefficient $\mu_s = 0.2$. Whereas, the current results are for $h = 10$ nm and $\mu_s = 0.3$ and both of these parameters influence the pull-off forces. This is discussed in detail in section 4.3.1d.

Moreover, when a seta attaches to a substrate after a perpendicular preload and parallel drag [1], it is not clear as to whether all the spatulae adhere to the surface or not. It is also doubtful that all the spatulae reach their force maximum at the same time. In the experiments of Huber et al. [66] with a seta with only four spatulae at its end, most of the time, only one or two of the spatulae adhered to the substrate. This shows that not all the spatulae adhere even after a considerable parallel drag of the seta. This behaviour was also observed at the animal level by Eason et al. [201], who measured the stress distribution and contact area on the toes of geckos. They observed that the stress distribution is non-uniform owing to the fact that a significant portion of the setal arrays on the gecko toes did not adhere to the substrate. Further, as estimated by Autumn et al. [158], for a seta to generate 200 µN force, the seta contact area must increase from 6% to 46%. This clearly shows that even at peak adhesion and friction, not even half of the seta area is in contact, which implies that not all the spatulae are in contact. Moreover, even if all the spatulae are in contact with the substrate, it is not clear at what angles spatulae shafts are inclined and at what angles they experience pull-off forces. As shown in section 4.3.1b, the shaft angle significantly affects the maximum pull-off forces reached during peeling.

Based on the setal density and branching characteristics, it is estimated that there are around 512 spatulae per seta [262]. To get an estimate of the total friction force per seta, two different spatula distributions are considered here. In the first distribution (Figure 4.19a), spatulae follow a normal distribution and experience the applied displacement $\bar{u}$ at a mean angle of $\theta_p = 50°$. By summing the maximum frictional forces per spatula at different peeling angles obtained in section 4.3.1a for this distribution, a total friction force of 422 µN per seta is obtained. Similarly, for the distribution in Figure 4.19b, in which 60% of total spatulae experience the applied displacement $\bar{u}$ at angles $\leq 30°$, the total friction force per seta is equal to 606 µN. However, these values correspond to the case when all the spatula are initially lying flat on the substrate i.e. $\theta_{sh} = 0°$ and experiencing forces at very low

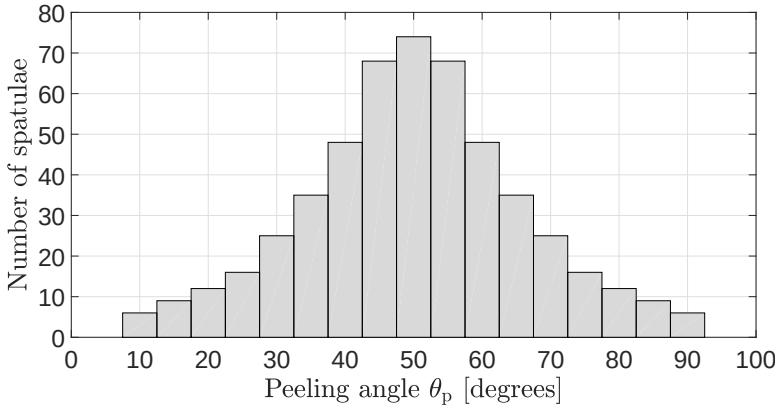

(a) Normal distribution

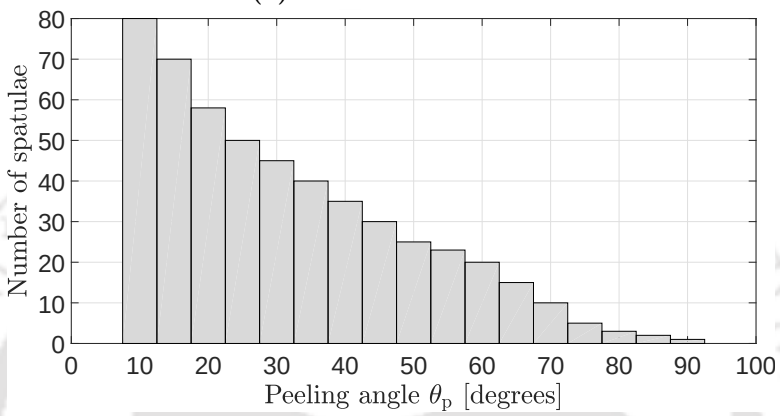

(b) Skewed distribution

Figure 4.19: Assumed spatula distributions for different peeling angles.

angles $\alpha = 5° - 20°$. But, it is shown in section 4.3.1b that the pull-off forces are also affected by the angle at which the spatula shafts are inclined to the substrate. Changing the shaft angle from 0° to 90° at constant peeling angle of $\theta_p = 90°$, decreases the pull-off forces by as much as 2.5 times. Moreover, the probability of the configuration of $\theta_{sh} = 0°$ is low as that could lead to crowding of the spatulae, i.e. the spatulae start to touch their neighbours and limit the adhesion. The setal shafts in their natural state are curved and are inclined to at an angle of 43° to the horizontal. When they deform and adhere to the substrate, the crowding model of Pesika et al. [263] showed that as their inclination decreases below 27.8° the setae in an array start to crowd and this impacts the clinging force generated by them. A critical tilt angle of 12.6° is reported by Pesika et al. [263], which limits maximum achievable adhesion. As the gecko adhesive pads are of hierarchical nature with structures in each level influencing the structures above and below them, it is reasonable to infer that a limiting tilt angle at the seta level also limits the spatula shaft angle. This, as shown in section 4.3.1b significantly influences the adhesion and friction forces generated. Hence, it is reasonable to conclude that the maximum frictional force of 200 µN measured by Autumn et al. [1] has to be understood as the summation of all the spatulae interactions accounting for different spatulae inclinations and pulling

angles. However, as pointed out by Puthoff et al. [262], it should be noted that the spatula distribution and the pull-off forces follow more sophisticated statistical principles than the rough estimates considered here. Hence, it can be concluded that any multiscale peeling model for gecko adhesion should consider the different spatula peeling and shaft angle distributions based on statistical principles.

4.3.1d Influence of the spatula pad thickness

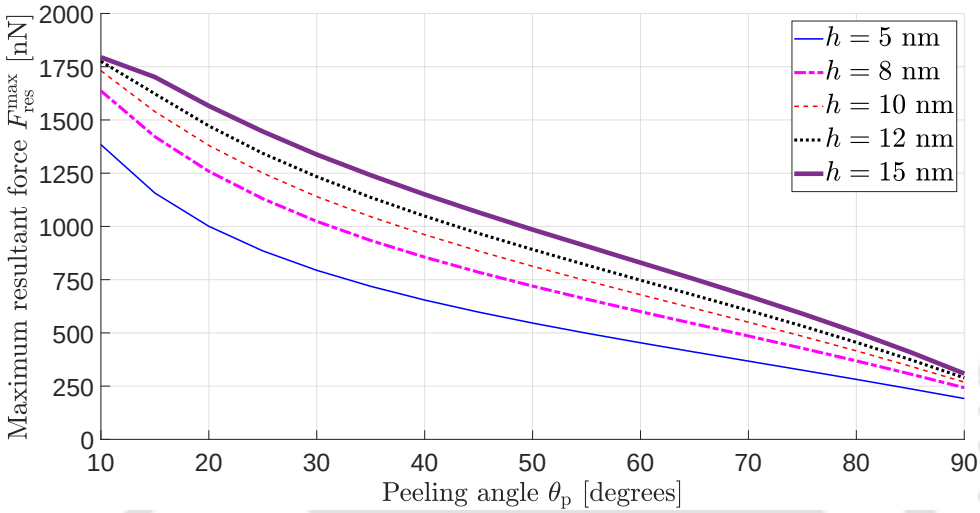

Figure 4.20: Evolution of the maximum resultant pull-off force F_{res}^{max} with the peeling angle θ_p for different pad thicknesses ("Type I" peeling).

In this section the influence of bending stiffness on the pull-off forces is studied by varying the spatula pad thickness h. Figure 4.20 shows the influence of the spatula pad thickness h on the variation of the maximum resultant pull-off forces with peeling angle θ_p. As the thickness increases, the maximum pull-off force achieved during the peeling increases. As the thickness increases, the bending stiffness of the spatula increases and a higher force is needed to peel the spatula from the substrate. However, as observed from Figure 4.20, this increase in the pull-off force is more significant for low h than for high h. This is clear from the fact that the minimum increase in the pull-off force for $h = 5$ to $h = 10$ nm is equal to 25%, whereas the maximum increase in pull-off force is only 22% for the increase $h = 10$ to $h = 15$ nm. At first, this increase in adhesion with spatula thickness might lead us to conclude that a large thickness is preferred. Geckos generate a large amount of friction and adhesion by increasing the area of contact with the help of the large number of thin spatulae. Although increasing the spatula thickness generates more adhesive forces, it also increases the volume (and mass) of the gecko body faster than the increase in the surface area [68], which for a dynamic species like gecko is undesirable. Rizzo et al. [74], in their investigation of the gecko spatula with an electron microscope, observed that the thickness of the gecko spatula pad is only

$5-10\,\text{nm}$. It has also been suggested by Persson and Gorb [68] that the spatula pad thickness needs to be approximately $5-10\,\text{nm}$, in order for it to be compliant enough to adhere to a variety of substrates which in nature are mostly rough. Moreover, as the bending stiffness scales as the third power of the thickness, a thicker spatula would be undesirable as it increases the effective modulus of the setal arrays, which as shown by Autumn et al. [158] is around 110 kPa in order to meet the Dahlquist criterion [157] for tackiness.

4.3.1e Influence of the material stiffness

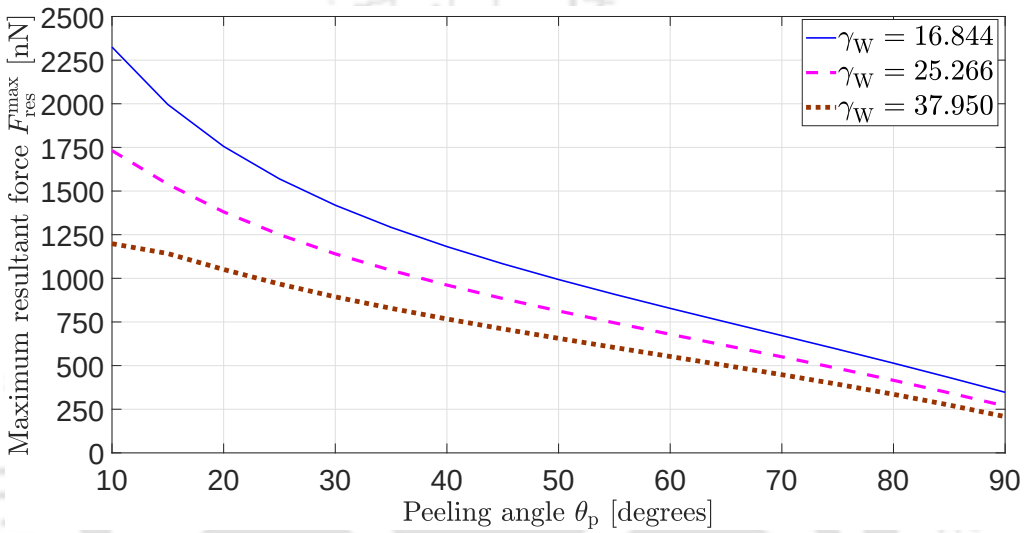

Figure 4.21: Evolution of the maximum resultant pull-off force $F_{\text{res}}^{\text{max}}$ with the peeling angle θ_{p} for different material stiffness ("Type I" peeling).

In this section, the influence of bending stiffness on the pull-off forces is studied by varying the material stiffness E_0 (via material paramter γ_{W}).

Geckos inhabit a wide range of environments such as tropics, urban, and deserts. As such, they have to endure changes in geographical and atmospheric conditions such as the temperature, wetness, and relative humidity (moisture) [264]. It has been experimentally observed that the humidity greatly affects the mechanical properties of gecko setae [58, 59, 264]. Prowse et al. [59] observed that at 80% relative humidity (RH), the complex elastic modulus E^*[6] of a single gecko decreased to one-third of its value at dry conditions. The elastic modulus E_0 has been found to decrease by a factor of 1.73 when RH increased from 30% to 80% i.e. the seta material becomes softer. This has been observed to affect the adhesion capabilities of the geckos [58]. Hence, it would be helpful to study how these changes in mechanical properties affect the adhesion behaviour using the current computational model.

[6] $|E^*| = \sqrt{(E')^2 + (E'')^2}$, where E' and E'' denote the storage and loss moduli, respectively.

Variation of the maximum resultant pull-off force with peeling angle θ_p for different values of material stiffness E_0 is shown in Figure 4.21. This is achieved by changing the material parameter γ_W. From the definition in Eq. (2.40),

$$\gamma_W := \frac{E_0}{\left(\frac{A_H}{2\pi r_0^3}\right)}, \tag{4.3}$$

it follows that an increase in γ_W corresponds to an increase in the material stiffness. As the material stiffness decreases, the pull-off force increases as seen from Figure 4.21. This is due to the fact that as the stiffness decreases, the spatula becomes more compliant and adheres to the substrate more readily. This is illustrated in Figure 4.22, which shows that at a given shaft angle of $\theta_{sh} = 90°$, the strip with lower material stiffness has more pad area that is still in contact with the substrate. Moreover, the stress developed at the peeling front increases as the material stiffness decreases. As such, even though compliant material can generate more adhesion and friction force, accumulation of high stresses in the peeling zone could potentially lead to failure of the material. These results can also be considered from the point of adhesion strength as increase in γ_W corresponds to decrease in the adhesion strength. This decrease in adhesion strength results in lower pull-off forces. The current results allow for a better insight into this complex system, which in turn allows for designing better gecko inspired synthetic adhesives.

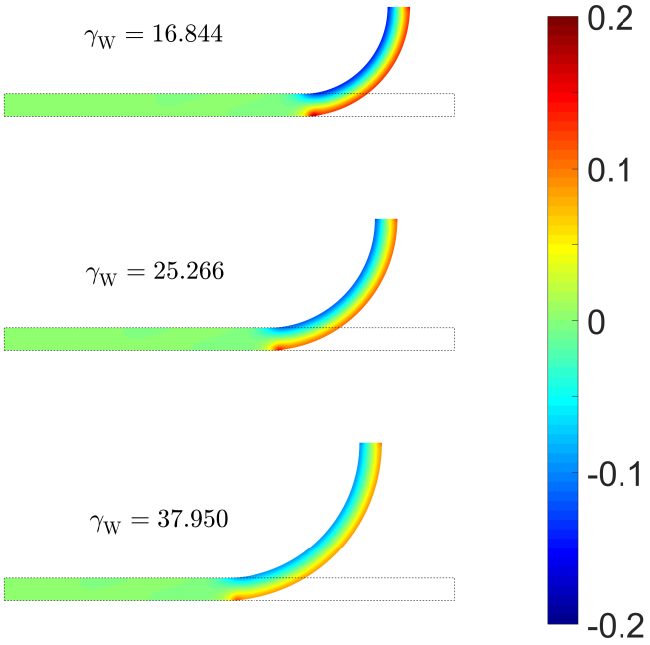

Figure 4.22: Deformation and stress for different material stiffnesses for a rotated configuration of $\theta_{sh} = 90°$. The colourbar shows the normalised stresses $I_1/E_0 = \mathrm{tr}(\boldsymbol{\sigma})/E_0$.

4.3.1f Influence of the friction coefficient

The friction coefficient between two surfaces is one of the key parameters in determining the interfacial contact and locomotion behaviour. Figure 4.23 shows the influence of the friction coefficient μ_s on variation of the maximum resultant pull-off forces F_{res}^{max} with the peeling angle θ_p. The current model predicts that as the friction coefficient decreases, the maximum pull-off forces achieved at any given peeling angle decreases, which is consistent with the known behaviour of dry friction phenomenon. Further, at high peeling angles, the relative influence of the friction coefficient diminishes, and the pull-off forces vary only slightly with the friction coefficient. From these results it can be understood that the friction forces, which are dominant at low angles, increase with increasing friction coefficient. This aids the gecko in achieving much better grip. At the same time, at high angles, this relatively low change in the pull-off force works in favour of the gecko to detach from any kind of surface more easily just by changing the angle of the resultant pull-off force. Interestingly, as the friction coefficient decreases, at low peeling angles, the maximum pull-off force seems to be independent of the peeling angle. For $\mu_s = 0.1$, the maximum pull-off force remains constant for peeling angles $\theta_p \leq 30°$.

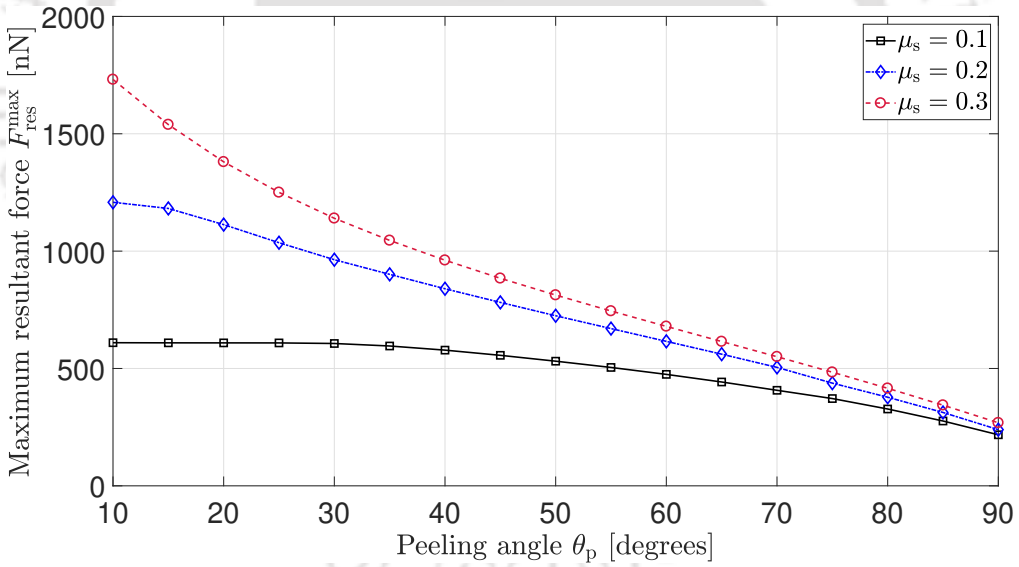

Figure 4.23: Evolution of the maximum resultant pull-off force F_{res}^{max} with the peeling angle θ_p for different friction coefficients μ_s ("Type I" peeling).

4.3.1g Vertical pulling and spatula detachment

Despite generating high attachment forces, geckos can detach from a substrate in just 20 ms and with very small force [265]. However, for the case of *tangentially-constrained* peeling discussed so far, at the point of detachment (shown by "$\bar{u}_e$" in Figure 4.7) the pull-off forces are still quite high (see Figures 4.9 and 4.10). As

such, in order to facilitate quick detachment with small force, the frictional forces should vanish. This can be achieved through *tangentially-free* peeling as described in section 4.2.1. As the spatula is pulled perpendicular to the substrate, this type of peeling is referred to as "vertical pulling" here.

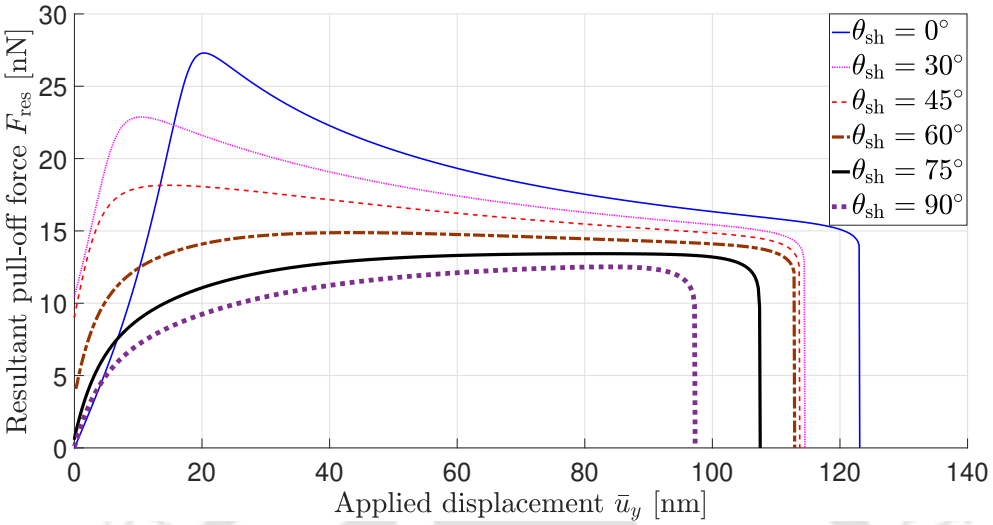

Figure 4.24: Evolution of the resultant pull-off force $F_{res} = F_N$ with the applied displacement $\bar{u}_y = \|\bar{\boldsymbol{u}}_y\|$ for different shaft angles θ_{sh} for vertical pulling (where $F_T = 0$).

Evolution of the corresponding resultant forces with the applied vertical displacement $\bar{u}_y$ for various shaft angles θ_{sh} is plotted in Figure 4.24. For this case, the tangential forces are zero by design. Similar to the behaviour observed in section 4.3.1b for *tangentially-constrained* peeling, the maximum pull-off force reached decreases as the shaft angle increases. The maximum pull-off force is lowest for $\theta_{sh} = 90°$ and is equal to 12.62 nN. This value is close to the value of 10 nN observed by Huber et al. [66] in their experiments, where the spatulae shafts are inclined at 90° and are pulled vertically. This result is also within the range of $2 - 16$ nN obtained experimentally by Sun et al. [55] for vertical pulling of the spatula. These results also match well with the beam results of Sauer [165]. Therefore, gecko spatulae can detach with very small amount of force by changing the shaft angle θ_{sh} to 90° and then peel like a tape perpendicular to the substrate as shown in Figure 4.25.

It has been observed that during the attachment step, geckos perform a roll-in action to grip their toes when they adhere to a substrate and they peel off their toes while detaching (which is called "digital hyperextension") [39, 266]. The gripping action causes the setae to slide very slightly and brings the spatulae in contact with the substrate. At the same time, this gripping action also changes the angle between the setal shaft and the substrate, which in turn decreases the angle between the spatula shaft and the substrate [99]. This dragging at a low angle causes the spatulae to stretch [103, 145], increasing the stored strain energy (see Figures 4.7

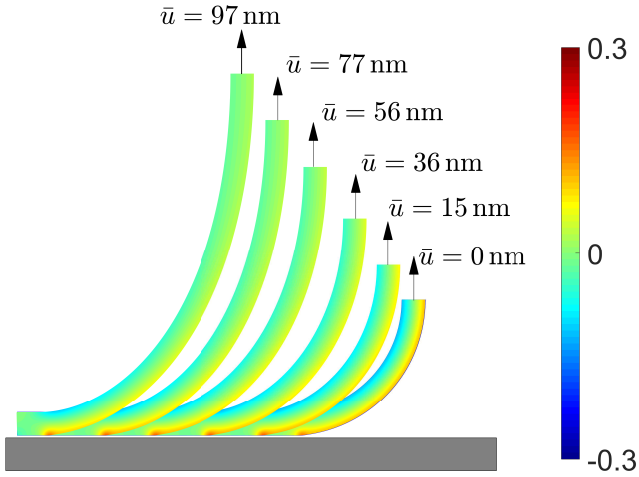

Figure 4.25: Deformed configurations of the strip for vertical pulling with $\theta_{\text{sh}} = 90°$ at various applied displacements $\bar{u}$. The colourbar shows the normalised stresses $I_1/E_0 = \text{tr}(\boldsymbol{\sigma})/E_0$.

and 4.12). This corresponds to *tangentially-constrained* peeling: As shown in in the previous sections (see Figures 4.9 to 4.14) the spatulae stretch and very high maximum pull-off forces are reached at small resultant force angles. Similarly, when the gecko hyperextends its toes to disengage from the substrate, this action again changes the angle between the seta shaft and the substrate. Rolling out the toes results in a lever action of the setal shafts as described by Tian et al. [99]. Autumn et al. [48] observed that the seta spontaneously detaches from the substrate when the angle between seta shaft and the substrate increases above 30°. At the spatula level, these actions increase the angle between the spatula shaft and the substrate to 90° and one by one each spatula disengages from the substrate. This spatula disengagement corresponds to *tangentially-free* peeling: As seen from the results in Figure 4.24 this action requires very small amount of force.

4.3.2 Critical detachment angle

This section[7] discusses presence of the critical detachment angle at the spatula level in the hierarchy of the gecko adhesion system. Influence of various parameters on the critical detachment angle is also discussed.

Autumn et al. [48] observed that irrespective of the applied load, at each level in the hierarchy of the gecko adhesive system, down to the setae, the structures detach from the substrate when the angle between the resultant force vector and

[7] A version of the results of this section are published in The Journal of Adhesion and can be found at https://doi.org/10.1080/00218464.2020.1746652

the substrate α, equals the critical detachment angle α^*. This critical detachment angle varies among setae ($\alpha^*_{\text{seta}} = 30°$), seta arrays ($\alpha^*_{\text{array}} = 24.6 \pm 0.9°$), and toes ($\alpha^*_{\text{toe}} = 25.5 \pm 0.2°$). However, since no experiments have been performed for the spatula, it is not clear if similar values are found at the spatula level. As such, in this section, presence of critical detachment angle at the spatula level in the hierarchy of gecko adhesive structures is examined.

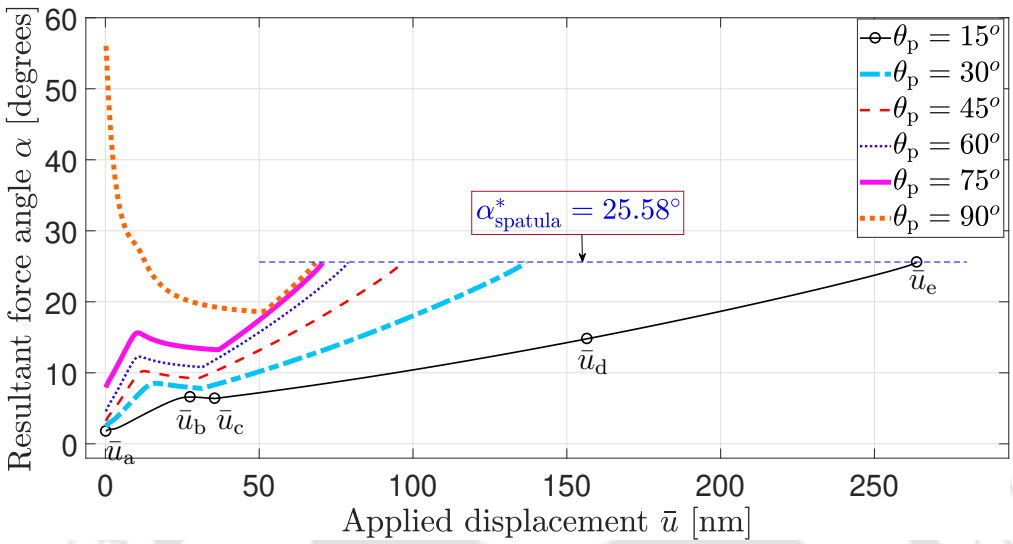

Figure 4.26: Evolution of the resultant force angle α with the applied displacement $\bar{u}$ for different peeling angles θ_p ("Type I" peeling). At detachment (point $\bar{u}_e$) the common value $\alpha^*_{\text{spatula}} = 25.58°$ is observed. The points $\bar{u}_a$ to $\bar{u}_e$ for the $\theta_p = 15°$ are analogous to those discussed in Figure 4.7.

Figure 4.26 shows the resultant force angle α with the applied displacement $\bar{u}$ for different peeling angles θ_p. It can be seen that the resultant force angle changes throughout the peeling process. Except for $\theta_p = 90°$, the resultant force angle curves follow similar paths. This is illustrated with the help of the curve for $\theta_p = 15°$. The points $\bar{u}_a$ to $\bar{u}_e$ on this curve directly correspond to those in Figures 4.9, 4.10, and 4.12. The point $\bar{u}_f$ is not shown here as at this point, both the normal and tangential forces become zero. The resultant force angle α initially increases up to a point $\bar{u}_b$, which is when the pad (PQ in Figure 4.1) starts to detach from the substrate[8]. The resultant force angle then decreases until it reaches the point $\bar{u}_c$, which, as seen from Figures 4.9, 4.10, and 4.12, is the point where the pull-off forces and the strain energy reach their maximum values. Beyond the point $\bar{u}_c$, α increases monotonically until the critical point $\bar{u}_e$ which is the jump-off contact point. For the case of $\theta_p = 90°$, points $\bar{u}_a$ and $\bar{u}_b$ coincide as the spatula pad starts to peel off as soon as the displacement is applied. This can be clearly seen from the evolution of

[8]As the L-J potential is a continuously varying function, a cut-off criterion is assumed in the current study to define when spatula detachment starts. It is assumed that detachment has started, if at least one of the contact surface points is displaced such that the adhesive traction acting at that point becomes less than 95% of the maximum adhesive traction.

the dimensionless strain energy and the dimensionless adhesion energy for different peeling angles shown in Figure 4.27. For $\theta_p = 90°$, there is a sharp increase in the adhesion energy from its initial value $-\Pi_{a,0}$ (see Eq. 4.2).

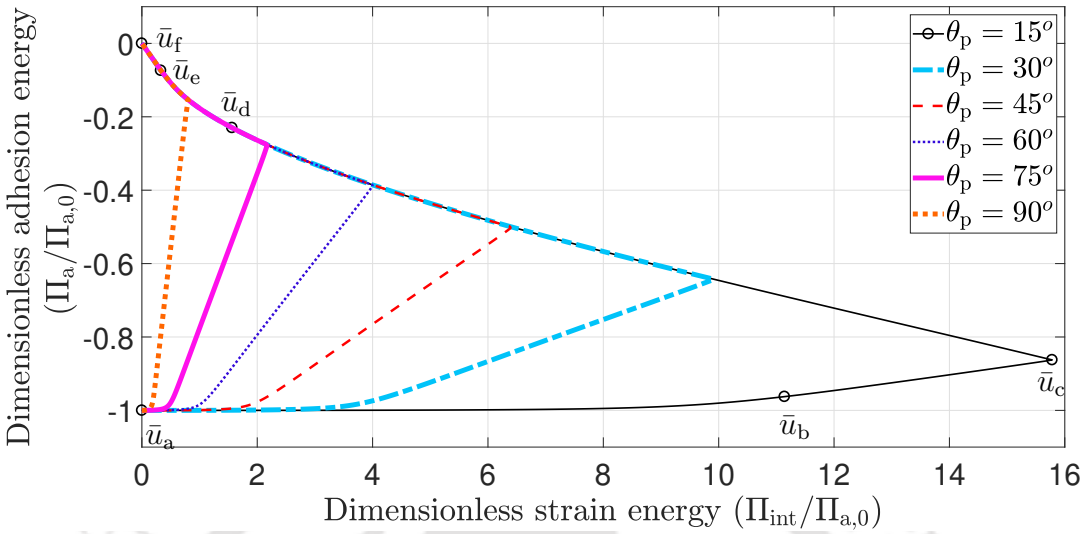

Figure 4.27: Evolution of the adhesion energy with the strain energy for different peeling angles θ_p ("Type I" peeling). Here, $\Pi_{a,0} = 1.523 \times 10^{-15}$ J. The points $\bar{u}_a$ to $\bar{u}_e$ for the $\theta_p = 15°$ are analogous to those discussed in Figure 4.7.

The most important observation from Figure 4.26 is that irrespective of the peeling angle θ_p, the spatula detaches from the substrate at a constant detachment angle of $\alpha^*_{spatula} = 25.58 \pm 0.07°$, even though α changes throughout the peeling process.

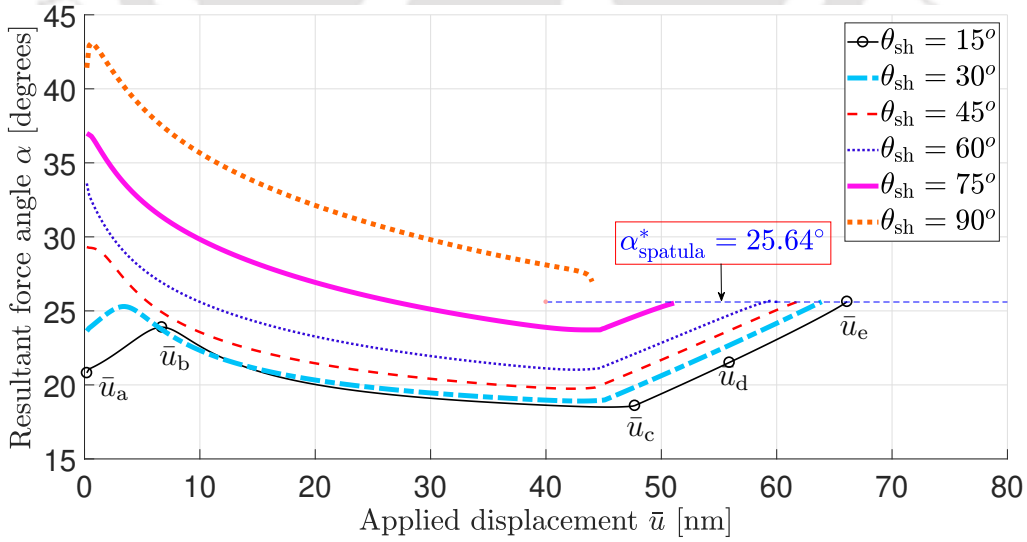

Figure 4.28: Evolution of the resultant force angle α with the applied displacement $\bar{u}$ for different shaft angles θ_{sh} and the peeling angle $\theta_p = 90°$ ("Type II" peeling). At detachment (point $\bar{u}_e$) the common value $\alpha^*_{spatula} = 25.64°$ is observed. The points $\bar{u}_a$ to $\bar{u}_e$ for the $\theta_p = 15°$ are analogous to those discussed in Figure 4.7.

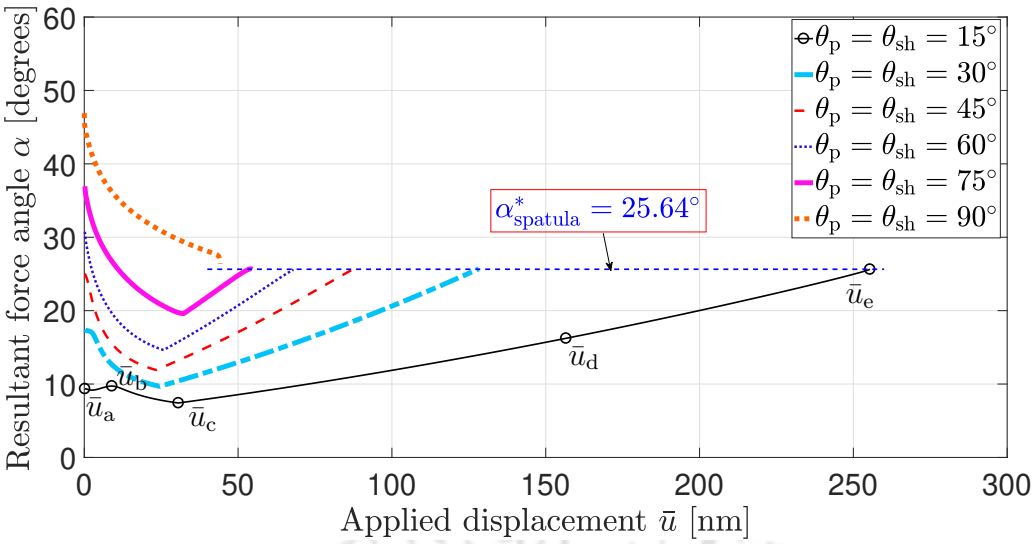

Figure 4.29: Evolution of the resultant force angle α with the applied displacement $\bar{u}$ for different peeling and shaft angles $\theta_p = \theta_{sh}$ ("Type III" peeling). At detachment (point $\bar{u}_e$) the common value $\alpha^*_{spatula} = 25.64°$ is observed. The points $\bar{u}_a$ to $\bar{u}_e$ for the $\theta_p = 15°$ are analogous to those discussed in Figure 4.7.

Similar behaviour is observed for "Type II" simulations when the spatula is pulled at a constant peeling angle $\theta_p = 90°$ from various pre-rotated configurations, i.e., with different shaft angles θ_{sh} as shown in Figure 4.28. These results show that irrespective of the shaft angle, the detachment angle is approximately the same for all peeling simulations and is equal to $\alpha^*_{spatula} = 25.64°$. Furthermore, "Type III" simulations (see Figure 4.29) also show similar behaviour with $\alpha^*_{spatula} = 25.64°$. In addition, the resultant force angle at the force maximum (point $\bar{u}_c$), denoted as α_c, is shown to increase with increasing peeling angle. However, this α_c is observed to be less than the critical detachment angle $\alpha^*_{spatula}$, except for $\theta_p = \theta_{sh} = 90°$ for which $\alpha_c = \alpha^*_{spatula}$. From all these results, it is clear that irrespective of the spatula shaft angle and the peeling angle, the critical detachment angle remains nearly invariant. It should be noted that the points $\bar{u}_a$ to $\bar{u}_e$ marked in Figures 4.28 and 4.29 correspond to the instances discussed at the start of section 4.3 and shown in Figure 4.7. Table 4.6 lists the critical detachment angle for all three types of simulations.

To understand the invariance of the detachment angle, evolution of the resultant pull-off force vs. the strain energy up to the critical point at which spatula snap-off occurs (at $\bar{u}_e$) is plotted for different peeling angles θ_p, see Figure 4.30. These curves show the strain energy and pull-off force values for which the spatula maintains attachment as it is peeled off the substrate. Even as the sliding starts (at $\bar{u}_c$) and the contact becomes unstable, the spatula resists detachment until it reaches the critical point $\bar{u}_e$. Also, the curves follow the same paths for the initial stretching and also after the sliding starts. Most importantly, irrespective of the peeling angle

Table 4.6: Critical detachment angle $\alpha^*_{\text{spatula}}$ for different types of simulations.

Type I ($\theta_{\text{sh}} = 0°$)		Type II ($\theta_{\text{p}} = 90°$)		Type III ($\theta_{\text{p}} = \theta_{\text{sh}}$)	
Peeling angle (θ_{p})	Critical detachment angle ($\alpha^*_{\text{spatula}}$)	Shaft angle (θ_{sh})	Critical detachment angle ($\alpha^*_{\text{spatula}}$)	Peeling angle ($\theta_{\text{p}} = \theta_{\text{sh}}$)	Critical detachment angle ($\alpha^*_{\text{spatula}}$)
10°	25.65°	10°	25.45°	10°	25.57°
15°	25.58°	15°	25.63°	15°	25.64°
20°	25.56°	20°	25.53°	20°	25.41°
25°	25.60°	25°	25.48°	25°	25.42°
30°	25.61°	30°	25.62°	30°	25.69°
35°	25.55°	35°	25.49°	35°	25.46°
40°	25.56°	40°	25.52°	40°	25.49°
45°	25.62°	45°	25.70°	45°	25.57°
50°	25.65°	50°	25.55°	50°	25.67°
55°	25.62°	55°	25.61°	55°	25.69°
60°	25.54°	60°	25.69°	60°	25.68°
65°	25.66°	65°	25.49°	65°	25.66°
70°	25.52°	70°	25.63°	70°	25.70°
75°	25.50°	75°	25.53°	75°	25.50°
80°	25.70°	80°	25.48°	80°	25.65°
85°	25.45°	85°	25.63°	85°	25.69°
90°	25.50°	90°	26.39°	90°	26.39°

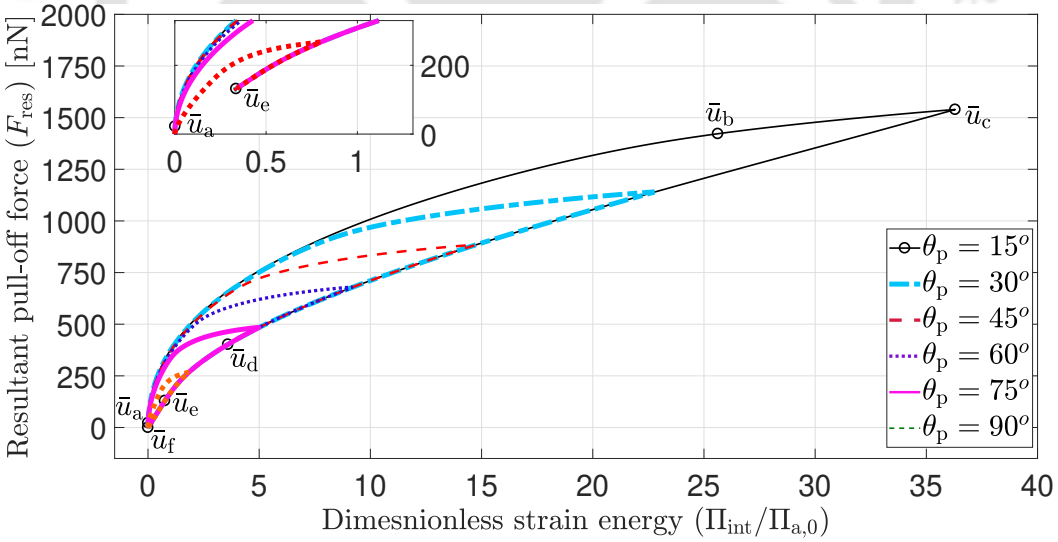

Figure 4.30: Resultant pull-off force and dimensional strain energy evolution for different peeling angles θ_{p} for "Type I" peeling. Here, $\Pi_{\text{a},0} = 1.523 \times 10^{-15}$ J. The inset shows an enlargement of the curves at the point of detachment at $\bar{u}_{\text{e}}$.

and the maximum force reached during the peeling process, the spatula reaches approximately the same critical point $\bar{u}_{\text{e}}$ (see inset in Figure 4.30). These curves are similar to the *stability envelopes* for the peeling of thin tapes shown by Federle

and Labonte [119]. In their work, these stability envelopes are obtained by plotting the pull-off force as a function of the pre-strain. For small peeling angles, the tape stretches such that the pre-strain exceeds a critical value called the minimum pre-strain $\varepsilon_{\min}$. Federle and Labonte [119] have shown that once the tape is stretched beyond $\varepsilon_{\min}$, it can be spontaneously detached by decreasing the applied force below the minimum force required to stabilize the contact. In the current study, these minimum force values are given by the resultant pull-off force values on the curve from $\bar{u}_{\mathrm{c}}$ to $\bar{u}_{\mathrm{e}}$. Further, the minimum strain of Federle and Labonte [119] can be related to the strain energy at point $\bar{u}_{\mathrm{e}}$.

Similar behavior can also be observed in Figure 4.27, which shows that all the peeling curves for all the peeling angles follow similar paths. Moreover, at the snap-off point $\bar{u}_{\mathrm{e}}$, all the peeling curves reach approximately the same energy state (see inset in Figure 4.27). These results reveal an interesting observation that irrespective of the peeling angle, the spatula follows similar paths in detaching from the substrate and finally reaches the same critical energy state beyond which it cannot sustain any more loading and detaches from the substrate completely.

According to the "frictional adhesion" model of Autumn et al. [48], the normal adhesive force is limited by the frictional force and the critical detachment angle α^* and is given by

$$\tan \alpha^* \geq \frac{F_{\mathrm{N}}}{F_{\mathrm{T}}} \,. \tag{4.4}$$

In the current work, where $\alpha^*_{\mathrm{spatula}} \approx 25.6°$, the maximum friction force must always be greater than 2.1 times the maximum normal adhesive force according to Eq. 4.4. From, the resultant force angle curves shown in Figure 4.26, it is clear that the ratio of the maximum friction force to the maximum normal force is always more than 2.1. For $\theta_p = 10°$, maximum value of the friction force can be as high as 8.6 times the maximum value of the normal force. As a consequence, even when the spatula starts to fully slide on the substrate (point $\bar{u}_{\mathrm{c}}$), it is still attached to the substrate until the critical point $\bar{u}_{\mathrm{e}}$ is reached. However, for $\theta_{\mathrm{p}} = \theta_{\mathrm{sh}} = 90°$ this is not true (see Figures 4.28 and 4.29), and as soon as the force maximum is reached and the spatula pad starts to fully slide on the substrate, it snaps-off from the substrate, i.e. points $\bar{u}_{\mathrm{c}}$ and $\bar{u}_{\mathrm{e}}$ coincide for $\theta_{\mathrm{p}} = \theta_{\mathrm{sh}} = 90°$. This supports the experimental observations of Autumn et al. [265] that when geckos adhere to a substrate, they generate much greater forces than are required for them to stay attached to the substrate according to Eq. (4.4) (a shear force of 5 times the adhesive force for the gecko front legs was measured by Autumn et al. [265], while we find a shear force as high as 8.6 times the adhesive force for the spatula). From these results, it can be concluded that adhesive friction, starting with the spatula level, is present at all hierarchy levels in the gecko adhesive system. Moreover, the critical detachment angle of 25.6° implies that at detachment, the adhesive force

is about half of the shear force. This particular trend is observed to be true for many of the climbing animals which use "dry" as well as "wet" adhesion [119]. This shows that the current model can be employed effectively to study other kinds of biological adhesive systems.

4.3.2a Influence of the spatula pad thickness

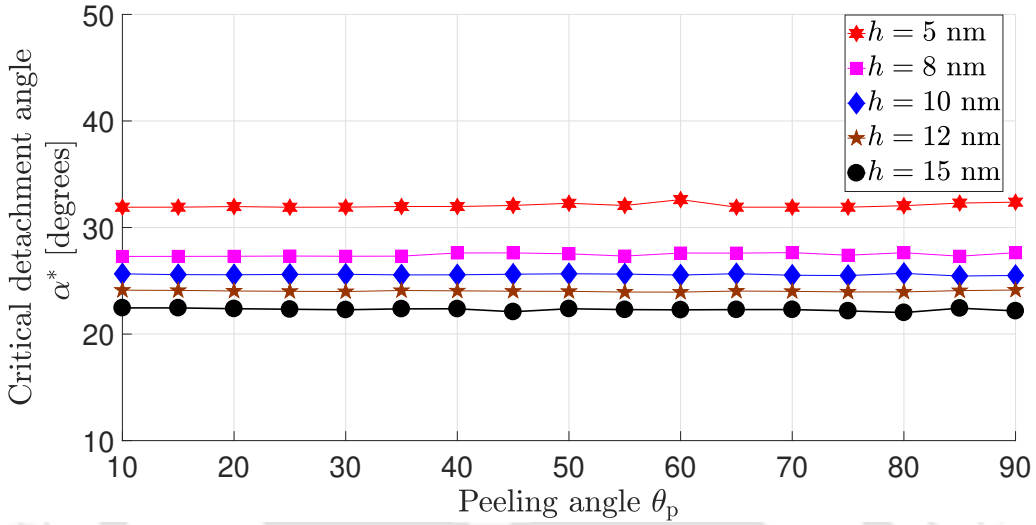

Figure 4.31: Variation of the critical detachment angle $\alpha^*_{\text{spatula}}$ with peeling angle θ_p for different spatula pad thicknesses h ("Type I" peeling).

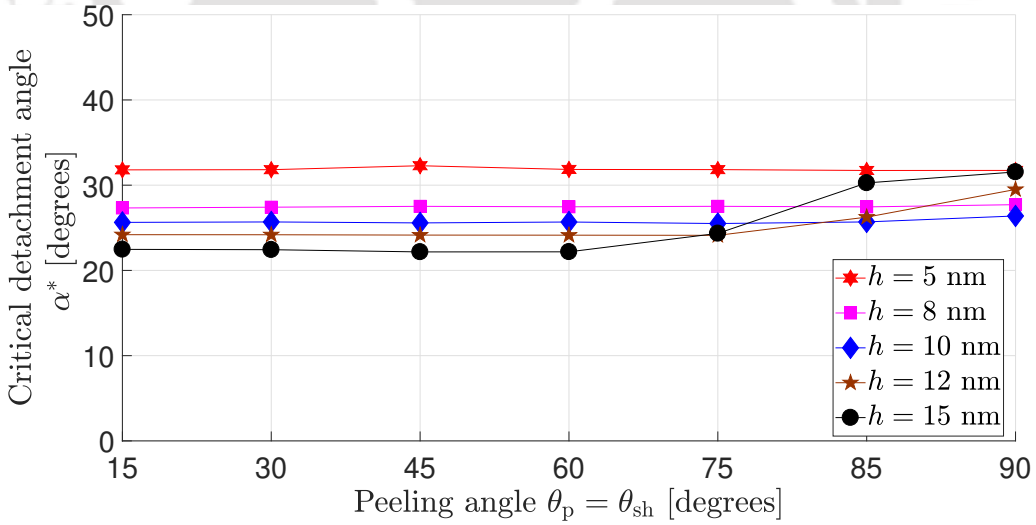

Figure 4.32: Variation of the critical detachment angle $\alpha^*_{\text{spatula}}$ with peeling angle $\theta_p = \theta_{sh}$ for different spatula pad thicknesses h ("Type III" peeling).

In Figure 4.31, variation of the critical detachment angle α^* with peeling angle θ_p for different spatula pad thicknesses h is shown. These results indicate that in general, as the thickness decreases the spatula detaches at higher angles. This trend is consistent with the theoretical results of Chen et al.[103]. These results also agree

well with the experimental observations of Schubert et al. [267], that stiffer fibrillar structures detach at lower critical angles than softer structures.

However, for "Type III" peeling simulations (see Figure 4.32) where the spatula is peeled from a pre-rotated configuration (see section 4.2.1), behaviour of the spatula to detach at a constant angle ($= \alpha^*$) irrespective of the peeling angle $\theta_p = \theta_{sh}$, is observed only for thickness values of $5 - 10\,\text{nm}$. For large thickness values i.e, $h = 12$ and $15\,\text{nm}$, it is found that the spatula does not detach at a constant angle for all the peeling and shaft angles. Instead, for a large value of the spatula pad thickness, at high angles, i.e., $\theta_p \geq 75°$, the detachment angle is considerably higher than that for low peeling angles, i.e., $\theta_p \leq 60°$.

In order to understand this behaviour, the horizontal displacement of point P (see Fig. 4.1) as a function of the applied displacement $\bar{u}$ is plotted in Figure 4.33 for different peeling angles $\theta_p = \theta_{sh}$ and spatula pad thicknesses. As seen from these figures, for large spatula pad thicknesses, at large peeling and shaft angles, there is still no full sliding of the spatula after the force maximum is reached. For $\theta_p = 85°$ sliding of the spatula is not observed for both $h = 12$ and $15\,\text{nm}$. Correlating these results with those in Figure 4.32, it is reasonable to concluded that full sliding of the spatula is needed for an invariant critical detachment angle $\alpha^*_{\text{spatula}}$.

The electron microscopy analyses of Rizzo et al. [74] revealed that the spatula pad of Tokay Gecko is only around $10\,\text{nm}$ thick. Persson and Gorb [68] suggested that the pad thickness is approximately $5 - 10\,\text{nm}$, making it compliant enough to adhere to any kind of substrate. This has also been confirmed by Sauer and Holl [162] through detailed 3D finite element simulations. From the results in Figure 4.32, it can be concluded that thickness of the spatula pad should be small enough to attain constant critical detachment angle. At the same time, as argued by Persson and Gorb [68] the pad thickness should be large enough to provide sufficient stiffness. In this regard, $h = 10\,\text{nm}$ seems to be an optimum value, i.e., it is the largest value of h with invariant $\alpha^*_{\text{spatula}}$.

4.3.2b Influence of the shaft length

Recently, Peng et al. [112] have shown that the film length significantly influences its peeling behaviour, particularly, evolution of the pull-off forces. In this section, influence of the spatula shaft length ("QR" in Figure 4.1) on the critical detachment angle $\alpha^*_{\text{spatula}}$ is examined. Keeping the spatula pad length constant ($\overline{\text{PQ}} = 150R_0$), a total of five different shaft lengths are investigated, i.e. $\overline{\text{QR}} = 0, 50R_0, 100R_0, 200R_0,$ and $400R_0$. "Type I" simulations are carried out for different peeling angles. It is observed that a critical detachment angle exists irrespective of the shaft length, i.e. for a given shaft length, irrespective of the

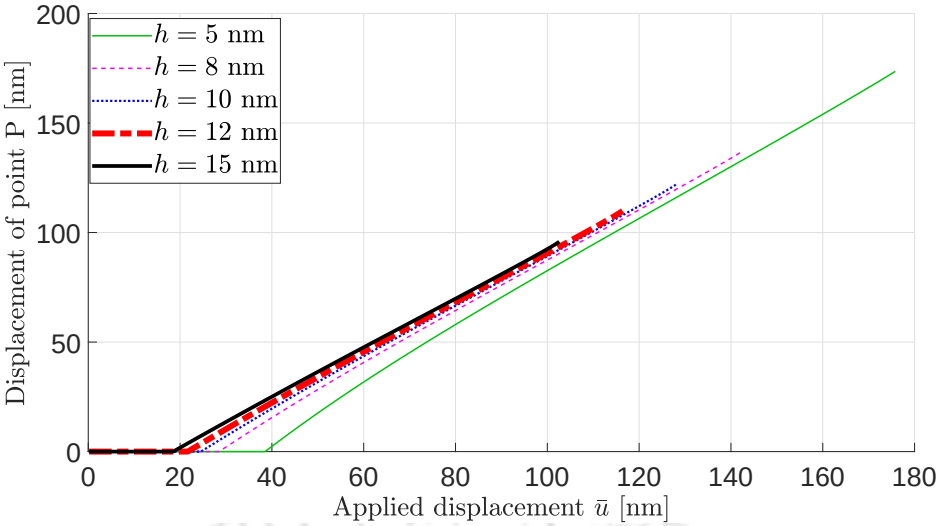

(a) $\theta_{\mathrm{p}} = \theta_{\mathrm{sh}} = 30°$

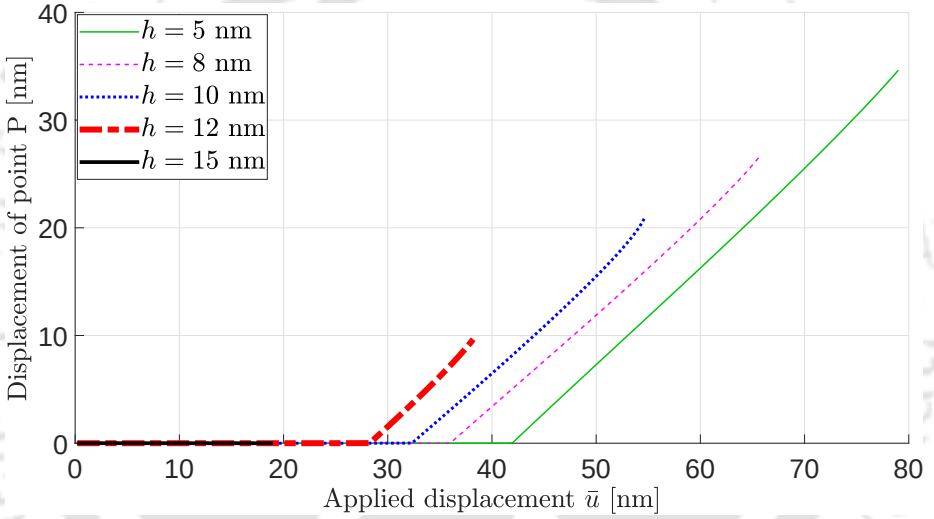

(b) $\theta_{\mathrm{p}} = \theta_{\mathrm{sh}} = 75°$

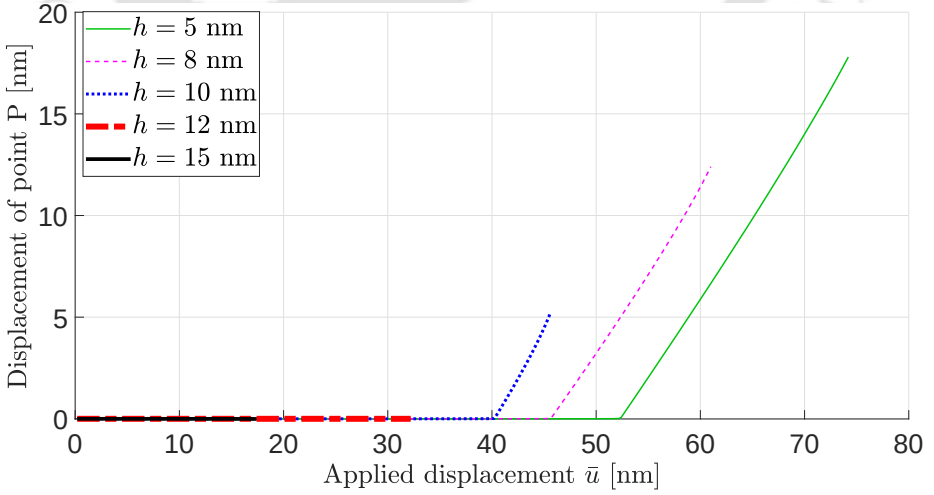

(c) $\theta_{\mathrm{p}} = \theta_{\mathrm{sh}} = 85°$

Figure 4.33: Horizontal displacement of strip point P (see Figure 4.1) with the applied displacement $\bar{u} = \|\bar{\boldsymbol{u}}\|$ at different peeling angles $\theta_{\mathrm{p}} = \theta_{\mathrm{sh}}$ for different values of strip thickness h ("Type III" peeling).

peeling angle the spatula detached at the same resultant force angle. Even when the entire length of the spatula interacts with the substrate, i.e. "QR" vanishes, there exists a critical detachment angle $\alpha^*_{\text{spatula}}$. The critical detachment angle for different shaft lengths is given in Table 4.7. For $\overline{\text{QR}} = 0$ to $200R_0$ very little change in the value of critical detachment angle is observed. However, for $\overline{\text{QR}} = 400R_0$ there is a slight decrease in the value of $\alpha^*_{\text{spatula}}$. These results indicate that the critical detachment angle is independent for a wide range of shaft lengths.

Table 4.7: Critical detachment angle $\alpha^*_{\text{spatula}}$ for different spatula shaft lengths. Here, $R_0 = 1$ nm is introduced for normalization.

Shaft length ($\overline{\text{QR}}$)	0	$50R_0$	$100R_0$	$200R_0$	$400R_0$
Critical detachment angle $\alpha^*_{\text{spatula}}$	25.46°	25.58°	25.45°	25.14°	24.16°

4.4 Three-dimensional spatula peeling

In addition to the investigations detailed in the previous sections, the finite element formulation has been extended to study the peeling of gecko spatulae using a three-dimensional (3D) finite element model. In this section, both frictionless and frictional peeling of the spatula using a 3D model are discussed.

The three-dimensional spatula model is taken from the work of Sauer and Holl [162], which is based on the atomic microscopy images of Rizzo et al. [74] as shown in Figure 4.34. The spatula structure is made up of a thin pad with a flat contact surface and a long shaft tapered down towards the pad. A finite element model of the idealized geometry of the spatula [162] shown in Figure 4.35. Trilinear hexahedral elements are used to mesh the spatula geometry. Figure 4.35a shows the top view of the spatula and Figure 4.35b shows the cross-sectional side view. The spatula pad is only $h = 10\,\text{nm}$ thick and has a maximum width of $w_{\text{pad}} = 250\,\text{nm}$. The pad length is taken to be $L_{\text{pad}} = 350\,\text{nm}$. The pad is surrounded by a comparatively thick rim. The maximum diameter of the shaft end is taken to be $d_{\text{sh}} = 120\,\text{nm}$, which tapers down and connects to the pad. Therefore, axis of the spatula shaft is inclined at an angle of $\theta_{\text{sh}} = 4.91°$ with the horizontal in its initial configuration. A detailed description of the construction of the idealized spatula geometry is discussed in Sauer and Holl [162].

In their FE analysis, Sauer and Holl [162] considered three different finite element meshes, viz. coarse, mesh, and fine. As the spatula is symmetric about the y-axis, only half of the spatula mesh is considered. The total number of elements and contact elements in these meshes is given in Table 4.8. The element size of the contact elements in these meshes is quite large when compared to the interfacial

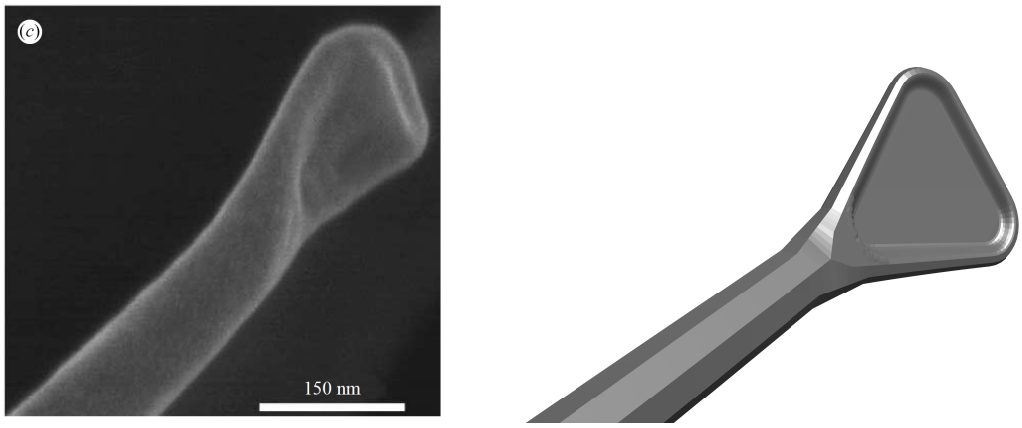

(a) (b)

Figure 4.34: Gecko spatula and its 3D model: (a) atomic microscopy image of the gecko spatula. Reprinted with permission from Rizzo et al. [74]. (b) idealized three-dimensional model.

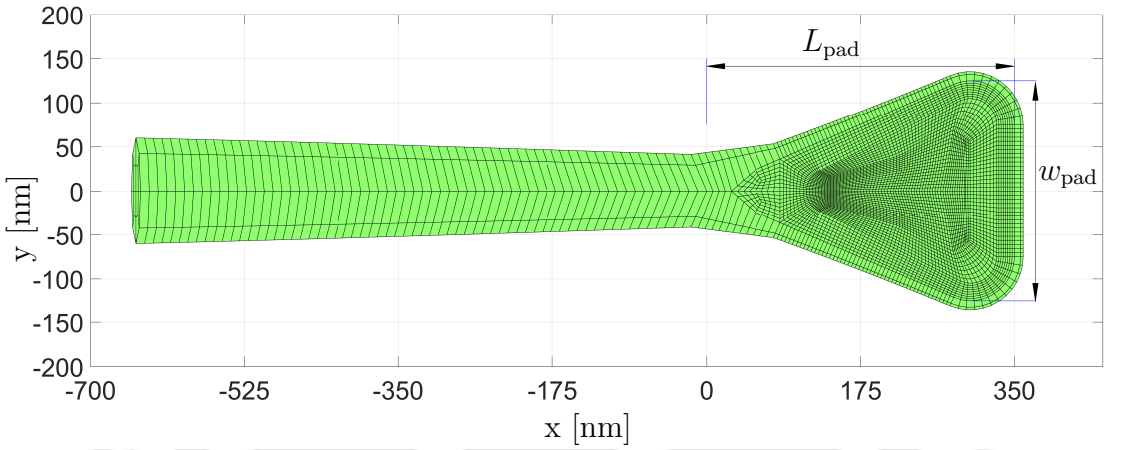

(a)

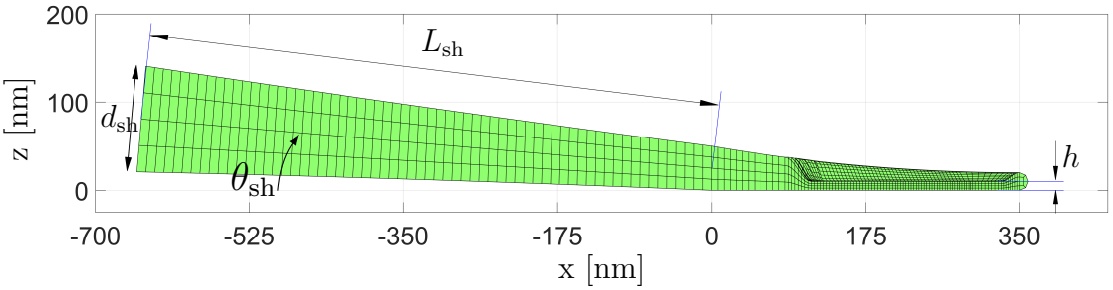

(b)

Figure 4.35: Gecko spatula mesh (a) top view (b) cross-sectional side view.

distances for van der Waals force. The maximum adhesive traction between the interacting surfaces occurs at a distance of 0.3057 nm according to the parameters considered for the gecko spatula adhesion in the current thesis (see Figure 2.4 and

Table 4.5). As such, these meshes combined with standard linear Lagrangian discretization (Q1C1) fail to capture nonlinear interfacial adhesive forces. As such, Sauer and Holl [162] employed the Q1C2 contact elements, i.e. contact surface is discretized using the second-order Lagrangian elements, whereas the bulk is discretized using linear Lagrangian elements. However, fine mesh is computationally quite expensive. Therefore, in the present work, to overcome this issue, the coarse mesh is employed in conjunction with the Q1C4 contact elements, i.e. the contact elements are described using the fourth-order Lagrangian approximations. The coarse mesh has 10 times fewer total elements and 4 times fewer contact elements. The Q1C4 formulation combined with the coarse mesh can provide comparable results as that of the fine mesh with Q1C2 formulation. This is due to the fact that the Q1C4 elements introduce 25 additional number of nodes on the contact surface when compared to the 5 additional nodes in Q1C2 element (see Figures 3.4a and 3.3a). These additional degrees of freedom at the contact interface results in accurate computation of the interfacial adhesive tractions.

Table 4.8: Details of the finite element meshes considered for half of the spatula [162].

Mesh	Total number of elements	Contact elements	Largest diameter of contact elements [nm]
Coarse	784	139	22.39
Medium	9808	2224	5.71
Fine	101728	8896	2.87

4.4.1 Frictionless peeling

In this section, results for the frictionless peeling of the spatula are described. Two types of peeling simulations are considered: (a) peeling by applied rotation and (b) peeling by vertical pulling.

4.4.1a Peeling by applied rotation

The spatula is peeled off by applying a rotation θ_{sh} to the shaft end face. Figure 4.36 shows the evolution of peeling moment with the angle of rotation of the shaft θ_{sh} as obtained by the current FE model and the results of Sauer and Holl [162]. Unlike the case of the peeling of a strip with constant thickness (see section 4.3.1b) the bending moment does not remain constant but varies throughout as the thickness of a 3D spatula is continuously varying.

In case of the peeling simulations of Sauer and Holl [162], the peeling moment initially increases linearly until $\theta_{\text{sh}} = 31°$, at which an instability occurs as a result

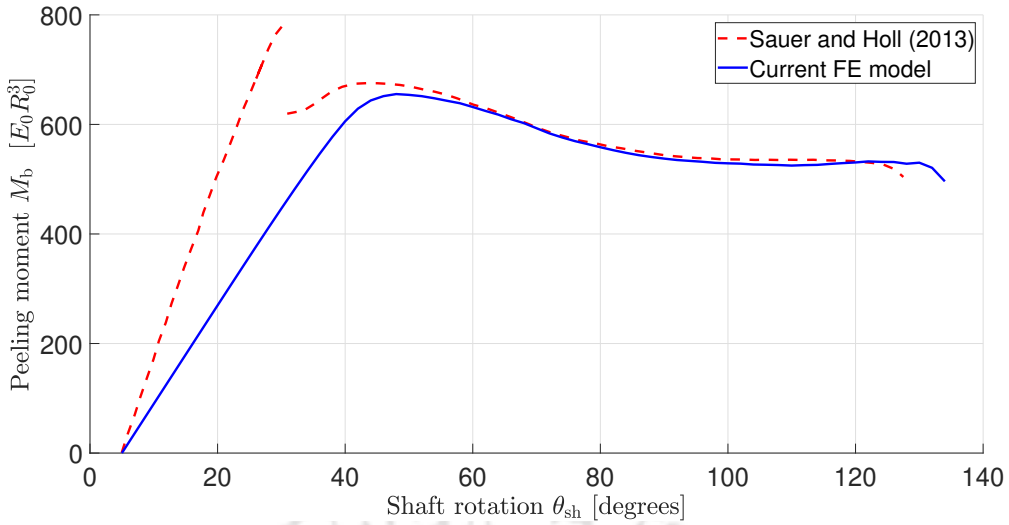

Figure 4.36: Variation of the peeling moment M_b with shaft rotation angle θ_{sh}. Here $E_0R_0^3 = 2\text{nN·nm}$.

there is a sudden drop in the peeling moment. This is caused by the sudden drop in the bending stiffness (due to sudden drop in the thickness) at the meeting point of shaft and the pad. Further, at this point the spatula pad starts to detach from the substrate on which highly nonlinear adhesive forces are acting. As a result, the FE model of Sauer and Holl [162], which employs fine mesh with Q1C2 formulation, is unable to resolve these sudden changes. However, use of the coarse mesh in conjunction with the Q1C4 elements allows the current model for more stable resolving of these sharp changes. As a result, the peeling moment curve obtained in the current work is continuously varying with no instabilities. Further, after this sudden drop, the peeling moment obtained by the current model follows the peeling moment obtained by Sauer and Holl [162] very closely. The current computations show that the spatula detaches from the substrate at an angle of $\theta_{sh} = 135°$ in contrast to $\theta_{sh} = 128°$ obtained by Sauer and Holl [162]. The two-dimensional strip, as seen from section 4.3.1b, can support rotations even up to 180°.

Figure 4.37 shows the deformed configurations of the spatula at different shaft angles along with the normalised first invariant of the Cauchy stress distribution. Similar to the case of strip peeling, at the peeling front large tensile and compressive stresses are observed on the bottom and top surface of the pad, respectively. As the spatula peels off the substrate, this peeling front moves across the surface of the spatula pad.

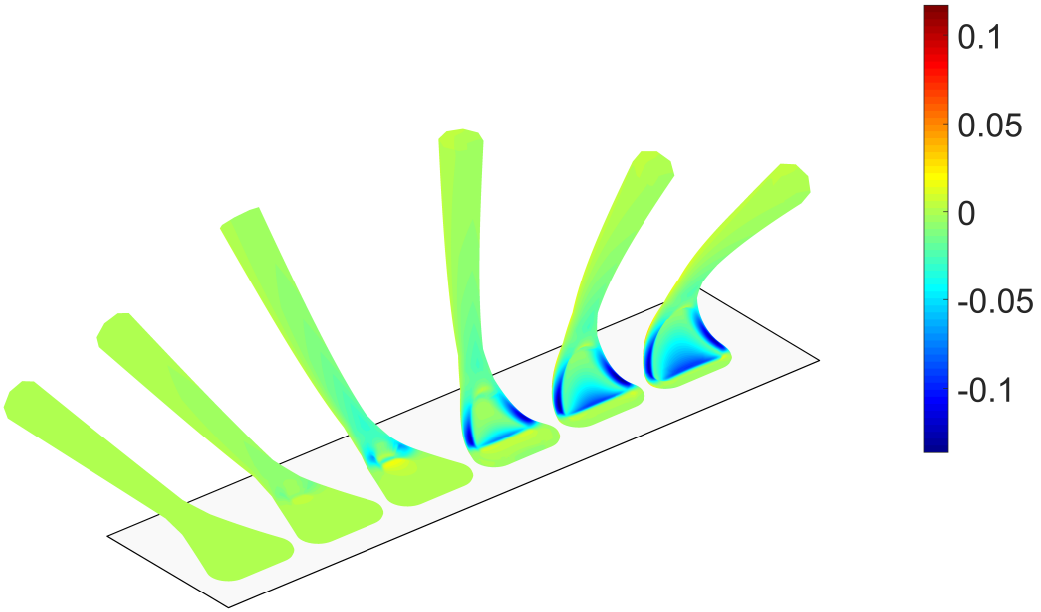

(a) Isometric view

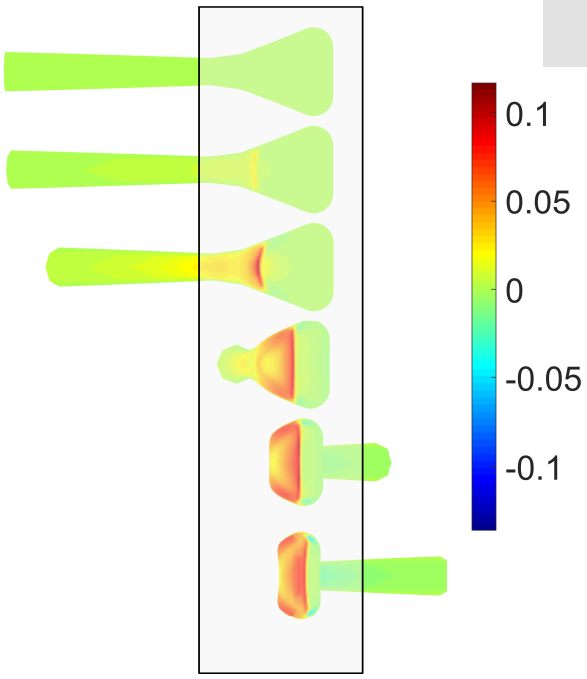

(b) Bottom view

Figure 4.37: Deformed configurations of the spatula during peeling by applied rotation at different shaft inclinations $\theta_{\text{sh}} = 0°$, $15°$, $45°$, $90°$, $120°$, and $135°$. The colourbar indicates the normalised stresses $I_1/E_0 = \text{tr}(\boldsymbol{\sigma})/E_0$.

4.4.1b Peeling by vertical pulling

In this section, results for the frictionless vertical pulling ("tangentially-free") of the spatula from various rotated configurations are presented. These results are then compared to those of Sauer and Holl [162]. The rotated configurations are obtained from the peeling simulations discussed in the previous section. The spatula is pulled by applying a displacement $\bar{u}_z$ in the vertical direction from a rotated configuration. Figure 4.38 shows the evolution of resultant pull-off force with the displacement of the shaft end face in the vertical direction Δu_z from different shaft angles θ_{sh}. The displacement of the shaft end face Δu_z is measured from the initial configuration shown in Fig. 4.35.

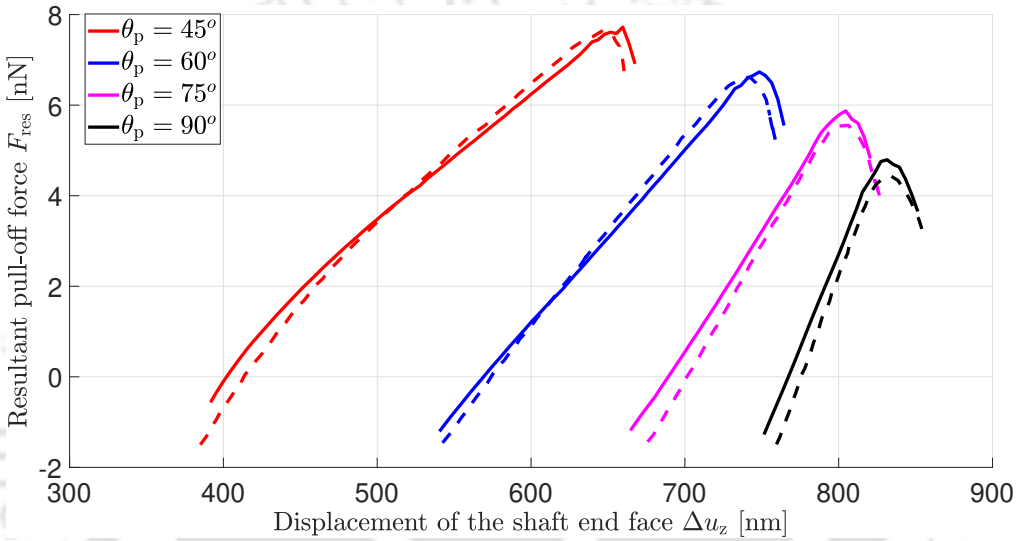

Figure 4.38: Evolution of the pull-off force with the vertical displacement of the shaft end face Δu_z. The dashed lines correspond to the results of Sauer and Holl [162] and the solid lines correspond to the results of the current FE model.

Results in Fig. 4.38 show that for a given shaft angle θ_{sh} the pull-off force increases up to a maximum value and then decreases. Also, as the shaft angle increases, the maximum force reached during the peeling decreases. The maximum value of the pull-off force ranges from 4.4 nN to 7.6 nN, which is very close to the results obtained by Sauer and Holl [162] as evident from Figure 4.38.

Figure 4.39 shows the deformed configurations at different values of Δu_z corresponding to vertical pulling of the spatula from shaft angle $\theta_{sh} = 60°$. At $\Delta u_z = 768$ nm, the spatula is completely separated from the substrate. Also, the stresses developed in the spatula during the vertical pulling are lower than those in peeling by applied rotation (see Figure 4.37).

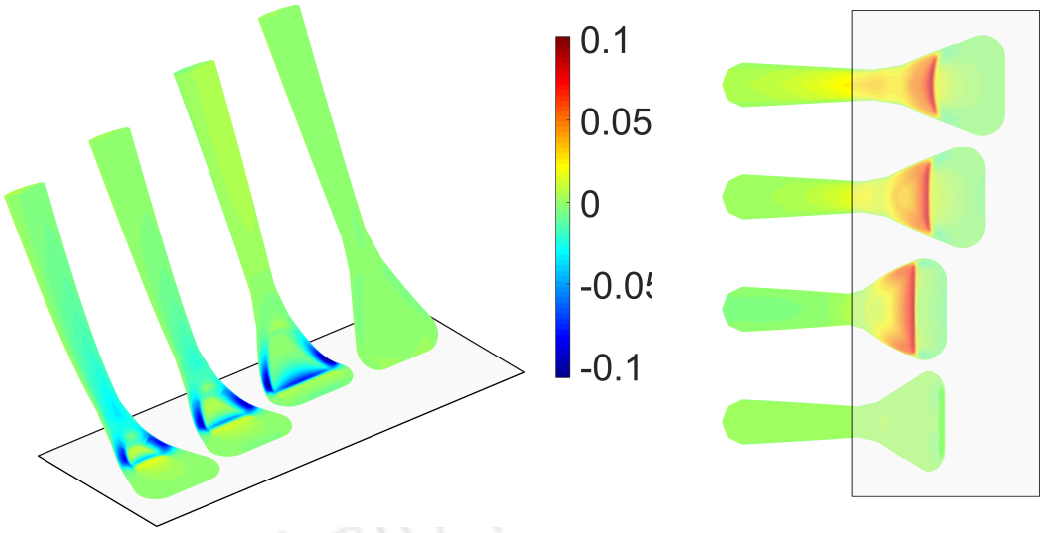

(a) Isometric view **(b)** Bottom view

Figure 4.39: Deformed configurations of the spatula during vertical pulling from a pre-rotated configuration with shaft angle $\theta_{sh} = 60°$ at different vertical displacements of the shaft end face $\Delta u_z = 548\,\text{nm}$, 610 nm, 690 nm, and 768 nm. The colourbar indicates the normalised stresses $I_1/E_0 = \text{tr}(\boldsymbol{\sigma})/E_0$.

4.4.2 Frictional peeling

This section presents the results obtained for frictional peeling of the gecko spatula from the rigid substrate. The spatula is peeled off by applying a displacement $\bar{\boldsymbol{u}}$ on the shaft end face at a peeling angle θ_p from its initial configuration shown in Fig. 4.35. These peeling simulations are same as the "Type I" peeling described in Section 4.2.1. As discussed in section 4.2.1, the displacement $\bar{\boldsymbol{u}}$ is applied on the shaft end face such that $u_x = \bar{\boldsymbol{u}} \cos\theta_p$ and $u_z = \bar{\boldsymbol{u}} \sin\theta_p$. As such, this constrains the tangential movement (in the x-direction) of the spatula shaft, resulting in considerable frictional forces. Extending the discussion on the influence of the friction coefficient from section 4.3.1f, here the peeling simulations are carried out for low friction coefficients. The default friction coefficient is taken as $\mu_s = 0.05$.

4.4.2a Influence of the peeling angle

The three-dimensional peeling simulations show that both the normal and tangential pull-off forces first increase up to maximum value and then decrease after that

Figures 4.40 and 4.41 show the evolution of F_N and F_T with the applied displacement $\bar{u}$ for different peeling angles. It can be observed that both F_N and F_T first increase up to a maximum value and then decrease after that. Except for $\theta_p = 90°$, the maximum value of both the normal and the tangential pull-off force remains invariant irrespective of the peeling angle θ_p.

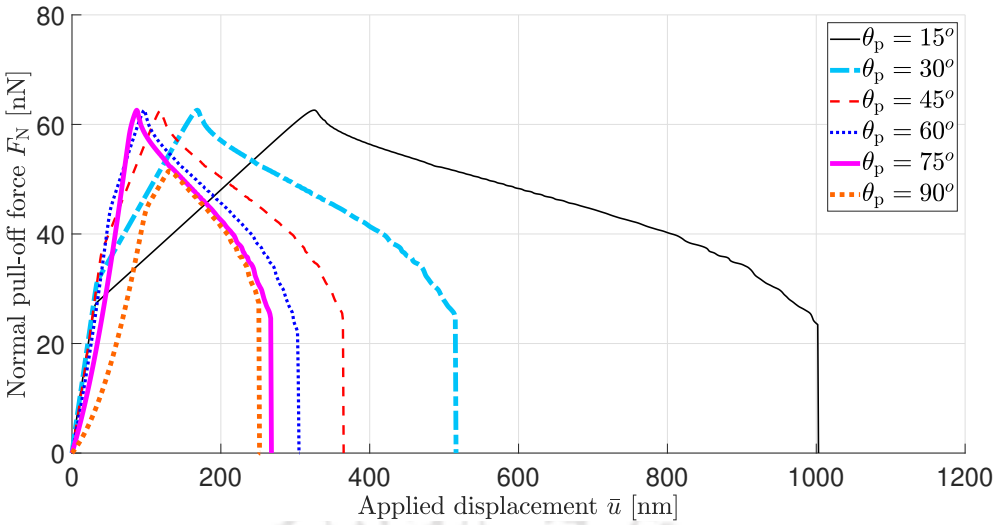

Figure 4.40: Evolution of the normal pull-off force F_N with applied displacement $\bar{u}$ for different peeling angles θ_p.

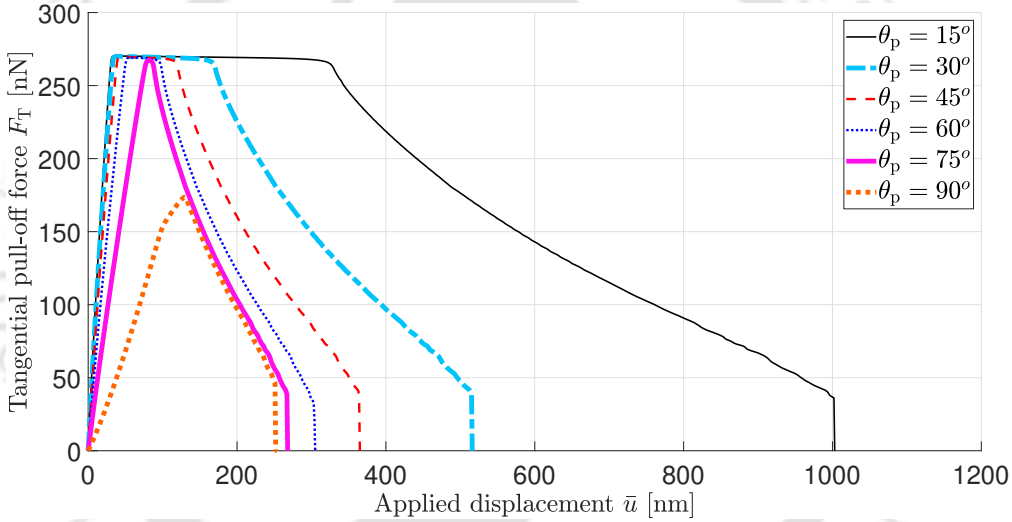

Figure 4.41: Evolution of the tangential pull-off force F_T with applied displacement $\bar{u}$ for different peeling angles θ_p.

These results differ from those for high friction coefficient $\mu_s = 0.3$ (Figs. 4.9 and 4.10). In case of high friction peeling, the maximum value of both F_N and F_T are reached when the strip starts to fully slide on the substrate. However, this is not the case for spatula peeling with low friction coefficient. Although the maximum value of the tangential traction F_T is reached when the spatula starts fully sliding, the maximum normal pull-off force is reached when the spatula pad first starts to peel off the substrate. Further, for low peeling angles, i.e. $\theta_p = 15°$ to $60°$, after the spatula starts to fully slide on the substrate, F_T decreases only very slightly, as such can be considered to achieve an apparent steady state. Finally, the tangential force monotonically decreases with the applied displacement as the spatula pad starts peeling off the substrate. Further, as the peeling angle increases, the length of the

steady state, i.e. the displacement range in which the tangential traction remains almost constant, decreases.

To clearly understand this behaviour of the pull-off force evolution for $\theta_p = 15°$ to 60°, peeling of the spatula at $\theta_p = 30°$ is selected. In this case, the spatula starts full-sliding around $\bar{u} = 40\,\text{nm}$, at which the tangential pull-off force F_T reaches maximum value. The normal pull-off force F_N reaches its maximum value around $\bar{u} = 160\,\text{nm}$. From $\bar{u} = 40$ to $160\,\text{nm}$, there is only a slight decrease in the tangential pull-off force F_T. Whereas, the normal pull-off force F_N continues to increase although at a lesser rate than before. Figures 4.42a to 4.42d show the deformed configurations of the spatula from $\bar{u} = 20\,\text{nm}$ to $180\,\text{nm}$. It can be observed that after $\bar{u} = 40\,\text{nm}$ the spatula starts sliding on the substrate. However, the spatula pad is still fully attached to the substrate. It is only after $\bar{u} = 160\,\text{nm}$, that the pad starts to gradually detach from the substrate as shown in Fig. 4.42d. At $\bar{u} = 180\,\text{nm}$ it can be clearly seen that a part of the spatula pad has detached from the substrate. From this point onwards, the normal force decreases as the pad area still attached to the substrate continues to decreases. As such, the maximum values of F_N and F_T occur at different values of $\bar{u}$.

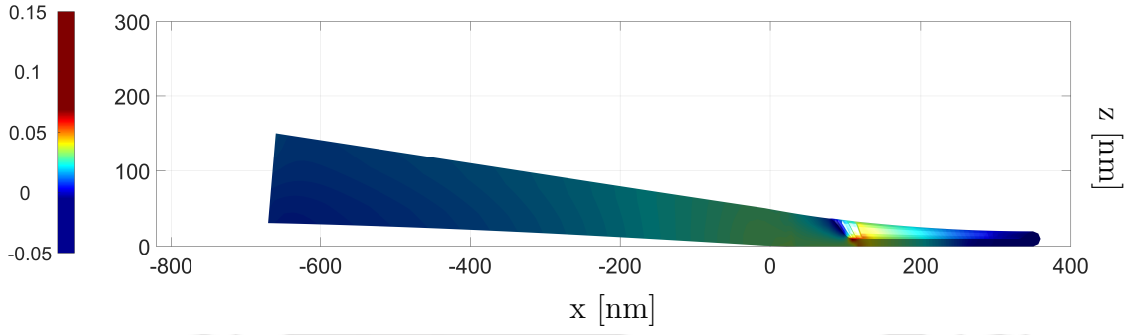

(a) $\bar{u} = 20$ nm.

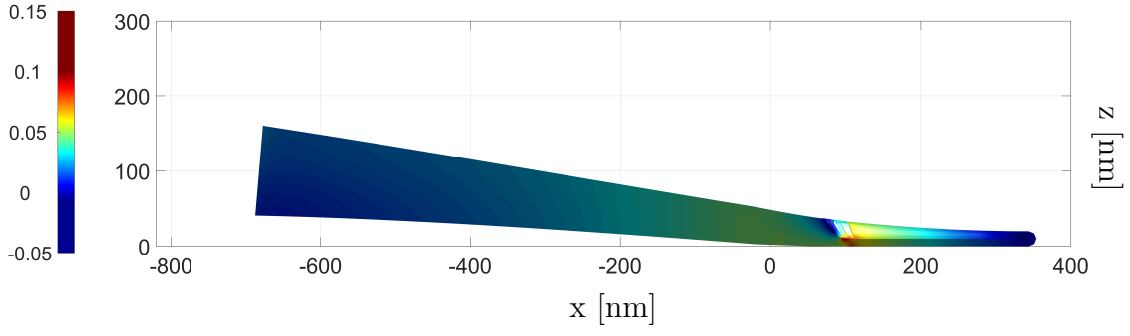

(b) $\bar{u} = 40$ nm.

In the pull-off force curves in Figures 4.40 and 4.41, towards the end of the peeling process, there are visible oscillations. This is due to the fact that even though the Q1C4 element formulation employed here is able to capture the nonlinear

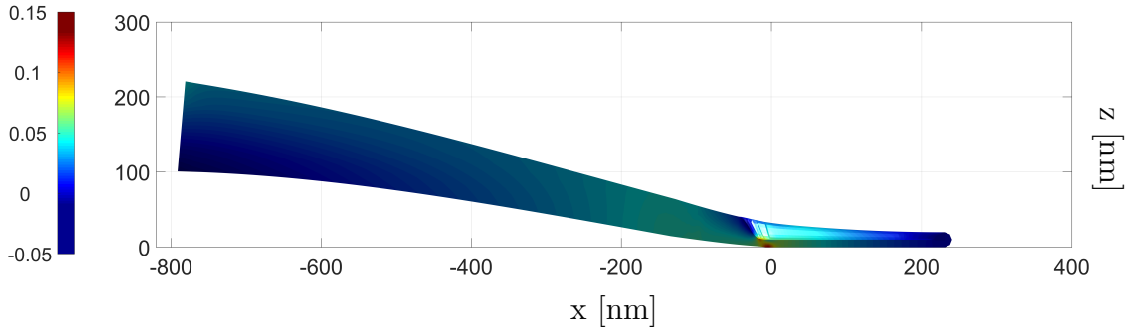

(c) $\bar{u} = 160$ nm.

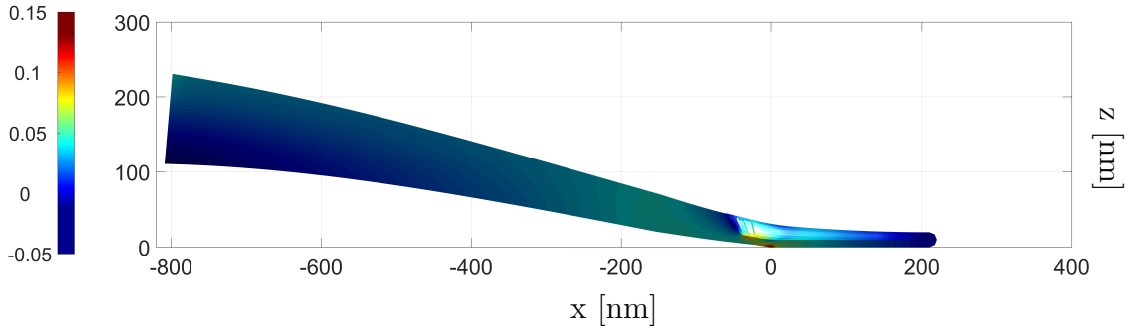

(d) $\bar{u} = 180$ nm.

Figure 4.42: Side-view of the deformed configurations of half of the spatula at different values of applied displacement $\bar{u}$. The colourbar indicates the normalised stresses $I_1/E_0 = \mathrm{tr}(\boldsymbol{\sigma})/E_0$.

adhesive tractions, the coarse mesh used is still not enough to provide a smooth response. As such, finer meshes are required to resolve this issue. Another way to overcome this issue is by using other local enrichment techniques, which represent the contact surface accurately. For example, Corbett and Sauer [268] proposed an enrichment technique, in which the contact surface is discretized by the NURBS basis functions, which can accurately represent the contact surface. While, the bulk is discretized by standard linear Lagrangian elements. This technique provides highly accurate and efficient contact solution.

Comparison with 2D peeling:

Figures 4.43 and 4.44 show evolution of the normal and the tangential pull-off forces with the applied displacement $\bar{u}$ for different peeling angles using the two-dimensional spatula model discussed in section 4.2 with the friction coefficient $\mu_s = 0.05$. Comparison of these results with those in Figures 4.40 and 4.41 shows that the maximum pull-off force values for any given peeling angle predicted by these two models are very close to each other. For example, the maximum normal pull-off force corresponding to $\theta_p = 15°$ computed using 2D model is 70.75 nN, while the 3D simulations predict a value of 62.6 nN. Similarly, the maximum tangential pull-off force values corresponding to $\theta_p = 15°$ are 276.6 nN and 270.3 nN, with 2D

and 3D model, respectively.

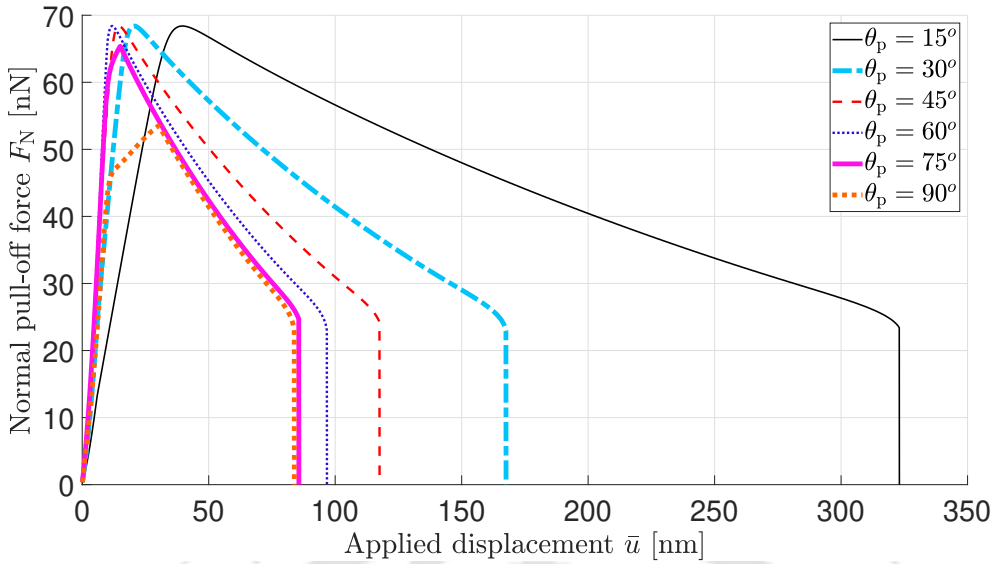

Figure 4.43: Evolution of the normal pull-off force F_N with applied displacement $\bar{u}$ for different peeling angles θ_p using the two-dimensional spatula model (see section 4.2).

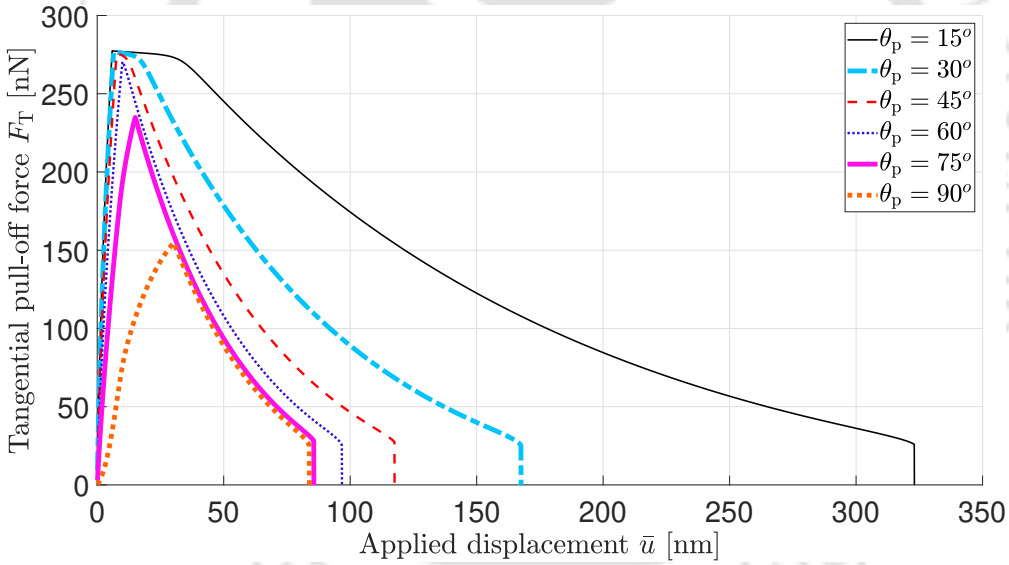

Figure 4.44: Evolution of the tangential pull-off force F_T with applied displacement $\bar{u}$ for different peeling angles θ_p using the two-dimensional spatula model (see section 4.2).

It can also be observed that invariance of the maximum pull-off forces reached for peeling angles $\theta_p \leq 60°$ is also observed for two-dimensional spatula model. Also, similar to the 3D simulations, the normal pull-off force and tangential pull-off force reach their maximum at different values of applied displacement. For the case of $\theta_p = 30°$, the maximum normal force occurs at $\bar{u} = 21\,\text{nm}$. Whereas, the maximum tangential force occurs very early on at $\bar{u} = 6.9\,\text{nm}$. Further, in these two-dimensional simulations, for low peeling angles $\theta_p \leq 30°$, the tangential pull-off force briefly reaches an apparent steady state, similar to the observations in

Figure 4.41. However, the length of the steady state, i.e. the displacement range in which the tangential traction remains almost constant, is less than that of the 3D simulations. This is due to the fact that the total length of the spatula considered in the 3D simulations (1000 nm) is much greater than that of the two-dimensional strip (200 nm). As observed by Peng et al. [112], for thin films with large lengths, the pull-off forces can reach steady state unlike thin films of small length. These results clearly indicate that two-dimensional spatula model employed in the current thesis has the potential to capture almost all the characteristics of the peeling behaviour of the actual gecko spatula.

4.4.2b Influence of the friction coefficient

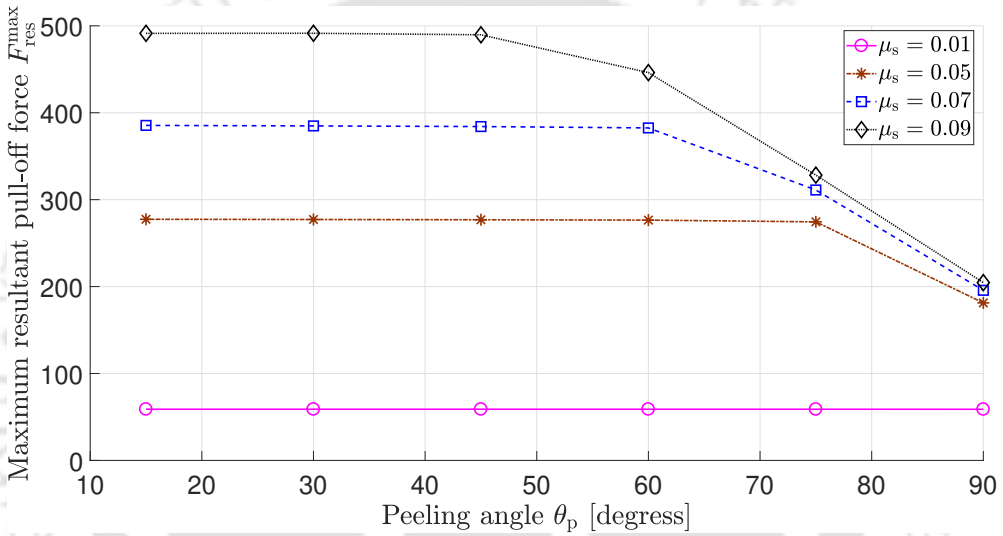

Figure 4.45: Variation of the maximum resultant pull-off force $F_{\text{res}}^{\max}$ with the peeling angle θ_{p} for different friction coefficients.

Figure 4.45 shows the variation of the magnitude of the resultant pull-off force F_{res} with the applied displacement $\bar{u}$ at peeling angle $\theta_{\text{p}} = 45°$ for friction coefficients $\mu_{\text{s}} = 0.01$, 0.05, 0.07, and 0.09. For really low friction coefficient $\mu_{\text{s}} = 0.01$, the resultant pull-off force is quite small and remains invariant with the peeling angle. The resultant pull-off force naturally increases as the friction coefficient increases. Further, as the friction coefficient is increased, this invariance of the resultant pull-off force is not observed at high peeling angles. Even for $\mu_{\text{s}} = 0.09$, the pull-off force remains constant for low peeling angles $\theta_{\text{p}} \leq 45°$ and decreases sharply as the peeling angle is increased. This behaviour shows that friction is an important factor for generating high adhesion as well as friction. Also, the sharp drop in pull-off forces at high peeling angles once again indicates how geckos can achieve easy detachment by pulling their toes at high angles.

भारतीय प्रौद्योगिकी संस्थान गुवाहाटी
Indian Institute of Technology Guwahati

Chapter 5

Application of Artificial Neural Networks To Peeling Computations

In this chapter, Bayesian regularization based backpropagation neural networks are employed to predict the peeling behaviour observed in the finite element analyses discussed in Chapter 4. This chapter contains three sections: Section 5.1 describes the Bayesian regularization based backpropagation neural network (BR-BPNN) employed in the current study, Section 5.2 discusses the implementation of the BR-BPNN, and Section 5.3 discusses the corresponding results.

5.1 Bayesian regularization based backpropagation neural network (BR-BPNN)

In this section, a backpropagation neural network (BPNN) along with the Bayesian regularization learning algorithm are described.

A classical neural network architecture mimics the function of the human brain. The brain neurons and their connections with each other form an equivalence relation with neural network neurons and their associated weight values (w). In a single layer network with multiple neurons, each element u_j of an input vector is associated with each neuron i with a corresponding weight w_{ij}. A constant scalar term called bias b_i corresponding to each neuron, which is like a weight, is generally introduced in order to increase the flexibility of the network. This bias b_i is multiplied by a scalar input value (chosen to be 1 here) and is added to the weighted sum $w_{ij}u_j$ of the vector components u_j to form a net input n_i. This net input n_i is then passed to an activation function f (also called transfer function) that produces an

output value a_i. In general, a neural network consists of two or more layers. Adding a hidden layer of neurons between the input layer and output layer constitutes a multi-layer neural network, also named shallow neural network. Furthermore, addition of more than one hidden layer in the multi-layer neural network is called a deep neural network.

Traditionally, a BPNN model, a kind of multi-layer neural network, comprises three layers: an input layer, one or more hidden layers, and an output layer, as shown in Fig. 5.1. The input layer associates the input vector $\mathbf{u}$ having R elements with input weight matrix $\mathbf{W}^1$ and first bias vector $\mathbf{b}^1$ to yield an effective input $\mathbf{n}^1$ to the activation function $\mathbf{f}^1$, which produces an output vector $\mathbf{a}^1$. The output vector $\mathbf{a}^1$ from the first layer forms the input to the hidden layer and is associated with the weight matrix $\mathbf{W}^2$ and bias vector $\mathbf{b}^2$ of the hidden layer. At last, the hidden layer output $\mathbf{a}^2$ is given as an input to the output layer and delivers a predicted output $\mathbf{a}^3$ with weight matrix $\mathbf{W}^3$ and bias vector $\mathbf{b}^3$. In a neural network with a total of n_l number of layers, the weight matrix $\mathbf{W}^l$ and bias vector $\mathbf{b}^l$ for layer l (where $l = 1, 2, \ldots, n_l$) can be written as

$$\mathbf{W}^l = \begin{bmatrix} w^l_{11} & w^l_{12} & w^l_{13} & \ldots & w^l_{1R} \\ w^l_{21} & w^l_{22} & w^l_{23} & \ldots & w^l_{2R} \\ \vdots & \vdots & \vdots & \ddots & \vdots \\ w^l_{N^l 1} & w^l_{N^l 2} & w^l_{N^l 3} & \ldots & w^l_{N^l R} \end{bmatrix}, \qquad \mathbf{b}^l = \begin{bmatrix} b^l_1 \\ b^l_2 \\ \vdots \\ b^l_{N^l} \end{bmatrix}, \tag{5.1}$$

where N^l denotes the number of neurons in layer l and the effective input $\mathbf{n}^l$ is then given as

$$\mathbf{n}^l = \mathbf{W}^l \mathbf{a}^{l-1} + \mathbf{b}^l, \qquad \text{with} \quad \mathbf{a}^0 = \mathbf{u}. \tag{5.2}$$

The number of neurons in the input layer (N^1) and output layer (N^3) is linked to the number of input and output vectors, respectively. However, the number of neurons in the hidden layer (N^2) are accountable for the quantification of the weights and biases. The optimal network structure is versed by the optimum number of neurons in each layer required for the training and denoted as N^1-N^2-N^3. A variety of activation functions are used in backpropagation neural network viz., hard limit, linear, sigmoid, log-sigmoid, hyperbolic tangent sigmoid [269]. In the current work, linear activation functions are employed in all the layers according to which, the output is equal to the input i.e. $\mathbf{a}^l = \mathbf{n}^l$.

The network error $\mathbf{e}$ is calculated by subtracting predicted output $\mathbf{a}_o$ from target output $\mathbf{t}_o$. The sensitivity $\mathbf{s}$, i.e. the measure of how the output of the network changes due to perturbations in the input, is back-propagated from output layer ($\mathbf{s}^3$) to input layer ($\mathbf{s}^1$) via the hidden layer ($\mathbf{s}^2$). Through the backpropagation

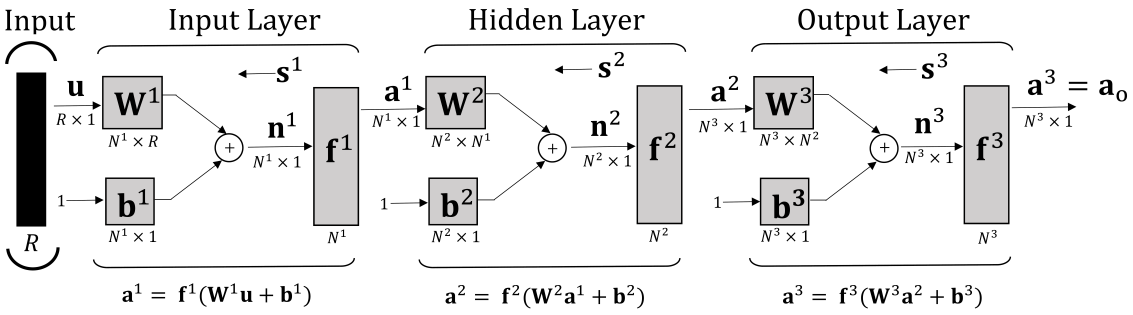

Figure 5.1: A typical backpropagation neural network with input, hidden, and output layers. Adapted with permission from Hagan et al. [270].

process, the error of the neurons in the hidden layer is estimated as the backward weighted sum of the sensitivity. Thereafter, to update weights, different learning algorithms are used in association with the sensitivity such as the steepest descent, LM, and conjugate gradient algorithms. The sensitivity at layer l is calculated using the recurrence relation [269]

$$\mathbf{s}^{l} = \dot{\mathbf{F}}^{l}\left(\mathbf{n}^{l}\right) \mathbf{W}^{l+1}\, \mathbf{s}^{l+1}, \quad \text{where } l = n_l - 1, \ldots, 2, 1, \tag{5.3}$$

$$\text{with} \quad \mathbf{s}^{n_l} = \dot{\mathbf{F}}^{n_l}\left(\mathbf{n}^{n_l}\right) \left(\mathbf{t}_{\mathrm{o}} - \mathbf{a}_{\mathrm{o}}\right), \tag{5.4}$$

where $\dot{\mathbf{F}}^{l}(\mathbf{n}^{l})$ is a diagonal matrix containing the partial derivatives of the activation function $\mathbf{f}^{l}$ with respect to the net inputs $\mathbf{n}^{l}$ and is given as

$$\dot{\mathbf{F}}^{l}\left(\mathbf{n}^{l}\right) = \begin{bmatrix} \dot{f}^{l}\left(n_1^{l}\right) & 0 & \ldots & 0 \\ 0 & \dot{f}^{l}\left(n_2^{l}\right) & \ldots & 0 \\ \vdots & \vdots & \ddots & \vdots \\ 0 & 0 & \ldots & \dot{f}^{l}\left(n_{N^l}^{l}\right) \end{bmatrix}, \quad \text{where} \quad \dot{f}^{l}\left(n_j^{l}\right) = \frac{\partial f^{l}\left(n_j^{l}\right)}{\partial n_j^{l}}, \tag{5.5}$$

and for the considered linear activation function is equal to the identity matrix.

The purpose of a backpropagation neural network model is to ensure a network with small deviations for the training dataset and supervise the unknown inputs effectively. The intricacy of the BPNN, monitored by neurons in the hidden layer and their associated weights, leads to overfitting, i.e. the network tries to make the error as small as possible for the training set but performs poorly when new data is presented. However, a robust network model should be able to generalize well, i.e. it should predict well even when presented with new data. Therefore, Bayesian regularization based learning of BPNN models is utilized to achieve better generalization and minimal over-fitting for the trained networks [236, 237].

Consider a neural network with training dataset D having n_t number of input

$\mathbf{u}$ and target $\mathbf{t}_{\mathrm{o}}$ vector pairs in the network model, i.e

$$D = \left\{ \left(\mathbf{u}_1, \mathbf{t}_{\mathrm{o}1}\right), \left(\mathbf{u}_2, \mathbf{t}_{\mathrm{o}2}\right), \ldots, \left(\mathbf{u}_{n_t}, \mathbf{t}_{\mathrm{o}n_t}\right) \right\}. \tag{5.6}$$

For each input to the network, the difference between target output ($\mathbf{t}_{\mathrm{o}}$) and predicted output ($\mathbf{a}_{\mathrm{o}}$) is computed as error $\mathbf{e}$. In order to evaluate the performance of the network, i.e. how well the neural network is fitting the test data, a quantitative measure is needed. This measure is called performance index of the network and is used to optimize the network parameters. The standard performance index $F(\bar{\mathbf{w}})$ is governed by the sum of the squared errors (SSE)

$$F(\bar{\mathbf{w}}) = E_D = \sum_{i=1}^{n_t} \left(\mathbf{e}_i\right)^2 = \sum_{i=1}^{n_t} \left(\mathbf{t}_{\mathrm{o}i} - \mathbf{a}_{\mathrm{o}i}\right)^{\mathrm{T}} \left(\mathbf{t}_{\mathrm{o}i} - \mathbf{a}_{\mathrm{o}i}\right) , \tag{5.7}$$

where $\bar{\mathbf{w}}$ denotes the vector of size K containing all the weights and biases of the network

$$\bar{\mathbf{w}}^{\mathrm{T}} = \left[\mathbf{w}^1,\ \mathbf{w}^2, \ldots,\ \mathbf{w}^{n_l}\right]_{1\times K} , \tag{5.8}$$

where

$$K = N^1 \left(R+1\right) + N^2 \left(N^1+1\right) + \ldots + N^{n_l} \left(N^{n_l-1}+1\right) , \tag{5.9}$$

and

$$\left(\mathbf{w}^l\right)^{\mathrm{T}} = \left[w^l_{11}\,,\ w^l_{12}\,, \ldots\,, w^l_{N^1 R}\,,\ \ b^l_1\,,\ b^l_2\,, \ldots\,, b^l_{N^l}\right] . \tag{5.10}$$

As described in the introduction, in order to generalize the neural network, the performance index of Eq. (5.7) is modified using a regularization method. A penalty term $(\mu_{\mathrm{r}}/\nu_{\mathrm{r}})E_{\mathrm{w}}$ is added to the performance index $F(\bar{\mathbf{w}})$ [271],

$$F\left(\bar{\mathbf{w}}\right) = \mu_{\mathrm{r}} E_{\mathrm{w}} + \nu_{\mathrm{r}} E_D\,, \tag{5.11}$$

where μ_{r} and ν_{r} are the regularization parameters and E_{w} represents the sum of the squared network weights (SSW), i.e.

$$E_{\mathrm{w}} = \bar{\mathbf{w}}^{\mathrm{T}}\, \bar{\mathbf{w}}. \tag{5.12}$$

Finding the optimum values for μ_{r} and ν_{r} is a challenging task, as their comparative values set up the basis for the training error. If $\mu_{\mathrm{r}} << \nu_{\mathrm{r}}$, smaller errors are generated, while if $\mu_{\mathrm{r}} >> \nu_{\mathrm{r}}$, there should be reduced weight size at the cost of network errors [240]. For the purpose of finding the optimum regularization parameters, a Bayesian regularization (BR) method is employed.

Considering the network weights $\bar{\mathbf{w}}$ as random variables, the aim is to choose the weights that maximize the posterior probability distribution of the weights $P\left(\bar{\mathbf{w}}|D, \mu_{\mathrm{r}}, \nu_{\mathrm{r}}, M_N\right)$ given a certain data D. According to Bayes' rule [236],

the posterior distribution of the weights depends on the likelihood function $P\big(D|\bar{\mathbf{w}}, \nu_{\mathrm{r}}, M_N\big)$, the prior density $P\big(\bar{\mathbf{w}}|\mu_{\mathrm{r}}, M_N\big)$, and the normalization factor $P\big(D|\mu_{\mathrm{r}}, \nu_{\mathrm{r}}, M_N\big)$ for a particular neural network model M_N and can be evaluated from

$$P\big(\bar{\mathbf{w}}|D, \mu_{\mathrm{r}}, \nu_{\mathrm{r}}, M_N\big) = \frac{P\big(D|\bar{\mathbf{w}}, \nu_{\mathrm{r}}, M_N\big)\, P\big(\bar{\mathbf{w}}|\mu_{\mathrm{r}}, M_N\big)}{P\big(D|\mu_{\mathrm{r}}, \nu_{\mathrm{r}}, M_N\big)}\,. \tag{5.13}$$

Considering that the noise in the training set has a Gaussian distribution, the likelihood function is given by

$$P\big(D|\bar{\mathbf{w}}, \nu_{\mathrm{r}}, M_N\big) = \frac{\exp\big(-\nu_{\mathrm{r}} E_D\big)}{Z_D\big(\nu_{\mathrm{r}}\big)}\,, \tag{5.14}$$

where $Z_D = \big(\pi/\nu_{\mathrm{r}}\big)^{Q/2}$ and $Q = n_t \times N^{n_l}$.

Similarly, assuming a Gaussian distribution for the network weights, the prior probability density $P\big(\bar{\mathbf{w}}|\mu_{\mathrm{r}}, M_N\big)$ is given as

$$P\big(\bar{\mathbf{w}}|\mu_{\mathrm{r}}, M_N\big) = \frac{\exp\big(-\mu_{\mathrm{r}} E_{\mathrm{w}}\big)}{Z_{\mathrm{w}}\big(\mu_{\mathrm{r}}\big)}\,, \tag{5.15}$$

where $Z_{\mathrm{w}} = \big(\pi/\alpha\big)^{K/2}$.

The posterior probability with the network weights $\bar{\mathbf{w}}$ can then be expressed as [240]

$$P\big(\bar{\mathbf{w}}|D, \mu_{\mathrm{r}}, \nu_{\mathrm{r}}, M_N\big) = \frac{\exp\big(-\mu_{\mathrm{r}} E_{\mathrm{w}} - \nu_{\mathrm{r}} E_D\big)}{Z_F\big(\mu_{\mathrm{r}}, \nu_{\mathrm{r}}\big)} = \frac{\exp\big(-F(\bar{\mathbf{w}})\big)}{Z_F\big(\mu_{\mathrm{r}}, \nu_{\mathrm{r}}\big)}\,, \tag{5.16}$$

where $Z_F\big(\mu_{\mathrm{r}}, \nu_{\mathrm{r}}\big) = Z_D\big(\nu_{\mathrm{r}}\big) Z_{\mathrm{w}}\big(\mu_{\mathrm{r}}\big)$ is the normalization factor.

The complexity of the model M_N is governed by regularization parameters μ_{r} and ν_{r}, which need to be estimated from the data. Therefore, Bayes' rule is again applied to optimize them as follows:

$$P\big(\mu_{\mathrm{r}}, \nu_{\mathrm{r}}|D, M_N\big) = \frac{P\big(D|\mu_{\mathrm{r}}, \nu_{\mathrm{r}}, M_N\big)\, P\big(\mu_{\mathrm{r}}, \nu_{\mathrm{r}}|M_N\big)}{P\big(D|M_N\big)}\,, \tag{5.17}$$

where $P\big(\mu_{\mathrm{r}}, \nu_{\mathrm{r}}|M_N\big)$ denotes the assumed uniform prior density for the parameters μ_{r} and ν_{r}. From Eq. (5.17), it is evident that maximizing the likelihood function $P\big(D|\mu_{\mathrm{r}}, \nu_{\mathrm{r}}, M_N\big)$ eventually maximizes the posterior probability $P\big(\mu_{\mathrm{r}}, \nu_{\mathrm{r}}|D, M_N\big)$. Moreover, it can be noted that the likelihood function in Eq. (5.17) is the normalization factor of Eq. (5.13). Therefore, solving for the likelihood function $P\big(D|\mu_{\mathrm{r}}, \nu_{\mathrm{r}}, M_N\big)$ and expanding the objective function in Eq. (5.11) around the minimal point $\bar{\mathbf{w}}^*$ via a Taylor series expansion, the optimum values of regulariza-

tion parameters can be evaluated as follows [272]

$$\mu_{\mathrm{r}}^{*}=\frac{\gamma_{\mathrm{ep}}}{2E_{\mathrm{w}}\left(\bar{\mathbf{w}}^{*}\right)} \qquad \text{and} \qquad \nu_{\mathrm{r}}^{*}=\frac{Q-\gamma_{\mathrm{ep}}}{2E_{D}\left(\bar{\mathbf{w}}^{*}\right)}\,, \tag{5.18}$$

where γ_{ep} signifies the "number" of effective parameters exhausted in minimizing the error function

$$\gamma_{\mathrm{ep}}=K-\mu_{\mathrm{r}}^{*}\mathrm{tr}\left(\mathbf{H}^{*}\right)^{-1}, \quad \text{for} 0\leq\gamma_{\mathrm{ep}}\leq K\,, \tag{5.19}$$

and $\mathbf{H}^{*}$ is the Hessian matrix of the objective function evaluated at $\bar{\mathbf{w}}^{*}$. This minimum point is found by using Levenberg-Marquardt algorithm and the Gauss-Newton approximation is used to evaluate Hessian matrix [269]

$$\mathbf{H}=\boldsymbol{\nabla}^{2}F(\mathbf{w}^{*})\approx 2\nu_{\mathrm{r}}\mathbf{J}^{\mathrm{T}}\mathbf{J}+2\mu_{\mathrm{r}}\mathbf{I}\,, \tag{5.20}$$

where $\mathbf{J}$ is the Jacobian matrix formed by the first derivatives of the network errors $\mathbf{e}$ with respect to network weights w_{ij}. In (5.19), $\mathrm{tr}(\cdot)$ denotes the trace operator. The normalization factor $Z_{F}(\mu_{\mathrm{r}},\nu_{\mathrm{r}})$ can then be approximated as [269]

$$Z_{F}\left(\mu_{\mathrm{r}},\nu_{\mathrm{r}}\right)\approx\left(2\pi\right)^{K/2}\left[\det\left(\mathbf{H}^{*}\right)\right]^{-1/2}\exp\left(-F\left(\bar{\mathbf{w}}^{*}\right)\right). \tag{5.21}$$

The problem of computing the Hessian matrix at the minimal point $\bar{\mathbf{w}}^{*}$ is implicitly solved in the Levenberg-Marquardt (LM) optimization algorithm while finding the minimum of $F(\bar{\mathbf{w}})$. The network weights and biases at the k^{th} iteration are updated following the Levenberg-Marquardt optimization algorithm as [236, 272]

$$\bar{\mathbf{w}}^{k+1}=\bar{\mathbf{w}}^{k}-\left[\mathbf{J}^{\mathrm{T}}\mathbf{J}+\lambda_{\mathrm{LM}}\mathbf{I}\right]^{-1}\mathbf{J}^{\mathrm{T}}\mathbf{e}\,, \tag{5.22}$$

where $\mathbf{J}^{\mathrm{T}}\mathbf{e}$ is the error gradient, which needs to be close to zero at end of the training. Here, λ_{LM} denotes the Levenberg's damping factor. As λ_{LM} increases, LM optimization algorithm approaches steepest descent algorithm with small learning rate, while as λ_{LM} is decreased to zero, the LM algorithm is identical to Gauss-Newton optimization.

5.2 Implementation of BR-BPNN

In this work, the inputs $\mathbf{u}$ of the BR-BPNN models are the seventeen peeling angle values θ_{p} ranging from 10° to 90° at an interval of 5°. The seventeen peeling angles are divided into the training, validation and testing sub-datasets as shown in Table 5.1. The training dataset is used to train the neural network model using

Table 5.1: Division of the input dataset.

Input Dataset	Peeling angles (θ_p)
Training set	$10°, 15°, 20°, 25°, 30°, 35°, 40°, 45°, 60°, 65°, 70°, 75°, 80°$
Validation set	Not required
Testing set	$50°, 55°, 85°, 90°$

Bayesian regularization method and the trained model is further validated with the validation dataset. The validation dataset, in other back-propagation training algorithms, is used to optimize the hyperparameters for effective training. The hyperparameters, like the number of neurons in the hidden layer and the learning parameters such as γ_{ep} and λ_{LM}, are defined as the variables required for training the neural network. However, for BR based learning networks, the hyperparameters in the form of the regularization parameters (μ_r, ν_r) are implicitly optimized using Eq. (5.11). Therefore, the validation set is not essentially required in this case for optimizing the network hyperparameters. Finally, the testing dataset is utilized to predict the targeted output $\mathbf{t}_o$ and analyze the model performance, accordingly. Appendix C.2 presents a simple algorithmic overview of BR-BPNN.

Next, three BR-BPNN models are formed with three different output datasets; each having two output vectors, as shown in Table 5.2. The two output vectors for BPNN-I are the applied displacement at force maximum $\bar{\boldsymbol{u}}^{max}$ and the maximum normal pull-off force $\boldsymbol{F}_N^{max}$, for BPNN-II they are the applied displacement at force maximum $\bar{\boldsymbol{u}}^{max}$ and the maximum tangential pull-off force $\boldsymbol{F}_T^{max}$, and for BPNN-III they are the applied displacement at detachment $\bar{\boldsymbol{u}}^{det}$ and the resultant force angle at detachment $\boldsymbol{\alpha}^{det}$, respectively. Each output vector consists of 17 elements in all three models. However, only thirteen elements corresponding to the input training dataset (see Table 5.1) are selected for training the BPNN models. Then, the input and output vectors are normalized by the corresponding maximum values. The performance of BR-BPNN models are estimated by comparing the MSE values with the number of neurons in the hidden layer and determining the optimal number. The MSE is computed using the network error and defined as the mean of the sum of squared networks errors, i.e.

$$\text{MSE} = \frac{1}{n_t} E_D. \tag{5.23}$$

5.3 Results and discussion

This section presents the BR based backpropagation neural network predictions of the maximum normal pull-off force F_N^{max}, the maximum tangential pull-off force

Table 5.2: Output dataset for three different BR-BPNN models (see Appendix C.1 for the FE results).

BPNN-I	
Applied displacement at force maximum	$\bar{\boldsymbol{u}}^{\max} := [\bar{u}_1^{\max}, \bar{u}_2^{\max}, \ldots\ldots, \bar{u}_{16}^{\max}, \bar{u}_{17}^{\max}]^{\mathrm{T}}$
Maximum normal pull-off force	$\boldsymbol{F}_{\mathrm{N}}^{\max} := \left[F_{N_1}^{\max}, F_{N_2}^{\max} \ldots\ldots, F_{N_{16}}^{\max}, F_{N_{17}}^{\max}\right]^{\mathrm{T}}$
BPNN-II	
Applied displacement at force maximum	$\bar{\boldsymbol{u}}^{\max} := [\bar{u}_1^{\max}, \bar{u}_2^{\max}, \ldots\ldots, \bar{u}_{16}^{\max}, \bar{u}_{17}^{\max}]^{\mathrm{T}}$
Maximum tangential pull-off force	$\boldsymbol{F}_{\mathrm{T}}^{\max} := \left[F_{T_1}^{\max}, F_{T_2}^{\max} \ldots\ldots, F_{T_{16}}^{\max}, F_{T_{17}}^{\max}\right]^{\mathrm{T}}$
BPNN-III	
Applied displacement at detachment	$\bar{\boldsymbol{u}}^{\mathrm{det}} := \left[\bar{u}_1^{\mathrm{det}}, \bar{u}_2^{\mathrm{det}}, \ldots\ldots, \bar{u}_{16}^{\mathrm{det}}, \bar{u}_{17}^{\mathrm{det}}\right]^{\mathrm{T}}$
Resultant force angle at detachment	$\boldsymbol{\alpha}^{\mathrm{det}} := \left[\alpha_1^{\mathrm{det}}, \alpha_2^{\mathrm{det}} \ldots\ldots, \alpha_{16}^{\mathrm{det}}, \alpha_{17}^{\mathrm{det}}\right]^{\mathrm{T}}$

$F_{\mathrm{T}}^{\max}$, and the resultant force angle at detachment α^{det} along with the corresponding displacements $\bar{u}^{\max}$ and $\bar{u}^{\mathrm{det}}$. Predictions of the networks are then compared with the finite element results obtained in Chapter 4 that have not been yet used for training.

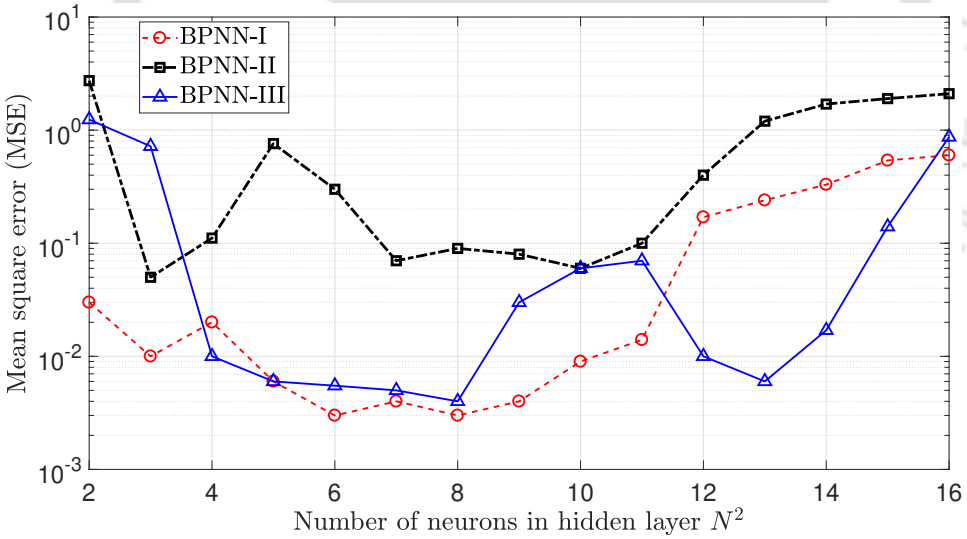

Figure 5.2: Mean square error vs. number of neurons in the hidden layer for different BPNN models.

To define the optimal structure of each network model, the mean square error (MSE) of Eq. (5.23) is investigated along with the number of neurons (1 to 16) in the hidden layer. For the three BR based BPNN models (BPNN- I, BPNN- II and BPNN- III), training is performed with 1 to 16 hidden neurons. The MSE values for all three models with only one hidden neuron are found to be very high i.e. $152, 9.47$ and 5.79, being incapable to form an efficient network. However, as

the number of hidden neurons increases to two, a sudden drop in the MSE values (0.03, 2.74, and 1.24) is recorded. Each model is trained 15 times independently for different number of neurons to mitigate the unfavorable effects by choosing random initial weights. Each network model is trained for a maximum of 2000 epochs. An epoch is completed when the entire training dataset is passed forward and backward through the network thus updating the weights once. For the BPNN-II, the mean square error attains a broad minimum and continuous to decrease between 8 and 10 hidden neurons as shown in Fig. 5.2. For N^2 greater than 11, the MSE value again starts to rise due to overfitting of the network models. Therefore, for BPNN- II the number of neurons in the hidden layer is selected as 8. The number of neurons in the input and output layers are taken as 1 and 2 as there is one input vector and two output vectors for each model. Then the optimal network structure of BPNN-II is formed as 1-8-2. Following a similar trend, the optimal number of hidden neurons for BPNN-I and BPNN-III models is found to be 6 and 5, forming the network structure 1-6-2 and 1-5-2, respectively (see Table 5.3).

Either of the following criteria are selected to terminate or complete the training process: maximum number of epochs reached, minimum value of performance gradient reached, minimum constant value of effective parameters (γ_{ep}) reached, maximum value of Levenberg's damping factor (λ_{LM}) attained, or MSE reached within the performance limits. The training results are achieved at 717, 1992, and 1000 epochs for the three different models having MSE of 0.003, 0.09, and 0.006. The minimal converged value of number of effective parameters γ_{ep} (Eq. (5.19)) for the three models are recorded as 19.5, 19.8, and 14.2, respectively. The other network training parameters like the training time, sum of square errors (SSE) (Eq. (5.7)), sum of square weights (SSW) (Eq. (5.12)), Levenberg's damping factor, and error gradient (Eq. (5.22)) values are also shown in Table 5.3.

Table 5.3: Training parameters for the three BR-BPNN models.

Network Models	Network Structure	Epochs	Time [Min:sec]	MSE	SSE (E_D)	SSW (E_w)	Number of effective parameters (γ_{ep})	LM Parameter (λ_{LM})	Gradient ($\mathbf{J}^{\text{T}}\mathbf{e}$)
BPNN-I	1-6-2	717	00 : 07	0.003	0.053	137	19.5	1.1×10^{10}	1.16×10^{-3}
BPNN-II	1-8-2	1992	00 : 55	0.090	1.097	70.8	19.8	1.1×10^{10}	8.18×10^{-4}
BPNN-III	1-5-2	1000	00 : 10	0.006	0.036	82.2	14.2	2.0×10^{10}	4.79×10^{-4}

After training the models with input-output dataset containing thirteen values, the testing dataset having the four peeling angles 50°, 55°, 85° and 90°, are utilized to predict the corresponding desired output values. The relative error (RE) is used to measure the accuracy of the network predictions. RE is calculated as the deviation of the predicted result from the desired target result, i.e.

$$\text{RE} = \left(\frac{t_i - a_i}{t_i} \right) , \tag{5.24}$$

where t_i and a_i denote the desired target result and the network prediction for a particular peeling angle of the testing data set, respectively.

5.3.1 Case I: Maximum normal pull-off force

Based on the training parameters from Table 5.3, Fig. 5.3 presents the predicted (BPNN-I) results of the maximum normal pull-off force $F_{\mathrm{N}}^{\max}$ and the corresponding applied displacement $\bar{u}^{\max}$. It can be seen from Fig. 5.3a that the predicted values of $F_{\mathrm{N}}^{\max}$ for $\theta_{\mathrm{p}} = 50°, 55°$, and $85°$ are very close to the desired target results (that are obtained by FE). However, for $\theta_{\mathrm{p}} = 90°$, the predicted results show slightly more deviation compared to the other testing angles. The predictions are similar for $\bar{u}^{\max}$ as shown in Fig. 5.3b. This can also be observed from Table 5.4, which lists the relative error (RE) for the four testing angles.

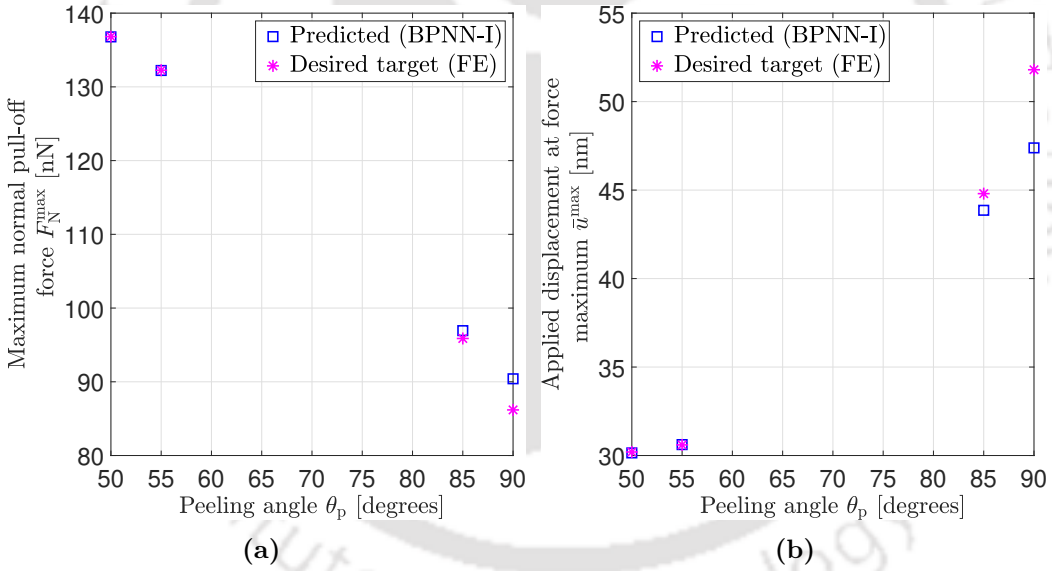

Figure 5.3: Predictions from BR-BPNN-I (a) maximum normal pull-off force $F_{\mathrm{N}}^{\max}$ and (b) applied displacement values at the force maximum $\bar{u}_{\max}$.

Table 5.4: Relative error (RE) for the predictions of BR-BPNN-I model.

Peeling angle θ_{p} [degrees]	RE in $\bar{u}^{\max}$[%]	RE in $F_{\mathrm{N}}^{\max}$[%]
50°	0.1008	0.0276
55°	0.0328	0.0244
85°	1.8180	0.7779
90°	8.5212	3.0867

5.3.2 Case II: Maximum tangential pull-off force

From Table 5.3, the training parameters of BPNN-II are utilized to predict the maximum tangential pull-off force $F_{\mathrm{T}}^{\max}$ and the corresponding applied displacement $\bar{u}^{\max}$ at the four testing angles. As shown in Fig. 5.4a, deviations of the values predicted using BR-BPNN for all the testing angles $\theta_{\mathrm{p}} = 50°$, $55°$, $85°$, and $90°$ are very small. However, for $\bar{u}^{\max}$ the predicted values show slightly larger deviation from the desired target results for $\theta_{\mathrm{p}} = 90°$. The RE for both $F_{\mathrm{T}}^{\max}$ and $\bar{u}^{\max}$ is given in Table 5.5. These results show that except for $\bar{u}^{\max}$ at $\theta_{\mathrm{p}} = 90°$, the current neural network is very accurate.

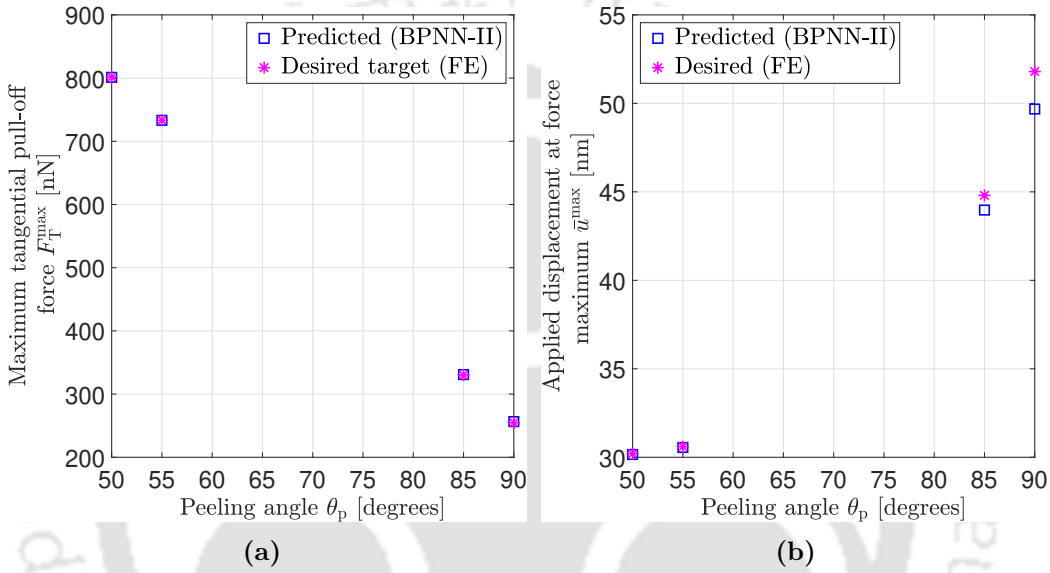

Figure 5.4: Predictions from BR-BPNN-II (a) maximum tangential pull-off force $F_{\mathrm{T}}^{\max}$ and (b) applied displacement values at the force maximum $\bar{u}_{\max}$, at four testing peeling angles.

Table 5.5: Relative error (RE) for the predictions of BR-BPNN-II model.

Peeling angle θ_{p} [degrees]	RE in $\bar{u}^{\max}$ [%]	RE in $F_{\mathrm{T}}^{\max}$ [%]
50°	0.0812	0.0301
55°	0.0860	0.0129
85°	1.6023	0.0935
90°	4.0927	0.2420

5.3.3 Case III: Resultant force angle at detachment

Figure 5.5 shows the predictions for the output dataset of BPNN-III, i.e. the applied displacement at detachment $\bar{u}^{\mathrm{det}}$ and the resultant force angle at detachment α^{det} using the corresponding training parameters from Table 5.3. As shown in Fig. 5.5b,

the predicted values of α^{det} are also very close to the desired target results as seen from Fig. 5.5a. The RE values corresponding to α^{det} predictions for 50°, 55°, 85°, and 90° are estimated to be $0.2\%, 0.08\%, 0.73\%$, and 0.61%, respectively. Similarly, the predicted values of $\bar{u}^{\text{det}}$ for $\theta_{\text{p}} = 50°$ and 90° are found to be very close to the desired target results (see Fig. 5.5a). This can also be observed from the RE results in Table 5.6. It can be observed that the predictions are very accurate even outside of the training data set.

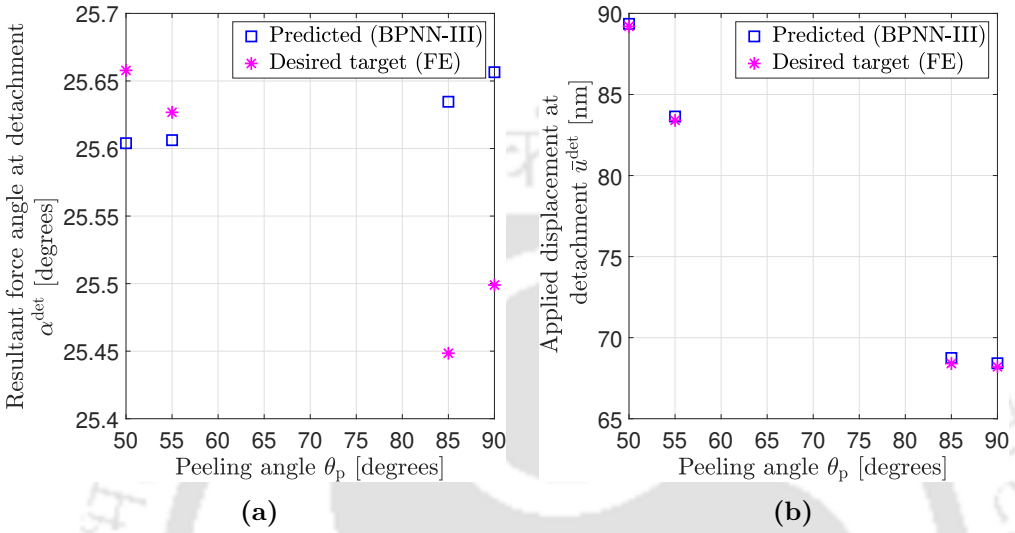

Figure 5.5: Predictions of BR-BPNN-III (a) the resultant force angle at detachment α^{det} and (b) applied displacement at detachment $\bar{u}_{\text{det}}$, at four testing peeling angles.

Table 5.6: Relative error (RE) for the predictions of BR-BPNN-III model.

Peeling angle θ_{p} [degrees]	RE in $\bar{u}^{\text{det}}$ [%]	RE in α^{det} [%]
50°	0.1748	0.2099
55°	0.2704	0.0803
85°	0.3880	0.7256
90°	0.2482	0.6140

From all these results, it can be observed that out of the three BR-BPNN models, predictions of BPNN-III are closer to the target outputs compared to other two models. Also, for BR-BPNN-I and BR-BPNN-II, deviations in the predictions are larger for $u^{\max}$ than for $F_{\text{N}}^{\max}$ and $F_{\text{T}}^{\max}$. BPNN-III performs better even for the data outside the training data set, which is due to the fact that α^{det} is fairly invariant with the peeling angle θ_{p} as observed in section 4.3.2. Thus, for this case, extrapolation is straightforward. Whereas, in case of BPNN-I and BPNN-II, the values of $\bar{u}^{\max}$, $F_{\text{N}}^{\max}$, and $F_{\text{T}}^{\max}$ vary significantly with the peeling angle θ_{p}. As such, extrapolation becomes difficult for the network. However, both BPNN-I and BPNN-II extrapolate reasonably well in case of maximum normal and tangential forces, but deviate in case of the corresponding applied displacement. This behaviour of the neural network

is consistent with the fact that the Bayesian regularization generalizes very well in interpolation but is not good at extrapolation [269].

The important advantage of these ANN models lies in the significant reduction in computational cost. As seen from Table 5.3, the time to train the networks with the data corresponding to 15 peeling angles for all the three networks is only one minute. Similarly, once the network is trained, any number of predictions can be made within minutes. In contrast, the finite element simulations of the two-dimensional spatula model for a particular peeling angle θ_p, take anywhere between 10 hours to 1 hour depending on the peeling angle. Thus, augmenting the FE models with ANNs can significantly reduce the computational times.

भारतीय प्रौद्योगिकी संस्थान गुवाहाटी
Indian Institute of Technology Guwahati

Chapter 6

Conclusions and Scope for the Future Work

This chapter concludes the thesis first by presenting a summary of the work carried out, followed by discussing the conclusions that can be drawn from the work. Finally, the possible extensions to the current work are presented.

6.1 Summary

A continuum-based computational framework is developed within the setting of nonlinear finite element analysis, to study the coupled adhesion and friction behaviour in gecko spatula peeling from a flat rigid substrate. The adhesive interactions between the atoms of the spatula and the substrate due to van der Waals forces are described by the Lennard-Jones potential. The global interaction potential is then computed using the methodology of homogenization and coarse-graining of these interatomic interactions [137, 138]. The weak form governing the normal (adhesive) interactions is then formulated using the principle of minimum potential energy. The constitutive relation governing the elastic response of the spatula is modelled using the isotropic, nonlinear Neo-Hookean material model. As the gecko can generate friction forces even for tensile normal loads, the classical Coulomb-Amontons friction law, which defines friction only for compressive normal loads, cannot be applied to evaluate the frictional response. As such, in order to model the interfacial friction due to adhesion a continuum model of Mergel et al. [202] is employed. A distance-dependent sliding traction threshold is defined which is a function of the normal adhesive traction to capture the sliding friction even for zero and negative normal pressures. If the tangential (frictional) traction becomes equal to or greater than this threshold value, the interacting bodies start to slide with respect to each other. Constitutive equations for the friction are formulated

following the elasto-plasticity framework in which principle of maximum dissipation is used to derive the evolution equation. An algorithmic treatment following the unbiased friction formulation of Sauer and DeLorenzis [258], which is based on the classical predictor-corrector algorithm, is outlined to solve the formulated evolution equation. The finite element method is employed to discretize to the weak form governing the adhesive friction contact. Following the isoparametric concept, the geometry and field variables of each finite element are approximated using the same shape functions. Using the finite element approximations for each element and performing assembly over all the elements, a global nonlinear boundary value problem is formulated. Expressions for the tangent matrices corresponding to internal and contact force vectors are derived. The nonlinear equation describing the system response is linearized and solved using the Newton-Raphson iterative method. To address the issue of convergence in Newton-Raphson iteration arising due to inaccurate capture of the nonlinear contact tractions and to reduce the computational cost in utilizing very fine finite element meshes, a local surface enrichment strategy is employed. In this strategy, the contact surface is discretized using higher-order Lagrange polynomials, while the bulk is described using standard linear Lagrangian approximations.

A nonlinear finite element code is developed to implement the finite element formulation. The code is first validated by solving the problem of peeling a two-dimensional thin strip from a flat rigid substrate. The performance of the enrichment strategy is evaluated, and the results are compared with those in the existing literature. The code is then used to analyse the coupled adhesion and friction behaviour in the peeling of gecko spatula. A thin strip under plane strain conditions is used to represent the spatula following other studies in the literature [99, 144, 165]. The coupled adhesion and friction phenomenon is investigated by studying the normal and tangential pull-off force characteristics and the presence of critical detachment angle at the spatula level. The influence of various parameters such as the peeling angle, the shaft angle, spatula pad thickness, material stiffness, friction coefficient, and the shaft length on the pull-off forces and the critical detachment angle is investigated. Next, a three-dimensional (3D) finite element model is also used to study the peeling behaviour of the gecko spatula. Both frictional and frictionless peeling of the 3D gecko spatula is analysed to estimate the pull-off forces and deformation of the spatula. Variation of the pull-off forces with peeling angle for small frictional coefficients is investigated.

Finally, the application of artificial neural networks to peeling computations is discussed. A Bayesian regularization based backpropagation learning method is used to train artificial neural networks (ANN) to predict certain aspects of the spatula peeling behaviour viz. the maximum normal force, the maximum tangential

force, and the resultant force angle at detachment corresponding to different peeling angles.

6.2 Conclusions

Based on the results presented in Chapters 4 and 5, the following conclusions are drawn:

6.2.1 Pull-off forces

(i) Partial sliding at the peeling front during the peeling off the spatula leads to an increase in the stored strain energy. This, in turn, increases the maximum pull-off force reached during peeling. The increase in strain energy is much higher when the spatula is pulled at low peeling angles as compared to high peeling angles. As a result, gecko spatula generates higher pull-off forces at low peeling angles.

(ii) Investigating the influence of peeling angle shows that the major part of large pull-off forces at small peeling angles is due to the large friction forces. The normal (adhesion) forces decrease as the peeling angle is increased despite the fact that the total area of contact on which the van der Waals forces act remains the same at any given peeling angle. This is because, although locally the normal forces are only dependent on the distance-dependent adhesion, globally, the effect of local tangential (friction) forces contribute to the total normal forces generated. Thus, as the tangential forces decrease at higher peeling angles, normal forces also decrease.

(iii) The maximum normal and the tangential pull-off forces obtained using the current computational model match well with the analytical results of Tian et al. [99].

(iv) Further, as the peeling angle is increased, the "adhesion region", which is the range of normal and tangential pull-off forces for which the spatula can remain attached to the substrate, decreases. However, the pull-off forces at the snap-off point remain invariant with the peeling angle.

(v) The partial sliding at the peeling front and the non-zero bending stiffness, significantly influence the pull-off forces as observed by comparing the current model to other analytical models [37, 49].

(vi) For a given peeling angle, the pull-off forces decrease, as the shaft angle increases. This is because the total area of the spatula pad in contact with the

substrate decreases. Further, configurations of the spatula with really small shaft angles and peeling angles probably do not occur as it could potentially lead to crowding of the neighbouring spatulae.

(vii) Spatula pad thickness significantly influences the maximum pull-off forces obtained during the peeling. However, this effect is greater for the increase in thickness from $5 - 10$ nm than for thickness greater than 10 nm. For thicknesses greater than 10 nm, the increase in pull-off forces comes at the cost of compliance and increase in the mass.

(viii) As the material stiffness decreases, the maximum pull-off forces increase. This is because, the spatula becomes more compliant and readily attaches to the substrate. As such, greater force is required to separate the small from the substrate. However, this increase in compliance also increases the stresses in the peeling zone, which could potentially rupture the spatula material.

(ix) Easy detachment of the spatulae is made possible by changing the shaft angle and pulling vertically such that no frictional forces develop. The corresponding results match well with the experimental observations of Huber et al. [66] and Sun et al. [55].

6.2.2 Critical detachment angle

(i) At any given peeling angle, as the spatula is peeled off the substrate, the resultant force angle changes throughout the peeling process. However, at the point of detachment, irrespective of the peeling angle and the shaft angle, the spatula detaches at a constant resultant pull-off force angle called critical detachment angle $\alpha^*_{\text{spatula}}$. For the considered parameters, it is approximately equal to 26°.

(ii) The spatula can stay attached to the substrate even after the sliding starts (and the contact becomes unstable) if the pull-off force and the strain energy values fall within the stability envelope (the pull-off force versus the strain energy curve) corresponding to that peeling angle. Once the spatula is stretched beyond a critical value, called the minimum pre-strain, the spatula can be spontaneously detached by decreasing the applied force below the values given by the stability envelopes. Further, irrespective of the peeling angle, the pull-off force versus the strain energy curves followed same paths initially and after the sliding starts. Moreover, the spatula reaches approximately the same critical energy state irrespective of the peeling angle, which could explain the invariance of the critical detachment angle.

(iii) The spatula exhibits the behaviour governed by the phenomenological "frictional adhesion" model [48]. Following the critical detachment angle of $\alpha^*_{\text{spatula}} \approx 26°$, irrespective of the peeling angle the maximum friction force is always greater than 2.1 times that of the maximum normal force.

(iv) The critical detachment angle, in general, decreases with increasing spatula pad thickness, consistent with the observations in the literature [267]. However, for thicknesses greater than 10 nm, the spatula does not detach at the same angle for large peeling and shaft angles. For large peeling and shaft angles, the spatula does not slide on the substrate, and this is found to influence the invariance of the critical detachment angle.

(v) Invariance of the critical detachment angle remains constant for a wide range of spatula shaft lengths.

6.2.3 Three-dimensional spatula peeling

(i) The Q1C4 contact element formulation even with a coarse mesh is observed to provide sufficiently accurate results compared to the Q1C2 formulation with a fine mesh used in the literature [162].

(ii) In case of the 3D spatula peeling simulations with low friction coefficient, at small peeling angles, an apparent steady-state is observed for tangential pull-off forces. Also, at small peeling angles, the maximum normal and the tangential pull-off forces reached are invariant with the peeling angle. As the friction coefficient decreases, the maximum pull-off forces reached remain constant with the peeling angle, even at high peeling angles.

(iii) Comparison with 2D spatula peeling simulations reveals that the 2D spatula model can capture most essential characteristics of the peeling behaviour observed with the 3D models.

6.2.4 Application of artificial neural networks to peeling computations

(i) Artificial neural networks trained using Bayesian regularization based backpropgation algorithms can provide sufficiently accurate predictions for peeling computations.

(ii) Artificial neural networks have the potential to significantly reduce the high computational times involved with finite element simulations.

6.3 Scope for the future work

In this section, various possible extensions to the current work are discussed.

- In the current work, the coupled adhesion and friction behaviour is evaluated for static peeling of the gecko spatula. However, in practice, the peeling phenomenon is a dynamic process. As such, the current formulation can be extended to investigate dynamic peeling behaviour and analyse the effects of peeling rate.

- The computational framework developed in the thesis is employed to study the gecko spatula peeling. However, the current computational model is not limited by geometrical, kinematical, and material restrictions. Therefore, one possible extension is to employ the current framework to study terminal structures having different geometries such as conical (in stick insects) and mushroom-shaped (in beetles and spiders). Further, the current model can also be extended to model the viscoelastic behaviour exhibited by many biological materials.

- The computational framework can also be used in the design and analysis of gecko-inspired synthetic adhesives.

- In the current work, the surface of the rigid substrate is considered to be smooth. However, in its natural habitat, gecko encounters surfaces which have roughness on various length scales. In order to model the peeling behaviour on these rough surfaces, the current model can be combined with different micromechanical models like that of De Lorenzis and Wriggers [273].

- The macroscale behaviour of the gecko adhesive pads is due to the complex interactions between individual structures in each level of the hierarchy. This behaviour can be modelled by casting the current coupled adhesion and friction model into a multiscale framework such as the one developed by Sauer [146].

- The finite element analysis of the detailed 3D solid model of the gecko spatula tends to be computationally expensive. Various approaches can be employed to reduce the computational time. One such method is to employ a reduced beam model as in the work of Sauer and Mergel [166], in which the 3D solid model is represented by a geometrically exact beam with continuously varying cross-section. Compared to the fine mesh of the 3D spatula model described in Section 4.4, reduced beam model of [166] has 100 times fewer degrees of freedom. This would lead to much lower computational time.

- Another approach to reduce the computational time as well as improve the accuracy of the solution is to employ a hybrid approach such as the one proposed by Corbett and Sauer [268]. This approach combines the accuracy of isogeometric analysis (IGA) with the efficiency of the finite element method. In this approach, the contact surface is described using NURBS basis functions, which can represent the surface geometry accurately. Whereas, the bulk is discretized using simple linear finite elements. Yet another approach is to employ the varying-order NURBS discretization method [274] to overcome the high computational costs involved in the traditional IGA technique. In this method, the contact surface is discretized using higher-order NURBS basis functions while the bulk is represented by the minimum order of NURBS basis functions capable of representing the geometry accurately.

- Further, the neural network models described in the current thesis can be extended to predict the influence of various geometrical, material, and environmental factors on strip peeling. Another interesting problem that can be investigated using BR-BPNN is the constitutive modelling for the hierarchical structures in the gecko adhesion mechanism.

भारतीय प्रौद्योगिकी संस्थान गुवाहाटी
Indian Institute of Technology Guwahati

Appendix A

Internal Tangent Matrices

A.1 Linearization of the internal virtual work

In this section, linearization of the internal virtual work and derivation of the corresponding tangent matrices is discussed. Linearization of the quantities associated with a nonlinear boundary value problem is required for their algorithmic treatment such as in the Newton-Raphson iterations used to solve the nonlinear equilibrium equation in Eq. (3.17). The linearization procedure is followed from the detailed discussion in Wriggers [259].

In general, any tensor-value function $\boldsymbol{f}(\boldsymbol{\varphi})$ can be linearized using the Taylor series expansion at $\bar{\boldsymbol{\varphi}}$ in the direction of the vector $\Delta\boldsymbol{\varphi}$ as

$$L(\boldsymbol{f})\Big|_{\boldsymbol{\varphi}=\bar{\boldsymbol{\varphi}}} = \boldsymbol{f}(\bar{\boldsymbol{\varphi}}) + \mathrm{D}\boldsymbol{f}(\bar{\boldsymbol{\varphi}})\,[\Delta\boldsymbol{\varphi}]\,, \tag{A.1}$$

where $\mathrm{D}\boldsymbol{f}(\bar{\boldsymbol{\varphi}})\,[\Delta\boldsymbol{\varphi}]$ represents the directional derivative of the function $\boldsymbol{f}$ in the direction of the vector $\Delta\boldsymbol{\varphi}$ evaluated at $\bar{\boldsymbol{\varphi}}$ as

$$\mathrm{D}\boldsymbol{f}(\bar{\boldsymbol{\varphi}})\,[\Delta\boldsymbol{\varphi}] = \frac{d}{d\epsilon^*}\left[\boldsymbol{f}(\bar{\boldsymbol{\varphi}} + \epsilon^*\Delta\boldsymbol{\varphi})\right]\Big|_{\epsilon^*=0}. \tag{A.2}$$

The virtual work done by the internal stresses is given by the first term of the weak form in Eq. (2.46) as (here the index k is dropped for brevity)

$$\delta W_{\mathrm{int}}(\boldsymbol{\varphi}, \delta\boldsymbol{\varphi}) = \int_{\Omega_0} \mathrm{Grad}(\delta\boldsymbol{\varphi}) : \boldsymbol{P}\,\mathrm{d}V \tag{A.3}$$

with

$$\mathrm{Grad}(\delta\boldsymbol{\varphi}) = \frac{\partial(\delta\boldsymbol{\varphi})}{\partial\boldsymbol{X}} = \delta\boldsymbol{F}\,. \tag{A.4}$$

Then, the directional derivative of $\delta W_{\mathrm{int}}(\boldsymbol{\varphi}, \delta\boldsymbol{\varphi})$ in the direction of $\delta\boldsymbol{\varphi}$ at $\bar{\boldsymbol{\varphi}}$ is

obtained as

$$D\delta W_{\text{int}}(\bar{\boldsymbol{\varphi}}, \delta\boldsymbol{\varphi})\,[\Delta\boldsymbol{\varphi}] = \int_{\Omega_0} \Big(D\boldsymbol{P}(\bar{\boldsymbol{\varphi}})\,[\Delta\boldsymbol{\varphi}] \Big) : \text{Grad}(\delta\boldsymbol{\varphi})\,\text{d}V\,. \tag{A.5}$$

Noting the relation $\boldsymbol{P} = \boldsymbol{F}\boldsymbol{S}$, we get

$$D\delta W_{\text{int}}(\bar{\boldsymbol{\varphi}}, \delta\boldsymbol{\varphi})\,[\Delta\boldsymbol{\varphi}] = \int_{\Omega_0} \Big\{ \Big[D\boldsymbol{F}(\bar{\boldsymbol{\varphi}})\,[\Delta\boldsymbol{\varphi}] \Big] \bar{\boldsymbol{S}} + \bar{\boldsymbol{F}} \Big[D\boldsymbol{S}(\bar{\boldsymbol{\varphi}})\,[\Delta\boldsymbol{\varphi}] \Big] \Big\} : \text{Grad}(\delta\boldsymbol{\varphi})\,\text{d}V\,, \tag{A.6}$$

where the $\bar{(\bullet)}$ indicates that the quantity is evaluated at $\boldsymbol{\varphi} = \bar{\boldsymbol{\varphi}}$. Using Eq. (A.2), the directional derivative of $\boldsymbol{F}$ at $\bar{\boldsymbol{\varphi}}$ in the direction of $\Delta\boldsymbol{\varphi}$ is given by

$$D\boldsymbol{F}(\bar{\boldsymbol{\varphi}})\,[\Delta\boldsymbol{\varphi}] = \text{Grad}(\Delta\boldsymbol{\varphi})\,. \tag{A.7}$$

Also, the directional derivative of the second Piola-Kirchoff stress tensor $\boldsymbol{S}$ at $\bar{\boldsymbol{\varphi}}$ in the direction of $\Delta\boldsymbol{\varphi}$ is given by

$$D\boldsymbol{S}(\bar{\boldsymbol{\varphi}})\,[\Delta\boldsymbol{\varphi}] = \frac{\partial \boldsymbol{S}}{\partial \boldsymbol{C}}\, D\boldsymbol{C}(\bar{\boldsymbol{\varphi}})\,[\Delta\boldsymbol{\varphi}] \tag{A.8}$$

$$= \frac{1}{2}\,\bar{\mathbb{C}}\,\left[\boldsymbol{F}^{\text{T}}\,\text{Grad}\Delta\boldsymbol{\varphi} + (\text{Grad}\Delta\boldsymbol{\varphi})^{\text{T}}\boldsymbol{F}\right] \tag{A.9}$$

$$= \bar{\mathbb{C}}\, D\boldsymbol{E}(\bar{\boldsymbol{\varphi}})\,[\Delta\boldsymbol{\varphi}]\,, \tag{A.10}$$

due to Eq. (2.3). Here, $\mathbb{C}$ is the material elasticity tensor corresponding to the second Piola-Kirchoff stress tensor $\boldsymbol{S}$ and is similar to the spatial elasticity tensor $\mathbb{c}$ defined in Eq. (2.14). By denoting the directional derivative of the Green-Lagrange strain tensor $\boldsymbol{E}$ at $\bar{\boldsymbol{\varphi}}$ in the direction of $\Delta\boldsymbol{\varphi}$ as

$$D\boldsymbol{E}(\bar{\boldsymbol{\varphi}})\,[\Delta\boldsymbol{\varphi}] = \Delta\bar{\boldsymbol{E}}\,, \tag{A.11}$$

Eq. (A.6) can be written as

$$D\delta W_{\text{int}}(\bar{\boldsymbol{\varphi}}, \delta\boldsymbol{\varphi})\,[\Delta\boldsymbol{\varphi}] = \int_{\Omega_0} \Big\{ \text{Grad}(\Delta\boldsymbol{\varphi})\,\bar{\boldsymbol{S}} + \bar{\boldsymbol{F}}\,\bar{\mathbb{C}}\Delta\bar{\boldsymbol{E}} \Big\} : \text{Grad}(\delta\boldsymbol{\varphi})\,\text{d}V \tag{A.12}$$

$$= \int_{\Omega_0} \Big\{ \text{Grad}(\Delta\boldsymbol{\varphi})\,\bar{\boldsymbol{S}} : \text{Grad}(\delta\boldsymbol{\varphi}) + \bar{\boldsymbol{F}}\,\bar{\mathbb{C}}\Delta\bar{\boldsymbol{E}} : \text{Grad}(\delta\boldsymbol{\varphi}) \Big\}\,\text{d}V \tag{A.13}$$

$$= \int_{\Omega_0} \Big\{ \text{Grad}(\Delta\boldsymbol{\varphi})\,\bar{\boldsymbol{S}} : \text{Grad}(\delta\boldsymbol{\varphi}) + \bar{\mathbb{C}}\Delta\bar{\boldsymbol{E}} : \bar{\boldsymbol{F}}^{\text{T}}\,\text{Grad}(\delta\boldsymbol{\varphi}) \Big\}\,\text{d}V\,. \tag{A.14}$$

Using the major and minor symmetry properties of the fourth-order tensor $\mathbb{C}$, the second term in the above equation can be rewritten as

$$\bar{\mathbb{C}}\Delta\bar{\boldsymbol{E}} : \boldsymbol{F}^{\mathrm{T}}\,\mathrm{Grad}(\delta\boldsymbol{\varphi}) = \bar{\mathbb{C}}\Delta\bar{\boldsymbol{E}} : \frac{1}{2}\Big(\bar{\boldsymbol{F}}^{\mathrm{T}}\,\mathrm{Grad}(\delta\boldsymbol{\varphi}) + \mathrm{Grad}^{\mathrm{T}}(\delta\boldsymbol{\varphi})\,\bar{\boldsymbol{F}}\Big)\,, \tag{A.15}$$

$$= \bar{\mathbb{C}}\Delta\bar{\boldsymbol{E}} : \delta\bar{\boldsymbol{E}} \tag{A.16}$$

due to the definition of the Green-Lagrange strain tensor $\boldsymbol{E}$, see Eq. (2.3). Then, the directional derivative of the internal virtual work in Eq. (A.14) can finally be written as

$$D\delta W_{\mathrm{int}}(\bar{\boldsymbol{\varphi}}, \delta\boldsymbol{\varphi})\,[\Delta\boldsymbol{\varphi}] = \int_{\Omega_0} \Big\{ \mathrm{Grad}(\Delta\boldsymbol{\varphi})\,\bar{\boldsymbol{S}} : \mathrm{Grad}(\delta\boldsymbol{\varphi}) + \bar{\mathbb{C}}\Delta\bar{\boldsymbol{E}} : \delta\bar{\boldsymbol{E}} \Big\}\,\mathrm{d}V\,, \tag{A.17}$$

where the first term corresponds to the geometrical nonlinearities arising from the finite deformations through the stress tensor $\boldsymbol{S}$ and the second term corresponds to the material nonlinearities through the material tensor $\mathbb{C}$. As such, it can be written that

$$D\delta W_{\mathrm{int}}(\bar{\boldsymbol{\varphi}}, \delta\boldsymbol{\varphi})\,[\Delta\boldsymbol{\varphi}] = D\delta W_{\mathrm{geo}}(\bar{\boldsymbol{\varphi}}, \delta\boldsymbol{\varphi})\,[\Delta\boldsymbol{\varphi}] \;+\; D\delta W_{\mathrm{mat}}(\bar{\boldsymbol{\varphi}}, \delta\boldsymbol{\varphi})\,[\Delta\boldsymbol{\varphi}] \tag{A.18}$$

with

$$D\delta W_{\mathrm{geo}}(\bar{\boldsymbol{\varphi}}, \delta\boldsymbol{\varphi})\,[\Delta\boldsymbol{\varphi}] \;=\; \int_{\Omega_0} \mathrm{Grad}(\Delta\boldsymbol{\varphi})\,\bar{\boldsymbol{S}} : \mathrm{Grad}(\delta\boldsymbol{\varphi})\,\mathrm{d}V \tag{A.19}$$

$$D\delta W_{\mathrm{mat}}(\bar{\boldsymbol{\varphi}}, \delta\boldsymbol{\varphi})\,[\Delta\boldsymbol{\varphi}] \;=\; \int_{\Omega_0} \bar{\mathbb{C}}\Delta\bar{\boldsymbol{E}} : \delta\bar{\boldsymbol{E}}\,\mathrm{d}V\,. \tag{A.20}$$

By using the approximations in Eq. (3.3) the gradients of $\delta\boldsymbol{\varphi}$ and $\Delta\boldsymbol{\varphi}$ at point $\boldsymbol{X}$ of an element 'e' can be obtained as

$$\mathrm{Grad}(\delta\boldsymbol{\varphi}) = \mathbf{v}^e \otimes \boldsymbol{\nabla}\mathbf{N}^e\,, \tag{A.21}$$

$$\mathrm{Grad}(\Delta\boldsymbol{\varphi}) = \Delta\boldsymbol{\varphi}^e \otimes \boldsymbol{\nabla}\mathbf{N}^e\,, \tag{A.22}$$

where $\boldsymbol{\nabla} = \partial/\partial\boldsymbol{X}$. Then, the geomterical part (A.19) can be modified as

$$D\delta W_{\mathrm{geo}}(\bar{\boldsymbol{\varphi}}, \delta\boldsymbol{\varphi})\,[\Delta\boldsymbol{\varphi}] = \bigcup_{e=1}^{n_{el}} \int_{\Omega_0^e} \Delta\boldsymbol{\varphi}^e \otimes \boldsymbol{\nabla}\mathbf{N}^e\,\bar{\boldsymbol{S}} : \mathbf{v}^e \otimes \boldsymbol{\nabla}\mathbf{N}^e\,\mathrm{d}V\,. \tag{A.23}$$

Observing that $\boldsymbol{S}$ is a symmetric tensor and using the rules of double contraction and dyadic product it can be written that

$$D\delta W_{\text{geo}}(\bar{\boldsymbol{\varphi}}, \delta\boldsymbol{\varphi})\,[\Delta\boldsymbol{\varphi}] = \bigcup_{e=1}^{n_{el}} \int_{\Omega_0^e} \bar{\boldsymbol{S}} : [\Delta\boldsymbol{\varphi}^e \otimes \boldsymbol{\nabla}\mathbf{N}^e]^{\mathrm{T}}\, \mathbf{v}^e \otimes \boldsymbol{\nabla}\mathbf{N}^e \,\mathrm{d}V \tag{A.24}$$

$$= \bigcup_{e=1}^{n_{el}} \int_{\Omega_0^e} \bar{\boldsymbol{S}} : \left[(\Delta\boldsymbol{\varphi}^e \cdot \mathbf{v}^e)\,(\boldsymbol{\nabla}\mathbf{N}^e)^{\mathrm{T}} \otimes \boldsymbol{\nabla} N_I\right] \mathrm{d}V \tag{A.25}$$

$$= \bigcup_{e=1}^{n_{el}} (\Delta\boldsymbol{\varphi}^e \cdot \mathbf{v}^e) \int_{\Omega_0^e} \left[\boldsymbol{\nabla}\mathbf{N}^e \cdot \bar{\boldsymbol{S}}\, \boldsymbol{\nabla}\mathbf{N}^e\right] \mathrm{d}V \tag{A.26}$$

which can be further modified by noting that $\Delta\boldsymbol{\varphi}^e \cdot \mathbf{v}^e = \Delta\boldsymbol{\varphi}^e \cdot \mathbf{I}\,\mathbf{v}^e$ to get

$$D\delta W_{\text{geo}}(\bar{\boldsymbol{\varphi}}, \delta\boldsymbol{\varphi})\,[\Delta\boldsymbol{\varphi}] = \bigcup_{e=1}^{n_{el}} \mathbf{v}^e \cdot \mathbf{k}^e_{\text{geo}}\, \Delta\boldsymbol{\varphi}^e\,, \tag{A.27}$$

where $\mathbf{k}^e_{\text{geo}}$ is called the elemental geometrical tangent matrix or the initial stress matrix. It is given as

$$\mathbf{k}^e_{\text{geo}} = \int_{\Omega_0^e} \left[\boldsymbol{\nabla}\mathbf{N}^e \cdot \bar{\boldsymbol{S}}\, \boldsymbol{\nabla}\mathbf{N}^e\right] \mathbf{I}\,\mathrm{d}V\,, \tag{A.28}$$

In the matrix form it is expressed as

$$[\mathrm{k}^e_{\text{geo}}]_{ij} = \int_{\Omega_0^e} (\mathbf{N}^e_{,X_k})^{\mathrm{T}}\, S_{kl}\, \mathbf{N}^e_{,X_l}\, \delta_{ij}\,\mathrm{d}V\,, \tag{A.29}$$

where $\mathbf{N}^e_{,X_k} = \partial\mathbf{N}^e/\partial X_k$ with $k = 1, 2, ..., d$. It can also be written in the current configuration as

$$[\mathrm{k}^e_{\text{geo}}]_{ij} = \int_{\Omega_0^e} (\mathbf{N}^e_{,x_i})^{\mathrm{T}}\, \sigma_{ij}\, \mathbf{N}^e_{,x_i}\, \delta_{ij}\,\mathrm{d}v\,. \tag{A.30}$$

Since the structure of $\Delta\bar{\boldsymbol{E}}$ and $\delta\bar{\boldsymbol{E}}$ is same as seen from Eqs. (A.9) and (3.22), the matrix form of $\Delta\boldsymbol{E}^e$ for a given finite element e follows from Eq. (3.24) as

$$\Delta\boldsymbol{E}^e = \mathbf{B}_{\text{TL}}\, \Delta\boldsymbol{\varphi}^e\,, \tag{A.31}$$

Inserting the above relation and Eq. (3.24) into Eq. (A.20) and writing the material elasticity tensor in $\mathbb{C}$ in Voigt notation as $\mathbb{C}_v$ leads to

$$D\delta W_{\text{mat}}(\bar{\boldsymbol{\varphi}}, \delta\boldsymbol{\varphi})\,[\Delta\boldsymbol{\varphi}] = \bigcup_{e=1}^{n_{el}} \mathbf{v}^e \cdot \int_{\Omega_0^e} \mathbf{B}^{\mathrm{T}}_{\text{TL}}\, \mathbb{C}_v\, \mathbf{B}_{\text{TL}}\,\mathrm{d}V\,, \tag{A.32}$$

$$= \bigcup_{e=1}^{n_{el}} \mathbf{v}^e \cdot \mathbf{k}^e_{\text{mat}}\, \Delta\boldsymbol{\varphi}^e\,, \tag{A.33}$$

from which the elemental material tangent matrix follows as

$$\mathbf{k}^e_{\text{mat}} = \int_{\Omega^e_0} \mathbf{B}^{\text{T}}_{\text{TL}}\, \mathbb{C}_v\, \mathbf{B}_{\text{TL}}\, \mathrm{d}V\,, \quad \text{in the reference configuration} \tag{A.34}$$

$$\mathbf{k}^e_{\text{mat}} = \int_{\Omega^e_0} \mathbf{B}^{\text{T}}_{\text{UL}}\, \mathbb{c}_v\, \mathbf{B}_{\text{UL}}\, \mathrm{d}v\,, \quad \text{in the current configuration}\,, \tag{A.35}$$

where $\mathbb{c}_v$ is the Voigt notation representation of the spatial elasticity tensor $\mathbb{c}$.

भारतीय प्रौद्योगिकी संस्थान गुवाहाटी
Indian Institute of Technology Guwahati

Appendix B

Contact Tangent Matrix

B.1 Tangent Matrix for Adhesive Friction

In this section, the tangent matrices corresponding to the contact forces is derived. This is done by linearizing the contact forces, which is required in the Newton-Raphson iterations. Following the procedure detailed in Sauer and De Lorenzis [257, 258], the contact force $\mathbf{f}^e_{ck}$ acting on any given surface element $\delta\Omega^{ae}_k$ can be linearized as

$$\mathbf{f}^e_{ck}(\mathbf{u}^e_k + \Delta\mathbf{u}^e_k, \mathbf{u}^e_l + \Delta\mathbf{u}^e_l) \approx \mathbf{f}^e_{ck}(\mathbf{u}^e_k, \mathbf{u}^e_l) + \mathbf{k}^e_{ckk}(\mathbf{u}^e_k, \mathbf{u}^e_l)\Delta\mathbf{u}^e_k + \mathbf{k}^e_{ckl}(\mathbf{u}^e_k, \mathbf{u}^e_l)\Delta\mathbf{u}^e_l \quad \text{(B.1)}$$

where $k = 1, 2$ and $l \neq k$. The two tangent matrices $\mathbf{k}_{ckk}$ and $\mathbf{k}_{ckl}$ can be obtained from Eq. (2.44) in the reference configuration as

$$\mathbf{k}^e_{ckk} = \frac{\partial \mathbf{f}^e_{ck}}{\partial \mathbf{u}^e_k} = -\int_{\partial\Omega^{ae}_{k0}} (\mathbf{N}^e_k)^{\mathrm{T}} \left[\frac{\partial \boldsymbol{T}_{ak}}{\partial \mathbf{u}^e_k} - \frac{\partial \boldsymbol{T}_{fk}}{\partial \mathbf{u}^e_k}\right] \mathrm{d}A_k \,, \quad \text{(B.2)}$$

$$\mathbf{k}^e_{ckl} = \frac{\partial \mathbf{f}_{ck}}{\partial \mathbf{u}^e_l} = -\int_{\partial\Omega^{ae}_{k0}} (\mathbf{N}^e_k)^{\mathrm{T}} \left[\frac{\partial \boldsymbol{T}_{ak}}{\partial \mathbf{u}^e_l} - \frac{\partial \boldsymbol{T}_{fk}}{\partial \mathbf{u}^e_l}\right] \mathrm{d}A_k \,, \quad \text{(B.3)}$$

where the partial derivatives of the normal (adhesive) and tangential (frictional) tractions are derived in the following sections.

B.1.1 Contact tangent in normal direction

The partial derivatives of the normal tractions $\dfrac{\partial \boldsymbol{T}_{ak}}{\partial \mathbf{u}^e_k}$ and $\dfrac{\partial \boldsymbol{T}_{ak}}{\partial \mathbf{u}^e_l}$ are derived in this section. Recalling the definition of adhesive contact traction in Eq. (2.36) and noting that $\theta_k = 1$ in the current thesis, it can be written that

$$\boldsymbol{T}_{ak} := \frac{T_{ak}\boldsymbol{n}_{\mathrm{p}}}{J_l} \quad \text{with} \quad T_{ak} = \frac{A_{\mathrm{H}}}{2\pi r_0^3}\left[\frac{1}{45}\left(\frac{r_0}{r_{\mathrm{s}}}\right)^9 - \frac{1}{3}\left(\frac{r_0}{r_{\mathrm{s}}}\right)^3\right] . \quad \text{(B.4)}$$

Using the approximations given by Eq. (3.5) and noting that $\mathbf{u}_k^e = \mathbf{x}_k^e - \mathbf{X}_k^e$, the partial derivative of the adhesive contact traction acting in the normal direction can be written as

$$\frac{\partial \boldsymbol{T}_{\mathrm{a}k}}{\partial \mathbf{u}_k^e} = \frac{\partial \boldsymbol{T}_{\mathrm{a}k}}{\partial \boldsymbol{x}_k} \frac{\partial \boldsymbol{x}_k}{\partial \mathbf{u}_k^e} = \frac{\partial \boldsymbol{T}_{\mathrm{a}k}}{\partial \boldsymbol{x}_k} \mathbf{N}_k^e \,. \tag{B.5}$$

Observing that the adhesive traction is a function of three parameters, i.e. $\boldsymbol{T}_{\mathrm{a}k} = \boldsymbol{T}_{\mathrm{a}k}(\boldsymbol{n}_{\mathrm{p}}, r_{\mathrm{s}}, J_l)$, and noting that for the Lennard-Jones potential, volume change is approximately equal to the local surface stretch, i.e. $J_l \approx J_{cl}$ (see Section 2.3), the partial derivative of the adhesive traction with respect to the point $\boldsymbol{x}_k$ in Eq. (B.5) can be rewritten as

$$\frac{\partial \boldsymbol{T}_{\mathrm{a}k}}{\partial \boldsymbol{x}_k} = \frac{1}{J_{cl}^e} \frac{\partial T_{\mathrm{a}k}}{\partial r_{\mathrm{s}}} \boldsymbol{n}_{\mathrm{p}} \otimes \frac{\partial r_{\mathrm{s}}}{\partial \boldsymbol{x}_k} + \frac{T_{\mathrm{a}k}}{J_{cl}^e} \frac{\partial \boldsymbol{n}_{\mathrm{p}}}{\partial \boldsymbol{x}_k} + \frac{\partial \boldsymbol{T}_{\mathrm{a}k}}{\partial J_{cl}^e} \otimes \frac{\partial J_{cl}^e}{\partial \boldsymbol{x}_k} \,. \tag{B.6}$$

Evaluation of the partial derivatives in the three terms in Eq. (B.6) is discussed in the following:

B.1.1a First term

In the first term of Eq. (B.6),

$$\boxed{\frac{\partial T_{\mathrm{a}k}(r_{\mathrm{s}})}{\partial r_{\mathrm{s}}} = T_{\mathrm{a}}'(r_{\mathrm{s}}) = -\frac{A_{\mathrm{H}}}{2\pi r_0^4} \left[\frac{1}{5} \left(\frac{r_0}{r_{\mathrm{s}}} \right)^{10} - \left(\frac{r_0}{r_{\mathrm{s}}} \right)^{4} \right] .} \tag{B.7}$$

Since $r_{\mathrm{s}} = |\boldsymbol{x}_k - \boldsymbol{x}_{\mathrm{p}}|$, the partial derivative of the normal distance with respect to the point $\boldsymbol{x}_k$ can be evaluated as

$$\frac{\partial r_{\mathrm{s}}}{\partial \boldsymbol{x}_k} = \left[\boldsymbol{I} - \left(\frac{\partial \boldsymbol{x}_{\mathrm{p}}}{\partial \boldsymbol{x}_k} \right)^{\mathrm{T}} \right] \boldsymbol{n}_{\mathrm{p}} \,. \tag{B.8}$$

From the mapping of the physical space to the parametric space given by Eq. (2.60) and FE approximations given by Eq. (3.5), we can write

$$\boldsymbol{x}_{\mathrm{p}} = \mathbf{N}_l^e(\boldsymbol{\xi}_{\mathrm{p}})\, \mathbf{x}_l^e \,, \qquad \frac{\partial \boldsymbol{x}_{\mathrm{p}}}{\partial \boldsymbol{x}_k} = \frac{\partial \boldsymbol{x}_{\mathrm{p}}}{\partial \xi_{\mathrm{p}}^\alpha} \otimes \frac{\partial \xi_{\mathrm{p}}^\alpha}{\partial \boldsymbol{x}_k} \,, \tag{B.9}$$

where the partial derivatives $\partial \boldsymbol{x}_{\mathrm{p}} / \partial \xi_{\mathrm{p}}^\alpha$ are simply the co-variant tangent vectors $\boldsymbol{a}_\alpha^{\mathrm{p}}$ $(\alpha = 1, 2)$ at the projection point as defined in Eq. (2.61). They can be evaluated as

$$\boldsymbol{a}_\alpha^{\mathrm{p}} = \frac{\partial \boldsymbol{x}_{\mathrm{p}}}{\partial \xi_{\mathrm{p}}^\alpha} = \mathbf{N}_{l,\alpha}^e(\boldsymbol{\xi}_{\mathrm{p}})\, \mathbf{x}_l^e \,, \tag{B.10}$$

where $\mathbf{N}_{l,\alpha}^e = \partial \mathbf{N}_l^e / \partial \xi^\alpha$. The parametric coordinates $\boldsymbol{\xi}$ of the surface at $\boldsymbol{x}_{\mathrm{p}}$ are

obtained from the nonlinear equation defined in Eq. (2.64) as

$$(\boldsymbol{x}_\mathrm{p} - \boldsymbol{x}_k) \cdot \boldsymbol{a}_\alpha^\mathrm{p} = 0\,, \tag{B.11}$$

which when differentiated with respect to $\boldsymbol{x}_k$, as shown by Sauer and DeLorenzis [257], gives the partial derivative $\partial\xi_\mathrm{p}^\alpha/\partial\boldsymbol{x}_k$ as

$$\frac{\partial \xi_\mathrm{p}^\alpha}{\partial \boldsymbol{x}_k} \;=\; c_\mathrm{p}^{\alpha\beta}\, \boldsymbol{a}_\beta^\mathrm{p}\,, \tag{B.12}$$

where the contra-variant components $c_\mathrm{p}^{\alpha\beta}$ of the tensor $\boldsymbol{c}_\mathrm{p}$ are obtained from the inversion of the covariant components of the tensor $\boldsymbol{d}$ defined as

$$\boldsymbol{d} = d_{\alpha\beta}^\mathrm{p}\, \boldsymbol{a}_\mathrm{p}^\alpha \otimes \boldsymbol{a}_\mathrm{p}^\beta\,, \quad \text{where } d_{\alpha\beta}^\mathrm{p} = \Big[\boldsymbol{a}_\alpha^\mathrm{p}\cdot\boldsymbol{a}_\beta^\mathrm{p} - r_\mathrm{s}\boldsymbol{n}_\mathrm{p}\cdot\boldsymbol{a}_{\alpha,\beta}^\mathrm{p}\Big] \quad \text{and } \boldsymbol{a}_{\alpha,\beta}^\mathrm{p} = \left.\frac{\partial \boldsymbol{a}_\alpha^\mathrm{p}}{\partial \xi_\mathrm{p}^\beta}\right|_{\boldsymbol{\xi}_\mathrm{p}}\,, \tag{B.13}$$

which leads to

$$\frac{\partial \boldsymbol{x}_\mathrm{p}}{\partial \boldsymbol{x}_k} \;=\; c_\mathrm{p}^{\alpha\beta}\, \boldsymbol{a}_\alpha^\mathrm{p} \otimes \boldsymbol{a}_\beta^\mathrm{p}\,. \tag{B.14}$$

The partial derivative in Eq. (B.8) can then be found using Eq. (B.14) as

$$\frac{\partial r_\mathrm{s}}{\partial \boldsymbol{x}_k} = \Big[\boldsymbol{I} - \big(c_\mathrm{p}^{\alpha\beta}\, \boldsymbol{a}_\alpha^\mathrm{p} \otimes \boldsymbol{a}_\beta^\mathrm{p}\big)^\mathrm{T}\Big]\boldsymbol{n}_\mathrm{p}\,. \tag{B.15}$$

From the definition of dyadic product

$$(\boldsymbol{a}_\alpha^\mathrm{p} \otimes \boldsymbol{a}_\beta^\mathrm{p})^\mathrm{T}\, \boldsymbol{n}_\mathrm{p} = (\boldsymbol{a}_\alpha^\mathrm{p} \cdot \boldsymbol{n}_\mathrm{p})\boldsymbol{a}_\beta^\mathrm{p}\,, \tag{B.16}$$

and as the covariant tangent vector $\boldsymbol{a}_\alpha^\mathrm{p}$ is always normal to the surface normal $\boldsymbol{n}_\mathrm{p}$ at the projection point $\boldsymbol{x}_\mathrm{p}$ it follows that

$$\boldsymbol{a}_\alpha^\mathrm{p} \cdot \boldsymbol{n}_\mathrm{p} = 0\,, \tag{B.17}$$

which finally results in

$$\boxed{\frac{\partial r_\mathrm{s}}{\partial \boldsymbol{x}_k} = \boldsymbol{n}_\mathrm{p}\,.} \tag{B.18}$$

B.1.1b Second term

In the second term of Eq. (B.6), the gradient of the surface normal $\boldsymbol{n}_\mathrm{p}$ with respect to $\boldsymbol{x}_k$ can be obtained by first recalling that

$$\boldsymbol{n}_\mathrm{p} = \frac{1}{r_\mathrm{s}}(\boldsymbol{x}_k - \boldsymbol{x}_\mathrm{p})\,. \tag{B.19}$$

Differentiating Eq. (B.19) with respect to $\boldsymbol{x}_k$, we get

$$\begin{aligned}\frac{\partial \boldsymbol{n}_\mathrm{p}}{\partial \boldsymbol{x}_k} &= \frac{1}{r_\mathrm{s}}\frac{\partial(\boldsymbol{x}_k-\boldsymbol{x}_\mathrm{p})}{\partial \boldsymbol{x}_k}+\frac{\partial}{\partial \boldsymbol{x}_k}\left(\frac{1}{r_\mathrm{s}}\right)\otimes(\boldsymbol{x}_k-\boldsymbol{x}_\mathrm{p})\\ &= \frac{1}{r_\mathrm{s}}\left[\frac{\partial \boldsymbol{x}_k}{\partial \boldsymbol{x}_k}-\frac{\partial \boldsymbol{x}_\mathrm{p}}{\partial \boldsymbol{x}_k}\right]+\frac{\partial}{\partial r_\mathrm{s}}\left(\frac{1}{r_\mathrm{s}}\right)\frac{\partial r_\mathrm{s}}{\partial \boldsymbol{x}_k}\otimes(\boldsymbol{x}_\mathrm{p}-\boldsymbol{x}_k)\,. \end{aligned} \tag{B.20}$$

This can be rewritten using Eqs. (B.18) and (B.19) as

$$\frac{\partial \boldsymbol{n}_\mathrm{p}}{\partial \boldsymbol{x}_k}=\frac{1}{r_\mathrm{s}}\left[\boldsymbol{I}-\frac{\partial \boldsymbol{x}_\mathrm{p}}{\partial \boldsymbol{x}_k}-\boldsymbol{n}_\mathrm{p}\otimes\frac{\partial r_\mathrm{s}}{\partial \boldsymbol{x}_k}\right], \tag{B.21}$$

Substituting Eqs. (B.14) and (B.18) into Eq. (B.21) finally results in

$$\boxed{\frac{\partial \boldsymbol{n}_\mathrm{p}}{\partial \boldsymbol{x}_k}=\frac{1}{r_s}\left[\boldsymbol{I}-c_\mathrm{p}^{\alpha\beta}\boldsymbol{a}_\alpha^\mathrm{p}\otimes\boldsymbol{a}_\beta^\mathrm{p}-\boldsymbol{n}_\mathrm{p}\otimes\boldsymbol{n}_\mathrm{p}\right].} \tag{B.22}$$

B.1.1c Third term

In the third term of Eq. (B.6), the partial derivative $\partial \boldsymbol{T}_{\mathrm{ak}}/\partial J_{cl}^e$, can be obtained from Eq. (B.4) as

$$\begin{aligned}\frac{\partial \boldsymbol{T}_{\mathrm{ak}}}{\partial J_{cl}^e} &= \frac{\partial}{\partial J_{cl}^e}\left(\frac{T_{\mathrm{ak}}\boldsymbol{n}_\mathrm{p}}{J_{cl}^e}\right)\\ &= -\frac{T_{\mathrm{ak}}\,\boldsymbol{n}_\mathrm{p}}{\left(J_{cl}^e\right)^2}\,. \end{aligned} \tag{B.23}$$

The local surface stretch J_{cl}^e of body $\mathcal{B}_l$ is defined as

$$J_{cl}^e := \frac{\|\boldsymbol{a}_1^\mathrm{p}\times\boldsymbol{a}_2^\mathrm{p}\|}{\|\boldsymbol{A}_1^\mathrm{p}\times\boldsymbol{A}_2^\mathrm{p}\|} \quad \text{in 3D}\,, \tag{B.24}$$

$$J_{cl}^e := \frac{\|\boldsymbol{a}^\mathrm{p}\|}{\|\boldsymbol{A}^\mathrm{p}\|} \qquad \text{in 2D}\,. \tag{B.25}$$

Its gradient can be obtained following Eq. (B.12) and Appendix D of Sauer and DeLorenzis [257]

$$\boxed{\frac{\partial J_{cl}^e}{\partial \boldsymbol{x}_k}=\frac{\partial J_{cl}^e}{\partial \xi_\mathrm{p}^\alpha}\frac{\partial \xi_\mathrm{p}^\alpha}{\partial \boldsymbol{x}_k}=J_{cl,\alpha}^e\,c^{\alpha\beta}\boldsymbol{a}_\beta^\mathrm{p}\,.} \tag{B.26}$$

Here,

$$J_{cl,\alpha}^e := \frac{\partial J_{cl}^e}{\partial \xi_\mathrm{p}^\alpha}=J_{cl}^e\left[\boldsymbol{a}_\mathrm{p}^\beta\cdot\frac{\partial \boldsymbol{a}_\beta^\mathrm{p}}{\partial \xi_\mathrm{p}^\alpha}-\boldsymbol{A}_\mathrm{p}^\beta\cdot\frac{\partial \boldsymbol{A}_\beta^\mathrm{p}}{\partial \xi_\mathrm{p}^\alpha}\right], \tag{B.27}$$

where $\boldsymbol{a}_{\mathrm{p}}^{\beta}$ and $\boldsymbol{A}_{\mathrm{p}}^{\beta}$ are the contra-variant tangent vectors corresponding to their co-variant counter parts $\boldsymbol{a}_{\beta}^{\mathrm{p}}$ and $\boldsymbol{A}_{\beta}^{\mathrm{p}}$, respectively. They are defined in Eq. (2.62) as

$$\begin{aligned}
\boldsymbol{a}_{\mathrm{p}}^{\beta} &= a^{\alpha\beta}\boldsymbol{a}_{\alpha}^{\mathrm{p}}\,; \quad \left[a^{\alpha\beta}\right] = \left[a_{\alpha\beta}\right]^{-1} \text{ and } a_{\alpha\beta} = \boldsymbol{a}_{\alpha}^{\mathrm{p}}\cdot\boldsymbol{a}_{\beta}^{\mathrm{p}}\,, \\
\boldsymbol{A}_{\mathrm{p}}^{\beta} &= A^{\alpha\beta}\boldsymbol{A}_{\alpha}^{\mathrm{p}}\,; \quad \left[A^{\alpha\beta}\right] = \left[A_{\alpha\beta}\right]^{-1} \text{ and } A_{\alpha\beta} = \boldsymbol{A}_{\alpha}^{\mathrm{p}}\cdot\boldsymbol{A}_{\beta}^{\mathrm{p}}\,.
\end{aligned} \tag{B.28}$$

The partial derivatives $\partial\boldsymbol{a}_{\beta}^{\mathrm{p}}/\partial\xi_{\mathrm{p}}^{\alpha}$ and $\partial\boldsymbol{A}_{\beta}^{\mathrm{p}}/\partial\xi_{\mathrm{p}}^{\alpha}$ can be computed following Eq. (B.10) as

$$\begin{aligned}
\frac{\partial\boldsymbol{a}_{\beta}^{\mathrm{p}}}{\partial\xi_{\mathrm{p}}^{\alpha}} &= \mathbf{N}_{l,\alpha\beta}^{e}(\boldsymbol{\xi}_{\mathrm{p}})\,\mathbf{x}_{l}^{e}\,, \\
\frac{\partial\boldsymbol{A}_{\beta}^{\mathrm{p}}}{\partial\xi_{\mathrm{p}}^{\alpha}} &= \mathbf{N}_{l,\alpha\beta}^{e}(\boldsymbol{\xi}_{\mathrm{p}})\,\mathbf{X}_{l}^{e}\,.
\end{aligned} \tag{B.29}$$

If the second body $\mathcal{B}_l$ is rigid and motionless then Eq. (B.26) becomes zero.

The partial derivatives of the adhesive traction $\boldsymbol{T}_{\mathrm{a}k}$ with respect to the nodal displacement vector $\mathbf{u}_{l}^{e}$ of body $\mathcal{B}_l$ (see Eq. (B.3)) can be obtained similarly as [257]

$$\frac{\partial\boldsymbol{T}_{\mathrm{a}k}}{\partial\mathbf{u}_{l}^{e}} = -T_{\mathrm{a}k}'\boldsymbol{n}_{\mathrm{p}}\otimes\boldsymbol{n}_{\mathrm{p}}\,\mathbf{N}_{l}^{e} + T_{\mathrm{a}k}\frac{\partial\boldsymbol{n}_{\mathrm{p}}}{\partial\mathbf{u}_{l}^{e}} - \frac{\boldsymbol{T}_{\mathrm{a}k}}{J_{cl}^{e}}\otimes\frac{\partial J_{cl}^{e}}{\partial\mathbf{u}_{l}^{e}}\,, \tag{B.30}$$

with

$$\frac{\partial\boldsymbol{n}_{\mathrm{p}}}{\partial\mathbf{u}_{l}^{e}} = -\frac{1}{r_{\mathrm{s}}}\Big[\boldsymbol{I}-\boldsymbol{n}_{\mathrm{p}}\otimes\boldsymbol{n}_{\mathrm{p}}-c_{\mathrm{p}}^{\alpha\beta}\boldsymbol{a}_{\mathrm{p}}^{\alpha}\otimes\boldsymbol{a}_{\mathrm{p}}^{\beta}\Big]\,\mathbf{N}_{l}^{e}(\boldsymbol{\xi}_{\mathrm{p}}) - c_{\mathrm{p}}^{\alpha\beta}\boldsymbol{a}_{\mathrm{p}}^{\alpha}\otimes\boldsymbol{n}_{\mathrm{p}}\,\mathbf{N}_{l,\beta}^{e}(\boldsymbol{\xi}_{\mathrm{p}}) \tag{B.31}$$

and

$$\frac{\partial J_{cl}^{e}}{\partial\mathbf{u}_{l}^{e}} = -J_{cl,\alpha}^{e}\,c_{\mathrm{p}}^{\alpha\beta}\,\boldsymbol{a}_{\mathrm{p}}^{\beta}\,\mathbf{N}_{l}^{e}(\boldsymbol{\xi}_{\mathrm{p}}) + \Big[J_{cl}^{e}\,\boldsymbol{a}_{\mathrm{p}}^{\beta} + r_{\mathrm{s}}\,J_{cl,\alpha}^{e}\,c_{\mathrm{p}}^{\alpha\beta}\,\boldsymbol{n}_{\mathrm{p}}\Big]\,\mathbf{N}_{l,\beta}^{e}(\boldsymbol{\xi}_{\mathrm{p}})\,. \tag{B.32}$$

Finally, substituting Eqs. (B.7), (B.18), (B.22), (B.26) into Eq. (B.6), the partial derivative of the adhesive traction with respect to the point $\boldsymbol{x}_k$ can be evaluated. This in turn can be used to compute the partial derivatives of the normal (adhesive) tractions in Eq. (B.2). Similarly by combining Eqs.(B.30) with Eqs. (B.31) and (B.32), the partial derivatives of the normal (adhesive) traction with respect to the nodal displacement vector $\mathbf{u}_{l}^{e}$ of body $\mathcal{B}_l$ in Eq. (B.3) can be computed.

B.2 Contact tangent in tangential direction

In this section, the contact tangent matrix related to the tangential tractions during sliding and sticking are derived following Appendix B of Sauer and DeLorenzis [258]. It should be noted that unless stated otherwise, all quantities refer to the current pseudo-time step $t+\Delta t$.

B.2.1 Tangential sticking

The tangential traction during sticking is given by the elastic predictor given by Eq. (2.69), i.e. $\boldsymbol{T}_{\mathrm{f}k} = (\boldsymbol{T}_{\mathrm{f}})_{\mathrm{tr}}$, where

$$(\boldsymbol{T}_{\mathrm{f}})_{\mathrm{tr}} = \varepsilon_{\mathrm{T}} \left[\boldsymbol{x}_l \left(\boldsymbol{\xi}_{\mathrm{p}}^{t+\Delta t} \right) - \boldsymbol{x}_l \left(\boldsymbol{\xi}_{\mathrm{s}}^{t} \right) \right] . \tag{B.33}$$

The partial derivative of $\boldsymbol{T}_{\mathrm{f}k}$ with respect to the nodal displacement $\mathbf{u}_k^e$ then follows with $\boldsymbol{x}_{\mathrm{p}} := \boldsymbol{x}_l(\boldsymbol{\xi}_{\mathrm{p}})$ [258]

$$\begin{aligned} \frac{\partial \boldsymbol{T}_{\mathrm{f}k}}{\partial \mathbf{u}_k^e} &= \frac{\partial (\boldsymbol{T}_{\mathrm{f}})_{\mathrm{tr}}}{\partial \boldsymbol{x}_k} \frac{\partial \boldsymbol{x}_k}{\partial \mathbf{u}_k^e} \\ &= \varepsilon_{\mathrm{T}} \frac{\partial \boldsymbol{x}_{\mathrm{p}}}{\partial \boldsymbol{x}_k} \frac{\partial \boldsymbol{x}_k}{\partial \mathbf{u}_k^e} \end{aligned} \tag{B.34}$$

Eq. (B.34) can be rewritten using Eq. (B.14) and approximations in Eq. (3.3) and (3.6) as

$$\frac{\partial \boldsymbol{T}_{\mathrm{f}k}}{\partial \mathbf{u}_k^e} = \varepsilon_{\mathrm{T}}\, c_{\mathrm{p}}^{\alpha\beta}\, \boldsymbol{a}_{\alpha}^{\mathrm{p}} \otimes \boldsymbol{a}_{\beta}^{\mathrm{p}}\, \mathbf{N}_k^e \,, \tag{B.35}$$

The partial derivatives of the tangential traction during sticking with respect to the nodal displacement vector $\mathbf{u}_l^e$ of body $\mathcal{B}_l$ can be obtained similarly as

$$\frac{\partial \boldsymbol{T}_{\mathrm{f}k}}{\partial \mathbf{u}_l^e} = \varepsilon_{\mathrm{T}} \left[\frac{\partial \boldsymbol{x}_{\mathrm{p}}}{\partial \mathbf{u}_l^e} - \frac{\partial \boldsymbol{x}_l(\boldsymbol{\xi}_{\mathrm{s}}^t)}{\partial \mathbf{u}_l^e} \right] . \tag{B.36}$$

Following Sauer and DeLorenzis [257] we can write,

$$\frac{\partial \boldsymbol{x}_{\mathrm{p}}}{\partial \mathbf{u}_l^e} = \mathbf{N}_l^e(\boldsymbol{\xi}_{\mathrm{p}}) - c_{\mathrm{p}}^{\alpha\beta}\, \boldsymbol{a}_{\alpha}^{\mathrm{p}} \otimes \left(\boldsymbol{a}_{\beta}^{\mathrm{p}}\, \mathbf{N}_l^e(\boldsymbol{\xi}_{\mathrm{p}}) - r_{\mathrm{s}}\, \boldsymbol{n}_{\mathrm{p}}\, \mathbf{N}_{l,\beta}^e(\boldsymbol{\xi}_{\mathrm{p}}) \right) ; \tag{B.37}$$

$$\frac{\partial \boldsymbol{x}_l(\boldsymbol{\xi}_{\mathrm{s}}^t)}{\partial \mathbf{u}_l^e} = \mathbf{N}_l^e(\boldsymbol{\xi}_{\mathrm{s}}^t) \,. \tag{B.38}$$

B.2.2 Tangential sliding

If the bodies in contact are sliding with respect to each other, then the tangential traction is given by Eq. (2.59) or Eq. (2.77) as

$$\boldsymbol{T}_{\mathrm{f}k} = T_{\mathrm{slide}}\, \boldsymbol{n}_{\mathrm{T}} \,, \quad \text{with} \quad \boldsymbol{n}_{\mathrm{T}} = \frac{(\boldsymbol{T}_{\mathrm{f}})_{\mathrm{tr}}}{\|(\boldsymbol{T}_{\mathrm{f}})_{\mathrm{tr}}\|} \,. \tag{B.39}$$

where the trial traction $(\boldsymbol{T}_{\mathrm{f}})_{\mathrm{tr}}$ is given by Eq. (2.77) and the superscript $t + \Delta t$ is omitted. Then, the partial derivatives of the tangential traction in Eqs. (B.2) and

(B.3) can be evaluated as [258]

$$\frac{\partial \boldsymbol{T}_{\mathrm{f}k}}{\partial \mathbf{u}_k^e} = T_{\mathrm{slide}} \frac{\partial \boldsymbol{n}_{\mathrm{T}}}{\partial \mathbf{u}_k^e} + \boldsymbol{n}_{\mathrm{T}} \otimes \frac{\partial T_{\mathrm{slide}}}{\partial \mathbf{u}_k^e}\,, \tag{B.40}$$

$$\frac{\partial \boldsymbol{T}_{\mathrm{f}k}}{\partial \mathbf{u}_l^e} = T_{\mathrm{slide}} \frac{\partial \boldsymbol{n}_{\mathrm{T}}}{\partial \mathbf{u}_l^e} + \boldsymbol{n}_{\mathrm{T}} \otimes \frac{\partial T_{\mathrm{slide}}}{\partial \mathbf{u}_l^e}\,, \tag{B.41}$$

From Eq. (B.39), we can compute

$$\frac{\partial \boldsymbol{n}_{\mathrm{T}}}{\partial \mathbf{u}_k^e} = \frac{\partial \boldsymbol{n}_{\mathrm{T}}}{\partial (\boldsymbol{T}_{\mathrm{f}})_{\mathrm{tr}}} \frac{\partial (\boldsymbol{T}_{\mathrm{f}})_{\mathrm{tr}}}{\partial \mathbf{u}_k^e}\,, \tag{B.42}$$

$$\frac{\partial \boldsymbol{n}_{\mathrm{T}}}{\partial \mathbf{u}_l^e} = \frac{\partial \boldsymbol{n}_{\mathrm{T}}}{\partial (\boldsymbol{T}_{\mathrm{f}})_{\mathrm{tr}}} \frac{\partial (\boldsymbol{T}_{\mathrm{f}})_{\mathrm{tr}}}{\partial \mathbf{u}_l^e}\,, \tag{B.43}$$

with

$$\frac{\partial \boldsymbol{n}_{\mathrm{T}}}{\partial (\boldsymbol{T}_{\mathrm{f}})_{\mathrm{tr}}} = \frac{1}{\|(\boldsymbol{T}_{\mathrm{f}})_{\mathrm{tr}}\|} \Big[\boldsymbol{I} - \boldsymbol{n}_{\mathrm{T}} \otimes \boldsymbol{n}_{\mathrm{T}}\Big]\,. \tag{B.44}$$

Using the above equations, Eqs. (B.40) and (B.41) can be rewritten as

$$\frac{\partial \boldsymbol{T}_{\mathrm{f}k}}{\partial \mathbf{u}_k^e} = T_{\mathrm{slide}} \frac{\partial \boldsymbol{n}_{\mathrm{T}}}{\partial (\boldsymbol{T}_{\mathrm{f}})_{\mathrm{tr}}} \frac{\partial (\boldsymbol{T}_{\mathrm{f}})_{\mathrm{tr}}}{\partial \mathbf{u}_k^e} + \boldsymbol{n}_{\mathrm{T}} \otimes \frac{\partial T_{\mathrm{slide}}}{\partial \mathbf{u}_k^e}\,, \tag{B.45}$$

$$\frac{\partial \boldsymbol{T}_{\mathrm{f}k}}{\partial \mathbf{u}_l^e} = T_{\mathrm{slide}} \frac{\partial \boldsymbol{n}_{\mathrm{T}}}{\partial (\boldsymbol{T}_{\mathrm{f}})_{\mathrm{tr}}} \frac{\partial (\boldsymbol{T}_{\mathrm{f}})_{\mathrm{tr}}}{\partial \mathbf{u}_l^e} + \boldsymbol{n}_{\mathrm{T}} \otimes \frac{\partial T_{\mathrm{slide}}}{\partial \mathbf{u}_l^e}\,, \tag{B.46}$$

The partial derivatives of the sliding threshold in the above equations can be derived from Eq. (2.50) as

$$\left[\frac{\partial T_{\mathrm{slide}}}{\partial \mathbf{u}_k^e}\right]^{\mathrm{T}} = \left[\frac{\mu_{\mathrm{s}}}{J_{cl}^e} T'_{\mathrm{a}k}(r_{\mathrm{s}})\, \boldsymbol{n}_{\mathrm{p}} - \frac{T_{\mathrm{slide}}}{J_{cl}^e} \frac{\partial J_{cl}^e}{\partial \boldsymbol{x}_k}\right]^{\mathrm{T}} \mathbf{N}_k^e\,, \tag{B.47}$$

$$\left[\frac{\partial T_{\mathrm{slide}}}{\partial \mathbf{u}_l^e}\right]^{\mathrm{T}} = \frac{\mu_{\mathrm{s}}}{J_{cl}^e} T'_{\mathrm{a}k}(r_{\mathrm{s}})\, \boldsymbol{n}_{\mathrm{p}}^{\mathrm{T}}\, \mathbf{N}_l^e - \frac{T_{\mathrm{slide}}}{J_{cl}^e} \left[\frac{\partial J_{cl}^e}{\partial \mathbf{u}_l^e}\right]^{\mathrm{T}}\,, \tag{B.48}$$

where $T'_{\mathrm{a}k}(r_{\mathrm{s}})$ is given by Eq. (B.7). The partial derivatives of the local surface stretch $\partial J_{cl}^e/\partial \boldsymbol{x}_k$ and $\partial J_{cl}^e/\partial \mathbf{u}_l^e$ are given by Eqs. (B.26) and (B.32), respectively. Similar equations can be obtained for the quantities in current configuration.

भारतीय प्रौद्योगिकी संस्थान गुवाहाटी
Indian Institute of Technology Guwahati

Appendix C

Supplementary Material for Bayesian Regularization Based Backpropagation

C.1 Results from finite element simulations

Table C1 lists the values of the maximum normal force $F_{\mathrm{N}}^{\max}$, maximum tangential force $F_{\mathrm{T}}^{\max}$, applied displacement at force maximum $\bar{u}^{\max}$, applied displacement at $\bar{u}^{\det}$, and resultant force angle at detachment $\alpha^{\det}$ for different peeling angles as obtained in Chapter 4 using nonlinear finite element analysis.

Table C1: Data from finite element results for "Type I" peeling of Section 4.3.1a.

No.	Peeling angle θ_{P} [degrees]	Applied displacement at force maximum $\bar{u}^{\max}$ [nm]	Maximum normal force $F_{\mathrm{N}}^{\max}$ [nN]	Maximum tangential force $F_{\mathrm{T}}^{\max}$ [nN]	Applied displacement at detachment $\bar{u}^{\det}$ [nm]	Resultant force angle at detachment $\alpha^{\det}$ [degrees]
1	10	41.8	174.1584	1722.719	393.4	25.64973
2	15	35.6	171.1613	1529.699	263.8	25.57726
3	20	33.8	165.5169	1370.545	199.6	25.56427
4	25	32.4	160.1255	1240.153	161.6	25.59890
5	30	31.2	155.0284	1129.391	136.6	25.60988
6	35	30.6	150.3356	1034.944	119.0	25.55115
7	40	30.2	145.7655	950.3074	106.2	25.55958
8	45	30.0	141.2537	872.9422	96.6	25.61840
9	50	30.2	136.8172	801.4117	89.2	25.65779
10	55	30.6	132.2554	733.2346	83.4	25.62680
11	60	31.4	127.5051	667.3803	78.8	25.53845
12	65	32.8	122.5176	602.7001	75.4	25.66338
13	70	34.4	117.0706	537.6730	72.6	25.51802
14	75	36.8	110.9777	471.2534	70.6	25.49363
15	80	40.2	104.0514	402.4569	69.4	25.69447
16	85	44.8	95.87533	330.1474	68.4	25.44845
17	90	51.8	86.18540	254.5306	68.2	25.49894

C.2 Framework of Bayesian regularization based backpropagation

The algorithm for the Bayesian regularization based backpropagation is composed of the following steps:

1. Pick training data set D containing the 13 cases specified in Table 5.1, 5.2 and Appendix C.1.
   (a) Input vector, $\mathbf{u}$: Peeling angles θ_{p}
   (b) Target output vector, $\mathbf{t}_{\mathrm{o}}$: $\bar{\boldsymbol{u}}^{\max}$, $\boldsymbol{F}_{\mathrm{N}}^{\max}$ (for BPNN-I)
   $\bar{\boldsymbol{u}}^{\max}$, $\boldsymbol{F}_{\mathrm{T}}^{\max}$ (for BPNN-II)
   $\bar{\boldsymbol{u}}^{\det}$, $\boldsymbol{\alpha}^{\det}$ (for BPNN-III)
2. Initialize neural network with
   (a) Number of neurons in the input layer equal to the number of input vectors, which is equal to 1 for all the three BPNN models as described in step 1(a), i.e. $N^1 = 1$.
   (b) Number of neurons in the output layer equal to the number of output vectors, which is equal to 2 for all the three BPNN models as described in Table 5.2, i.e. $N^3 = 2$.
   (c) Number of neurons in the hidden layer equal to one, i.e. $N^2 = 1$.
3. Set learning method to Bayesian regularization
   (a) Set maximum number of epochs to 2000.
   (b) Divide the training data set as per Table 5.1.
4. Train the network
   (a) Compute regularization parameters μ_{r} and ν_{r} using Eq. (5.18).
   (b) Backpropagate sensitivities calculated using Eqs. (5.3) and (5.4).
   (c) Update weights using Eq. (5.22).
5. Compute mean square error (MSE) using Eq. (5.23).
6. Loop over steps 4 and 5 with different number of neurons in the hidden layer.
7. Plot the MSE vs. number of neurons in the hidden layer as in Fig. 5.2.

8. Select the number of neurons in the hidden layer to be the value from which MSE attains a broad minimum and decreases as N^2 is further increased. This determines the optimal network structure N^1-N^2-N^3.

9. Retrain the neural network model with optimal network structure from step 8.

10. Save the model parameters (as in Table 5.3) along with weights and biases.

11. Using the saved parameters in step 10, predict for the testing data set in Table 5.1.

भारतीय प्रौद्योगिकी संस्थान गुवाहाटी
Indian Institute of Technology Guwahati

References

[1] Autumn, K., Liang, Y. A., Hsieh, S. T., Zesch, W., Chan, W. P., Kenny, T. W., Fearing, R., and Full, R. J., "Adhesive force of a single gecko foot-hair", *Nature*, Vol. 405, No. 6787, 681–685, **2000**, DOI: 10.1038/35015073.

[2] Autumn, K., Sitti, M., Liang, Y. A., Peattie, A. M., Hansen, W. R., Sponberg, S., Kenny, T. W., Fearing, R., Israelachvili, J. N., and Full, R. J., "Evidence for van der Waals adhesion in gecko setae", *Proc. Natl. Acad. Sci.*, Vol. 99, No. 19, 12252–12256, **2002**, DOI: 10.1073/pnas.192252799.

[3] Autumn, K., "Gecko adhesion: structure, function, and applications", *MRS Bull.*, Vol. 32, No. 6, 473–478, **2007**, DOI: 10.1557/mrs2007.80.

[4] Menon, C., Murphy, M., and Sitti, M., "Gecko inspired surface climbing robots", in: *IEEE International Conference on Robotics and Biomimetics (ROBIO)*, Shenyang, China, **2004**, 431–436, DOI: 10.1109/ROBIO.2004.1521817.

[5] Asbeck, A., Dastoor, S., Parness, A., Fullerton, L., Esparza, N., Soto, D., Heyneman, B., and Cutkosky, M., "Climbing rough vertical surfaces with hierarchical directional adhesion", in: *IEEE International Conference on Robotics and Automation*, Kobe, Japan, **2009**, 2675–2680, DOI: 10.1109/ROBOT.2009.5152864.

[6] Hawkes, E. W., Christensen, D. L., and Cutkosky, M. R., "Vertical dry adhesive climbing with a 100× bodyweight payload", in: *IEEE International Conference on Robotics and Automation (ICRA)*, Seattle, WA, USA, **2015**, 3762–3769, DOI: 10.1109/ICRA.2015.7139722.

[7] Christensen, D. L., Hawkes, E. W., Suresh, S. A., Ladenheim, K., and Cutkosky, M. R., "μTugs: Enabling microrobots to deliver macro forces with controllable adhesives", in: *IEEE International Conference on Robotics and Automation (ICRA)*, Seattle, WA, USA, **2015**, 4048–4055, DOI: 10.1109/ICRA.2015.7139765.

[8] Raut, H. K., Baji, A., Hariri, H. H., Parveen, H., Soh, G. S., Low, H. Y., and Wood, K. L., "Gecko-inspired dry adhesive based on micro–nanoscale hierarchical arrays for application in climbing devices", *ACS Appl. Mater. Interfaces*, Vol. 10, No. 1, 1288–1296, **2018**, DOI: 10.1021/acsami.7b09526.

[9] Drotlef, D.-M., Amjadi, M., Yunusa, M., and Sitti, M., "Bioinspired composite microfibers for skin adhesion and signal amplification of wearable sensors", *Adv. Mater.*, Vol. 29, No. 28, 1701353, **2017**, DOI: 10.1002/adma.201701353.

[10] Jiang, H. et al., "A robotic device using gecko-inspired adhesives can grasp and manipulate large objects in microgravity", *Sci. Robot.*, Vol. 2, No. 7 **2017**, DOI: 10.1126/scirobotics.aan4545.

[11] Hou, X., Su, Y., Jiang, S., Li, L., Chen, T., Sun, L., and Deng, Z., "Adhesion mechanism of space-climbing robot based on discrete element and dynamics", *Adv. Mech. Engg.*, Vol. 10, No. 4, 1687814018772934, **2018**, DOI: 10.1177/1687814018772934.

[12] Wang, Z., Wang, Z., Dai, Z., and Gorb, S. N., "Bio-inspired adhesive footpad for legged robot climbing under reduced gravity: Multiple toes facilitate stable attachment", *Appl. Sci.*, Vol. 8, No. 1 **2018**, DOI: 10.3390/app8010114.

[13] Pugno, N. M., "Spiderman gloves", *Nano Today*, Vol. 3, 35–41, **2008**, DOI: 10.1016/S1748-0132(08)70063-X.

[14] Hawkes, E. W., Eason, E. V., Christensen, D. L., and Cutkosky, M. R., "Human climbing with efficiently scaled gecko-inspired dry adhesives.", *J. R. Soc. Interface*, Vol. 12, 20140675, **2015**, DOI: 10.1098/rsif.2014.0675.

[15] Autumn, K., Niewiarowski, P. H., and Puthoff, J. B., "Gecko adhesion as a model system for integrative biology, interdisciplinary science, and bioinspired engineering", *Annu. Rev. Ecol. Evol. Syst.*, Vol. 45, No. 1, 445–470, **2014**, DOI: 10.1146/annurev-ecolsys-120213-091839.

[16] Arnold, E. N. and Poinar, G., "A 100 million year old gecko with sophisticated adhesive toe pads, preserved in amber from Myanmar", *Zootaxa*, Vol. 1847, No. 1, 62–68, **2008**, DOI: 10.11646/zootaxa.1847.1.5.

[17] Aristotle, *Historia animalium, Book IX, transl. DW Thompson.* UK: Clarendon: Oxford, **1910**.

[18] Home, E., "Some account of the feet of those animals whose progressive motion can be carried on in opposition to gravity", *Philos. Trans. R. Soc. London*, Vol. 106, 149–155, plates VII and VIII, **1816**, DOI: 10.1098/rstl.1816.0010.

[19] Home, E., "Farther observations on the feet of animals whose progressive motion can be carried on against gravity", *Philos. Trans. R. Soc. London*, Vol. 106, 322–330, plates XVII–XXI, **1816**, DOI: 10.1098/rstl.1816.0024.

[20] Cartier, O., "Studien über den feineren bau der haut bei den reptilien I. abt epidermis der geckotiden verhandlungen der würzburger", *Phys-Med Gesellschaft*, Vol. 1, 83–96, **1872**.

[21] Simmermacher, G., "Haftapparate bei wirbeltieren", *Zool. Garten*, Vol. 25, 289–301, **1884**.

[22] Wagler, J. G., *Natürliches system der amphibien: mit vorangehender vlassification der säugethiere und vögel: ein beitrag zur vergleichenden zoologie*, Munich: J.G. Cotta'scchen Buchhandlung, **1830**, 380.

[23] Tornier, G., "Ein eidechsenschwanz mit saugscheibe", *Biol. Centralblatt*, Vol. 19, 549–552, **1899**.

[24] Schmidt, H. R., "Zur anatomie und physiologie der geckopfote", *Jena. Z. Naturwiss.*, Vol. 39, 551–580, **1904**.

[25] Dellit, W. F., "Zur anatomie und physiologie der geckozehe.", *Jena. Z. Naturwiss.*, Vol. 38, 613–656, **1934**.

[26] Haase, A., "Untersuchungen über den bau und die entwicklung der haftlappen bei den geckotiden.", *Arch. Naturgesch.*, Vol. 66, 321–345, **1900**.

[27] Hora, S. L., "The adhesive apparatus on the toes of certain geckos and tree frogs", *J. Proc. Asiat. Soc. Beng.*, Vol. 9, 137–145, **1923**.

[28] Mahendra, B. C., "Contributions to the bionomics, anatomy, reproduction and development of the Indian house-gecko, *Hemidactylus flaviviridis* Rüppel Part II. The problem of locomotion", *Proc. Indian Acad. Sci. Sect. B*, Vol. 13, 288–306, **1941**.

[29] Maderson, P. F. A., "Keratinized epidermal derivatives as an aid to climbing in gekkonid lizards", *Nature*, Vol. 203, 780–781, **1964**.

[30] Altevogt, R., "Probleme eines fusses", *Kosmos*, Vol. 50, 428–430, **1954**.

[31] Ruibal, R. and Ernst, V., "The structure of the digital setae of lizards", *J. Morphol.*, Vol. 117, 271–293, **1965**.

[32] Hiller, U., "Untersuchungen zum feinbau und zur funktion der haftborsten von reptilien", *Z. Morph. Tiere.*, Vol. 62, 307–362, **1968**.

[33] Hiller, U., "Correlation between corona-discharge of polyethylene-films and the adhering power of *Tarentola m. mauritanica* (Rept.)", *Forma et funct.*, Vol. 1, 350–352, **1969**.

[34] Hiller, U., "Comparative studies on the functional morphology of two gekkonid lizards", *J. Bombay Nat. Hist. Soc.*, Vol. 73, 278–282, **1975**.

[35] Stork, N. E., "Experimental analysis of adhesion of *Chrysolina polita* (Chrysomelidae: Coleoptera) on a variety of surfaces", *J. Exp. Biol.*, Vol. 88, No. 1, 91–108, **1980**.

[36] Irschick, D. J., Austin, C. C., Petren, K., Fisher, R. N., Losos, J. B., and Ellers, O., "A comparative analysis of clinging ability among pad-bearing lizards", *Biol. J. Linn. Soc.*, Vol. 59, No. 1, 21–35, **1996**, DOI: 10.1111/j.1095-8312.1996.tb01451.x.

[37] Jagota, A. and Hui, C.-Y., "Adhesion, friction, and compliance of bio-mimetic and bio-inspired structured interfaces", *Mater. Sci. Eng. R Rep.*, Vol. 72, No. 12, 253–292, **2011**, DOI: https://doi.org/10.1016/j.mser.2011.08.001.

[38] Russell, A. P., "Integrative functional morphology of the gekkotan adhesive system (Reptilia: Gekkota)", *Integr. Comp. Biol.*, Vol. 42, No. 6, 1154–1163, **2002**, DOI: 10.1093/icb/42.6.1154.

[39] Autumn, K. and Peattie, A. M., "Mechanisms of adhesion in geckos", *Integr. Comp. Biol.*, Vol. 42, No. 6, 1081–1090, **2002**, DOI: 10.1093/icb/42.6.1081.

[40] Autumn, K., "How gecko toes stick: The powerful, fantastic adhesive used by geckos is made of nanoscale hairs that engage tiny forces, inspiring envy among human imitators", *Am. Sci.*, Vol. 94, No. 2, 124–132, **2006**, DOI: 10.1511/2006.58.124.

[41] Russell, A. P., Stark, A. Y., and Higham, T. E., "The integrative biology of gecko adhesion: historical review, current understanding, and grand challenges", *Integr. Comp. Biol.*, Vol. 59, No. 1, 101–116, **2019**, DOI: 10.1093/icb/icz032.

[42] Sitti, M. and Fearing, R. S., "Synthetic gecko foot-hair micro/nano-structures as dry adhesives", *J. Adhes. Sci. Tech.*, Vol. 17, No. 8, 1055–1073, **2003**, DOI: 10.1163/156856103322113788.

[43] Gao, H., Wang, X., Yao, H., Gorb, S., and Arzt, E., "Mechanics of hierarchical adhesion structures of geckos", *Mech. Mater.*, Vol. 37, No. 2, 275–285, **2005**, DOI: https://doi.org/10.1016/j.mechmat.2004.03.008.

[44] Chen, B., Wu, P. D., and Gao, H., "Hierarchical modelling of attachment and detachment mechanisms of gecko toe adhesion", *Proc. R. Soc. A: Math. Phys. Engg. Sci.*, Vol. 464, No. 2094, 1639–1652, **2008**, DOI: 10.1098/rspa.2007.0350.

[45] Russell, A. P., "A contribution to the functional analysis of the foot of the Tokay, *Gekko gecko* (Reptilia: Gekkonidae)", *J. Zool.*, Vol. 176, No. 4, 437–476, **1975**, DOI: 10.1111/j.1469-7998.1975.tb03215.x.

[46] Russell, A. P., "Descriptive and functional anatomy of the digital vascular system of the tokay, Gekko gecko", *J. Morphol.*, Vol. 169, No. 3, 293–323, **1981**, DOI: 10.1002/jmor.1051690305.

[47] Stewart, W. J. and Higham, T. E., "Passively stuck: death does not affect gecko adhesion strength", *Biol. Lett.*, Vol. 10, No. 12, 20140701, **2014**, DOI: 10.1098/rsbl.2014.0701.

[48] Autumn, K., Dittmore, A., Santos, D., Spenko, M., and Cutkosky, M., "Frictional adhesion: a new angle on gecko attachment", *J. Exp. Biol.*, Vol. 209, No. 18, 3569–3579, **2006**, DOI: 10.1242/jeb.02486.

[49] Kendall, K., "Thin-film peeling-the elastic term", *J. Phys. D. Appl. Phys.*, Vol. 8, 1449–1452, **1975**, DOI: 10.1088/0022-3727/8/13/005.

[50] Gravish, N., Wilkinson, M., and Autumn, K., "Frictional and elastic energy in gecko adhesive detachment", *J. R. Soc. Interface*, Vol. 5, No. 20, 339–348, **2008**, DOI: 10.1098/rsif.2007.1077.

[51] Labonte, D. and Federle, W., "Biomechanics of shear-sensitive adhesion in climbing animals: peeling, pre-tension and sliding-induced changes in interface strength", *J. R. Soc. Interface*, Vol. 13, No. 122, 20160373, **2016**, DOI: 10.1098/rsif.2016.0373.

[52] Schleich, H. H. and Kästle, W., "Ultrastrukturen an geckoZehen (Reptilia: Sauria: Gekkonidae)", *Amphibia-Reptilia*, Vol. 7, 141–166, **1986**, DOI: https://doi.org/10.1163/156853886X00361.

[53] Israelachvili, J. N. and Tabor, D., "The calculation of van der Waals dispersion forces between macroscopic bodies", *Proc. R. Soc. London. A. Math. Phys. Sci.*, Vol. 331, No. 1584, 39–55, **1972**, DOI: 10.1098/rspa.1972.0163.

[54] Johnson, K. L., Kendall, K., and Roberts, A. D., "Surface energy and the contact of elastic solids", *Proc. R. Soc. London. A. Math. Phys. Sci.*, Vol. 324, No. 1558, 301–313, **1971**, DOI: 10.1098/rspa.1971.0141.

[55] Sun, W., Neuzil, P., Kustandi, T. S., Oh, S., and Samper, V. D., "The nature of the gecko lizard adhesive force", *Biophys. J.*, Vol. 89, No. 2, L14–L17, **2005**, DOI: https://doi.org/10.1529/biophysj.105.065268.

[56] Huber, G., Mantz, H., Spolenak, R., Mecke, K., Jacobs, K., Gorb, S. N., and Arzt, E., "Evidence for capillarity contributions to gecko adhesion from single spatula nanomechanical measurements", *Proc. Natl. Acad. Sci.*, Vol. 102, No. 45, 16293–16296, **2005**, DOI: 10.1073/pnas.0506328102.

[57] Niewiarowski, P. H., Lopez, S., Ge, L., Hagan, E., and Dhinojwala, A., "Sticky gecko feet: The role of temperature and humidity", *PLOS ONE*, Vol. 3, No. 5, 1–7, **2008**, DOI: 10.1371/journal.pone.0002192.

[58] Puthoff, J. B., Prowse, M. S., Wilkinson, M., and Autumn, K., "Changes in materials properties explain the effects of humidity on gecko adhesion", *J. Exp. Biol.*, Vol. 213, No. 21, 3699–3704, **2010**, DOI: 10.1242/jeb.047654.

[59] Prowse, M. S., Wilkinson, M., Puthoff, J. B., Mayer, G., and Autumn, K., "Effects of humidity on the mechanical properties of gecko setae", *Acta Biomater.*, Vol. 7, No. 2, 733–738, **2011**, DOI: https://doi.org/10.1016/j.actbio.2010.09.036.

[60] Huber, G., Orso, S., Spolenak, R., Wegst, U. G. K., Enders, S., Gorb, S., and Arzt, E., "Mechanical properties of a single gecko seta", *Int. J. Mater. Res.*, Vol. 99, 1113–1118, **2008**, DOI: 10.3139/146.101750.

[61] Peattie, A. M., Majidi, C., Corder, A., and Full, R. J., "Ancestrally high elastic modulus of gecko setal β-keratin", *J. R. Soc. Interface*, Vol. 4, No. 17, 1071–1076, **2007**, DOI: 10.1098/rsif.2007.0226.

[62] Bhushan, B. and Sundararajan, S., "Micro/nanoscale friction and wear mechanisms of thin films using atomic force and friction force microscopy", *Acta Material.*, Vol. 46, No. 11, 3793–3804, **1998**, DOI: https://doi.org/10.1016/S1359-6454(98)00062-7.

[63] Sundararajan, S. and Bhushan, B., "Development of AFM-based techniques to measure mechanical properties of nanoscale structures", *Sensors Actuators A*, Vol. 101, No. 3, 338–351, **2002**, DOI: https://doi.org/10.1016/S0924-4247(02)00268-6.

[64] Gianola, D. S. and Eberl, C., "Micro- and nanoscale tensile testing of materials", *JOM*, Vol. 61, 24, **2009**, DOI: https://doi.org/10.1007/s11837-009-0037-3.

[65] Hill, G. C., Soto, D. R., Peattie, A. M., Full, R. J., and Kenny, T. W., "Orientation angle and the adhesion of single gecko setae", *J. R. Soc. Interface*, Vol. 8, No. 60, 926–933, **2011**, DOI: 10.1098/rsif.2010.0720.

[66] Huber, G., Gorb, S. N., Spolenak, R., and Arzt, E., "Resolving the nanoscale adhesion of individual gecko spatulae by atomic force microscopy", *Biol. Lett.*, Vol. 1, No. 1, 2–4, **2005**, DOI: 10.1098/rsbl.2004.0254.

[67] Huber, G., Gorb, S., Hosoda, N., Spolenak, R., and Arzt, E., "Influence of surface roughness on gecko adhesion", *Acta Biomater.*, Vol. 3, No. 4, 607–610, **2007**, DOI: 10.1016/j.actbio.2007.01.007.

[68] Persson, B. N. J. and Gorb, S., "The effect of surface roughness on the adhesion of elastic plates with application to biological systems", *J. Chem. Phys.*, Vol. 119, No. 21, 11437–11444, **2003**, DOI: 10.1063/1.1621854.

[69] Pillai, R., Nordberg, E., Riedel, J., and Schwarzkopf, L., "Nonlinear variation in clinging performance with surface roughness in geckos", *Ecol. Evol.*, Vol. 10, No. 5, 2597–2607, **2020**, DOI: 10.1002/ece3.6090.

[70] Pugno, N. M. and Lepore, E., "Observation of optimal gecko's adhesion on nanorough surfaces", *Biosystems*, Vol. 94, No. 3, 218–222, **2008**, DOI: https://doi.org/10.1016/j.biosystems.2008.06.009.

[71] Briggs, G. A. D. and Briscoe, B. J., "The effect of surface topography on the adhesion of elastic solids", *J. Phys. D: Appl. Phys.*, Vol. 10, No. 18, 2453–2466, **1977**, DOI: 10.1088/0022-3727/10/18/010.

[72] Fuller, K. N. G. and Tabor, D., "The effect of surface roughness on the adhesion of elastic solids", *Proc. R. Soc. London. A. Math. Phys. Sci.*, Vol. 345, No. 1642, 327–342, **1975**, DOI: 10.1098/rspa.1975.0138.

[73] Hertz, H., "Uber die berührung fester elastischer Körper (On the contact of elastic solids)", *J. Reine. Angew. Math.*, Vol. 92, 156–171, **1882**.

[74] Rizzo, N. W., Gardner, K. H., Walls, D. J., Keiper-Hrynko, N. M., Ganzke, T. S., and Hallahan, D. L., "Characterization of the structure and composition of gecko adhesive setae", *J. R. Soc. Interface*, Vol. 3, No. 8, 441–451, **2006**, DOI: 10.1098/rsif.2005.0097.

[75] Arzt, E., Gorb, S., and Spolenak, R., "From micro to nano contacts in biological attachment devices", *Proc. Natl. Acad. Sci.*, Vol. 100, No. 19, 10603–10606, **2003**, DOI: 10.1073/pnas.1534701100.

[76] Federle, W., "Why are so many adhesive pads hairy?", *J. Exp. Biol.*, Vol. 209, No. 14, 2611–2621, **2006**, DOI: 10.1242/jeb.02323.

[77] Tang, T., Hui, C.-Y., and Glassmaker, N. J., "Can a fibrillar interface be stronger and tougher than a non-fibrillar one?", *J. R. Soc. Interface*, Vol. 2, No. 5, 505–516, **2005**, DOI: 10.1098/rsif.2005.0070.

[78] Derjaguin, B., Muller, V., and Toporov, Y., "Effect of contact deformations on the adhesion of particles", *J. Coll. Interface Sci.*, Vol. 53, No. 2, 314–326, **1975**, DOI: https://doi.org/10.1016/0021-9797(75)90018-1.

[79] Gao, H. and Yao, H., "Shape insensitive optimal adhesion of nanoscale fibrillar structures", *Proc. Natl. Acad. Sci.*, Vol. 101, No. 21, 7851–7856, **2004**, DOI: 10.1073/pnas.0400757101.

[80] Gao, H., Ji, B., Jäger, I. L., Arzt, E., and Fratzl, P., "Materials become insensitive to flaws at nanoscale: Lessons from nature", *Proc. Natl. Acad. Sci.*, Vol. 100, No. 10, 5597–5600, **2003**, DOI: 10.1073/pnas.0631609100.

[81] Gao, H. and Chen, S., "Flaw tolerance in a thin strip under tension", *ASME J. Appl. Mech.*, Vol. 72, No. 5, 732–737, **2005**, DOI: 10.1115/1.1988348.

[82] Hansen, W. R. and Autumn, K., "Evidence for self-cleaning in gecko setae", *Proc. Natl. Acad. Sci.*, Vol. 102, No. 2, 385–389, **2005**, DOI: 10.1073/pnas.0408304102.

[83] Spolenak, R., Gorb, S., Gao, H., and Arzt, E., "Effects of contact shape on the scaling of biological attachments", *Proc. R. Soc. A: Math. Phys. Engg. Sci.*, Vol. 461, No. 2054, 305–319, **2005**, DOI: 10.1098/rspa.2004.1326.

[84] Varenberg, M., Pugno, N. M., and Gorb, S. N., "Spatulate structures in biological fibrillar adhesion", *Soft Matter*, Vol. 6, 3269–3272, 14 **2010**, DOI: 10.1039/C003207G.

[85] Israelachvili, J. N., *Intermolecular and surface forces*, 3rd, London: Academic Press, **2011**.

[86] Peng, Z. and Chen, S., "Effects of the relative humidity and water droplet on adhesion of a bio-inspired nano-film", *Colloids Surf. B: Biointerface*, Vol. 88, No. 2, 717–721, **2011**, DOI: https://doi.org/10.1016/j.colsurfb.2011.08.006.

[87] Peng, Z., "Effects of surface roughness and film thickness on the adhesion of a bio-inspired nanofilm", in: *Bio-inspired studies on adhesion of a thin film on a rigid substrate*, Berlin, Heidelberg: Springer Berlin Heidelberg, **2015**, 55–70, DOI: 10.1007/978-3-662-46955-2_5.

[88] Nosonovsky, M. and Bhushan, B., "Multiscale friction mechanisms and hierarchical surfaces in nano- and bio-tribology", *Mater. Sci. Eng. R*, Vol. 58, No. 3, 162–193, **2007**, DOI: https://doi.org/10.1016/j.mser.2007.09.001.

[89] Rabinowicz, E., "The intrinsic variables affecting the stick-slip process", *Proc. Phys. Soc.*, Vol. 71, No. 4, 668–675, **1958**, DOI: 10.1088/0370-1328/71/4/316.

[90] Dieterich, J. H., "Time-dependent friction in rocks", *J. Geophys. Res.*, Vol. 77, No. 20, 3690–3697, **1972**, DOI: 10.1029/JB077i020p03690.

[91] Baumberger, T. and Caroli, C., "Solid friction from stick–slip down to pinning and aging", *Adv. Phys.*, Vol. 55, No. 3-4, 279–348, **2006**, DOI: 10.1080/00018730600732186.

[92] Ruina, A., "Slip instability and state variable friction laws", *J. Geophys. Res.*, Vol. 88, No. B12, 10359–10370, **1983**, DOI: 10.1029/JB088iB12p10359.

[93] Johannes, V. I., Green, M. A., and Brockley, C. A., "The role of the rate of application of the tangential force in determining the static friction coefficient", *Wear*, Vol. 24, No. 3, 381–385, **1973**, DOI: https://doi.org/10.1016/0043-1648(73)90166-X.

[94] Persson, B. N. J., Sivebaek, I. M., Samoilov, V. N., Zhao, K., Volokitin, A. I., and Zhang, Z., "On the origin of Amonton's friction law", *J. Phys.: Condens. Matter*, Vol. 20, No. 39, 395006, **2008**, DOI: 10.1088/0953-8984/20/39/395006.

[95] Derjaguin, B., "Molekulartheorie der äußeren reibung", *Z. Phys.*, Vol. 88, 661–675, **1934**, DOI: 10.1007/BF01333114.

[96] Homola, A. M., Israelachvili, J. N., McGuiggan, P. M., and Gee, M. L., "Fundamental experimental studies in tribology: The transition from 'interfacial' friction of undamaged molecularly smooth surfaces to 'normal' friction with wear", *Wear*, Vol. 136, No. 1, 65–83, **1990**, DOI: https://doi.org/10.1016/0043-1648(90)90072-I.

[97] Bowden, F. P. and Tabor, D., "Friction, lubrication and wear: a survey of work during the last decade", *Brit. J. Appl. Phys.*, Vol. 17, No. 12, 1521–1544, **1966**, DOI: 10.1088/0508-3443/17/12/301.

[98] Majidi, C. et al., "High friction from a stiff polymer using microfiber arrays", *Phys. Rev. Lett.*, Vol. 97, 076103, **2006**, DOI: 10.1103/PhysRevLett.97.076103.

[99] Tian, Y., Pesika, N., Zeng, H., Rosenberg, K., Zhao, B., McGuiggan, P., Autumn, K., and Israelachvili, J., "Adhesion and friction in gecko toe attachment and detachment", *Proc. Natl. Acad. Sci.*, Vol. 103, No. 51, 19320–19325, **2006**, DOI: 10.1073/pnas.0608841103.

[100] Israelachvili, J., Maeda, N., Rosenberg, K. J., and Akbulut, M., "Effects of sub-ångstrom (pico-scale) structure of surfaces on adhesion, friction, and bulk mechanical properties", *J. Mater. Res.*, Vol. 20, No. 8, 1952–1972, **2005**, DOI: 10.1557/JMR.2005.0255.

[101] Pesika, N. S., Tian, Y., Zhao, B., Rosenberg, K., Zeng, H., McGuiggan, P., Autumn, K., and Israelachvili, J. N., "Peel-zone model of tape peeling based on the gecko adhesive system", *J. Adhes.*, Vol. 83, No. 4, 383–401, **2007**, DOI: 10.1080/00218460701282539.

[102] Zhou, M., Tian, Y., Pesika, N., Zeng, H., Wan, J., Meng, Y., and Wen, S., "The extended peel zone model: effect of peeling velocity", *J. Adhes.*, Vol. 87, No. 11, 1045–1058, **2011**, DOI: 10.1080/00218464.2011.609455.

[103] Chen, B., Wu, P., and Gao, H., "Pre-tension generates strongly reversible adhesion of a spatula pad on substrate", *J. R. Soc. Interface*, Vol. 6, No. 35, 529–537, **2009**, DOI: 10.1098/rsif.2008.0322.

[104] Zhilong, P. and Shaohua, C., "Effect of pre-tension on the peeling behavior of a bio-inspired nano-film and a hierarchical adhesive structure", *Appl. Phys. Lett.*, Vol. 101, No. 16, 163702, **2012**, DOI: 10.1063/1.4758481.

[105] Zeng, H., Pesika, N., Tian, Y., Zhao, B., Chen, Y., Tirrell, M., Turner, K. L., and Israelachvili, J. N., "Frictional adhesion of patterned surfaces and implications for gecko and biomimetic systems", *Langmuir*, Vol. 25, No. 13, 7486–7495, **2009**, DOI: 10.1021/la900877h.

[106] Yamaguchi, T., Gravish, N., Autumn, K., and Creton, C., "Microscopic modeling of the dynamics of frictional adhesion in the gecko attachment system", *J. Phys. Chem. B*, Vol. 113, No. 12, 3622–3628, **2009**, DOI: 10.1021/jp8067415.

[107] Begley, M. R., Collino, R. R., Israelachvili, J. N., and McMeeking, R. M., "Peeling of a tape with large deformations and frictional sliding", *J. Mech. Phys. Solids*, Vol. 61, No. 5, 1265–1279, **2013**, DOI: https://doi.org/10.1016/j.jmps.2012.09.014.

[108] Afferrante, L., Carbone, G., Demelio, G., and Pugno, N., "Adhesion of elastic thin films: Double peeling of tapes versus axisymmetric peeling of membranes", *Tribol. Lett.*, Vol. 52, 439–447, **2013**, DOI: 10.1007/s11249-013-0227-6.

[109] Gialamas, P., Völker, B., Collino, R. R., Begley, M. R., and McMeeking, R. M., "Peeling of an elastic membrane tape adhered to a substrate by a uniform cohesive traction", *Int. J. Solid Struct.*, Vol. 51, No. 18, 3003–3011, **2014**, DOI: https://doi.org/10.1016/j.ijsolstr.2014.04.001.

[110] Dugdale, D. S., "Yielding of steel sheets containing slits", *J. Mech. Phys. Solids*, Vol. 8, No. 2, 100–104, **1960**, DOI: https://doi.org/10.1016/0022-5096(60)90013-2.

[111] Peng, Z. and Chen, S., "Effect of bending stiffness on the peeling behavior of an elastic thin film on a rigid substrate", *Phys. Rev. E*, Vol. 91, 042401, 4 **2015**, DOI: 10.1103/PhysRevE.91.042401.

[112] Peng, Z., Yin, H., Yao, Y., and Chen, S., "Effect of thin-film length on the peeling behavior of film-substrate interfaces", *Phys. Rev. E*, Vol. 100, 032804, 3 **2019**, DOI: 10.1103/PhysRevE.100.032804.

[113] He, L., Lou, J., Kitipornchai, S., Yang, J., and Du, J., "Peeling mechanics of hyperelastic beams: Bending effect", *Int. J. Solid. Struct.*, Vol. 167, 184–191, **2019**, DOI: https://doi.org/10.1016/j.ijsolstr.2019.03.011.

[114] He, L., Lou, J., Dong, Y., Kitipornchai, S., and Yang, J., "Variational modeling of plane-strain hyperelastic thin beams with thickness-stretching effect", *Acta. Mech.*, 4845–4861, **2018**, DOI: https://doi.org/10.1007/s00707-018-2258-4.

[115] Kwak, J.-S. and Kim, T. W., "A review of adhesion and friction models for gecko feet", *Int. J. Precis. Eng. Manuf.*, Vol. 11, 171–186, **2010**, DOI: 10.1007/s12541-010-0020-5.

[116] Zhou, M., Pesika, N., Zeng, H., Tian, Y., and Israelachvili, J., "Recent advances in gecko adhesion and friction mechanisms and development of gecko-inspired dry adhesive surfaces", *Friction*, Vol. 1, 114–129, **2013**, DOI: 10.1007/s40544-013-0011-5.

[117] Kasar, A. K., Ramachandran, R., and Menezes, P.-L., "Natural adhesion system leads to synthetic adhesives", *J. Bio- Tribo-Corrosion*, Vol. 4, 1–17, **2018**, DOI: 10.1007/s40735-018-0160-1.

[118] Seale, M., Cummins, C., Viola, I. M., Mastropaolo, E., and Nakayama, N., "Design principles of hair-like structures as biological machines", *J. R. Soc. Interface*, Vol. 15, No. 142, 20180206, **2018**, DOI: 10.1098/rsif.2018.0206.

[119] Federle, W. and Labonte, D., "Dynamic biological adhesion: mechanisms for controlling attachment during locomotion", *Phil. Trans. R. Soc. B: Biol. Sci.*, Vol. 374, No. 1784, 20190199, **2019**, DOI: 10.1098/rstb.2019.0199.

[120] Sauer, R. A. and Wriggers, P, "Formulation and analysis of a three-dimensional finite element implementation for adhesive contact at the nanoscale", *Comp. Meth. Appl. Mech. Eng.*, Vol. 198, No. 49–52, 3871–3883, **2009**, DOI: https://doi.org/10.1016/j.cma.2009.08.019.

[121] Derjaguin, B., "Untersuchungen über die reibung und adhäsion, IV", *Kolloid Z.*, Vol. 69, 155–164, **1934**, DOI: https://doi.org/10.1007/BF01433225.

[122] Suh, A. Y., Yu, N., Lee, K. M., Polycarpou, A. A., and Johnson, H. T., "Crystallite coalescence during film growth based on improved contact mechanics adhesion models", *J. Appl. Phys.*, Vol. 96, No. 3, 1348–1359, **2004**, DOI: 10.1063/1.1766099.

[123] Liu, T., Liu, G., Xie, Q., and Wang, Q. J., "An EFG-FE coupling method for microscale adhesive contacts", *J. Tribol. T. ASME.*, Vol. 128, No. 1, 40–48, **2005**, DOI: 10.1115/1.2114931.

[124] Kadin, Y., Kligerman, Y., and Etsion, I., "Loading–unloading of an elastic–plastic adhesive spherical microcontact", *J. Colloid Interf. Sci.*, Vol. 321, No. 1, 242–250, **2008**, DOI: https://doi.org/10.1016/j.jcis.2007.12.046.

[125] Radhakrishnan, H. and Mesarovic, S. D., "Adhesive contact of elastic spheres revisited: Numerical models and scaling", *Proc. R. Soci. A: Math. Phys. Eng. Sci.*, Vol. 465, No. 2107, 2231–2249, **2009**, DOI: 10.1098/rspa.2009.0118.

[126] Eid, H., Joshi, N., McGruer, N. E., and Adams, G. G., "A model of contact with adhesion of a layered elastic-plastic microsphere with a rigid flat surface", *J. Tribol.*, Vol. 133, No. 3 **2011**, DOI: 10.1115/1.4004343.

[127] Tworzydlo, W., Cecot, W., Oden, J. T., and Yew, C. H., "Computational micro- and macroscopic models of contact and friction: formulation, approach and applications", *Wear*, Vol. 220, No. 2, 113–140, **1998**, DOI: https://doi.org/10.1016/S0043-1648(98)00194-X.

[128] Du, Y., Chen, L., McGruer, N. E., Adams, G. G., and Etsion, I., "A finite element model of loading and unloading of an asperity contact with adhesion and plasticity", *J. Colloid Interf. Sci.*, Vol. 312, No. 2, 522–528, **2007**, DOI: https://doi.org/10.1016/j.jcis.2007.03.040.

[129] Li, F., Pan, J., and Sinka, C., "Modelling adhesive contact between fine particles using material point method", *Mech. Mater.*, Vol. 43, No. 3, 157–167, **2011**, DOI: https://doi.org/10.1016/j.mechmat.2011.02.004.

[130] Jin, C., Jagota, A., and Hui, C.-Y., "An easy-to-implement numerical simulation method for adhesive contact problems involving asymmetric adhesive contact", *J. Phys. D: Appl. Phys.*, Vol. 44, No. 40, 405303, **2011**, DOI: 10.1088/0022-3727/44/40/405303.

[131] Argento, C., Jagota, A., and Carter, W. C., "Surface formulation for molecular interactions of macroscopic bodies", *J. Mech. Phys. Solids*, Vol. 45, No. 7, 1161–1183, **1997**, DOI: https://doi.org/10.1016/S0022-5096(96)00121-4.

[132] Ardito, R., Corigliano, A., and Frangi, A., "Multiscale finite-element models for predicting spontaneous adhesion in MEMS", *Méc. Ind.*, Vol. 11, No. 3–4, 177–182, **2010**, DOI: 10.1051/meca/2010028.

[133] Cho, S.-S. and Park, S., "Finite element modeling of adhesive contact using molecular potential", *Tribol. Int.*, Vol. 37, No. 9, 763–769, **2004**, DOI: https://doi.org/10.1016/j.triboint.2004.04.007.

[134] Bobji, M. S., Xavier, S., Jayadeep, U. B., and Jog, C. S., "Adhesion-induced instability in asperities.", *Tribol. Lett.*, Vol. 39, 201–209, **2010**, DOI: https://doi.org/10.1007/s11249-010-9637-x.

[135] Jayadeep, U. B., Bobji, M. S., and Jog, C. S., "Energy loss due to adhesion in longitudinal impact of elastic cylinders", *Eur. J. Mech. A/Solids*, Vol. 45, 20–31, **2014**, DOI: https://doi.org/10.1016/j.euromechsol.2013.11.010.

[136] Jayadeep, U. B., Bobji, M. S., and Jog, C. S., "Energy loss in the impact of elastic spheres on a rigid half-space in presence of adhesion", *Tribol. Lett.*, Vol. 53, 79–89, **2014**, DOI: https://doi.org/10.1007/s11249-013-0245-4.

[137] Sauer, R. A. and Li, S., "A contact mechanics model for quasi-continua", *Int. J. Numer. Meth. Eng.*, Vol. 71, No. 8, 931–962, **2007**, DOI: 10.1002/nme.1970.

[138] Sauer, R. A. and Li, S., "An atomic interaction-based continuum model for adhesive contact mechanics", *Finite Elem. Anal. Des.*, Vol. 43, No. 5, 384–396, **2007**, DOI: https://doi.org/10.1016/j.finel.2006.11.009.

[139] Tvergaard, V. and Hutchinson, J. W., "The relation between crack growth resistance and fracture process parameters in elastic-plastic solids", *J. Mech. Phys. Solids*, Vol. 40, No. 6, 1377–1397, **1992**, ISSN: 0022-5096, DOI: https://doi.org/10.1016/0022-5096(92)90020-3.

[140] Tvergaard, V. and Hutchinson, J. W., "Effect of strain-dependent cohesive zone model on predictions of crack growth resistance", *Int. J. Solids Struct.*, Vol. 33, No. 20, 3297–3308, **1996**, DOI: https://doi.org/10.1016/0020-7683(95)00261-8.

[141] Sauer, R. A., "A survey of computational models for adhesion", *J. Adhes.*, Vol. 92, No. 2, 81–120, **2016**, DOI: 10.1080/00218464.2014.1003210.

[142] Crocombe, A. D. and Adams, R. D., "Peel analysis using the finite element method", *J. Adhes.*, Vol. 12, No. 2, 127–139, **1981**, DOI: 10.1080/00218468108071194.

[143] Anderson, G. P., DeVries, K. L., and Williams, M. L., "Finite element in adhesion analyses", *Int. J. Fract.*, Vol. 9, No. 4, 421–436, **1973**, DOI: https://doi.org/10.1007/BF00036323.

[144] Peng, Z. L., Chen, S. H., and Soh, A. K., "Peeling behavior of a bio-inspired nano-film on a substrate", *Int. J. Solids Struct.*, Vol. 47, No. 14, 1952–1960, **2010**, DOI: https://doi.org/10.1016/j.ijsolstr.2010.03.035.

[145] Cheng, Q. H., Chen, B., Gao, H. J., and Zhang, Y. W., "Sliding-induced non-uniform pre-tension governs robust and reversible adhesion: a revisit of adhesion mechanisms of geckos", *J. R. Soc. Interface*, Vol. 9, No. 67, 283–291, **2012**, DOI: 10.1098/rsif.2011.0254.

[146] Sauer, R. A., "Multiscale modelling and simulation of the deformation and adhesion of a single gecko seta", *Comp. Meth. Biomec. Biomed. Eng.*, Vol. 12, No. 6, PMID: 19319703, 627–640, **2009**, DOI: 10.1080/10255840902802917.

[147] Simo, J. C., "A finite strain beam formulation. The three-dimensional dynamic problem. Part I", *Comp. Meth. Appl. Mech. Eng.*, Vol. 49, No. 1, 55–70, **1985**, ISSN: 0045-7825, DOI: https://doi.org/10.1016/0045-7825(85)90050-7.

[148] Simo, J. C. and Vu-Quoc, L., "A three-dimensional finite-strain rod model. part II: Computational aspects", *Comp. Meth. Appl. Mech. Eng.*, Vol. 58, No. 1, 79–116, **1986**, DOI: https://doi.org/10.1016/0045-7825(86)90079-4.

[149] Sauer, R. A., "A computational model for nanoscale adhesion between deformable solids and its application to gecko adhesion", *J. Adhes. Sci. Tech.*, Vol. 24, No. 11-12, 1807–1818, **2010**, DOI: 10.1163/016942410X507588.

[150] Bhushan, B., Peressadko, A. G., and Kim, T.-W., "Adhesion analysis of two-level hierarchical morphology in natural attachment systems for 'smart adhesion'", *J. Adhes. Sci. Tech.*, Vol. 20, No. 13, 1475–1491, **2006**, DOI: 10.1163/156856106778666408.

[151] Yu, J., Chary, S., Das, S., Tamelier, J., Turner, K. L., and Israelachvili, J. N., "Friction and adhesion of gecko-inspired PDMS flaps on rough surfaces", *Langmuir*, Vol. 28, No. 31, 11527–11534, **2012**, DOI: 10.1021/la301783q.

[152] Cañas, N., Kamperman, M., Völker, B., Kroner, E., McMeeking, R. M., and Arzt, E., "Effect of nano- and micro-roughness on adhesion of bioinspired micropatterned surfaces", *Acta Biomater.*, Vol. 8, No. 1, 282–288, **2012**, DOI: https://doi.org/10.1016/j.actbio.2011.08.028.

[153] Kim, T. and Bhushan, B., "Adhesion analysis of multi-level hierarchical attachment system contacting with a rough surface", *J. Adhes. Sci. Tech.*, Vol. 21, No. 1, 1–20, **2007**, DOI: 10.1163/156856107779976097.

[154] Kim, T. and Bhushan, B., "Effect of stiffness of multi-level hierarchical attachment system on adhesion enhancement", *Ultramicroscopy*, Vol. 107, No. 10, 902–912, **2007**, DOI: 10.1016/j.ultramic.2006.11.008.

[155] Kim, T. W. and Bhushan, B., "The adhesion model considering capillarity for gecko attachment system", *J. R. Soc. Interface*, Vol. 5, No. 20, 319–327, **2008**, DOI: 10.1098/rsif.2007.1078.

[156] Schargott, M., "A mechanical model of biomimetic adhesive pads with tilted and hierarchical structures", *Bioinspir. Biomim.*, Vol. 4, No. 2, 026002, **2009**, DOI: 10.1088/1748-3182/4/2/026002.

[157] Dahlquist, C. A., "Pressure-sensitive adhesives", in: *Treatise on adhesion and adhesives*, ed. by Patrick, R. L., vol. 2, Dekker: New York, **1969**, 219–260.

[158] Autumn, K., Majidi, C., Groff, R. E., Dittmore, A., and Fearing, R., "Effective elastic modulus of isolated gecko setal arrays", *J. Exp. Biol.*, Vol. 209, No. 18, 3558–3568, **2006**, DOI: 10.1242/jeb.02469.

[159] Glassmaker, N. J., Jagota, A., Hui, C.-Y., and Kim, J., "Design of biomimetic fibrillar interfaces: 1. Making contact", *J. R. Soc. Interface*, Vol. 1, No. 1, 23–33, **2004**, DOI: 10.1098/rsif.2004.0004.

[160] Hui, C.-Y., Glassmaker, N. J., Tang, T., and Jagota, A., "Design of biomimetic fibrillar interfaces: 2. Mechanics of enhanced adhesion", *J. R. Soc. Interface*, Vol. 1, No. 1, 35–48, **2004**, DOI: 10.1098/rsif.2004.0005.

[161] Spolenak, R., Gorb, S., and Arzt, E., "Adhesion design maps for bio-inspired attachment systems", *Acta Biomater.*, Vol. 1, No. 1, 5–13, **2005**, DOI: https://doi.org/10.1016/j.actbio.2004.08.004.

[162] Sauer, R. A. and Holl, M, "A detailed 3D finite element analysis of the peeling behaviour of a gecko spatula", *Comp. Meth. Biomech. Biomed. Engin.*, Vol. 16, No. 6, 577–591, **2013**, DOI: 10.1080/10255842.2011.628944.

[163] Sauer, R. A., "Enriched contact finite elements for stable peeling computations", *Int. J. Numer. Meth. Eng.*, Vol. 87, 593–616, **2011**, DOI: 10.1002/nme.3126.

[164] Gautam, S. S. and Sauer, R. A., "A composite time integration scheme for dynamic adhesion and its application to gecko spatula peeling", *Int. J. Comp. Methods*, 1350104, **2014**, DOI: 10.1142/S0219876213501041.

[165] Sauer, R. A., "The peeling behavior of thin films with finite bending stiffness and the implications on gecko adhesion", *J. Adhes.*, Vol. 87, No. 7-8, 624–643, **2011**, DOI: 10.1080/00218464.2011.596084.

[166] Sauer, R. A. and Mergel, J. C., "A geometrically exact finite beam element formulation for thin film adhesion and debonding", *Finite Elem. Anal. Des.*, Vol. 86, 120–135, **2014**, DOI: https://doi.org/10.1016/j.finel.2014.03.009.

[167] Reissner, E., "On one-dimensional finite-strain beam theory: The plane problem", *J. Appl. Math. Phys. (ZAMP)*, Vol. 23, 795–804, **1972**, DOI: https://doi.org/10.1007/BF01602645.

[168] Grill, M. J., Wall, W. A., and Meier, C., "A computational model for molecular interactions between curved slender fibers undergoing large 3D deformations with a focus on electrostatic, van der Waals, and repulsive steric forces", *In. J. Numer. Meth. Eng.*, Vol. 121, No. 10, 2285–2330, **2020**, DOI: 10.1002/nme.6309.

[169] Grill, M. J., Meier, C., and Wall, W. A., "Investigation of the peeling and pull-off behavior of adhesive elastic fibers via a novel computational beam interaction model", *J. Adhes.* **2019**, DOI: 10.1080/00218464.2019.1699795.

[170] Zhang, X., Zhang, X., and Wen, S., "Finite element modeling of the nanoscale adhesive contact and the geometry-based pull-off force", *Tribol. Lett.*, Vol. 41, 65–72, **2011**, DOI: https://doi.org/10.1007/s11249-010-9686-1.

[171] Gorb, S., Varenberg, M., Peressadko, A., and Tuma, J., "Biomimetic mushroom-shaped fibrillar adhesive microstructure", *J. R. Soc. Interface*, Vol. 4, No. 13, 271–275, **2007**, DOI: 10.1098/rsif.2006.0164.

[172] Gorb, S. N. and Varenberg, M., "Mushroom-shaped geometry of contact elements in biological adhesive systems", *J. Adhes. Sci. Tech.*, Vol. 21, No. 12-13, 1175–1183, **2007**, DOI: 10.1163/156856107782328317.

[173] Campo, A. del, Greiner, C., and Arzt, E., "Contact shape controls adhesion of bioinspired fibrillar surfaces", *Langmuir*, Vol. 23, No. 20, 10235–10243, **2007**, DOI: 10.1021/la7010502.

[174] Carbone, G., Pierro, E., and Gorb, S. N., "Origin of the superior adhesive performance of mushroom-shaped microstructured surfaces", *Soft Matter*, Vol. 7, 5545–5552, 12 **2011**, DOI: 10.1039/C0SM01482F.

[175] Chary, S., Tamelier, J., and Turner, K., "A microfabricated gecko-inspired controllable and reusable dry adhesive", *Smart Mater. Struct.*, Vol. 22, No. 2, 025013, **2013**, DOI: 10.1088/0964-1726/22/2/025013.

[176] Heepe, L., Carbone, G., Pierro, E., Kovalev, A. E., and Gorb, S. N., "Adhesion tilt-tolerance in bio-inspired mushroom-shaped adhesive microstructure", *Appl. Phys. Lett.*, Vol. 104, No. 1, 011906, **2014**, DOI: 10.1063/1.4860991.

[177] Hu, H., Tian, H., Shao, J., Wang, Y., Li, X., Tian, Y., Ding, Y., and Lu, B., "Friction contribution to bioinspired mushroom-shaped dry adhesives", *Adv. Mater. Interf.*, Vol. 4, No. 9, 1700016, **2017**, DOI: 10.1002/admi.201700016.

[178] Heepe, L., Kovalev, A. E., Varenberg, M., Tuma, J., and Gorb, S. N., "First mushroom-shaped adhesive microstructure: A review", *Theor. Appl. Mech. Lett.*, Vol. 2, No. 1, 014008, **2012**, DOI: https://doi.org/10.1063/2.1201408.

[179] Pantano, A., Pugno, N. M., and Gorb, S. N., "Numerical simulations demonstrate that the double tapering of the spatualae of lizards and insects maximize both detachment resistance and stability", *Int. J. Fract.*, Vol. 171, 169–175, **2011**, DOI: https://doi.org/10.1007/s10704-011-9596-8.

[180] Mergel, J. C., Sauer, R. A., and Saxena, A., "Computational optimization of adhesive microstructures based on a nonlinear beam formulation", *Struct. Multidisc. Optim.*, Vol. 50, 1001–1017, **2014**, DOI: https://doi.org/10.1007/s00158-014-1091-1.

[181] Xu, X.-P. and Needleman, A., "Void nucleation by inclusion debonding in a crystal matrix", *Model. Simul. Mater. Sci. Eng.*, Vol. 1, No. 2, 111–132, **1993**, DOI: 10.1088/0965-0393/1/2/001.

[182] Mergel, J. C. and Sauer, R. A., "On the optimum shape of thin adhesive strips for various peeling directions", *J. Adhes.*, Vol. 90, No. 5–6, 526–544, **2014**, DOI: 10.1080/00218464.2013.840538.

[183] Gillies, A. G. and Fearing, R. S., "Simulation of synthetic gecko arrays shearing on rough surfaces", *J. R. Soc. Interface*, Vol. 11, No. 95, 20140021, **2014**, DOI: 10.1098/rsif.2014.0021.

[184] Milstein, F., "Applicability of exponentially attractive and repulsive interactomic potential functions in the description of cubic crystals", *J. Appl. Phys.*, Vol. 44, No. 9, 3825–3832, **1973**, DOI: 10.1063/1.1662857.

[185] Chiu, J., Lin, Y., Shen C. Lo, S.-P., and Wu, W.-J., "Atomic-scale finite-element model of tension in nanoscale thin film", *Int. J. Adv. Manuf. Technol.*, Vol. 37, 76–82, **2008**, DOI: https://doi.org/10.1007/s00170-007-0959-2.

[186] Filippov, A., Popov, V. L., and Gorb, S. N., "Shear induced adhesion: Contact mechanics of biological spatula-like attachment devices", *J. Theor. Biol.*, Vol. 276, No. 1, 126–131, **2011**, DOI: https://doi.org/10.1016/j.jtbi.2011.01.049.

[187] Mishra, S., Annepu, H., and Sarkar, J., "A finite element study of adhesion of soft thin elastic films cast on rough surfaces", *Int. J. Adhes. Adhesiv.*, Vol. 79, 102–110, **2017**, DOI: https://doi.org/10.1016/j.ijadhadh.2017.09.013.

[188] Kovalev, A., Filippov, A. E., and Gorb, S. N., "Critical roughness in animal hairy adhesive pads: A numerical modeling approach", *Bioinspir. Biomim.*, Vol. 13, No. 6, 066004, **2018**, DOI: 10.1088/1748-3190/aadd66.

[189] Tvergaard, V., "Effect of fibre debonding in a whisker-reinforced metal", *Mater. Sci. Eng. A*, Vol. 125, No. 2, 203–213, **1990**, DOI: https://doi.org/10.1016/0921-5093(90)90170-8.

[190] Lissenden, C. J. and Herakovich, C. T., "Numerical modelling of damage development and viscoplasticity in metal matrix composites", *Comp. Meth. Appl. Mech. Eng.*, Vol. 126, No. 3, 289–303, **1995**, DOI: https://doi.org/10.1016/0045-7825(95)00810-N.

[191] Chaboche, J., Girard, R., and Schaff, A., "Numerical analysis of composite systems by using interphase/interface models", *Comput. Mech.*, Vol. 20, 3–11, **1997**, DOI: https://doi.org/10.1007/s004660050209.

[192] Raous, M., Cangémi, L., and Cocu, M., "A consistent model coupling adhesion, friction, and unilateral contact", *Comp. Meth. Appl. Mech. Eng.*, Vol. 177, No. 3, 383–399, **1999**, DOI: https://doi.org/10.1016/S0045-7825(98)00389-2.

[193] Raous, M. and Monerie, Y., "Unilateral contact, friction and adhesion: 3D cracks in composite materials", in: *Contact Mechanics*, Dordrecht: Springer Netherlands, **2002**, 333–346.

[194] Cocou, M., Schryve, M., and Raous, M., "A dynamic unilateral contact problem with adhesion and friction in viscoelasticity", *Z. Angew. Math. Phys.*, Vol. 61, 721–743, **2010**, DOI: https://doi.org/10.1007/s00033-009-0027-x.

[195] Snozzi, L. and Molinari, J.-F., "A cohesive element model for mixed mode loading with frictional contact capability", *Int. J. Numer. Meth. Eng.*, Vol. 93, No. 5, 510–526, **2013**, DOI: 10.1002/nme.4398.

[196] Alfano, G. and Sacco, E., "Combining interface damage and friction in a cohesive-zone model", *Int. J. Numer. Meth. Eng.*, Vol. 68, No. 5, 542–582, **2006**, DOI: 10.1002/nme.1728.

[197] Sacco, E. and Toti, J., "Interface elements for the analysis of masonry structures", *Int. J. Comput. Meth. Eng. Sci. Mech.*, Vol. 11, No. 6, 354–373, **2010**, DOI: 10.1080/15502287.2010.516793.

[198] Sacco, E. and Lebon, F., "A damage–friction interface model derived from micromechanical approach", *Int. J. Solid. Struct.*, Vol. 49, No. 26, 3666–3680, **2012**, DOI: https://doi.org/10.1016/j.ijsolstr.2012.07.028.

[199] Deng, Z., Smolyanitsky, A., Li, Q., Feng, X.-Q., and Cannara, R. J., "Adhesion-dependent negative friction coefficient on chemically modified graphite at the nanoscale", *Nature Mater.*, Vol. 11, 1032–1037, **2012**, DOI: https://doi.org/10.1038/nmat3452.

[200] Jiang, J.-W. and Park, H. S., "A Gaussian treatment for the friction issue of Lennard-Jones potential in layered materials: Application to friction between graphene, MoS2, and black phosphorus", *J. Appl. Phys.*, Vol. 117, No. 12, 124304, **2015**, DOI: 10.1063/1.4916538.

[201] Eason, E. V., Hawkes, E. W., Windheim, M., Christensen, D. L., Libby, T., and Cutkosky, M. R., "Stress distribution and contact area measurements of a gecko toe using a high-resolution tactile sensor", *Bioinspir. Biomim.*, Vol. 10, No. 1, 016013, **2015**, DOI: 10.1088/1748-3190/10/1/016013.

[202] Mergel, J. C., Sahli, R., Scheibert, J., and Sauer, R. A., "Continuum contact models for coupled adhesion and friction", *J. Adhes.*, Vol. 95, No. 12, 1101–1133, **2019**, DOI: 10.1080/00218464.2018.1479258.

[203] Mergel, J. C., Scheibert, J., and Sauer, R. A., *Contact with coupled adhesion and friction: Computational framework, applications, and new insights*, **2020**, arXiv: 2001.06833 [cs.CE].

[204] Yagawa, G. and Okuda, H., "Neural networks in computational mechanics", *Arch. Comput. Methods Eng.*, Vol. 3, No. 4, 435–512, **1996**, DOI: 10.1007/BF02818935.

[205] Hambli, R., "Numerical procedure for multiscale bone adaptation prediction based on neural networks and finite element simulation", *Finite Elem. Anal. Des.*, Vol. 47, No. 7, 835–842, **2011**, DOI: 10.1016/j.finel.2011.02.014.

[206] Sengupta, N., Sahidullah, M., and Saha, G., "Lung sound classification using cepstral-based statistical features", *Comput. Biol. Med.*, Vol. 75, 118–129, **2016**, DOI: 10.1016/j.compbiomed.2016.05.013.

[207] Alizadeh, E., Lyons, S., Castle, J., and Prasad, A., "Measuring systematic changes in invasive cancer cell shape using Zernike moments", *Integr. Biol.*, Vol. 8, No. 11, 1183–1193, **2016**, DOI: 10.1039/C6IB00100A.

[208] Oishi, A. and Yagawa, G., "Computational mechanics enhanced by deep learning", *Comput. Methods Appl. Mech. Eng.*, Vol. 327, 327–351, **2017**, DOI: 10.1016/j.cma.2017.08.040.

[209] Islam, S. and Kim, A., "Machine learning enabled wearable brain deformation sensing system", in: *2019 IEEE Signal Process. Med. Biol. Symp.* IEEE, **2019**, 1–3, DOI: 10.1109/SPMB47826.2019.9037843.

[210] Sattari Baboukani, B., Ye, Z., Reyes, K. G., and Nalam, P. C., "Prediction of nanoscale friction for two-dimensional materials using a machine learning approach", *Tribol. Lett.*, Vol. 68, 57, **2020**, DOI: https://doi.org/10.1007/s11249-020-01294-w.

[211] Lagaris, I. E., Likas, A., and Fotiadis, D. I., "Artificial neural networks for solving ordinary and partial differential equations", *IEEE Trans. Neural Networks*, Vol. 9, No. 5, 987–1000, **1998**, DOI: 10.1109/72.712178, eprint: 9705023.

[212] Hakim, S. J. S. and Razak, H. A., "Structural damage detection of steel bridge girder using artificial neural networks and finite element models", *Steel Compos. Struct.*, Vol. 14, No. 4, 367–377, **2013**, DOI: 10.12989/scs.2013.14.4.367.

[213] Sadegh, H., Mehdi, A. N., and Mehdi, A., "Classification of acoustic emission signals generated from journal bearing at different lubrication conditions based on wavelet analysis in combination with artificial neural network and genetic algorithm", *Tribol. Int.*, Vol. 95, 426–434, **2016**, DOI: 10.1016/j.triboint.2015.11.045.

[214] Liang, L., Liu, M., Martin, C., and Sun, W., "A deep learning approach to estimate stress distribution: A fast and accurate surrogate of finite-element analysis", *J. R. Soc. Interface*, Vol. 15, No. 138, 20170844, **2018**, DOI: 10.1098/rsif.2017.0844.

[215] Zurada, J., *Introduction to artificial neural systems*, USA: West Publishing Co., **1992**.

[216] Yoshimura, S., Matsuda, A., and Yagawa, G., "New regularization by transformation for neural network based inverse analyses and its application to structure identification", *Int. J. Numer. Methods Eng.*, Vol. 39, No. 23, 3953–3968, **1996**, DOI: 10.1002/(SICI)1097-0207(19961215)39:23<3953::AID-NME31>3.0.CO;2-O.

[217] Lopez, R., Balsa-Canto, E., and Oñate, E., "Neural networks for variational problems in engineering", *Int. J. Numer. Methods Eng.*, Vol. 75, No. 11, 1341–1360, **2008**, DOI: 10.1002/nme.2304.

[218] Furukawa, T. and Yagawa, G., "Implicit constitutive modelling for viscoplasticity using neural networks", *Int. J. Numer. Methods Eng.*, Vol. 43, No. 2, 195–219, **1998**, DOI: 10.1002/(SICI)1097-0207(19980930)43:2<195::AID-NME418>3.0.CO;2-6.

[219] Huber, N. and Tsakmakis, C., "A neural network tool for identifying the material parameters of a finite deformation viscoplasticity model with static recovery", *Comput. Meth. Appl. Mech. Eng.*, Vol. 191, No. 3–5, 353–384, **2001**, DOI: 10.1016/S0045-7825(01)00278-X.

[220] Man, H. and Furukawa, T., "Neural network constitutive modelling for nonlinear characterization of anisotropic materials", *Int. J. Numer. Methods Eng.*, Vol. 85, No. 8, 939–957, **2011**, DOI: 10.1002/nme.2999.

[221] Li, X., Roth, C. C., and Mohr, D., "Machine-learning based temperature- and rate-dependent plasticity model: Application to analysis of fracture experiments on DP steel", *Int. J. Plast.*, Vol. 118, 320–344, **2019**, DOI: https://doi.org/10.1016/j.ijplas.2019.02.012.

[222] Liu, S., Huang, J. H., Sung, J., and Lee, C., "Detection of cracks using neural networks and computational mechanics", *Comput. Methods Appl. Mech. Eng.*, Vol. 191, No. 25–26, 2831–2845, **2002**, DOI: 10.1016/S0045-7825(02)00221-9.

[223] Zacharias, J., Hartmann, C., and Delgado, A., "Damage detection on crates of beverages by artificial neural networks trained with finite-element data", *Comput. Methods Appl. Mech. Eng.*, Vol. 193, No. 6-8, 561–574, **2004**, DOI: 10.1016/j.cma.2003.10.009.

[224] Manevitz, L., Yousef, M., and Givoli, D., "Finite-Element mesh generation using self-organizing neural networks", *Comput. Civ. Infrastruct. Eng.*, Vol. 12, No. 4, 233–250, **1997**, DOI: 10.1111/0885-9507.00060.

[225] Rapetto, M. P., Almqvist, A., Larsson, R., and Lugt, P. M., "On the influence of surface roughness on real area of contact in normal, dry, friction free, rough contact by using a neural network", *Wear*, Vol. 266, No. 5, 592–595, **2009**, DOI: https://doi.org/10.1016/j.wear.2008.04.059.

[226] Gyurova, L. A. and Friedrich, K., "Artificial neural networks for predicting sliding friction and wear properties of polyphenylene sulfide composites", *Tribol. Int.*, Vol. 44, No. 5, 603–609, **2011**, DOI: 10.1016/j.triboint.2010.12.011.

[227] Hamdia, K. M., Ghasemi, H., Bazi, Y., AlHichri, H., Alajlan, N., and Rabczuk, T., "A novel deep learning based method for the computational material design of flexoelectric nanostructures with topology optimization", *Finite Elem. Anal. Des.* **2019**, DOI: 10.1016/j.finel.2019.07.001.

[228] Gu, G. X., Chen, C.-T., Richmond, D. J., and Buehler, M. J., "Bioinspired hierarchical composite design using machine learning: simulation, additive manufacturing, and experiment", *Mater. Horiz.*, Vol. 5, 939–945, 5 **2018**, DOI: 10.1039/C8MH00653A.

[229] Oishi, A. and Yoshimura, S., "A new local contact search method using a multi-layer neural network", *Comput. Model. Eng. Sci.* **2007**, DOI: 10.3970/cmes.2007.021.093.

[230] Oishi, A. and Yagawa, G., "A surface-to-surface contact search method enhanced by deep learning", *Comput. Mech.*, Vol. 65, No. 4, 1125–1147, **2020**, DOI: 10.1007/s00466-019-01811-2.

[231] Nowell, D. and Nowell, P., "A machine learning approach to the prediction of fretting fatigue life", *Tribol. Int.*, Vol. 141, 105913, **2020**, DOI: 10.1016/j.triboint.2019.105913.

[232] Kim, Y., Yang, C., Kim, Y., Gu, G. X., and Ryu, S., "Designing an adhesive pillar shape with deep learning-based optimization", *ACS Appl. Mater. Interf.*, Vol. 12, No. 21, 24458–24465, **2020**, DOI: 10.1021/acsami.0c04123.

[233] Khoei, A. R., Moslemi, H., and Seddighian, M. R., "An efficient stress recovery technique in adaptive finite element method using artificial neural network", *Eng. Fract. Mech.*, Vol. 237, 107231, **2020**, ISSN: 0013-7944, DOI: https://doi.org/10.1016/j.engfracmech.2020.107231.

[234] Nelder, J. A. and Mead, R., "A simplex method for function minimization", *The Computer Journal*, Vol. 7, No. 4, 308–313, **1965**, DOI: 10.1093/comjnl/7.4.308.

[235] Argatov, I. I. and Chai, Y. S., "An artificial neural network supported regression model for wear rate", *Tribol. Int.*, Vol. 138, 211–214, **2019**, DOI: 10.1016/j.triboint.2019.05.040.

[236] MacKay, D., "A practical bayesian framework for backpropagation networks", *Neural Comput.*, Vol. 4, No. 3, 448–472, **1992**, DOI: 10.1162/neco.1992.4.3.448.

[237] Burden, F. and Winkler, D., "Bayesian regularization of neural networks", in: *Methods Mol. Biol.* **2008**, 23–42, DOI: 10.1007/978-1-60327-101-1_3.

[238] Saini, L. M. and Soni, M. K., "Artificial neural network based peak load forecasting using Levenberg–Marquardt and quasi-Newton methods", *IEE Proc. - Gener. Transm. Distrib.*, Vol. 149, No. 5, 578, **2002**, DOI: 10.1049/ip-gtd:20020462.

[239] Hagan, M. T. and Menhaj, M. B., "Training feedforward networks with the Marquardt algorithm", *IEEE Trans. Neural Networ.*, Vol. 5, No. 6, 989–993, **1994**, DOI: 10.1109/72.329697.

[240] Kayri, M., "Predictive abilities of Bayesian regularization and Levenberg–Marquardt algorithms in artificial neural networks: A comparative empirical study on social Data", *Math. Comput. Appl.*, Vol. 21, No. 2, 20, **2016**, DOI: 10.3390/mca21020020.

[241] Lefik, M. and Schrefler, B. A., "Artificial neural network as an incremental non-linear constitutive model for a finite element code", *Comput. Methods Appl. Mech. Eng.*, Vol. 192, No. 28–30, 3265–3283, **2003**, DOI: 10.1016/S0045-7825(03)00350-5.

[242] Li, H.-F. and Lee, S.-Y., "Mining frequent itemsets over data streams using efficient window sliding techniques", *Expert Syst. Appl.*, Vol. 36, No. 2, 1466–1477, **2009**, DOI: 10.1016/j.eswa.2007.11.061.

[243] Ticknor, J. L., "A Bayesian regularized artificial neural network for stock market forecasting", *Expert Syst. Appl.*, Vol. 40, No. 14, 5501–5506, **2013**, DOI: 10.1016/j.eswa.2013.04.013.

[244] Koroglu, S., Sergeant, P., and Umurkan, N., "Comparison of analytical, finite element and neural network methods to study magnetic shielding", *Simul. Model. Pract. Theory*, Vol. 18, No. 2, 206–216, **2010**, DOI: 10.1016/j.simpat.2009.10.007.

[245] Yang, K. and Xiong, M., "Prediction of CH4 adsorption on different activated carbons by developing an optimal multilayer perceptron artificial neural network", *Energ. Sources, Part A.*, Vol. 41, No. 17, 2061–2072, **2019**, DOI: 10.1080/15567036.2018.1549161.

[246] Frenkel, D. and Smit B., *Understanding molecular simulation: From algorithms to applications*, 2nd, San Diego: Academic Press, **2001**.

[247] Tadmor, E. B., Ortiz, M., and Phillips, R., "Quasicontinuum analysis of defects in solids", *Phil. Mag. A*, Vol. 73, No. 6, 1529–1563, **1996**, DOI: 10.1080/01418619608243000.

[248] Shenoy, V. B., Miller, R., Tadmor, E. B., Rodney, D., Phillips, R., and Ortiz, M., "An adaptive finite element approach to atomic-scale mechanics—the quasicontinuum method", *J. Mech. Phys. Solids*, Vol. 47, No. 3, 611–642, **1999**, DOI: https://doi.org/10.1016/S0022-5096(98)00051-9.

[249] Knap, J. and Ortiz, M., "An analysis of the quasicontinuum method", *J. Mech. Phys. Solids*, Vol. 49, No. 9, 1899–1923, **2001**, DOI: https://doi.org/10.1016/S0022-5096(01)00034-5.

[250] Wriggers, P., *Computational contact mechanics*, Berlin, Heidelberg: Springer, **2006**.

[251] Konyukhov, A. and Izi, R., *Introduction to computational contact mechanics: A geometrical approach*, 1st, John Wiley & Sons Ltd, **2015**.

[252] Laursen, T. A., *Computational contact and impact mechanics: fundamentals of modeling interfacial phenomena in nonlinear finite element analysis*, Engineering online library. Springer, **2003**.

[253] Jog, C. S, *Continuum mechanics: Foundations and applications of mechanics*, 3rd, vol. 1, Cambridge University Press, **2015**, DOI: 10.1017/CBO9781316134054.

[254] Bonet, J. and Wood, R. D, *Nonlinear continuum mechanics for finite element analysis*, 2nd, Cambridge: Cambridge University Press, **2008**.

[255] Ogden R. W., *Non-linear elastic deformations*, Chichester: Ellis Horwood and John Wiley, **1984**.

[256] Tabor, D, "Surface forces and surface interactions", *J. Coll. Inter. Sci.*, Vol. 58, 2–13, **1977**, DOI: 10.1016/0021-9797(77)90366-6.

[257] Sauer, R. A. and De Lorenzis, L., "A computational contact formulation based on surface potentials", *Comp. Meth. Appl. Mech. Eng.*, Vol. 253, 369–395, **2013**, DOI: https://doi.org/10.1016/j.cma.2012.09.002.

[258] Sauer, R. A. and De Lorenzis, L., "An unbiased computational contact formulation for 3D friction", *Int. J. Numer. Meth. Eng.*, Vol. 101, No. 4, 251–280, **2015**, DOI: 10.1002/nme.4794.

[259] Wriggers, P., *Nonlinear finite element methods*, Berlin, Heidelberg: Springer, **2008**.

[260] Hu, C. and Greaney, P. A., "Role of seta angle and flexibility in the gecko adhesion mechanism", *J. Appl. Phys.*, Vol. 116, No. 7, 074302, **2014**, DOI: 10.1063/1.4892628.

[261] Sekiguchi, Y., Takahashi, K., and Sato, C., "Adhesion mechanism of a gecko-inspired oblique structure with an adhesive tip for asymmetric detachment", *J. Phys. D: Appl. Phys.*, Vol. 48, No. 47, 475301, **2015**, DOI: 10.1088/0022-3727/48/47/475301.

[262] Puthoff, J. B., Holbrook, M., Wilkinson, M. J., Jin, K., Pesika, N. S., and Autumn, K., "Dynamic friction in natural and synthetic gecko setal arrays", *Soft Matter*, Vol. 9, 4855–4863, 19 **2013**, DOI: 10.1039/C3SM50267H.

[263] Pesika, N. S., Gravish, N., Wilkinson, M., Zhao, B., Zeng, H., Tian, Y., Israelachvili, J., and Autumn, K., "The crowding model as a tool to understand and fabricate gecko-inspired dry adhesives", *J. Adhes.*, Vol. 85, No. 8, 512–525, **2009**, DOI: 10.1080/00218460902996390.

[264] Stark, A. Y., Sullivan, T. W., and Niewiarowski, P. H., "The effect of surface water and wetting on gecko adhesion", *J. Exp. Biol.*, Vol. 215, No. 17, 3080–3086, **2012**, DOI: 10.1242/jeb.070912, eprint: https://jeb.biologists.org/content/215/17/3080.full.pdf.

[265] Autumn, K., Hsieh, S. T., Dudek, D. M., Chen, J., Chitaphan, C., and Full, R. J., "Dynamics of geckos running vertically", *J. Exp. Biol.*, Vol. 209, No. 2, 260–272, **2006**, DOI: 10.1242/jeb.01980.

[266] Hu, S., Lopez, S., Niewiarowski, P. H., and Xia, Z., "Dynamic self-cleaning in gecko setae via digital hyperextension", *J. R. Soc. Interface*, Vol. 9, No. 76, 2781–2790, **2012**, DOI: 10.1098/rsif.2012.0108.

[267] Schubert, B., Lee, J., Majidi, C., and Fearing, R. S., "Sliding-induced adhesion of stiff polymer microfibre arrays. II. Microscale behaviour", *J. R. Soc. Interface*, Vol. 5, No. 25, 845–853, **2008**, DOI: 10.1098/rsif.2007.1309.

[268] Corbett, C. J. and Sauer, R. A., "NURBS-enriched contact finite elements", *Comput. Meth. Appl. Mech. Eng.*, Vol. 275, 55–75, **2014**, DOI: https://doi.org/10.1016/j.cma.2014.02.019.

[269] Demuth, H., Beale, M., De Jess, O., and Hagan, M., *Neural network design*, 2nd, Martin Hagan, **2014**.

[270] Hagan, M. T., Demuth, H. B., and Jesús, O. D., "An introduction to the use of neural networks in control systems", *Int. J. Robust Nonlinear Control*, Vol. 12, No. 11, 959–985, **2002**, DOI: 10.1002/rnc.727.

[271] Tikhonov, A., "The solution of ill-posed problems and the regularization method", *Dokl. Akad. Nauk SSSR*, Vol. 151, 501–504, **1963**.

[272] Dan Foresee, F. and Hagan, M., "Gauss-Newton approximation to Bayesian learning", in: *Proc. Int. Conf. Neural Networks*, vol. 3, IEEE, **1997**, 1930–1935, DOI: 10.1109/ICNN.1997.614194.

[273] De Lorenzis, L. and Wriggers, P., "Computational homogenization of rubber friction on rough rigid surfaces", *Comput. Mater. Sci.*, Vol. 77, 264–280, **2013**, DOI: https://doi.org/10.1016/j.commatsci.2013.04.049.

[274] Agrawal, V. and Gautam, S. S., "Varying-order NURBS discretization: An accurate and efficient method for isogeometric analysis of large deformation contact problems", *Comput. Meth. Appl. Mech. Eng.*, Vol. 367, 113125, **2020**, DOI: https://doi.org/10.1016/j.cma.2020.113125.

भारतीय प्रौद्योगिकी संस्थान गुवाहाटी
Indian Institute of Technology Guwahati

List of Publications

Journals (Accepted)

1. Gouravaraju, S.; Sauer, R. A.; Gautam, S. S. Investigating the normal and tangential peeling behaviour of gecko spatulae using a coupled adhesion–friction model, The Journal of Adhesion, 2020 (In Press, DOI: https://doi.org/10.1080/00218464.2020.1719838).

2. Gouravaraju, S.; Sauer, R. A.; Gautam, S. S. On the presence of a critical detachment angle in gecko spatula peeling – A numerical investigation using an adhesive friction model, The Journal of Adhesion, 2020 (In Press, DOI: https://doi.org/10.1080/00218464.2020.1719838).

Conferences (Published/Accepted)

1. Gouravaraju, S.; Gautam. S. S. Nonlinear finite element analysis of a gecko spatula adhesion on a rigid substrate, 1st International Conference on Future Learning Aspects of Mechanical Engineering (FLAME) Amity University, Noida, 3^{rd} –5^{th} October, 2018.

2. Gouravaraju, S.; Gautam, S. S. Investigating the influence of geometrical and material parameters on peeling behaviour of a gecko spatula. 1st International Conference on Applied Mechanical Engineering Research (IC-AMER), NIT Warangal, India, 02^{nd} – 05^{th} May, 2019.

3. Gouravaraju, S.; Agrawal, V.; Sauer, R. A.; Gautam, S. S. Numerical analysis of a gecko spatula peeling using adhesive friction model, 7th International Congress on Computational Mechanics and Simulation (ICCMS), IIT Mandi, India, 11^{th} – 13^{th} December, 2019.

4. Gouravaraju, S.; Sauer, R. A.; Gautam, S. S. Critical detachment angle in gecko spatula peeling – a finite element study using an adhesive friction model, 14th World Congress in Computational Mechanics (WCCM) ECCOMAS Congress, Paris, France, 11^{th} – 15^{th} January, 2021 (Accepted).

Poster Presentation

1. Gouravaraju, S.; Gautam, S. S. Gecko adhesion – Explaining the strong attachment and easy detachment at nanoscale spatula level, Research Conclave (RC), IIT Guwahati, India, 14th – 17th March, 2019 (Awarded 2nd Prize).